

Document Version

Final published version

Citation (APA)

Kolah Kaj, P. (2026). *Improving geomechanical and thermal rock property prediction of Dutch geothermal plays*. [Dissertation (TU Delft), Delft University of Technology]. <https://doi.org/10.4233/uuid:8efba807-22a3-4f9f-b73e-5afbce251966>

Important note

To cite this publication, please use the final published version (if applicable). Please check the document version above.

Copyright

In case the licence states "Dutch Copyright Act (Article 25fa)", this publication was made available Green Open Access via the TU Delft Institutional Repository pursuant to Dutch Copyright Act (Article 25fa, the Taverne amendment). This provision does not affect copyright ownership. Unless copyright is transferred by contract or statute, it remains with the copyright holder.

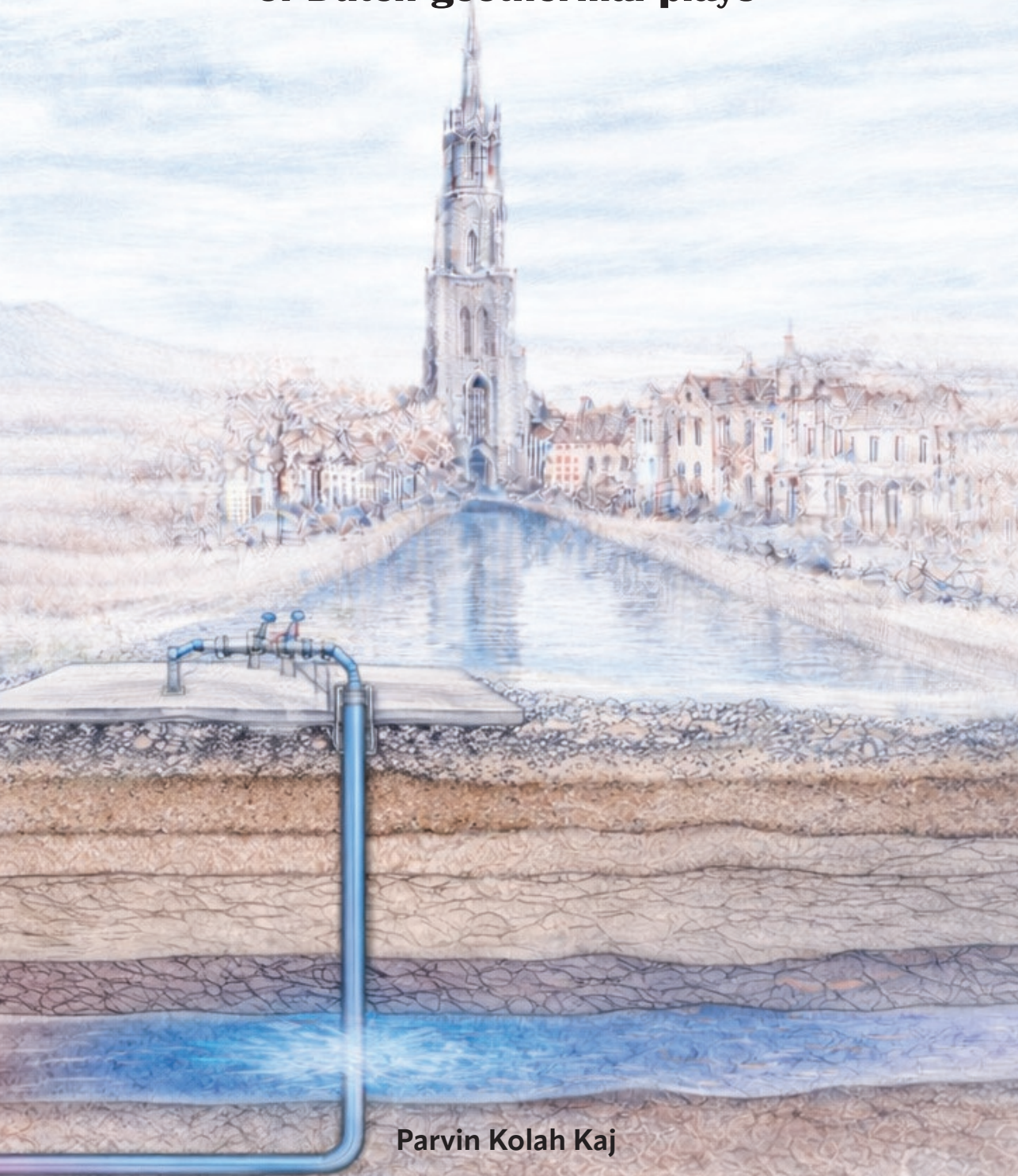
Sharing and reuse

Other than for strictly personal use, it is not permitted to download, forward or distribute the text or part of it, without the consent of the author(s) and/or copyright holder(s), unless the work is under an open content license such as Creative Commons.

Takedown policy

Please contact us and provide details if you believe this document breaches copyrights. We will remove access to the work immediately and investigate your claim.

Improving geomechanical and thermal rock property prediction of Dutch geothermal plays



Parvin Kolah Kaj

Propositions accompanying the thesis

Improving geomechanical and thermal rock property prediction of Dutch geothermal plays

by

Parvin Kolah Kaj

1. Porosity is the primary control on thermal conductivity in sandstones, but the systematic offsets between the Buntsandstein and Rotliegend demonstrate that mineralogy and diagenesis must also be considered (This thesis).
2. Predicting thermal diffusivity from well logs alone is unrealistic; mineralogical input from sampled material should be considered essential (This thesis).
3. Dynamic-to-static modulus conversions must be formation-specific; applying generic formulas to geothermal reservoirs is unreliable (This thesis).
4. Real progress in the long journey of the energy transition requires new generations to preserve old knowledge and companies to share resources for new knowledge.
5. Any transition that ignores energy poverty is unsustainable, no matter how green.
6. Double standards exist in both science and society, and are equally undesirable in both.
7. Nations that rely on migrants should value their well-being as much as their labour.
8. Knowledge security should protect sensitive knowledge from misuse, not filter certain nationalities.
9. Courses and meetings are valuable only when they accomplish something that cannot be achieved through an email or a document.
10. Succeeding grows from motivation, while winning stems from perfectionism; one may win without succeeding.

These propositions are regarded as opposable and defensible, and have been approved as such by the promoters Dr. H. A. Abels, Dr. A. Barnhoorn, Prof. dr. P. J. Vardon.

Improving geomechanical and thermal rock property prediction of Dutch geothermal plays

Improving geomechanical and thermal rock property prediction of Dutch geothermal plays

Dissertation

for the purpose of obtaining the degree of doctor

at Delft University of Technology

by the authority of the Rector Magnificus Prof.dr. H. Bijl

chair of the Board for Doctorates

to be defended publicly on

Monday March 16th, 2026, at 17:30

by

Parvin KOLAH KAJ

This dissertation has been approved by the promotor.

Composition of the doctoral committee:

Rector Magnificus	Chairman
Dr. H. A. Abels	Delft University of Technology, promotor
Dr. A. Barnhoorn	Delft University of Technology, promotor
Prof. dr. P. J. Vardon	Delft University of Technology, promotor

Independent members:

Dr. S. Hangx	Utrecht University
Dr. A.M.H. Pluymakers	Delft University of Technology
Prof.dr.ir. L.V. Socco	Delft University of Technology
Prof.dr.ir. F. Vossepoel	Delft University of Technology
Dr. J.E.A. Storms	Delft University of Technology, reserve member

This thesis was part of and supported by the ProperBase project, a project within the Topsector Energie executed by Rijksdienst voor Ondernemend Nederland (RVO), project TSE-18-19-01-Geo-energie.



Key words: Geothermal reservoirs, thermal properties, rock physics, petrophysical properties, mineralogy, acoustic velocities, elastic moduli, well logs, machine learning, Dutch subsurface

Printed by: www.proefschriftmaken.nl

Cover: designed by Parvin Kolah Kaj and generated by ChatGPT 5.2

Copyright: 2026 © by P. Kolah Kaj

ISBN: 978-94-6534-262-7

An electronic copy of this dissertation is available at:

<https://doi.org/10.4233/uuid:8efba807-22a3-4f9f-b73e-5afbce251966>

To my Ahmed and my family,
all that I am and all that I have.

Contents

Summary.....	IX
Samenvatting.....	XIII
1. Introduction.....	1
1.1. Motivation and background.....	2
1.2. Scope and objectives.....	5
1.3. Structure of the thesis and chapter interconnections.....	8
2. Thermal and acoustic characterisation of Permian Rotliegend sandstones: evaluating the effects of porosity and mineralogy on predicting thermal properties.....	9
2.1. Introduction.....	10
2.2. Study area and materials.....	13
2.3. Methods.....	15
2.4. Results.....	16
2.4.1. Mineralogy and grain size.....	23
2.5. Discussion.....	28
2.5.1. Acoustic properties.....	29
2.5.2. Thermal properties.....	30
2.5.3. Quantitative comparison of property relationships in this and previous studies.....	33
2.6. Conclusion.....	35
2.7. Appendix 1.....	36
2.8. Appendix 2.....	38
3. Porosity and Mineralogical Controls on Thermal and Acoustic Properties of Sandstones from the Triassic Main Buntsandstein Subgroup and Permian Upper Rotliegend Group in the Netherlands.....	41
3.1. Introduction.....	42
3.1.1. Thermo-physical properties.....	44
3.1.2. Geological background.....	45
3.2. Material and methods.....	48
3.3. Results.....	49
3.3.1. Exploratory data analysis: Triassic versus Permian.....	49
3.3.2. Principal Component and Canonical Correlation Analysis.....	53
3.3.3. Core plug descriptions.....	55
3.4. Discussion.....	60
3.4.1. Acoustic Properties.....	61
3.4.2. Thermal Properties.....	64
3.5. Conclusion.....	69
4. Coupled mechanical and thermo-physical characterisation of the lower Cretaceous Delft Sandstone Member for geothermal applications.....	71
4.1. Introduction.....	72
4.2. Study area and materials.....	80
4.3. Methodology.....	82
4.3.1. Laboratory measurements.....	83
4.3.2. Downhole petrophysical log data.....	85
4.3.3. Data analysis and modelling workflow.....	86
4.4. Results.....	90
4.4.1. Exploratory data analysis.....	90
4.4.2. Static versus dynamic Young's modulus.....	98
4.4.3. Dynamic elastic moduli from log and laboratory data.....	102
4.5. Discussion.....	105
4.5.1. Cross property analysis.....	105
4.5.2. Correlating static and dynamic Young's modulus.....	109
4.6. Conclusion.....	112
4.7. Appendix 1.....	114
4.7.1. Static Young's modulus for shale, indirect method.....	114
4.7.2. Dynamic shear and bulk moduli, and Poisson's ratio.....	115

5. Integrating experimental and log data to predict thermal rock properties in geothermal plays using machine learning.....	119
5.1. Introduction	120
5.1.1. Literature review.....	122
5.2. Methodology.....	123
5.2.1. Study area and material.....	123
5.2.2. Data preparation.....	125
5.2.3. Prediction workflows.....	126
5.3. Results	129
5.3.1. Experimental data	129
5.3.2. Integration of experimental data and petrophysical logs	137
Feature importance analysis.....	149
5.4. Discussion	156
5.4.1. Interpretation of experimental data.....	157
5.4.2. Evaluation of the ML models	158
5.5. Conclusions	161
6. Synthesis and Conclusions.....	163
6.1. Integrated dataset and experimental insights	164
6.2. Formation-specific observations and comparisons	165
6.3. Log-based estimation and machine learning approaches.....	167
6.4. Broader contributions and applications	168
6.5. Final remarks and recommendations	172
References.....	173
Authors Contributions.....	193
Acknowledgments	195
Curriculum Vitae	199
List of Publications	201

Summary

The energy transition requires reliable and cost-efficient subsurface resources to meet the growing societal demands for sustainable energy. In the Netherlands, geothermal energy is considered a major contributor to achieving our climate and energy goals. The success of geothermal projects depends strongly on our understanding of the reservoir. To do so, knowing thermo-physical and mechanical properties of the reservoir rocks, which govern both heat transfer and mechanical stability are important. However, these properties are often poorly constrained due to high measurement costs, the substantial time required for laboratory testing, and limited availability of suitable rock material. In addition, reliable rock property prediction is challenging because of strong heterogeneity in lithology, mineralogical composition, and diagenetic history. This thesis generates a comprehensive database of thermal, acoustic, and mechanical properties for key Dutch geothermal formations. Based on the measured data, and by integrating them with downhole petrophysical logs, several predictive equations and models were generated, also with the use of machine learning techniques. These equations and models improve property predictions tailored for the Dutch subsurface, while together improving the characterisation of geothermal reservoirs in general.

The research begins with a comprehensive study of Permian Rotliegend sandstones, a key targeted geothermal reservoir in the Netherlands. More than 1100 core plugs were studied to determine porosity, bulk density, acoustic velocities, thermal properties, and mineralogy. The results confirm that porosity is the primary controlling factor on most other rock properties. Higher porosity corresponds to lower density, acoustic velocity, thermal conductivity, and diffusivity. Nevertheless, systematic deviations from the main trends were observed that could sometimes be explained by mineralogical effects as well as structural and diagenetic factors. For example, the presence of nacrite and other kaolinite-group minerals enhanced thermal conductivity beyond porosity-based predictions, while other clay types normally reduced thermal conductivity. These findings highlight that porosity is the dominant control, but mineralogy and texture impose measurable and predictable deviations that can be accounted for in property estimations.

The thesis then extends the analysis to the Triassic Main Buntsandstein Subgroup, a formation of growing interest for geothermal exploitation. Over 700 core plugs were studied and compared directly with the Rotliegend dataset. Similar porosity-dependent trends were confirmed, yet systematic differences emerged between the formations. At equal porosity, Buntsandstein samples exhibited consistently lower thermal conductivity compared to Rotliegend samples. Based on the available data and analysis, the reason was conjectured to be the higher authigenic clay in the Rotliegend and higher detrital clay in the Buntsandstein. The clay type information, which was not completely available for both formations, could in addition have explained the higher acoustic velocities of the Buntsandstein samples relative to the Rotliegend sandstones. Mineralogical variations, such as dolomite cementation and

replacive clays, were shown to modify both thermal and acoustic responses. These comparisons demonstrate that, although porosity governs the primary trends, formation-specific mineralogical controls lead to systematic differences, underlining the need for tailored property models across stratigraphic units.

To complement the thermo-physical investigations, the lower Cretaceous Delft Sandstone Member was studied with emphasis on its coupled mechanical and thermal behaviour. Laboratory experiments on sandstone and shale plugs from the Delft geothermal project included, besides standard rock properties, ultrasonic velocity measurements, thermal property determination, and uniaxial and triaxial mechanical testing. Dynamic elastic moduli derived from ultrasonic velocities were systematically higher than static moduli measured under mechanical loading. A lithology-specific, two-step workflow was established to convert dynamic to static Young's modulus, enabling the construction of continuous static-modulus logs. The results confirm that static Young's modulus values in sandstones (5–22 GPa) are substantially lower than dynamic estimates, with even wider gaps in values for shales. The Cretaceous samples are divided into sandstone and clay groups. The Cretaceous sandstones follow a trend similar to that of the Permian sandstones. Although the Cretaceous clays are expected to have lower thermal conductivity, their extremely low porosity compensates for this and results in increased thermal conductivity, causing the Cretaceous clays to align with the sandstone trend.

The final component of the thesis focuses on predictive modelling of thermal properties using machine learning. Laboratory datasets from Rotliegend and Buntsandstein samples were integrated with well-log data to evaluate empirical and data-driven approaches. Regression models based on laboratory properties showed that adding more correlated predictors improves accuracy, but not necessarily in a linear manner with the number of added properties, and the properties do not have the same influence on this improvement. Machine learning models trained on petrophysical logs included ensemble methods such as gradient boosting (XGBoost, LightGBM) and random forest, as well as a regularised linear model (Ridge regression) achieved promising results for thermal conductivity prediction (average $R^2 > 0.5$), even when tested on unseen wells. Thermal diffusivity, however, remained poorly predictable, reflecting both its sensitivity to mineralogical and microstructural factors not captured by conventional logs, and the inverse relationship between conductivity and heat capacity, which reduces its variance. Feature importance analysis confirmed that density and acoustic features dominate conductivity predictions, whereas no single predictor controls diffusivity. These results demonstrate the potential of machine learning to provide continuous thermal conductivity estimates across wells, while also clarifying the limitations for diffusivity.

This thesis provides a coherent framework for understanding and predicting the thermo-physical and mechanical behaviour of Dutch geothermal sandstones. Porosity provides the primary control, but mineralogy, pore structure, and lithology-specific effects impact secondary property trends. Laboratory measurements establish the physical basis of these

relationships, while machine learning applied to well logs extends predictive capability beyond cored intervals.

The integration of these approaches advances geothermal reservoir characterisation by enabling improved predictions of thermal conductivity and mechanical properties, which are essential for heat flow modelling, wellbore stability assessment, and long-term reservoir management. This thesis therefore contributes both with fundamental insights and practical tools for geothermal development in the Netherlands. It provides formation-specific datasets and correlations, establishes methodologies for petrophysical property characterisations, workflows to bridge laboratory and log-derived properties, and demonstrates the value and limitations of machine learning for thermal property prediction. These advances support more accurate and reliable geothermal resource assessment and, by extension, contribute to the wider deployment of sustainable subsurface energy systems.

Samenvatting

De energietransitie vraagt om betrouwbare en kostenefficiënte ondergrondse hulpbronnen om te voldoen aan de groeiende maatschappelijke vraag naar duurzame energie. In Nederland wordt geothermie beschouwd als een belangrijke bijdrage aan het realiseren van de klimaat- en energiedoelstellingen. Het succes van geothermische projecten hangt in sterke mate af van ons begrip van het reservoir, zodat de verschillende fasen van het ontwikkelplan daarop kunnen worden aangepast. Hiervoor is kennis van de thermofysische en mechanische eigenschappen van de reservoirgesteenten, die zowel warmtetransport als mechanische stabiliteit bepalen, essentieel. Deze eigenschappen zijn echter vaak onvoldoende bekend vanwege uitdagingen bij de metingen, zoals de kosten hiervan, de benodigde tijd en een gemis aan gesteentesamples, evenals de moeilijkheid van het voorspellen van deze eigenschappen door een grote heterogeniteit van de lithologie en mineralogie van het gesteente en door een complexe primaire en diagenetische geschiedenis. Dit proefschrift levert een uitgebreide databank van thermische, akoestische en mechanische eigenschappen voor belangrijke Nederlandse geothermische formaties. Op basis van de gemeten data en door deze te integreren met geofysische logdata uit boorputten, zijn verschillende vergelijkingen en modellen ontwikkeld mede met behulp van artificiële intelligentie. Deze modellen verbeteren de gesteenteeigenschaps-voorspellingen en zijn afgestemd op de Nederlandse ondergrond, maar geven ook beter inzicht in gesteenten elders op de wereld. Gezamenlijk versterken deze inspanningen de karakterisering van geothermische formaties.

Het onderzoek begint met een uitgebreide studie van zandstenen van de Permische Boven-Rotliegend Groep, het meest onderzochte reservoirgesteente in Nederland. Daar voegen wij onderzoek aan toe van meer dan 1100 kernpluggen waarin wij de porositeit, bulkdichtheid, akoestische snelheden, thermische eigenschappen en mineralogie bepalen. De resultaten tonen aan dat porositeit de primaire bepalende factor is voor verschillende andere eigenschappen. Hogere porositeit gaat samen met lagere dichtheid, akoestische snelheid, thermische geleidbaarheid en diffusie. Toch worden systematische afwijkingen van de hoofdtrends waargenomen, die soms kunnen worden verklaard door mineralogische effecten en structurele of diagenetische factoren. Deze bevindingen benadrukken dat porositeit de dominante controle vormt, maar dat mineralogie en textuur meetbare en voorspelbare afwijkingen veroorzaken die in eigenschapsramingen moeten worden meegenomen.

Het proefschrift breidt de analyse vervolgens uit naar de Hoofd-Bontzandsteen Subgroep uit het Trias, een formatie die steeds meer in de belangstelling staat voor geothermische benutting. Van deze sub-groep zijn meer dan 700 kernpluggen onderzocht en direct vergeleken met de Rotliegend-dataset. Vergelijkbare porositeitsafhankelijke trends werden bevestigd, maar systematische verschillen komen naar voren tussen de formaties. Bij gelijke porositeit vertonen Buntsandstein-monsters consequent een lagere thermische geleidbaarheid dan Rotliegend-monsters. Op basis van de beschikbare data en analyse wordt verondersteld dat dit te wijten is aan een hoger gehalte aan autigene klei in het Rotliegend en een hoger gehalte aan detritische

klei in de Bontzandsteen. Informatie over kleitypes, die we niet volledig beschikbaar hebben voor beide formaties, kan mogelijk ook de hogere akoestische snelheden van de Bontzandsteen ten opzichte van de Rotliegend zandstenen verklaren. Mineralogische variaties, zoals dolomietcementatie en klei die de plaats vervangt van andere mineralen, blijken zowel thermische als akoestische responsen te beïnvloeden. Deze vergelijkingen laten zien dat, hoewel porositeit de primaire trends bepaalt, formatie-specifieke mineralogische invloeden leiden tot systematische verschillen, wat het belang onderstreept van eigenschapsmodellen die zijn afgestemd op stratigrafische eenheden.

Ter aanvulling van de thermofysische onderzoeken is het Onder-Krijt Delft Zandsteen Laagpakket bestudeerd, met nadruk op het gekoppelde mechanische en thermische gedrag. Laboratoriumexperimenten op zandsteen- en schaliepluggen uit het geothermieproject op de Delftse universiteits campus omvatten ultrasone snelheidsmetingen, thermische bepalingen en uniaxiale en triaxiale mechanische testen. Dynamische elastische moduli, afgeleid van ultrasone snelheden, blijken systematisch hoger dan statische moduli gemeten onder mechanische belasting. Er is een lithologie-specifieke *twee-stappen plan* ontwikkeld om dynamische eigenschappen om te rekenen naar statische Young's modulus, waardoor continue putlogreeksen van statische moduli kon worden opgesteld. De resultaten bevestigen dat statische stijfheidswaarden in zandstenen (5–22 GPa) aanzienlijk lager zijn dan de dynamische schattingen, met nog grotere verschillen in schalie. De gekalibreerde correlaties bieden een robuuste basis voor geomechanische modellen van boorgatstabiliteit en reservoircompactie en dienen als blauwdruk voor lithologie-afhankelijke conversie werkwijzes in andere formaties.

Het laatste onderdeel van het proefschrift richt zich op voorspellend modelleren van thermische eigenschappen met artificiële intelligentie. Laboratoriumdatasets van Rotliegend- en Bontzandsteen-monsters zijn geïntegreerd met putlogdata om empirische en data-gedreven benaderingen te evalueren. Regressiemodellen gebaseerd op laboratoriumeigenschappen tonen aan dat het toevoegen van meer gecorreleerde voorspellers de nauwkeurigheid verbetert, maar niet noodzakelijk lineair met het aantal toegevoegde parameters, en dat de eigenschappen niet allemaal evenveel bijdragen aan de verbetering. Artificiële-intelligentie-modellen getraind op petrofysische putlogs omvatten ensemblemethoden zoals gradient boosting (XGBoost, LightGBM) en random forest, evenals een geregulariseerd lineair model (Ridge regressie). Deze benaderingen geven veelbelovende resultaten voor het voorspellen van thermische geleidbaarheid (gemiddelde $R^2 > 0,5$), zelfs bij toepassing op tot dan toe voor de analyse onbekende putten. Thermische diffusie blijkt echter moeilijk voorspelbaar, wat de gevoeligheid weerspiegelt voor mineralogische en microstructurele factoren die niet door conventionele putlogs worden vastgelegd. Analyse van de variabelenbelang bevestigt dat dichtheid en akoestische parameters domineren bij de voorspelling van geleidbaarheid, terwijl geen enkele voorspeller bepalend is voor diffusie. Deze resultaten tonen het potentieel van artificiële intelligentie om continue schattingen van thermische geleidbaarheid over meerdere putten te leveren, maar verduidelijken tevens de beperkingen voor diffusie.

De vier onderzoekshoofdstukken bieden samen een samenhangend kader voor het begrijpen en voorspellen van het thermofysische en mechanische gedrag van Nederlandse geothermische zandstenen. Porositeit vormt de primaire controle, maar mineralogie, poriënstructuur en lithologie-specifieke effecten kunnen eigenschapstrends verschuiven. Laboratoriummetingen leggen de fysische basis van deze relaties vast, terwijl machine learning toegepast op putlogs de voorspellende mogelijkheden uitbreidt buiten de gekerde intervallen. De integratie van deze benaderingen bevordert de karakterisering van geothermische reservoirs door verbeterde voorspellingen van thermische geleidbaarheid en mechanische stijfheid mogelijk te maken, die essentieel zijn voor warmtestroommodellering, boorgatstabiliteitsbeoordeling en reservoirbeheer op de langere termijn.

Dit proefschrift levert daarmee zowel fundamentele inzichten als praktische instrumenten voor geothermische ontwikkeling in Nederland. Het biedt formatie-specifieke datasets en correlaties, stelt processen vast om laboratorium- en putlog-afgeleide eigenschappen te overbruggen, en toont de waarde en beperkingen van artificiële intelligentie voor de voorspelling van thermische eigenschappen. Deze vooruitgang ondersteunt een nauwkeurigere en betrouwbaardere beoordeling van geothermische hulpbronnen en draagt daarmee bij aan de bredere toepassing van duurzame ondergrondse energiesystemen.

1.Introduction

1.1. Motivation and background

With escalating climate change and the global requirement to reduce greenhouse gas emissions, the transition to low-carbon energy systems has become a central policy objective for many nations. International frameworks, such as the Paris Agreement call for limiting global warming to below 2 °C, have key near-term milestones, such as peaking emissions by 2025 and substantial reductions by 2030, which require rapid reductions in emissions and a large-scale deployment of renewable and low-carbon technologies. This has stimulated investments in a wide range of solutions, including solar power, wind, hydropower, bioenergy, and carbon capture and storage, each contributing in different ways to the decarbonisation of energy systems. Yet challenges remain, as many of these technologies are non-continuous, land-intensive, or constrained by resource availability, highlighting the need for complementary, reliable, and spatially efficient options. Among the suite of renewable energy technologies available, geothermal energy holds a unique position due to its ability to provide low-emission, and long-duration heat and power. Unlike wind and solar, which are intermittent by nature, geothermal systems offer a stable and controllable energy supply, making them an attractive complement to other renewable technologies. For the Netherlands, an urbanized, densely-populated country with an extensive heating demand and limited land area, geothermal energy offers a particularly compelling solution for decarbonizing the built environment and reducing reliance on fossil fuels (Harings, 2023; Hill et al., 2025).

The Dutch energy transition is guided by ambitious national and EU-level targets, including achieving net-zero emissions by 2050 (Morgan & Stam, 2025). Within this framework, the role of geothermal energy is expected to increase substantially, especially in sectors where electrification is less effective or prohibitively expensive. These include large-scale district heating systems, agricultural greenhouse heating, and high-temperature industrial applications. Policy reports from Energie Beheer Nederland (EBN) emphasise the strategic importance of geothermal heat, projecting it as a critical contributor to the low-carbon heat mix. EBN estimates that geothermal energy could provide heat for more than 2.6 million homes, over a quarter of the Dutch housing stock, and potentially supply around 26% of the heat demand in the built environment through heat networks (Harings, 2023). However, realizing this geothermal potential hinges on our ability to reduce the technical and economic risks associated with geothermal development. Key risks arise from uncertainties in subsurface architecture and reservoir energy potential, as well as in the reservoir response to engineering operations.

Effective geothermal planning and reservoir modelling require detailed knowledge of the thermal and mechanical properties of subsurface formations (Mahmoodpour et al., 2021). These rock properties are central to multiple aspects of project development, from identifying suitable target intervals and estimating heat-in-place, to simulating heat flow and ensuring long-term wellbore and reservoir integrity. Yet, in practice, reliable subsurface property data are often sparse, inconsistent, or unavailable at the scales needed for decision-making. This lack of high-resolution, formation-specific data presents a major challenge in geothermal

context, where new wells are expensive, and, therefore, the subsurface properties must be defined as accurately as possible prior to drilling to avoid uneconomic projects.

Thermal, hydraulic, and mechanical properties are the three groups of rock properties particularly important for geothermal assessments (Ghassemi, 2012; Sha et al., 2020; Xi et al., 2022). Each provides different, yet interconnected, insights into how the subsurface behaves during geothermal operations. Thermal conductivity, thermal diffusivity, and volumetric heat capacity govern how heat is transported, stored, and exchanged in the reservoir. For example, thermal conductivity influences how quickly heat moves through the rock matrix, while volumetric heat capacity determines how much energy can be extracted from a given volume (Robertson, 1988). These thermal properties also control how injected cold water interacts with the reservoir, as they govern the rate of heat transfer from the surrounding rock to the fluid. High thermal conductivity enhances conductive heat transfer within the rock matrix and promotes faster redistribution of heat toward cooled regions. Conversely, higher heat capacity enables the reservoir to buffer larger amounts of energy, delaying temperature decline and extending production sustainability. Thermal expansion is also an essential property, as it controls stress changes in the reservoir during temperature variations and may contribute to induced thermally triggered seismicity. It is not examined in this thesis because most available laboratory methods are destructive. A non-destructive method was developed in this thesis and applied to more than 120 samples; however, despite the measured values falling within reported ranges, the accuracy of the setup and methodology did not meet established experimental protocols and was therefore not considered sufficiently reliable. Mechanical properties, including Young's modulus and Poisson's ratio, affect how the formation will deform under thermal and hydraulic stress, impacting wellbore stability, fracture propagation, and reservoir compaction (Chang et al., 2006; Zoback, 2010). These parameters are critical not only in deep geothermal systems but also in shallow geothermal applications, where they control ground deformation and stability under cyclic thermal loading. In deep or fractured reservoirs, thermal–mechanical coupling can further magnify deformation, potentially leading to induced seismicity or structural failure if not properly accounted for (De Simone et al., 2013).

Despite the critical nature of rock thermal, hydraulic, and mechanical properties, obtaining enough data in an integrated way that reflects actual subsurface conditions is challenging. Laboratory measurements on core samples offer the most accurate values but are inherently limited in their spatial and vertical coverage due to the high costs and restricted availability of core material. Furthermore, laboratory data are typically collected under ambient conditions, and their extrapolation to in-situ subsurface conditions often requires assumptions or correction factors that introduce uncertainty. On the other hand, sonic logs provide continuous depth profiles but usually capture dynamic mechanical moduli derived from wave propagation velocities, which tend to overestimate rock stiffness compared to static laboratory measurements (King, 1983). Moreover, thermal properties are not directly measured in standard logging suites, making their estimation highly uncertain and often reliant on empirical correlations with other petrophysical or mineralogical parameters (Fuchs & Förster, 2014; Hartmann et al., 2005).

In oil and gas research, several studies have demonstrated the value of integrating diverse subsurface datasets for a better understanding of reservoir rock properties, while also illustrating the associated difficulties. Richard et al. (2022) presented a case study from the Cretaceous Abu Roash F carbonate reservoir in Egypt, where core observations, thin-sections, borehole images, well logs, seismic data, and limited dynamic measurements were jointly analysed to characterize fracture typologies and their role in reservoir productivity. Integration across scales, from microscopic to seismic, was essential to build conceptual fracture models and constrain dynamic simulations. However, the authors emphasised the challenge of scale discrepancy, mentioning that the fine detail captured in core and image logs must be homogenized into coarse simulation grids, which inevitably introduces uncertainty and forces simplifications. A different approach was taken by Jeong (2010), who developed a workflow for immature exploration fields with few wells by integrating electrofacies detected from well logs, petrophysical properties from logs and cores, and spatial trends derived from seismic attributes such as acoustic impedance. This method allowed extension of wellbore information to field scale, but the study also reported that heterogeneity and weak correlations between seismic and petrophysical properties could reduce the reliability of predictions. Chaki et al. (2018) focused on the integration of well-log and seismic data using signal processing and machine learning techniques, where pseudologs were generated by linking sparse but high-resolution well measurements with continuous but lower-resolution seismic attributes. Their work showed that such integration can effectively predict lithological properties over large areas but highlighted technical challenges in reconciling differences in sampling rates, resolution, and frequency content between seismic and well-log data. Finally, Tureyen and Caers (2005) proposed a parallel multiscale reservoir modelling approach in which fine-scale geological realisations and coarse-scale flow models are updated simultaneously, with non-uniform upscaling providing the link between scales. This preserved geological information while conditioning production data, but the authors noted that upscaling errors and computational demands remain important limitations. Together, these studies illustrate that integrated use of core, well, seismic, and dynamic data can generate valuable insights into reservoir architecture and behaviour, yet always involve negotiating trade-offs between geological realism, computational feasibility, and uncertainty management.

To bridge this gap, recent geothermal studies have emphasised the integration of laboratory data, petrophysical well logs, and predictive modelling techniques, including machine learning (Chaki et al., 2018; Jarzyna et al., 2021; Tureyen & Caers, 2005; Vivas & Salehi, 2021). It appeared that the success of such integrative approaches critically depends on the availability of high-quality, well-documented datasets that cover the geological formations of interest (Békési et al., 2020; Mijnlief, 2020).

In the Netherlands, much of the existing rock property data has historically been collected for hydrocarbon exploration and is often concentrated in a few extensively-drilled intervals, such as the Permian Upper Rotliegend Group. However, even for the Rotliegend, the available measurements, while valuable, remain relatively sparse and unevenly distributed, such as the prime focus of these data on structural highs in the subsurface and on the Groningen gas field.

As a result, these datasets do not fully capture the heterogeneity of formations targeted in geothermal projects, nor do they provide sufficient coverage across the Triassic and Cretaceous intervals that are now of growing interest (Mijnlieff, 2020; Willems et al., 2020).

1.2. Scope and objectives

The motivation for this thesis lies in the urgent need to reduce subsurface uncertainty in geothermal development, including in the Dutch context where both policy and public investments are accelerating. This work aims to improve subsurface property prediction and with that support safer and more efficient geothermal development by assembling an unparalleled dataset. This means a large and comprehensive dataset in terms of property coverage, selecting properties of direct relevance to geothermal operations, and applying both traditional and data-driven modelling approaches. The findings are not only relevant for academic research but also directly applicable to ongoing and future geothermal projects in the Netherlands and similar geological settings worldwide. This thesis addresses these challenges by compiling and analysing one of the most extensive datasets of measured rock properties in the Dutch geothermal context. The data were collected under the framework of the ProperBase project and include over 2000 core plug samples across multiple geothermal wells. The samples represent three stratigraphic intervals of significant geothermal interest (Buijze et al., 2023; Pluymaekers et al., 2012).

The primary aim of this thesis is to address the absence of extensive, integrated, and representative rock property datasets and predictive methods for geothermal applications. The work concentrated on improving the understanding of thermal and mechanical rock properties in Dutch geothermal plays. This was carried out through the integration of laboratory experiments, well-log data, and data-driven modelling approaches, aimed at improving property prediction to reduce subsurface risk and cost while increasing the efficiency of future geothermal projects. To achieve this, the work began with a systematic analysis of rock properties in the Upper Rotliegend Group, which serves as a reference due to its extensive previous characterisation and geothermal relevance. The Permian Upper Rotliegend Group has been the focus of gas exploration and is relatively known in terms of reservoir quality and thickness (Mijnlieff, 2020; Van Adrichem Boogaert & Kouwe, 1993; Wees et al., 2012). The Upper Rotliegend Group serves as a benchmark formation for geothermal studies due to its often high permeability and extensive existing data.

The next step expanded the scope to the Triassic Buntsandstein Subgroup, a formation that has received comparatively less attention despite its geothermal potential. The Triassic Main Buntsandstein Subgroup in the Dutch subsurface, a fluvial-dominated system with growing geothermal relevance (Cecchetti et al., 2024b). It shows somewhat greater variability in petrophysical properties, which can be linked to its more complex depositional environment and diagenetic overprint, although the overall ranges partly overlap with those observed in the Rotliegend.

The thesis then turns to the lower Cretaceous Delft Sandstone Member, the target of the TU Delft campus geothermal project (Vardon et al., 2024b; Vardon et al., 2024a), which presents challenges related to heterogeneity, lithological complexity, and mechanical stability. By measuring the same set of properties and comparing them to those of the Rotliegend and Buntsandstein rocks, the study evaluates the extent to which empirical relationships and trends can be transferred between formations. This comparison also offers insight into how depositional environments, such as fluvial-aeolian versus fluviodeltaic systems, influence rock behaviour. Unlike the previous parts that focused primarily on evaluating rock strength using sonic wave velocities, the study of Delft sandstone rock samples provides a more detailed investigation of mechanical behaviour by incorporating results from laboratory mechanical tests. A combined dataset of laboratory measurements and well logs is used to derive lithology-specific conversions between dynamic and static elastic moduli. These conversions address a key challenge in geothermal reservoir modelling including the need for realistic static mechanical properties that are rarely available from logs alone. By validating different conversion workflows against core-scale measurements, the study contributes practical tools for improving wellbore stability assessments in geothermal projects.

By including formations that vary widely in their depositional environments, lithofacies, porosity structure, and mineralogy, this dataset allows for cross-formation comparisons that are rarely possible in geothermal studies. The large sample size also permits statistically robust analyses, the development of empirical relationships with higher confidence, and the validation of predictive models across geologically diverse conditions. The scale of the dataset alone sets it apart from most previous work, where studies have often relied on tens of samples rather than hundreds, focused narrowly on a single formation, or used partly-weathered outcrop samples.

The properties measured in this study were chosen based on their engineering relevance and predictive potential. These include thermal conductivity, thermal diffusivity, and volumetric heat capacity, measured under dry, ambient conditions using laboratory techniques. Ultrasonic wave velocities, compressional wave velocity (V_p) and shear wave velocity (V_s), used to calculate dynamic elastic moduli and to provide input for well-log interpretations. Porosity and bulk density, which serve as inputs to both thermal and mechanical models. Mineralogical composition, determined via complementary techniques such as X-ray diffraction (XRD) and Fourier-transform infrared spectroscopy (FTIR) to assess its role in controlling rock behaviour. Static mechanical properties, including Young's modulus, bulk modulus, and Poisson's ratio, measured only for the Delft Sandstone Member, enabling the calibration of dynamic-to-static conversion workflows, which remain a key challenge in geomechanical modelling.

Understanding the interrelations among these properties is vital for improving geothermal system design. In this study, the analysis was not limited to direct measurements but was extended by integrating complementary datasets. Laboratory results were interrelated with known properties from existing databases, such as petrography data, derived from the same plugs, allowing for cross-validation and explaining trends and some outliers. For a selection of

plugs, additional information such as sedimentary descriptions was incorporated to place the measured properties in a broader geological context. This multi-source approach ensured that the analysis captured as much available information as possible, thereby strengthening the reliability and applicability of the findings for subsurface applications. For example, high thermal conductivity may not always correlate with high porosity or mechanical stability. Similarly, the presence of certain minerals (e.g., quartz vs. clay vs. carbonates) can enhance or degrade both thermal and elastic responses, depending on their abundance and distribution. This complexity necessitates a multivariate approach, which this study addresses through both analytical and machine learning-based modelling frameworks.

The final part of the thesis explores the use of machine learning to predict thermal properties from standard well-log and laboratory data. To extend the spatial and depth coverage beyond limited core data, petrophysical well logs were used to estimate dynamic elastic moduli and to explore relationships between petrophysical properties and thermo-mechanical behaviour. All well-log data used in this study were retrieved from the Dutch national subsurface database, www.nlog.nl. While traditional petrophysical correlations can capture some trends, they often fail to account for complex, nonlinear relationships, and interactions between variables as they may not adequately capture formation-specific variability. Researchers have developed approaches that often relied on simple linear or regression-based relationships between thermal conductivity and porosity, density, or mineral composition (e.g., Hartmann et al. (2005)). More recently, statistical and machine learning methods have been explored for petrophysical property prediction, showing advantages in handling nonlinear and heterogeneous relationships (e.g., Fuchs and Förster (2014); Luo et al. (2023); Pang et al. (2023)). Machine learning offers a complementary approach by training models on a large, diverse dataset spanning multiple wells and formations. The performance of these models is evaluated using several metrics, and the results are interpreted with attention to model generalisation, well-to-well variability, and the influence of formation-specific characteristics. Building on this development, ensemble machine learning methods, such as Random Forest, XGBoost, and LightGBM, are applied in this present work to learn complex, nonlinear patterns from large datasets. By training models on the integrated dataset compiled in this study, the goal is to produce generalizable and reliable predictors that can be applied in wells where core data are lacking. The performance of these models is rigorously assessed using per-well validation, cross-formation testing, and multiple error metrics. In this thesis, a machine learning framework was developed to predict thermal conductivity and thermal diffusivity from standard well-log inputs. The models tested include ridge regression, random forest, gradient boosting (XGBoost), and LightGBM selected for their ability to capture both linear and non-linear relationships in heterogeneous datasets. Model performance was evaluated using multiple per-well metrics, including the coefficient of determination (R^2), mean absolute error (MAE), mean absolute percentage error (MAPE), and normalized mean square error (NMSE). The goal was to assess model generalizability and reliability across different geological formations.

1.3. Structure of the thesis and chapter interconnections

Besides the current chapter, Chapter 1 (Introduction), and Chapter 6 (Conclusions), this thesis comprises four core research chapters.

- Chapter 2 focuses on the Permian Rotliegend Formation. It presents a comprehensive laboratory analysis of over 1100 core samples from four Dutch geothermal wells. By integrating thermal, acoustic, porosity, and mineralogical data, the chapter explores how physical and compositional properties co-vary, offering insights into their controls on thermal behaviour.
- Chapter 3 extends the analytical framework to the Triassic Buntsandstein Subgroup, a less-well characterized but potentially valuable geothermal target. The chapter emphasises comparison with the Permian results, highlighting geological and petrophysical contrasts. This comparative approach evaluates the transferability of relationships and models across stratigraphic units.
- Chapter 4 investigates the mechanical behaviour of the lower Cretaceous Delft Sandstone, including both sandstone and shale facies. The focus is on establishing reliable dynamic-to-static modulus conversion workflows using lab and well-log data. This addresses a key challenge in mechanical modelling where only dynamic data are available from logs.
- Chapter 5 explores the use of machine learning to predict thermal properties (especially conductivity and diffusivity) from both laboratory data and standard petrophysical logs. Two modelling workflows are developed and assessed across wells from the Permian and Triassic formations. The chapter evaluates the accuracy, generalizability, and limitations of such data-driven approaches, particularly considering formation heterogeneity.

These chapters are linked through a progressive structure: beginning with foundational experimental analysis (Chapters 2–3), extending to mechanical calibration (Chapter 4), and culminating in predictive modelling (Chapter 5). Together, they support the thesis aim of advancing thermal and mechanical property estimation for geothermal systems.

**2. Thermal and acoustic characterisation of
Permian Rotliegend sandstones:
evaluating the effects of porosity and
mineralogy on predicting thermal
properties**

Abstract: Thermal and acoustic properties of subsurface rocks are essential for assessing the energy potential and mechanical behaviour of geological formations, guiding geothermal energy applications, therefore enabling sustainable development. The Permian Rotliegend Formation, though well studied for hydrocarbon exploration, remains underexplored in terms of its thermal and acoustic properties for geothermal applications. These properties are mainly governed by mineralogy and compaction, yet large, integrated datasets required to analyse these controls and build predictive models are lacking. This study addresses that gap using over 1130 sandstone core plugs from four Dutch wells.

Our results reveal porosity and bulk density are key controllers of thermal and acoustic properties. Higher porosity correlates linearly with lower bulk density, lower compressional (V_p) and shear (V_s) wave velocities, and lower thermal conductivity and diffusivity. Acoustic data show that denser, lower porosity samples generally have higher wave velocities and thermal properties. The scatter is greatest in the relatively more lithified intervals, further enhanced by drying and condition changes after sample retrieval from the subsurface. The scatter likely reflects local mineralogical variability and grain size variation. At the same time, both volumetric and specific heat capacity show a weaker dependence on porosity. Mineralogical variations, such as differences in primary and authigenic clay content and clay type are interpreted to impact thermal properties. The kaolinite-group mineral nacrite increases thermal conductivity beyond what would be expected from general property trends, most likely because this mineral replaces mica keeping grain-bonding intact while increasing porosity. Increases in detrital clays lower the thermal conductivity compared to its main trend with porosity, because porosity is lowered while grain bonding is poor amongst detrital clay. Increases in intergranular cements, such as dolomite, reduce porosity and thermal properties but do not alter the overall trends. Based on these trends, we provide predictive equations for thermal properties as a function of porosity and V_p . The determination coefficient of the linear regression equations for thermal conductivity is 0.63–0.67 and for other thermal properties is below 0.42. The accurate prediction of thermal and acoustic behaviour requires consideration of both primary rock properties and diagenetic history. Scatter in all models is largely due to localised mineralogical effects and grain size variations. To predict thermal and acoustic properties reliably as a function of porosity, additional information such as mineral composition and mineral phase distribution must be incorporated.

2.1. Introduction

Characterising rock physical properties, and where necessary mineralogy, is crucial for subsurface applications such as geothermal energy production, carbon capture and storage (CCS), and hydrogen storage (Pluymaekers et al., 2012; Rezk & Ibrahim, 2025). In geothermal reservoirs, thermal conductivity, thermal diffusivity, and heat capacity control heat transfer efficiency (Anees et al., 2024; Jin et al., 2024) and influence the spatial and temporal temperature distribution. Popov et al. (2011) studied over 400 volcanic, carbonate, metamorphic, and siliciclastic rocks samples and found significant differences in thermal

conductivity across rock types. They identified correlations between thermal conductivity ratios, the ratio of thermal conductivity of water-saturated to dry samples, and porosity. Popov et al. (2011) reported that thermal conductivity is mainly controlled by porosity, and mildly by mineral type, cracks, and rock heterogeneity, while anisotropy has little effect.

Thermal conductivity is heavily controlled by mineral composition and porosity (Brigaud & Vasseur, 1989; Clauser & Huenges, 1995b). Only in dry, high-porosity rocks does porosity become a stronger modulator, but even then, mineralogy remains foundational (Brigaud & Vasseur, 1989; Clauser & Huenges, 1995a; Lasheen et al., 2023; Robertson, 1988). Kämmlin and Stollhofen (2019) studied a total of 707 Permo–Triassic sandstone samples from Bavaria (southeast Germany) comprising 615 core samples from several deep wells as well as shallow wells, and 92 outcrop samples covering stratigraphic units not accessible through coring. The dataset represents a broad lithological spectrum with heterogeneous mineralogical composition and cementation types. They found that the proportions of thermally conductive minerals such as quartz and dolomite, together with saturation conditions, exert a strong control on thermal conductivity.

Acoustic properties, i.e. compressional wave velocity (V_p) and shear wave velocity (V_s), provide insights into rock stiffness and mechanical integrity (Verma et al., 2024). Acoustic property data of rocks can be used at various stages of geothermal reservoir development, including resource exploration, reservoir characterisation, numerical modelling, and long-term performance assessment, and can enhance prediction accuracy and subsurface understanding. The acoustic properties are reasonably easy to measure using downhole logs and are known to be correlated to rock properties. It therefore improves rock property predictions, enhancing subsurface understanding, especially when direct measurements of physical properties is limited or uncertain (El Sayed & El Sayed, 2019; El Sayed & El Sayed, 2024; Fuchs & Balling, 2016; Tatar et al., 2021). Acoustic velocities in rock are influenced by mineral composition, porosity, fluid saturation, and pressure conditions. They can reflect various subsurface features, making their measurement essential for subsurface characterisation and reservoir evaluation (Al-Dousari et al., 2016; Olutoki et al., 2024; Setyowiyoto & Samsuri, 2012; Winkler & Murphy III, 1995).

Both thermal and acoustic properties are influenced by the same underlying rock characteristics, with porosity commonly identified as an important control on their variability. (Assefa et al., 2003), mineralogy, grain size, and diagenetic processes introduce additional complexities that require detailed investigation (Kim et al., 1985; Peltonen et al., 2009; Vorobiev et al., 2024). Numerous studies have explored the relationships between them (El Sayed & El Sayed, 2019; Esteban et al., 2015; Hartmann et al., 2005; Mielke et al., 2017b; Pimienta et al., 2014; Popov et al., 2003; Zamora et al., 1993). For example (Mielke et al., 2017b), examined thermal conductivity– V_p relationships in Permian Rotliegend sandstones from northwestern Germany, using both laboratory and log-derived data. They reported a

positive correlation, with the slope and intercept influenced by porosity, mineral composition, and microstructure.

As the results from Kämmlein and Stollhofen (2019) demonstrated, empirical models for predicting thermal conductivity based solely on individual parameters such as porosity or V_p are inadequate for accurate predictions in mineralogically heterogeneous sandstones. This highlights the need for site-specific calibration in geothermal applications. Such relationships between thermal and acoustic properties are not yet well characterised for geothermal applications in the Dutch subsurface. In particular, the combined effects of porosity, mineralogy, and their interactions are poorly constrained, limiting the reliable prediction of reservoir behaviour. Reviewing previous studies on the Dutch subsurface helps clarify the knowledge gap that this work addresses.

Hartmann et al. (2005) measured thermal conductivity and sonic velocity on 400 core samples from various lithologies in Germany, the Netherlands, and the UK. They developed empirical equations to predict thermal conductivity from sonic velocity and density logs, enabling improved subsurface thermal modelling and geothermal resource assessment. Establishing such relationships is highly valuable, as acoustic properties can be measured both in the laboratory and in situ using downhole logging tools, enabling the indirect determination of thermal properties in the subsurface. Given that acoustic parameters (e.g., sonic velocity and impedance) are sensitive to microstructural characteristics that influence thermal conductivity, these measurements could serve as an effective intermediary to link physical properties with thermal properties. These results provide a key reference for the present study, which evaluates similar relationships in Dutch Rotliegend samples.

Veldkamp et al. (2022) assessed the geothermal potential of the Slochteren Formation, a Permian-age sandstone unit within the Upper Rotliegend Group in the Dutch subsurface, in the Central Netherlands Basin by analysing porosity, permeability, and burial history. They found that permeability varies significantly with facies and tectonic history, and that national-scale models like ThermoGIS may misestimate geothermal potential at the field or well scale.

Veenigen and Könitzer (2016b) performed a detailed petrographic study of the Upper Rotliegend Group sandstones from six Dutch offshore wells from the K and F blocks using thin-section analysis, scanning electron microscopy (SEM), and X-ray diffraction (XRD). Their work documented mineralogical composition, grain-size distribution, and diagenetic features such as quartz overgrowths, feldspar dissolution, and clay mineral formation. By linking these observations to depositional facies and burial history, they demonstrated how mineralogy and diagenesis influence porosity and permeability trends in the Rotliegend. These findings provide essential geological context for the present study, which applies complementary laboratory measurements to investigate how such mineralogical and textural variations relate to thermal and acoustic properties.

Later, Soustelle et al. (2022) reported an important but limited set of laboratory measurements of thermal conductivity, heat capacity, and P-wave velocity on 32 core plugs from Dutch Rotliegend and Triassic reservoir formations, analysing their correlations for geothermal reservoir characterisation.

Given the complexity of thermal and acoustic properties, and the absence of large, integrated datasets that capture spatial variability in the Dutch subsurface, a systematic evaluation of porosity, mineralogy, and grain size effects on these properties in Permian sandstones of the Dutch North Sea is still needed. This study addresses that gap. We investigate four Permian wells (K18-08, K18-07x, ZRP-03a, and E18-05) to establish a more comprehensive understanding of relationships between acoustic and thermal properties, porosity, permeability, and bulk density as well as mineralogy and grain size. A key focus is to investigate the relationships between thermal and acoustic properties and their dependence on porosity. All measurements in this study were conducted on dry core plugs as these were available for study. Fluid saturation does influence the absolute values of thermal and acoustic properties, though investigating these effects was beyond the scope of this work. Nevertheless, the dry-sample measurements provide internally consistent trends and comparative relationships that are useful for understanding variations within the studied dataset and for informing geothermal reservoir assessments. Additionally, the study examines how variations in grain size and mineralogy influence these properties, providing insights into their role in controlling rock behaviour.

2.2. Study area and materials

The Rotliegend sandstone is a lithostratigraphic group of Permian age, extending partly into the North Sea and partly into northwestern Europe (Figure 2.1a) (van Adrichem Boogaert, 1976). These deposits are suitable for geothermal development because of their porosity, permeability, total thickness and high net-to-gross ratio (Mijnlieff, 2020).

In Rotliegend sandstones, clay minerals occur in two principal forms. Detrital clays, which are transported into the depositional system and integrated within the sedimentary framework, and authigenic clays, which form in place during diagenesis, most notably through feldspar leaching that produces grain coatings and pore-filling illite and chlorite (Bär et al., 2011; Molenaar & Felder, 2018). Detrital clays merely contribute their inherently low thermal conductivity to the rock matrix. In contrast, authigenic clays, especially when they precipitate as continuous grain coatings or pore-fill material, more effectively disrupt grain-to-grain contacts and conductive pathways, thereby more substantially reducing the bulk thermal conductivity of the sandstone (Kämmlein & Stollhofen, 2019). The degree to which the thermal conductivity of a sandstone is affected depends not only on the proportion of clay to quartz, but also on the type of clay (detrital versus authigenic), the spatial arrangement of clay relative to higher-conductivity framework minerals such as quartz within the matrix, and the distribution of clay minerals within the porous medium, whether in the matrix or in the pore spaces.

Thermal and acoustic characterisation of Permian Rotliegend sandstones: evaluating the effects of porosity and mineralogy on predicting thermal properties

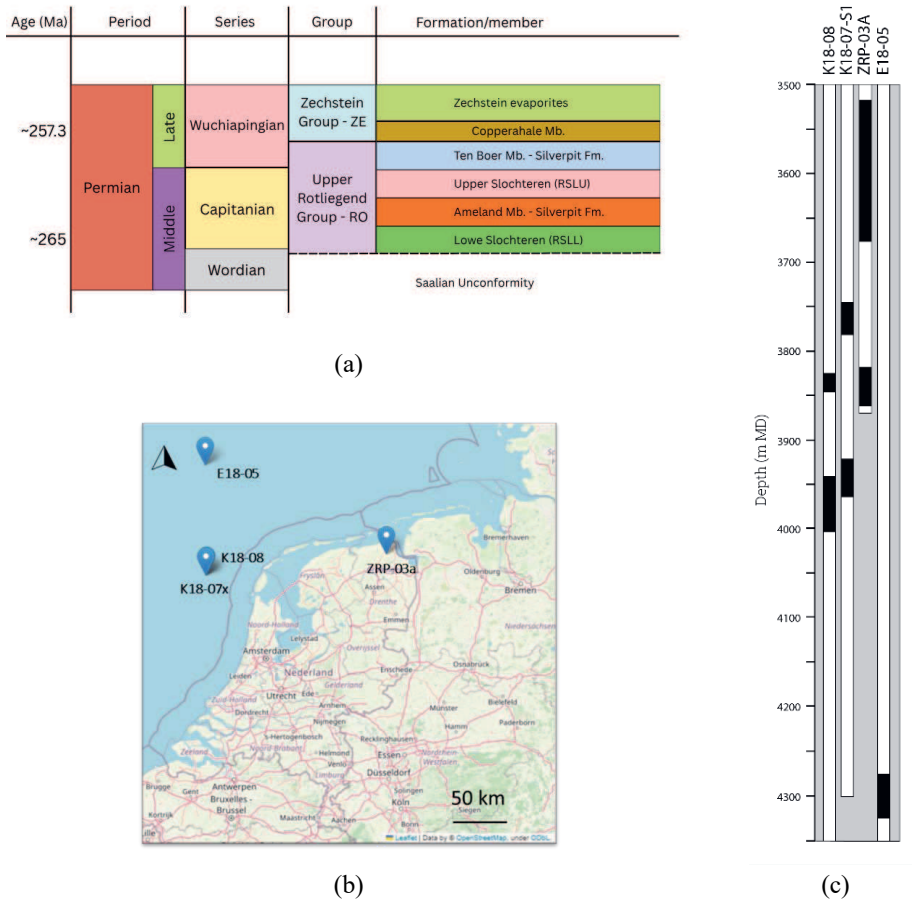


Figure 2.1. (a) Simplified stratigraphic column of the Netherlands, highlighting the Upper Rotliegend Group (RO) and Lower Rotliegend Group (RL), which are the focus of this study (after (DINOloket; Geluk & Röhling, 1997) The Upper Rotliegend Group (RO) consists of the sandy-conglomeratic Slochteren Formation (ROSL) and the claystone–evaporite Silverpit Formation (ROCL). The Slochteren Formation is further subdivided into the Lower Slochteren Formation (RSSL), which is sand-dominated and contains conglomeratic layers, and the Upper Slochteren Formation (RSLU), which is also sandstone-dominated but less conglomeratic than the lower unit (Adrichem-Boogaert & Kouwe, 1993). (b) the locations of the studied wellbores across the Netherlands (Google Maps, accessed Dec 2024). The offshore wells K18-08 and K18-07x are in the K block, and the E18-05 is in the E block of the North Sea. The onshore well ZRP-03a is in the Groningen province of the Netherlands. (c) visualisation of the wellbore depth samples were retrieved from.

This study is focused on three offshore, K18-08, K18-07x, E18-05, and one onshore, ZRP-03a, wellbores in the Dutch subsurface (Figure 2.1b). The aim was to capture variation in rock properties among these locations within the same group. This study analyses in total 1130 core plug samples, each with complete acoustic, physical, and thermal property values made available to the project by Wintershall Noordzee in Rijswijk, the Netherlands and the

Nederlandse Aardolie Maatschappij (NAM) in Assen, the Netherlands. The core material was recovered from depths between ~3500 and 4300 m (MD), with 481 samples from K18-08, 351 from ZRP-03a, 270 from K18-07x, and 27 from E18-05 (Figure 2.1c).

The samples obtained were all reddish and grey sandstones, some of which were laminated, as well as conglomerates. The reddish colour reflects the presence of iron oxides (van Adrichem Boogaert, 1976), which may indicate oxidizing depositional conditions and potentially greater cementation, whereas the grey colour suggests reducing conditions that may preserve higher primary porosity. Lamination can introduce anisotropy in physical properties, influencing both permeability and acoustic wave propagation. Some samples, particularly from the Upper Slochteren Formation in well K18-08, were poorly consolidated and exhibited the widest range of grain sizes in the dataset, from fine- to coarse-grained sandstone, including occasional conglomeratic layers. Several of these samples displayed visible lamination, whereas others were more homogeneous.

In this work, we measured the acoustic and thermal properties. Permeability data was retrieved from multiple reports from Geological Survey of the Netherlands (TNO, 2024), with the sources individually referenced in our database. In addition, porosity data was partially sourced from (TNO, 2024), and measured when it was not available. Mineralogy data discussed in this present paper were produced as part of this study through XRD and FTIR measurements on samples from K18-08 and K18-7x. In addition to the 1130 core plugs analysed in this study, the dataset contains other samples with incomplete property measurements. These were excluded from the analysis but remain available in the associated database (Kolah-Kaj et al., 2024).

2.3. Methods

Thermal properties were measured using the [Hot Disk TPS2200](#) at the TU Delft geolaboratory, Delft, the Netherlands (Figure 2.2a). This device works based on the transient plane source technique that can measure thermal conductivity, thermal diffusivity, and volumetric heat capacity (HC) from an applied current over a disk. Two different sizes of standard Kapton-insulated sensors: (model 5465 F2 and model 5501 F2) were used for the smaller samples (average diameter = 25 mm, average length = 40) and the larger samples (average diameter = 37 mm, average length = 50) samples, respectively. The Hot Disk system is a widely used and reliable method, and repeated measurements on selected samples confirmed good accuracy. Nonetheless, minor scatter in thermal conductivity may partly reflect uncertainties from surface roughness, sensor contact, or internal heterogeneity. Improvements could involve better surface preparation, controlled contact pressure, or validation with steady-state methods.

The compressional and shear wave velocities were measured using an active acoustic setup (Figure 2.2b) in the rock mechanics lab of TU Delft. This setup consists of an amplifier, a wave generator, an oscilloscope, and a pair of S-wave transducers to record the arrival of both compressional and shear waves (Veltmeijer et al., 2022). The frequency and voltage for the

measurements were 1 MHz and 200-800 mV, respectively. Porosity and grain density was measured using a helium gas pycnometer ([Ultrapyc 5000](#)) located at rock mechanics lab in TU Delft. All the measurements have been conducted on dry rock samples at room temperature and pressure.

As a first step, mineralogical analysis was carried out on approximately 60 samples using X-ray diffraction (XRD) at Qmineral B.V, Heverlee, Belgium. XRD is a reliable method for identifying and quantifying minerals (Al-Jaroudi et al., 2007; Hardy, 1988). The XRD results were then used to validate and support the Fourier Transform Infrared Spectroscopy (FTIR) measurements also conducted by Qmineral. FTIR offers good accuracy and faster measurement speed compared XRD (Jozanikohan & Abarghoeei, 2022; Mroczkowska-Szerszeń & Orzechowski, 2018). Based on these findings, FTIR was applied to a larger number of samples, enabling a broader assessment of mineralogical composition through the identification of functional groups and chemical bonds. Regarding measurement reproducibility, the average standard deviation was 55.10 m/s for compressional waves and 40.12 m/s for shear waves. Thermal properties were measured with a reproducibility of 0.078 W/m³·K for thermal conductivity, 0.070 mm²/s for thermal diffusivity, and 0.081 MJ/m³·K for volumetric heat capacity.

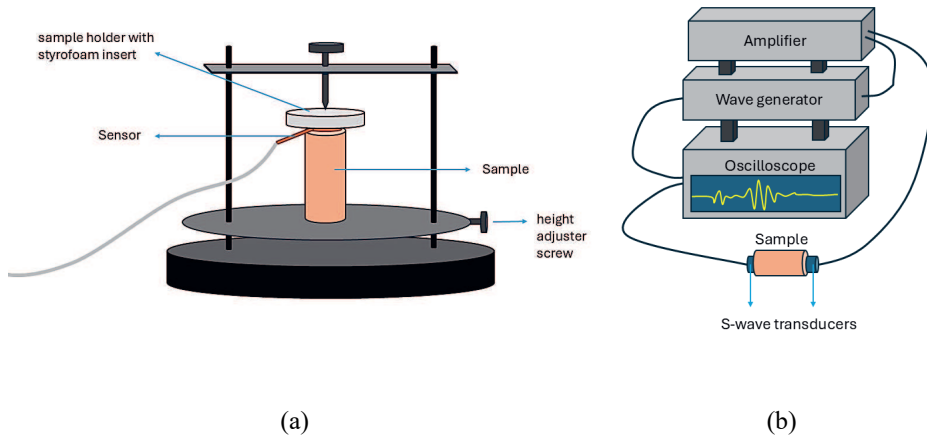


Figure 2.2. (a) Thermal constant analyser (*HotDisk TPS2200*) sample set-up for thermal properties measurement and (b) active acoustic set-up for the compressional and shear wave velocity measurement.

2.4. Results

Before analysing trends and correlations, the dataset was examined to quantify variability and identify potential anomalies. Compressional (V_p) and shear (V_s) wave velocities show large

spreads, with standard deviations of approximately 719 m/s and 505 m/s, respectively, and minimum values of 640 m/s and 411 m/s. The lowest values occur mainly in samples from the ZRP-03a well. Porosity ranges from 1.3 % to 29.8 % (standard deviation 5.48 %), with the upper range also represented in ZRP-03a. Bulk density varies between 1888 and 2771 kg/m³, with a standard deviation of 164 kg/m³. Thermal conductivity spans from 0.74 to 5.31 W/m·K, with a standard deviation of 0.78 W/m·K. These statistics indicate the presence of both typical variability and a small number of extreme values, which are examined in more detail in subsequent sections.

A strong linear negative correlation between bulk density and porosity is observed for all Upper Rotliegend Group Slochteren Formation core plugs (Figure 2.3a) with a small standard deviation. A larger standard deviation occurs for the strong positive linear relationship between gas horizontal permeability and porosity (Figure 2.3b). A negative linear relationship is seen between compressional wave velocity (V_p) and porosity (Figure 2.3c), and V_p and shear wave velocity (V_s) shows a narrow positive linear relationship (Figure 2.3d). The data points from all wellbores are tightly clustered along the latter linear trend, suggesting a consistent relationship between V_p and V_s across the entire dataset.

The data from four individual wellbores all contribute to these observed trends. The few samples of E18-05 are mostly dense with low porosity, while the many samples of ZRP-03a are least dense and most porous. The K18-08 and K18-07x wells, located close to each other, show very similar property ranges in between these extremes. Altogether, the sample sets from the four wells provide a complete dataset across a wide porosity range from around 2 to 30% and for bulk density, porosity, V_p and V_s .

Thermal and acoustic characterisation of Permian Rotliegend sandstones: evaluating the effects of porosity and mineralogy on predicting thermal properties

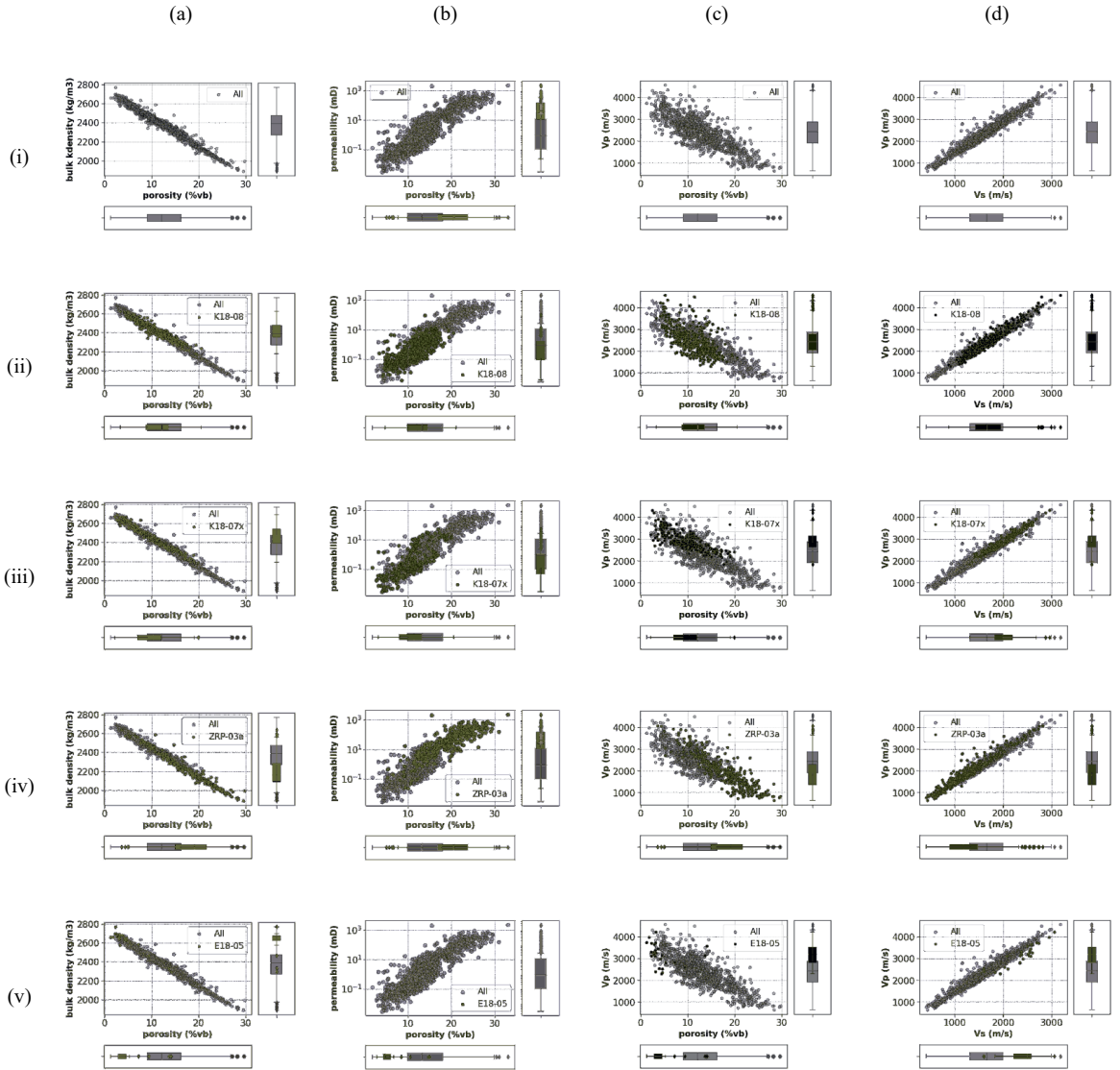


Figure 2.3. Cross plots showing the property relationship as measured on Rotliegend core-plugs of the Dutch subsurface between (a) bulk density versus porosity, (b) Klinkenberg permeability versus porosity, (c) V_p versus porosity, and (d) V_p versus V_s of samples from (i) all wells, (ii) K18-08, (iii) K18-07x, (iv) ZRP-03a, and (v) E18-05. The corresponding boxplots illustrate the distribution of each property. The boxplots provide an overview of the data spread, median, and potential outliers for each variable.

Across all wells, there is a negative linear relationship between thermal conductivity and porosity (Figure 2.4a). A broader range of thermal conductivity values is observed at low porosity than at high porosity values. Part of the more scattered thermal conductivity values at lower porosity ranges belong to the K18-08 and E18-05 (see Figure 2.4a-ii and Figure 2.4a-v), while overall ZRP-03a thermal conductivity values appear on the low end along with the high-end porosity ranges of this well. Above the main trend, a group of scattered outliers with higher thermal conductivity occur between 2 and 15% porosity, mostly from well K18-08. Another scattered outlier group occurs at low porosity with relatively low thermal conductivity. Most of these datapoints are from well E18-05. The lowest thermal conductivity values occur between 18 and 30% porosity in the ZRP-3a well, with a significant trend disappearing above around 23% porosity.

Less significant negative trends are observed between volumetric heat capacity ($\text{MJ/m}^3 \cdot \text{K}$) and porosity (Figure 2.4b) and between thermal diffusivity (mm^2/s) and porosity (Figure 2.4c). This reflects, similar to thermal conductivity, a pore space impact on temperature transfer. A clear relationship seems to lack between specific heat capacity ($\text{kJ/kg} \cdot \text{K}$) and porosity (Figure 2.4d). Specific heat capacity values range between 0.2 and 1.0 $\text{kJ/kg} \cdot \text{K}$ seemingly regardless of porosity. For both volumetric heat capacity and thermal diffusivity, it is the data from well K18-08 that shows the least trend with porosity. Combining the data from ZRP-3a and K18-07x shows a reasonable trend between these two properties and porosity. However, while a lot of the data from K18-08 does fit this same trend, there is also a large group of data with lower volumetric heat capacity and higher thermal diffusivity, including the respectively lowest and highest outliers of these properties in the entire dataset.

Thermal and acoustic characterisation of Permian Rotliegend sandstones: evaluating the effects of porosity and mineralogy on predicting thermal properties

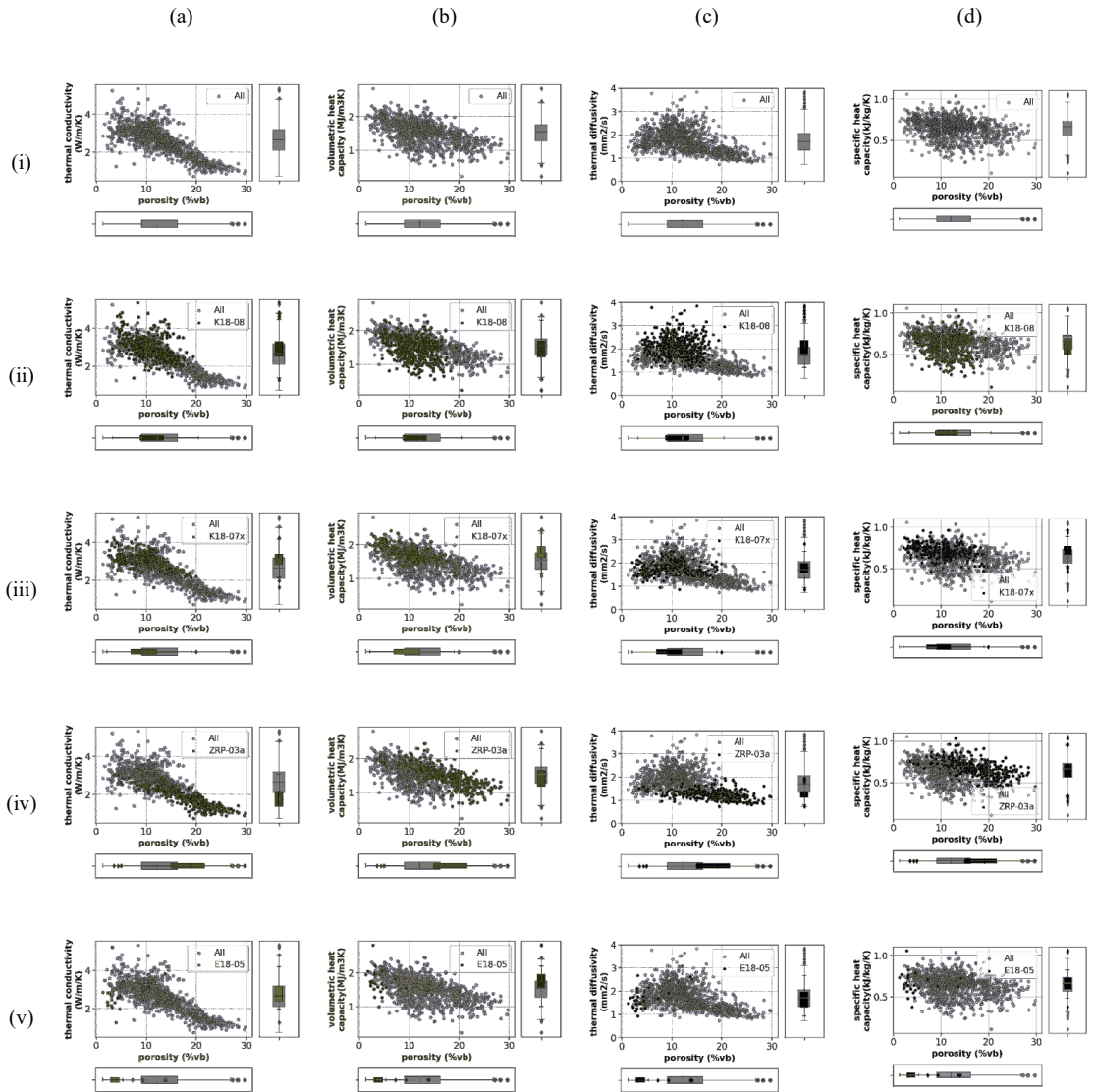


Figure 2.4. Cross plots of properties of core-plugs of the Dutch Rotliegend showing the relationship between (a) thermal conductivity versus porosity, (b) volumetric heat capacity versus porosity, (c) thermal diffusivity versus porosity, and (d) specific heat capacity versus porosity of samples from (i) all wells, (ii) K18-08, and (iii) K18-07x, (iv) ZRP-03a, and (v) E18-05.

Trends are calculated for the acoustic and thermal properties compared to each other and porosity and bulk density (Figure 2.5 and Table 2.1). R^2 and standard deviations are provided with each comparison. This exercise includes the entire dataset including potential outliers such

as the group of relatively high thermal conductivity compared to porosity from well K18-08, discussed above.

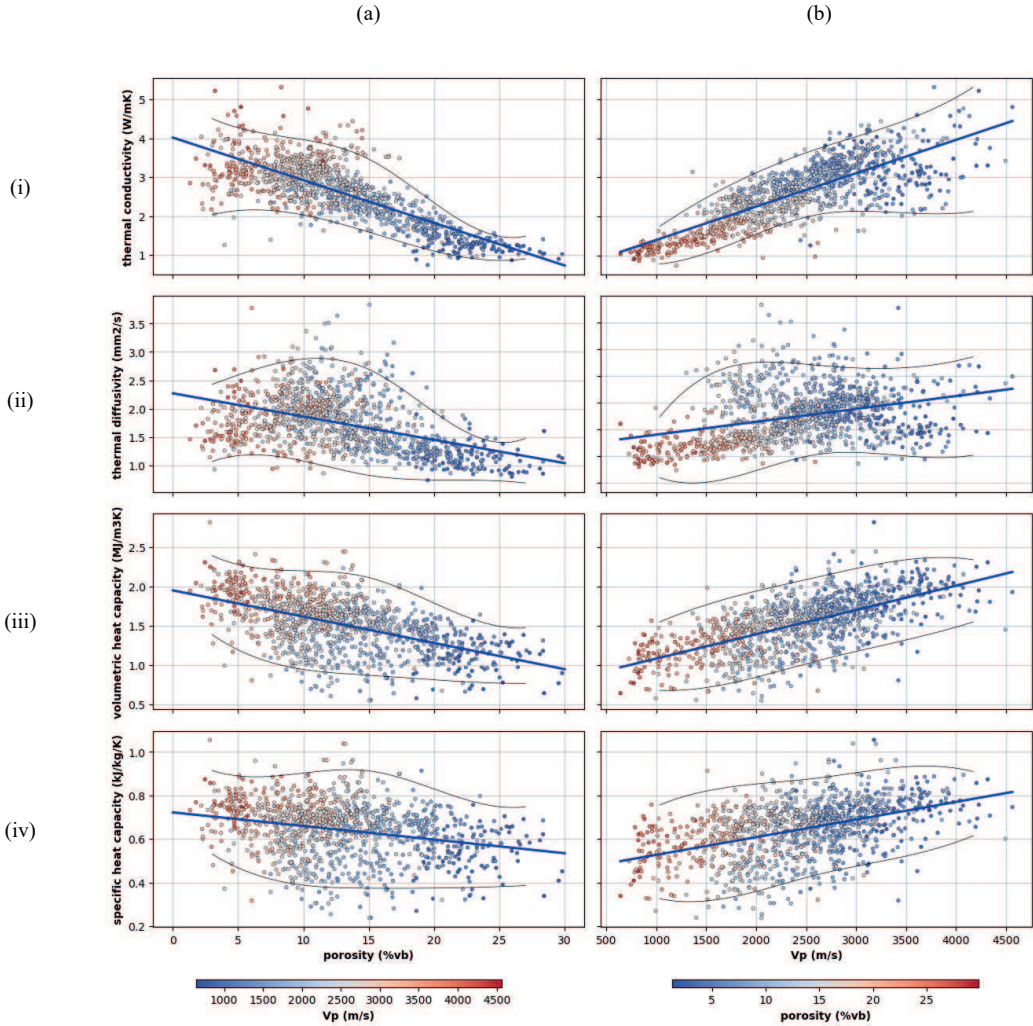


Figure 2.5. Linear regression trendlines of (i) thermal conductivity, (ii) thermal diffusivity, (iii) volumetric heat capacity, and (iv) specific heat capacity versus porosity. The data points are coloured by (a) V_p and (b) porosity. The narrow black lines show the confidence interval ($\pm 2SD$) of 95%. Points are coloured according to the other independent variable (e.g., porosity plots are coloured by V_p , and vice versa), providing a tertiary dimension that helps visually compare how both parameters jointly influence thermal behaviour

Table 2.1 shows that thermal conductivity has the strongest correlations with other properties ($R^2 = 0.58\text{--}0.67$), particularly when estimated from V_s or V_p . Volumetric heat capacity displays moderate correlations (R^2 up to 0.42), whereas thermal diffusivity and specific heat capacity exhibit weaker relationships ($R^2 < 0.27$). The results indicate that while acoustic velocities and porosity can reliably estimate thermal conductivity, they are less effective for predicting other thermal properties. The regression results show that thermal conductivity can be predicted with the highest accuracy, particularly when using V_s ($R^2 = 0.67$) or V_p ($R^2 = 0.63$) as predictors, followed closely by models based on porosity ($R^2 = 0.60$) and bulk density ($R^2 = 0.58$). Volumetric heat capacity can be estimated with moderate accuracy from V_p ($R^2 = 0.42$) and V_s ($R^2 = 0.40$), whereas predictions for thermal diffusivity and specific heat capacity yield considerably lower R^2 values regardless of the predictor used. This indicates that acoustic velocities and porosity are most reliable for estimating thermal conductivity, while other thermal properties require additional parameters to achieve comparable predictive performance.

Table 2.1. Equations, standard deviation, and normalised standard deviation (calculated as the standard deviation divided by the mean, providing a dimensionless measure of variability relative to the dataset average), along with the coefficient of determination (R^2) for linear regression trendlines predicting thermal properties from porosity (ϕ), bulk density (ρ_b), V_p , or V_s . Equations with R^2 values greater than 0.5 are highlighted in green to indicate stronger predictive capability. Corresponding upper and lower standard deviation trendline equations are provided in Table A 1 in Appendix A. the abbreviations stand for: Th_Cond (thermal conductivity $W/m\cdot K$), Th_Diff (thermal diffusivity mm^2/s), VHC (volumetric heat capacity $MJ/m^3/K$), and SHC (specific heat capacity $kJ/kg\cdot K$)

	Correlation	Standard deviation	Normalised standard deviation	Determination coefficient (R^2)
1	$Th_Cond = 1.26 \times 10^{-3} \times V_s + 0.5287$	0.45	0.17	0.67
2	$Th_Cond = 8.56 \times 10^{-4} \times V_p + 0.5393$	0.47	0.18	0.63
3	$Th_Cond = -1.10 \times 10^{-1} \times \phi + 4.0187$	0.49	0.19	0.60
4	$Th_Cond = 3.61 \times 10^{-3} \times \rho_b - 5.9231$	0.50	0.19	0.58
5	$VHC = 3.10 \times 10^{-4} \times V_p + 0.7719$	0.27	0.17	0.42
6	$VHC = 4.30 \times 10^{-4} \times V_s + 0.8082$	0.27	0.18	0.40
7	$VHC = -3.36 \times 10^{-2} \times \phi + 1.9528$	0.29	0.19	0.28
8	$VHC = 1.09 \times 10^{-3} \times \rho_b - 1.0444$	0.30	0.20	0.27
9	$SHC = 8.20 \times 10^{-5} \times V_p + 0.4442$	0.16	0.18	0.21
10	$Th_Diff = 1.38 \times 10^{-3} \times \rho_b - 1.5159$	0.45	0.26	0.20
11	$Th_Diff = -4.01 \times 10^{-2} \times \phi + 2.2624$	0.46	0.26	0.19
12	$SHC = 1.09 \times 10^{-4} \times V_s + 0.4608$	0.12	0.18	0.18
13	$Th_Diff = 3.75 \times 10^{-4} \times V_s + 1.1254$	0.47	0.27	0.14
14	$Th_Diff = 2.35 \times 10^{-4} \times V_p + 1.1776$	0.48	0.27	0.11
15	$SHC = -6.36 \times 10^{-3} \times \phi + 0.7230$	0.12	0.19	0.07
16	$SHC = 1.92 \times 10^{-4} \times \rho_b + 0.1868$	0.13	0.20	0.06

2.4.1. Mineralogy and grain size

The mineralogy of plug samples was estimated through FTIR and XRD measurements on the cores of K18-8 and K18-7x at the locations of the plugs or in their proximity. To produce mineralogy data directly at the plug locations, interpolation was used (see the methods section). No mineralogy data were available nor produced for ZRP-3a and E18-05, such the mineralogical analysis in the current work is restricted to K18 block wells only, meaning a lower range of porosity could be analysed than the full range in the total study. ZRP-3a plug represent the highest porosity and E18-05 the lowest. For the latter well, information on the grain size was available and could thus be analysed.

To further investigate these effects, we examined mineralogical trends within the K18-08 and K18-07x wells, focusing on how specific mineral phases, especially clays, relate to deviations from the general porosity–thermal property relationships. Figure 2.6 presents the example of well K18-08, where the interplay between clay mineral content, kaolin-group minerals, and nacrite is explored in relation to thermal conductivity and porosity.

Thermal conductivity in K18-08 varies with depth, largely reflecting changes in porosity (b-i & ii). Quartz content remains consistently high across the investigated interval, with no marked shifts within the shaded zones (Figure 2.6a-iii). Total clay minerals, which include both the mica group (illite + illite/smectite and muscovite) and the kaolin group (kaolinite, nacrite, and dickite), show distinct increases in the middle and lower shaded zones (Figure 2.6a-iv).

When focusing on the kaolin group alone (Figure 2.6a-v), variability with depth becomes more pronounced, with the largest changes occurring in the same shaded intervals. Among the kaolin minerals, nacrite (Figure 2.6a-vi) displays the highest variability, particularly in the middle and lower shaded zones. Additional information on the distribution of other kaolin minerals is provided in Figure A 1 and Figure A 2. These patterns suggest that intervals enriched in kaolin minerals, and especially in nacrite, tend to correspond with higher thermal conductivity values despite the typically low thermal conductivity of clay minerals. This indicates that mineralogical composition, type, and distribution, in conjunction with porosity, play a key role in controlling thermal conductivity in these samples.

Thermal and acoustic characterisation of Permian Rotliegend sandstones: evaluating the effects of porosity and mineralogy on predicting thermal properties

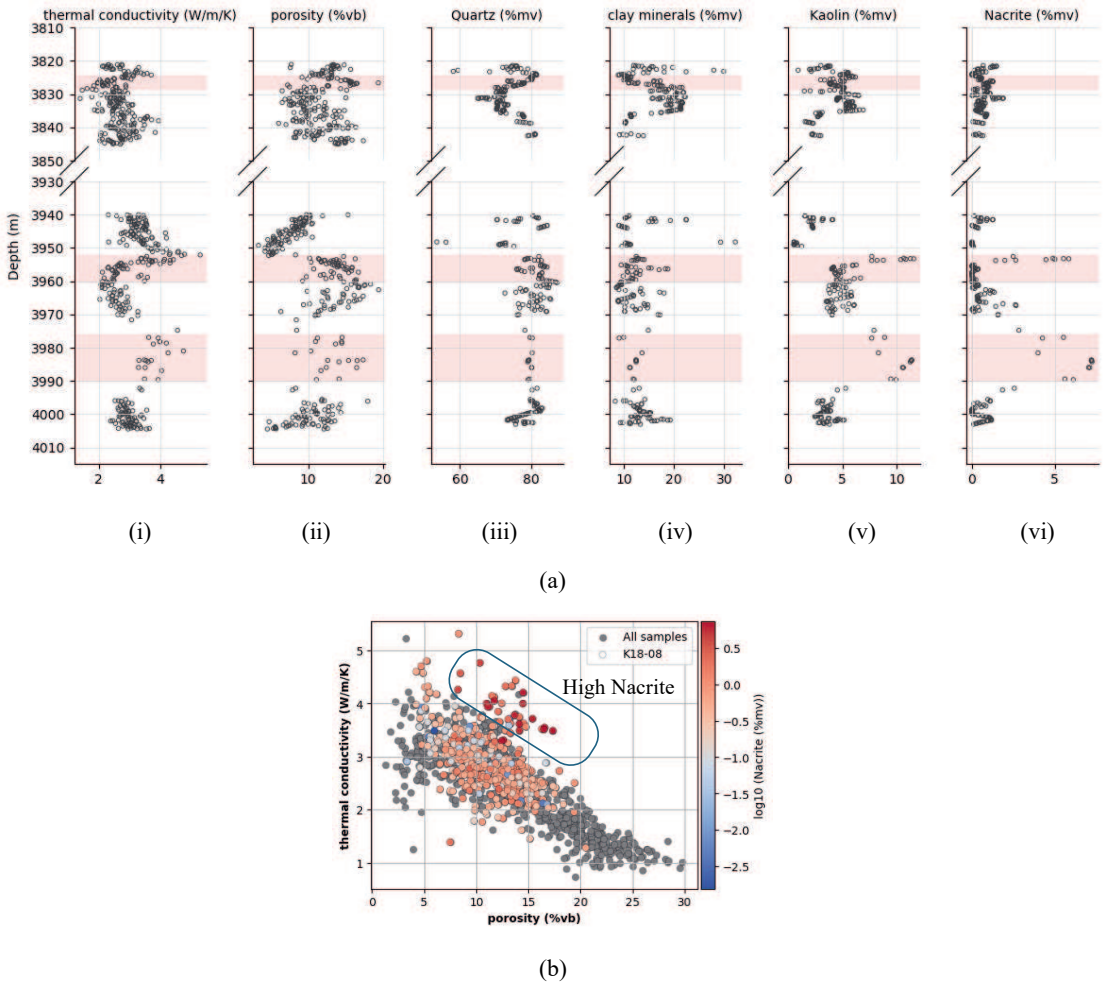


Figure 2.6 Mineralogical trends in the K18-08 samples in percent modal volume (%mv). (a) (i) thermal conductivity, (ii) porosity, (iii) quartz (%mv), (iv) clay minerals (mica group including illite+illite/smectite, muscovite and kaolin group including kaolinite, nacrite and dickite) (%mv), (v) kaolin group (kaolinite, nacrite and dickite) (%mv) and (vi) nacrite (%mv) versus depth. (b) Distribution of nacrite content on the thermal conductivity–porosity plot, with outliers shown in dark red to indicate high nacrite content. The pink shaded zones in subfigure (a) mark the depth intervals from which these outliers originated. Colours represent the base-10 logarithm of mineral content to enhance visual contrast.

The total clay content represented as ‘mean clay’ in the FTIR and XRD results combines clay recognized in the analysis (Figure 2.7). As nacrite, a kaolinite group mineral, is found to impact thermal properties, the plug samples with high nacrite and high kaolinite were excluded from the analysis of the impact of clay mean. It is found that high clay results in lower thermal

conductivity relatively to porosity compared to the main trend. V_p is also found to be lower relatively to the trend with porosity, though more overlap with the main trend occurs. Clay content seems to lower thermal diffusivity relative to porosity but not really impact volumetric or specific heat capacity.

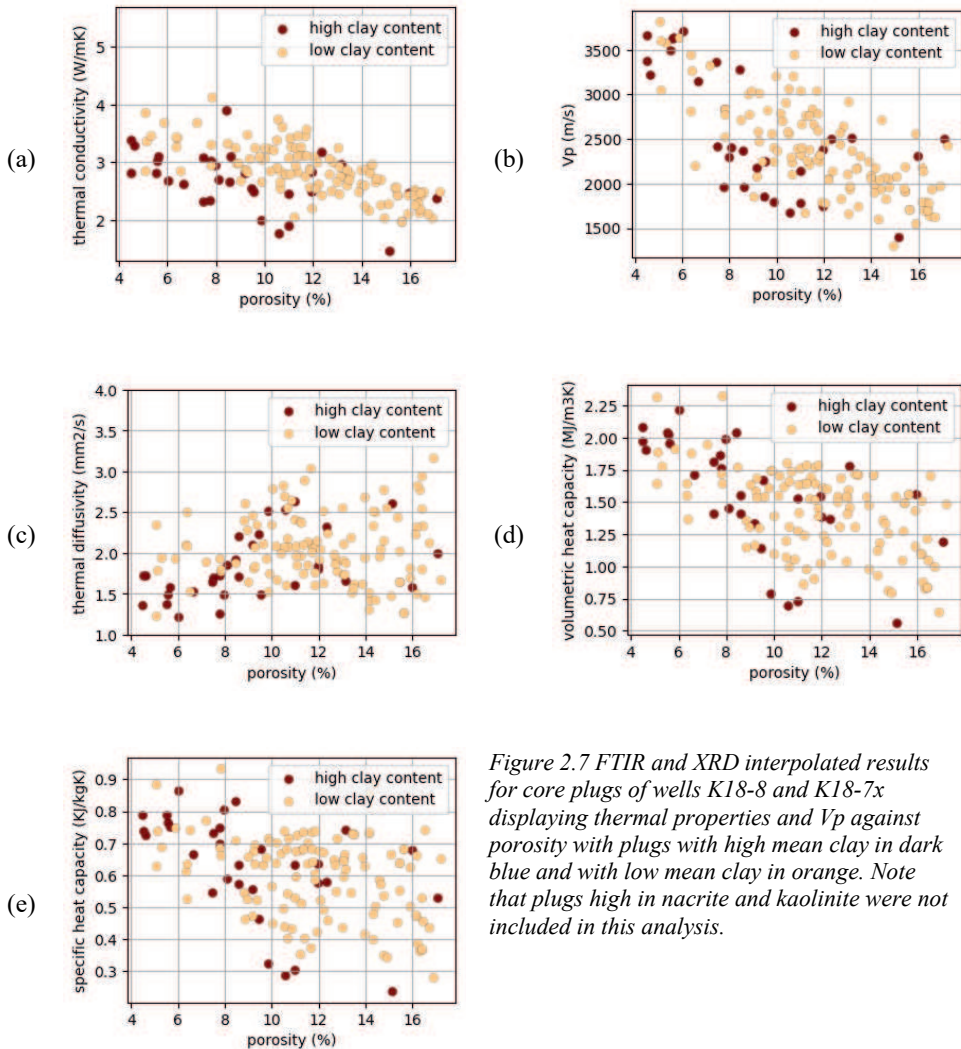


Figure 2.7 FTIR and XRD interpolated results for core plugs of wells K18-8 and K18-7x displaying thermal properties and V_p against porosity with plugs with high mean clay in dark blue and with low mean clay in orange. Note that plugs high in nacrite and kaolinite were not included in this analysis.

Nacrite is a kaolinite group clay mineral and is found to occur in plug samples with relatively higher thermal conductivity compared to the common trend between this property and porosity (Figure 2.8). Nacrite-rich samples occur as a separate outlier group, both in thermal

conductivity versus porosity plots as in V_p versus porosity plots. Compressional wave velocities are higher in samples high in nacrite compared to the common trend. Nacrite-rich samples all have a relatively high porosity between 8 and 18%. Both volumetric and specific heat capacity seem to be slightly higher in samples enriched in nacrite.

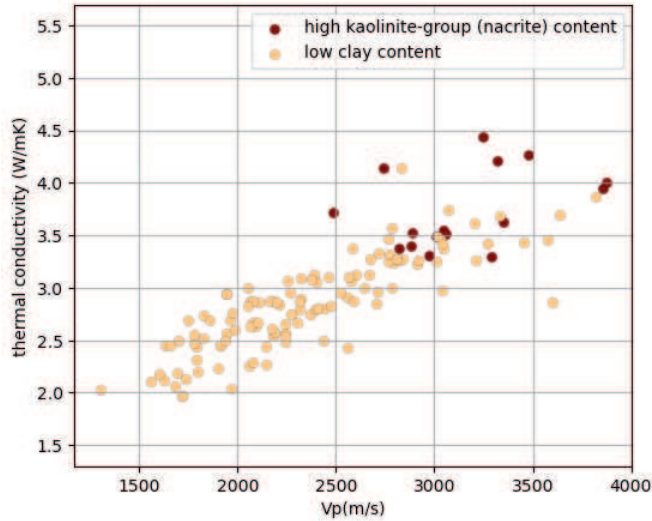


Figure 2.8 Thermal properties and V_p against porosity for plug samples of K18-8 and K18-7x with samples enriched in the kaolinite-group mineral nacrite in dark blue and other samples in orange. Note that samples high in clay are not plotted in this analysis.

Figure 2.9 reveals the compositional control of dolomite/ankerite content (FTIR-derived) on thermal conductivity that is most pronounced at lower porosities. At porosities below $\sim 10\%$ vb, samples with higher dolomite/ankerite content tend to have higher thermal conductivity values. In contrast, at higher porosities ($>15\%$ vb), the influence of mineralogy becomes less apparent, with porosity exerting a stronger control regardless of dolomite/ankerite content. The distribution also highlights that dolomite/ankerite-rich samples are more common in the low-porosity range, suggesting that cementation by carbonate minerals both reduces porosity and enhances thermal conductivity.

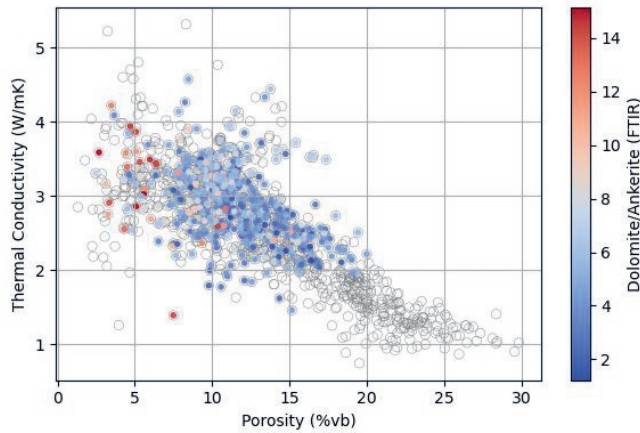


Figure 2.9 Thermal conductivity versus porosity for K18-08 and K18-07x samples, coloured by dolomite/ankerite content measured using the FTIR method. Grey symbols represent samples from other wells or without FTIR mineralogical data. The colour scale shows dolomite/ankerite (%mv), with warmer colours indicating higher abundances. Overall, thermal conductivity decreases with increasing porosity, with higher dolomite/ankerite contents generally occurring at lower porosities.

The detailed analysis of mineralogy and grain size showed that while wells differ in these factors, which influence their V_p , V_s , and thermal and physical properties, similar trends appear in all wells. This consistency allows us to analyse the relationships between thermal, physical, and acoustic properties collectively (Figure 2.5). Thermal conductivity and thermal diffusivity generally decrease with increasing porosity (Figure 2.5a) and increase with V_p (Figure 2.5b). More porous samples exhibit lower variability, whereas less porous samples show greater standard deviation, indicating an increased heterogeneity at lower porosities. Volumetric and specific heat capacities follow similar trends, though their correlations with porosity and V_p are weaker.

Some of the analysed plugs contain pebble-sized clasts, mostly from the K18-08 well (Figure 2.10). Nearly all these pebble-bearing plugs have a low porosity between 4 and 10%. Thermal properties and V_p are in line with the expected trend of each property with porosity.

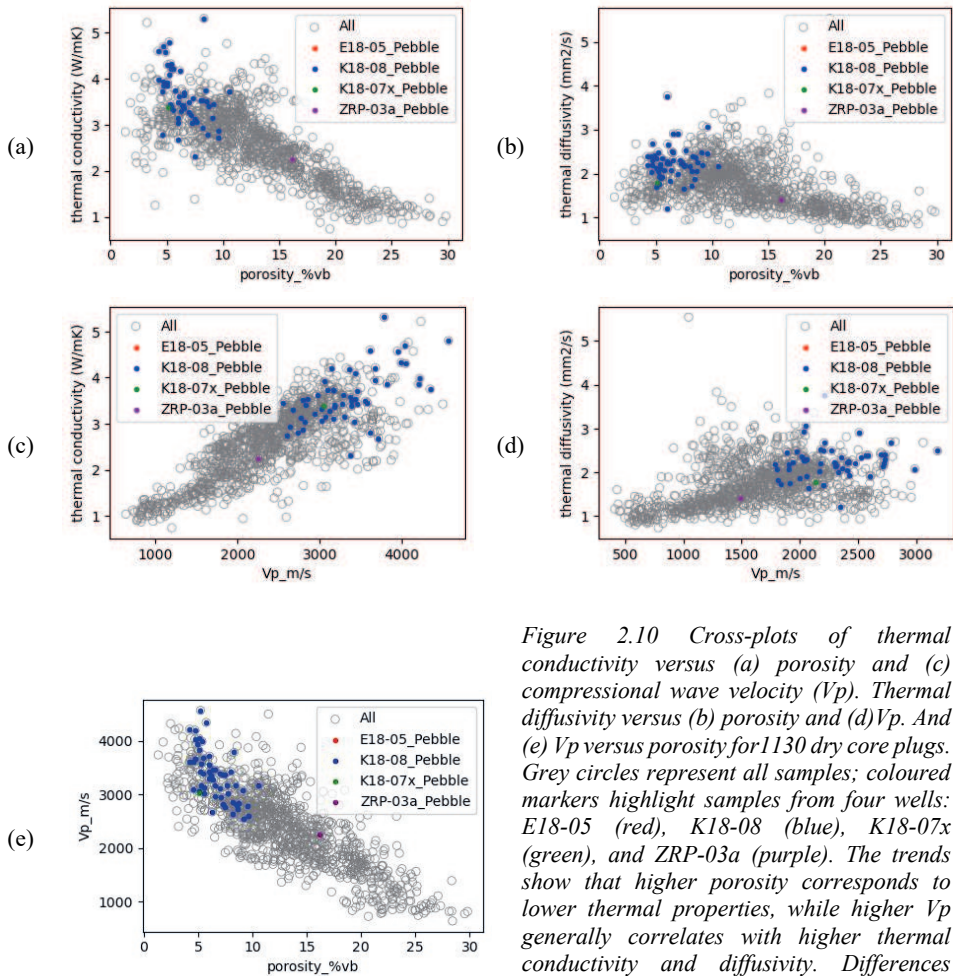


Figure 2.10 Cross-plots of thermal conductivity versus (a) porosity and (c) compressional wave velocity (V_p). Thermal diffusivity versus (b) porosity and (d) V_p . And (e) V_p versus porosity for 1130 dry core plugs. Grey circles represent all samples; coloured markers highlight samples from four wells: E18-05 (red), K18-08 (blue), K18-07x (green), and ZRP-03a (purple). The trends show that higher porosity corresponds to lower thermal properties, while higher V_p generally correlates with higher thermal conductivity and diffusivity. Differences between wells reflect variations in lithification and mineralogical composition.

2.5. Discussion

The core-plug analysis of four Dutch Upper Rotliegend Group wells provides insights into the relationships between thermal, acoustic, and physical properties, and the impact of mineralogy and grain size on these properties. Consistent patterns are observed for some of these properties despite variations driven by mineralogy and grain size. This offers a framework for understanding the controls on thermal and acoustic properties in these regional sandstone reservoirs while at the same time providing insights into the controls on thermal and acoustic properties of clastic rocks, in line with previous work (Brigaud & Vasseur, 1989; Popov et al., 2003).

The studied core plugs display the common strong trends between porosity and bulk density and porosity and permeability according to the theoretical expectations and previous research (Athy, 1930; Lin et al., 2015; Miller & Stewart, 1991; Nelson, 1994) apart from potential measurement errors. There is no reason to disregard any of the studied plugs from the further analysis of thermal and acoustic properties based on these primary rock properties. In the following chapters, we will first discuss the acoustic properties and then the thermal properties to come to an outlook and implication section.

2.5.1. Acoustic properties

The strong negative linear relationship V_p and porosity (Figure 2.3c) demonstrates the influence of porosity on acoustic velocities and, indirectly on rock elastic moduli. With increasing porosity, the ability of the sandstones to transmit P-waves decreases as acoustic waves travel faster through denser media (Yabe et al., 2022). While each subset related to individual wells exhibits its own range of porosity and V_p values, the overall pattern remains similar, and the overall trend found is regarded to be of use to predict acoustic properties based on porosity or bulk density (Table 2).

Overall, the plugs displaying lower porosity show a greater V_p variability resulting in nearly doubling of V_p at the same porosity for different plugs. Such differences may be influenced by variations in primary mineralogy, cementation and recrystallisation, or compaction (Kuijper, 2003; Veeningen & Könitzer, 2016a). Veeningen and Könitzer (2016a) reported that the rock properties of ZRP-03a are partly controlled by mineralogy. These sandstones consist of a dominant quartz framework with leached feldspar contributing to microporosity, and clay minerals are dispersed throughout the matrix, particularly as coating on grains.

The slope of the V_p - V_s trendline depends on rock type and mineralogy (Pelletier, 2009) (Figure 2.3d). It should be noted that uncertainties remain in identifying the P-wave and S-wave arrivals in the measurement data due to low waves amplitude in unconsolidated samples that cause acoustic wave attenuation. To address this, the signal frequency and amplification were adjusted to improve the visibility of attenuated P- and S-wave arrivals. While this enhanced detectability, significant changes can introduce a trade-off between resolution, noise, and picking precision. Band-pass filtering, signal stacking, and envelope detection enhance signal clarity and aid accurate arrival picking. The consistent trends observed between V_p and V_s in the four wells indicate that we broadly deal with similar rock types across the entire dataset. The few outliers belong to the ZRP-03a, mostly with higher V_p compared to V_s , and E18-05, mostly with lower V_p compared to V_s . This should relate to mineralogy and compaction, as discussed above, causing grain boundary and pore structure differences as well as mineralogical differences.

2.5.2. Thermal properties

The large database produced here shows the dominant relation between porosity and thermal conductivity. To a lesser extent, volumetric heat capacity and thermal diffusivity show a trend along with porosity. Specific heat capacity does not show such a trend (Figure 2.4 and Figure 2.5). Scatter occurs on these trends likely due to different geological characteristics, such as mineralogy or microstructure and possibly to device and operator error or plug deterioration over time. These limitations could be mitigated in future studies by using freshly drilled plugs, applying more automated or higher-resolution measurement systems, and ensuring stricter control over sample preservation and handling.

2.5.2.1. Thermal conductivity

Of all measured thermal properties, particularly thermal conductivity shows a rather clean trend with porosity, bulk density and V_p (Table 2.1) as expected from previous research (Popov et al., 2003). As porosity, bulk density and V_p are strongly related, we further discuss here thermal conductivity along with porosity. The Hot Disk system is a widely used and reliable method. Repeated measurements with four replicates per sample indicate that the measurement uncertainty, expressed as the mean standard error, is approximately 0.04 W/m·K for thermal conductivity, 0.03 mm²/s for thermal diffusivity, and 0.03 MJ/m³·K for volumetric heat capacity. These values represent the typical experimental error in this study. Nonetheless, scatter in thermal conductivity may partly reflect uncertainties from surface roughness, sensor contact, or internal heterogeneity. Improvements could involve better surface preparation, controlled contact pressure, or validation with steady-state methods.

Similar to the scatter of acoustic velocity and porosity, such a scatter occurs when comparing thermal conductivity and porosity (Figure 2.5). At lower porosity, this scatter of thermal conductivity and porosity relations is much larger than at higher porosity. Understanding the trend and the scatter around these trendlines may help to improve predictability of thermal conductivity by porosity data. We will attempt to analyse these trends and scatter using the mineralogical analysis and literature, as mineralogy and compaction both exert the dominant controls on thermal properties, like acoustic properties.

Most of the higher porosity plugs are from the ZRP-03a well that is reported to show porosity reduction due to mechanical compaction rather than authigenic minerals or dissolution, even though that occurs (Veenings & Könitzer, 2016a). Primary mineralogy in the ZRP-3a samples is also reported to be rather similar, such one could suggest that the cleaner trend between thermal conductivity and porosity in this well (Figure 2.6a-iv) relates mostly to mechanical compaction on similar minerals. The relatively small scatter that does occur on these data could then be related to the primary and secondary mineralogical changes that are observed in the well. A series of the ZRP-3a samples show considerably lower degree of lithification and plugs and core deteriorate over time as grains are loose and fall off. This in particular occurs with coarse-grained sandstones. The finer grained and the gravels are mostly well lithified. It is not

known what causes this poor lithification in these coarse-grained samples but it may have to do with poor sorting or higher primary mineralogical heterogeneity causing less quartz to quartz grain contacts and a higher degree of clay-rimming and feldspar and mica occurrence, which was observed frequently in this well (Veeningen & Könitzer, 2016a).

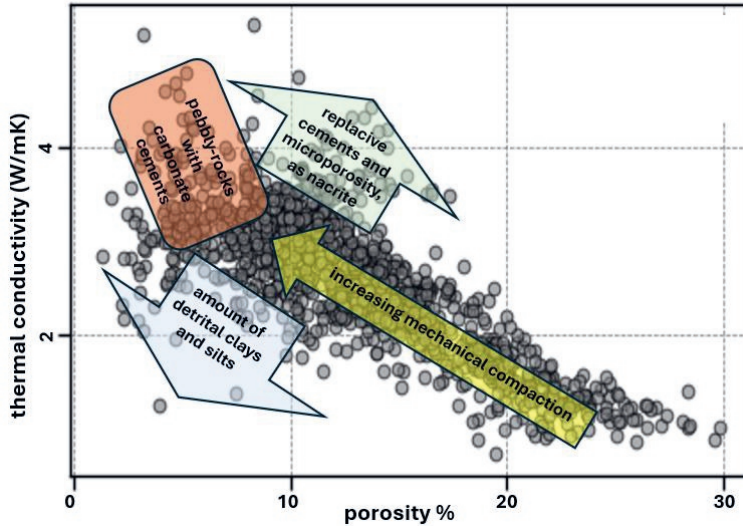


Figure 2.11 Tentative explanations for the main trend and outlier groups in the thermal conductivity versus porosity data of the 1130 Upper Rotliegend Group core plugs in this study.

The total clay content of the FTIR and XRD measurements increases towards lower porosity and lower thermal conductivity. Samples highest in clay show a lower average thermal conductivity compared to the common trend between thermal conductivity and porosity (Figure 2.11) (Cathles, 1999; Glover, 2012; Iranfar et al., 2023; Lei et al., 2019).

Clay minerals have in general lower thermal conductivity than quartz (Brigaud & Vasseur, 1989; Midttomme et al., 1998; Robertson, 1988) which could explain the observed trends. At the same time, samples high in nacrite, a kaolinite-group clay mineral, show higher than expected thermal conductivity compared to the trend (Figure 2.6a). A detailed petrographic study of K18-08 and K18-07s suggests that the nacrite may be coarse-grained replacive authigenic mineral phase replacing feldspar and mostly mica (Nortier et al., 2005). One likely explanation is the role of nacrite in enhancing thermal conductivity through its textural arrangement within the rock. Kaolinite-group minerals, including nacrite, can have relatively higher intrinsic thermal conductivity than other clay minerals due to their tightly packed layered crystal structure. The new grown nacrite connects the surrounding grains such thermal conductivity can remain high while porosity increases by the microporosity of the recrystallised grain in between the nacrite clay crystals.

Plugs rich in pebbles mostly occur in well K18-08 in this study. These show reduced porosity and increase thermal conductivity approximately along with the main trend line of these two properties (Figure 2.11).

2.5.2.2. Thermal diffusivity

Porosity also has a negative impact on thermal diffusivity (Figure 2.4c) because higher porosity reduces the solid pathways for heat transfer, increasing thermal resistance. This is consistent with the previous studies, where Goto and Matsubayashi (2009) proposed a thermal diffusivity-porosity relation for unconsolidated marine sediments (35%–80% porosity) based on the geometric mean model for thermal conductivity and the arithmetic mean model for volumetric heat capacity. Their model effectively predicts thermal diffusivity in two-component sediment systems (e.g., sand or clay with seawater). Fuchs et al. (2021) validated this relation for consolidated sedimentary rocks with lower porosities (3%–35%), demonstrating that it remains applicable in more mineralogically complex materials. Their findings confirmed that higher porosity reduces thermal diffusivity, with pore-fluid saturation further modifying heat transfer properties. Maqsood and Kamran (2005) measured thermal conductivity and diffusivity of five types of Khewra sandstone samples in Pakistan with varying porosity (8–17%) at room temperature and 1 atm pressure and found that both properties decrease with increasing porosity. They found that higher porosity decreases thermal conductivity and diffusivity in Khewra sandstones due to increased air-filled voids, which lower bulk density and heat transfer efficiency.

Their data also show that mineralogical composition plays a crucial role, with quartz-rich samples exhibiting higher thermal conductivity (~3.8–4.2 W/m·K), while dolomite- and calcite-rich samples have lower values (~2.8–3.2 W/m·K). In our data, a similar effect of quartz and calcite on thermal conductivity was observed. However, the impact of dolomite is positive on increasing thermal conductivity and diffusivity (Figure 2.9). The increasing thermal conductivity of samples with high dolomite/ankerite content (FTIR-derived) at porosities below ~10 %vb is consistent with the relatively high intrinsic thermal conductivity of these carbonates compared to the dominant siliciclastic minerals in the dataset.

The reduced influence of mineralogy at higher porosities, compared to the stronger compositional control observed at lower porosities, underscores the role of carbonate cementation, particularly dolomite and ankerite, in simultaneously decreasing porosity and enhancing thermal conductivity (Figure 2.9). This dual effect reinforces the importance of considering mineralogical variations, particularly carbonate content, when predicting thermal properties from petrophysical data. Dolomite's positive impact on the increase in thermal diffusivity and conductivity was also demonstrated by Miao and Zhou (2018) and Kämmlin and Stollhofen (2019). Miao and Zhou (2018) measured thermal diffusivity and conductivity of seven rocks, including four sandstones and three carbonates. In carbonates, dolomite showed the highest values, followed by limestone and marble, while in sandstones, quartz-rich samples had higher values and porosity reduced heat transfer.

2.5.2.3. Heat capacities

The observed negative relationship between volumetric heat capacity and porosity in Figure 2.4b reflects the influence of pore space on the ability of rocks to store heat. As porosity increases, the required heat to increase the temperature of one unit volume of rock becomes less as there is less matrix to heat up. This leads to lower volumetric heat capacity. Kibikas et al. (2025) studied the thermophysical properties of the Ghareb Formation, a porous calcite-rich carbonate rock resembling chalk or mudstone, with high porosity (20–45%) and low strength, and is of relatively soft, sedimentary origin. Their research Kibikas et al. (2025) demonstrated that volumetric heat capacity decreases with increasing porosity, primarily due to the presence of air or fluid-filled voids within the rock matrix, which was before indicated by Somerton (1958) studying a small sample set of eight sedimentary rock samples of different rock types.

Clauser (2011) similarly stated that as porosity increases, the volumetric heat capacity decreases due to the differing heat capacities of the fluid and solid matrix. Though no specific formula was provided, this follows from volumetric heat capacity being the product of density and specific heat, and density is strongly negatively affected by porosity.

In contrast, the relationship between specific heat capacity and porosity in the dataset shows no clear trend (Figure 2.4d). Robertson (1988) reported that specific heat capacity can be calculated from the mineral composition of a rock, suggesting that variations in specific heat are more closely related to mineralogical differences than to porosity values. Abdulagaov et al. (2019) measured the specific heat capacity of sandstone samples across a range of temperatures and found that changes in specific heat were primarily due to temperature effects and microstructural changes, with porosity having a minimal impact. Quartz, a dominant mineral in sandstones, has a specific heat capacity of approximately 0.73 J/g/K (Waples & Waples, 2004), while clay minerals and feldspars typically exhibit higher values (~0.9–1.0 J/g/K). The influence of pore space is minimal unless the pores are filled with fluids like water, which has a much higher specific heat capacity (4.18 J/g/K (Čermák & Rybach, 1982)). In contrast, air-filled pores have a negligible effect due to the low specific heat capacity of air.

2.5.3. Quantitative comparison of property relationships in this and previous studies

Some studies have examined the relationship between thermal conductivity and V_p in various rock types, including sandstones, using both linear and exponential regression models. For instance, Mielke et al. (2017a) analysed 554 dry sandstone plug samples from Permo-Carboniferous in Germany. They are both outcrop and core plugs that cover a wide range of porosity and grain size. Their study confirmed that both linear and exponential models could describe the thermal conductivity- V_p relationship, with prediction accuracies of ± 0.5 W/m·K and confidence levels exceeding 80% for sediments and mafic volcanics. Kämmlein and Stollhofen (2019) investigated mineralogically heterogeneous Permo-Triassic sandstones from Bavaria and found that combining V_p with mineralogical data, such as quartz volume fractions, improves predictions of bulk thermal conductivity. Their dataset shows wide but overlapping

ranges with ours, with thermal conductivity spanning approximately 1 to 6 W/m·K and V_p between about 1000 and 6000 m/s. In both studies, this broad distribution likely reflects variability in mineral composition, porosity, and cementation. Figure 2.12 compares these three studies, showing similar overall trends despite differences in geological setting and stratigraphic coverage.

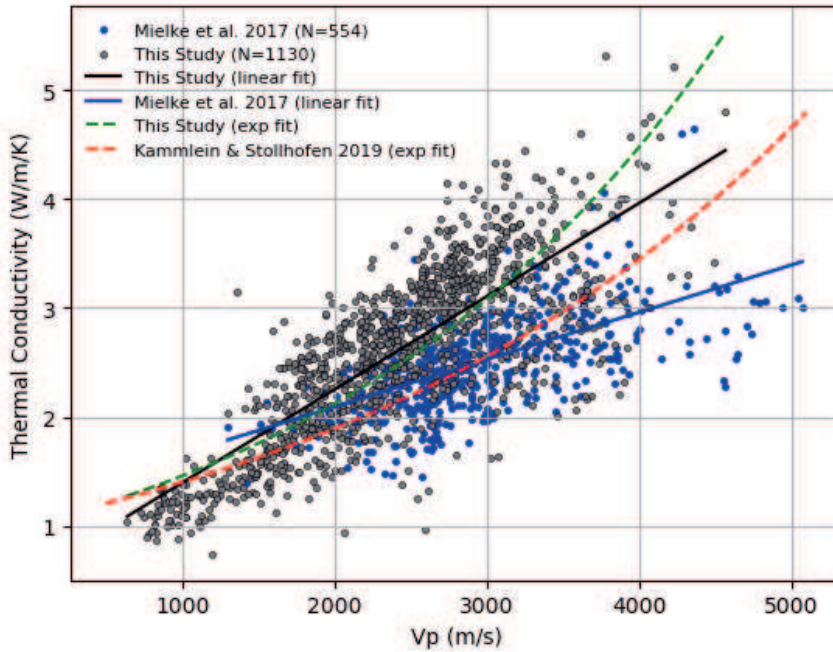


Figure 2.12. Comparison between the data from this study and the study of Mielke et al. (2017a) and (Kämmlin & Stollhofen, 2019). The statistics of the trendlines are (This Study [Linear]: $k = 0.0009 \cdot V_p + 0.5393$, $R^2 = 0.628$, $N = 1130$), (This Study [Exp]: $k = 1.0035 \cdot e^{(0.00037 \cdot V_p)}$, $R^2 = 0.540$, $N = 1130$), (Mielke [Linear]: $k = 0.0004 \cdot V_p + 1.2248$, $R^2 = 0.376$, $N = 554$), and (Kämmlin and Stollhofen (2019)[Exp]: $k = 1.0383 \cdot e^{(0.0003 \cdot V_p)}$, $R^2 = 0.740$). The data of Kämmlin and Stollhofen (2019) were not available to add to the cross plot and only their developed trendlines was included here.

The comparison shows strong consistency between the three studies, all exhibiting a positive correlation between thermal conductivity and V_p . Our data points (in grey) are more scattered, likely reflecting greater variation in porosity, grain size, mineralogy, and microstructural characteristics compared to the dataset of Mielke et al. (2017b) (blue). Compared to Mielke's regression ($k = 0.0004 \cdot V_p + 1.2248$), our linear fit ($k = 0.0009 \cdot V_p + 0.5393$) exhibits a steeper slope and lower intercept. These differences are most likely linked to the broader property ranges and heterogeneity in our dataset rather than geographic setting. The higher R^2 (0.628 vs. 0.376) and larger sample size ($N = 1130$ vs. 554) of our present study indicate a stronger correlation in the present dataset. Kämmlin and Stollhofen (2019) fitted a relationship ($R^2 = 0.563$), suggesting some variability in how these sandstones respond to changes in V_p .

Based on our data, a linear trendline predicts thermal conductivity as a function of V_p better than an exponential function. Additionally, Kämmlin and Stollhofen (2019) identified a subset of their sandstone samples containing more than 85 vol.% total quartz, which plotted as outliers with comparatively high thermal conductivities for a given porosity. In their air-saturated dataset, this quartz-rich zone corresponds roughly to 3.0–5.2 W/m·K and 3000–6200 m/s, while in their water-saturated dataset it spans approximately 3.0–5.8 W/m·K and 2500–5500 m s⁻¹ (Figure 2.9 in (Kämmlin & Stollhofen, 2019)). Although their raw measurements are not available for direct overlay, our Permian samples fall within these reported ranges, indicating a comparable quartz-rich composition, as shown in Figure 2.6a, and similar influence on thermal and acoustic properties. Their study suggested that empirical models solely based on porosity or V_p were insufficient, indicating the need for more complex models that may include both linear and exponential components. This aligns with the findings of Luo et al. (2016), who also observed a positive relationship between thermal conductivity and V_p in silty sandstone, further supporting the need to evaluate both linear and exponential models based on the specific characteristics of the samples.

In summary, both linear and exponential regression (non-linear) models have been employed to describe the relationship between thermal conductivity and V_p in sandstones and other rock types. The choice between linear and exponential models often depends on the specific characteristics of the rock samples, including porosity, mineral composition, and anisotropy. Therefore, it is essential to consider these factors when selecting the most appropriate model for predicting thermal conductivity from V_p .

2.6. Conclusion

This study of Permian reservoir formations in four wells (K18-08, K18-07x, ZRP-03a, and E18-05) reveals that porosity dominates variations in permeability, bulk density, acoustic wave velocities (V_p and V_s), thermal conductivity, volumetric heat capacity, thermal diffusivity, and permeability. At higher porosities, reduced solid matrix explains the lower acoustic velocities and heat-transfer efficiency, while improved pore connectivity boosts permeability.

A higher lithification degree reduces porosity and so results in higher acoustic and thermal properties. Mineralogy has a secondary effect on these relations, with clay-rich samples tending toward lower thermal conductivity and larger quartz grains slight decrease wave transmission. Intergranular cementation, such as by dolomite results in lower porosity and higher thermal and acoustic porosity along the common trendline between these two properties. On the other hand, an increase in detrital clay and silt, results in low porosity and lower than average thermal conductivity and V_p . Increasing the amount of replacive authigenic cement, here in the form of nacrite, raises both porosity by microporosity and thermal conductivity and V_p higher above the trend between these properties.

Linear regression equations (Table 2.1) confirm that porosity and V_p can reliably estimate thermal properties, with mineralogy and microstructural features explaining outliers. These

findings can guide enhanced reservoir characterisation and well-completion strategies in geothermal projects as well as inform carbon capture and hydrogen storage initiatives, where understanding porosity-driven behaviour is crucial for efficient and secure subsurface operations. Although all measurements were made on dry samples, the internally consistent relationships observed between porosity, mineralogy, and thermal/acoustic properties remain valuable for interpreting variations within the dataset and for providing baseline information in geothermal reservoir studies.

2.7. Appendix 1

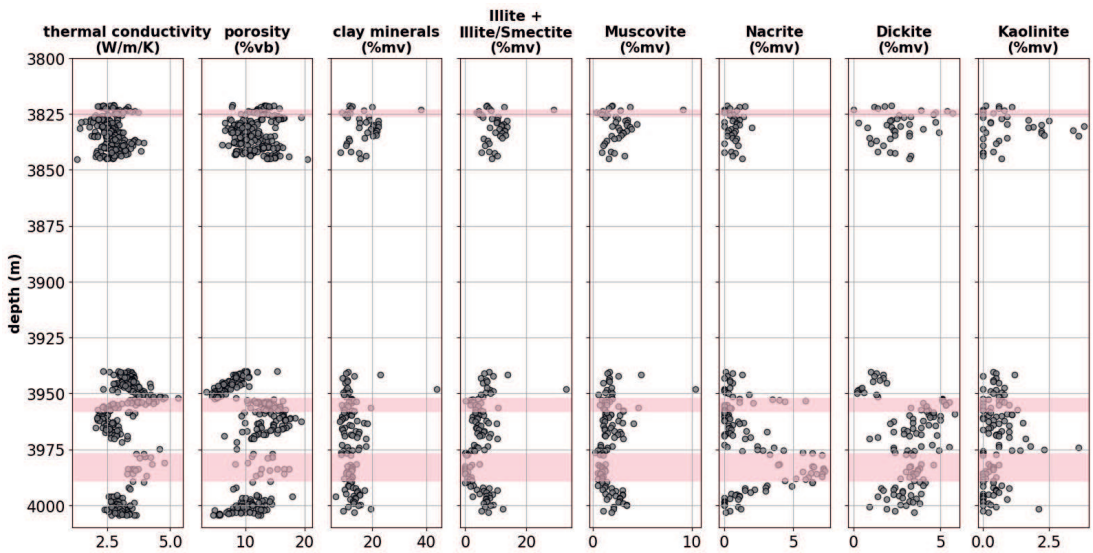


Figure A 1. The experimental data for K18-08 samples including (from left to right) thermal conductivity (W/m·K), porosity (%vb), clay minerals (%mv), illite+illite/smectite (%mv), Muscovite (%mv), Nacrite (%mv), Dickite(%mv), and Kaolinite(%mv).

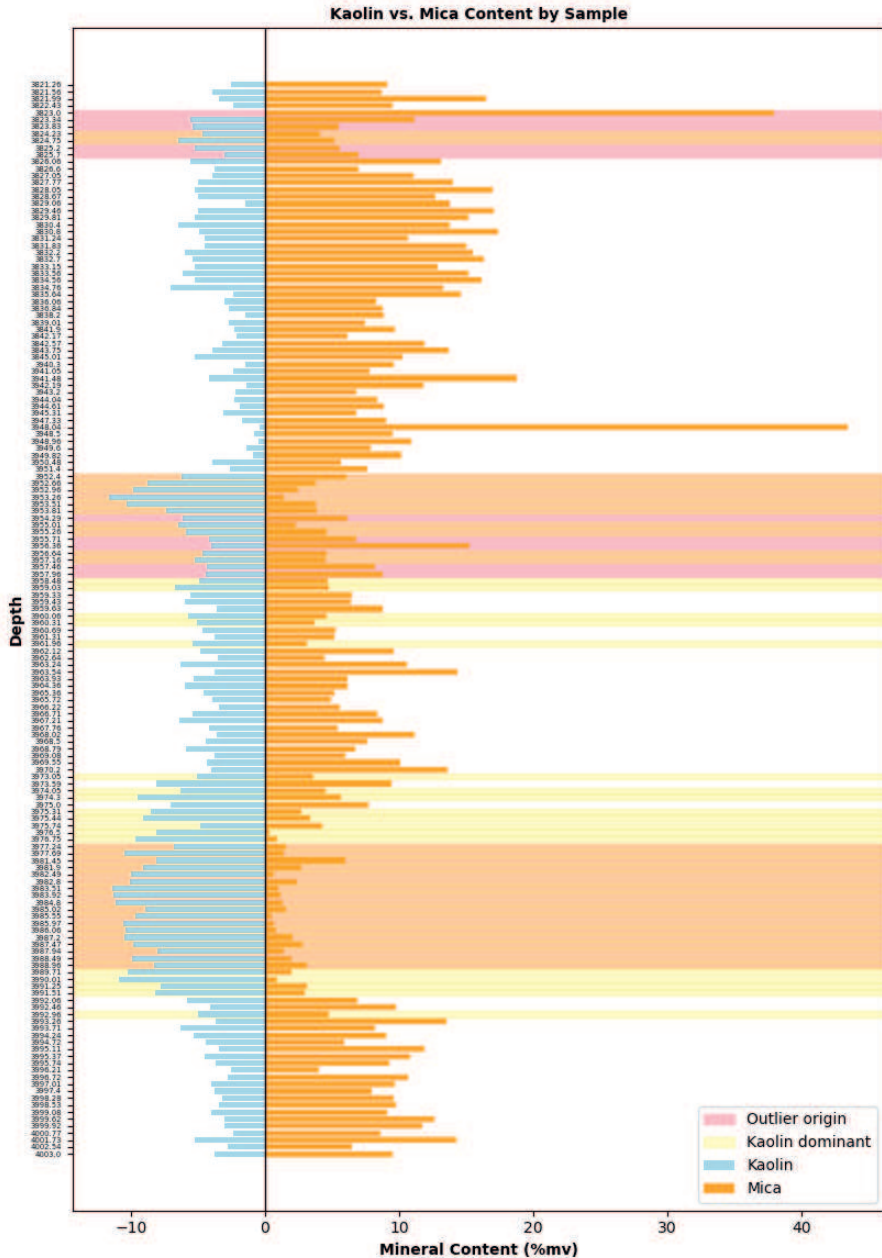


Figure A 2. Kaolin minerals (Dickite + Nacrite + Kaolinite) and Mica (illite + illite/smectite + Muscovite) versus depth. The yellow zones are where kaolin minerals are more than minerals.

Thermal and acoustic characterisation of Permian Rotliegend sandstones: evaluating the effects of porosity and mineralogy on predicting thermal properties

Table A 1. Equations and R^2 values for the upper and lower trendlines defining the uncertainty bands (± 2 standard deviations) in the relationship of thermal conductivity, thermal diffusivity, volumetric and specific heat capacities with porosity, and V_p .

y=2×standard deviation	Upper trendlines equation	R^2	Lower trendline equation	R^2
Thermal conductivity	$3.057 \times 10^{-4} \times \varphi^3$ $- 0.01793\varphi^2$ $+ 0.1614\varphi + 3.901$	0.9886	$3.826 \times 10^{-4} \times \varphi^3$ $- 0.01806\varphi^2$ $+ 0.1813\varphi + 1.639$	1
Thermal diffusivity	$4.522 \times 10^{-4} \times \varphi^3$ $- 0.02611\varphi^2$ $+ 0.3733\varphi + 1.342$	0.9809	$1.473 \times 10^{-4} \times \varphi^3$ $- 5.957 \times 10^{-3} \times \varphi^2$ $+ 0.04228\varphi + 1.082$	0.9596
Volumetric heat capacity	$2.215 \times 10^{-5} \times \varphi^3$ $- 2.602 \times 10^{-3} \times \varphi^2$ $+ 0.02164\varphi + 2.244$	0.9786	$-1.07 \times 10^{-4} \times \varphi^3$ $+ 6.128 \times 10^{-3} \times \varphi^2$ $- 0.1221\varphi + 1.668$	0.9922
Specific heat capacity	$3.214 \times 10^{-6} \times \varphi^3$ $- 8.413 \times 10^{-4} \times \varphi^2$ $+ 0.01567\varphi$ $+ 0.8358$	0.9337	$-3.969 \times 10^{-5} \times \varphi^3$ $+ 2.347 \times 10^{-3} \times \varphi^2$ $- 0.04397\varphi + 0.6342$	0.9914
Thermal conductivity	$1.105 \times 10^{-10} \times V_p^3$ $- 9.5 \times 10^{-7} \times V_p^2$ $+ 3.563 \times 10^{-3} \times V_p$ $- 1.084$	0.9997	$-2.38e - 11V_p^3$ $- 8.28e - 08V_p^2$ $+ 1.402 \times 10^{-3} \times V_p$ $- 0.712$	0.9818
Thermal diffusivity	$2.159 \times 10^{-10} \times V_p^3$ $- 1.836 \times 10^{-6} \times V_p^2$ $+ 4.997 \times 10^{-3} \times V_p$ $- 1.634$	0.9819	$-6.139 \times 10^{-11} \times V_p^3$ $+ 3.61 \times 10^{-7} \times V_p^2$ $- 3.458 \times 10^{-4} \times V_p$ $+ 0.4919$	0.9252
Volumetric heat capacity	$-1.423 \times 10^{-11} \times V_p^3$ $+ 4.635 \times 10^{-8} \times V_p^2$ $+ 3.353 \times 10^{-4} \times V_p$ $+ 1.196$	0.9980	$-2.111 \times 10^{-11} \times V_p^3$ $+ 1.848 \times 10^{-7} \times V_p^2$ $- 2.043 \times 10^{-4} \times V_p$ $+ 0.6901$	0.9984
Specific heat capacity	$-2.452 \times 10^{-12} \times V_p^3$ $+ 3.816 \times 10^{-9} \times V_p^2$ $+ 8.497 \times 10^{-5} \times V_p$ $+ 0.6844$	0.9795	$-9.078 \times 10^{-12} \times V_p^3$ $+ 8.163 \times 10^{-8} \times V_p^2$ $- 1.258 \times 10^{-4} \times V_p$ $+ 0.3595$	0.9937

2.8. Appendix 2

The dataset supporting this study is publicly available through the 4TU.ResearchData repository (Kolah-Kaj et al., 2024). This database is a collection of all data generated and retrieved as part of the ProperBase project at TU Delft, Netherlands, which investigates key geothermal plays in the Dutch subsurface. The database contains the information of material at various scales such as wellbore, core, plug sample, as well as their data imaging, mineralogy,

acoustic and thermal properties, grain size analysis, and petrography. Basic rock and flow properties, acoustic data, and thermal properties are included, covering both existing and newly measured properties of core samples.

3.Porosity and Mineralogical Controls on Thermal and Acoustic Properties of Sandstones from the Triassic Main Buntsandstein Subgroup and Permian Upper Rotliegend Group in the Netherlands

Abstract: Thermal and acoustic properties of reservoir sandstones are critical for characterising and understanding the subsurface, evaluating the feasibility, safety, and sustainability of geothermal energy exploitation, and constraining the lithological and diagenetic factors that govern reservoir behaviour. Most previous studies focused on small datasets or isolated properties, meaning comparative analysis was limited. This study investigates the thermal, acoustic, and petrophysical properties of sandstones from the Triassic Main Buntsandstein subgroup of more than 700 core plugs and compared to the Permian Rotliegend Group data (Chapter 1) both from the Dutch subsurface. Both datasets were analysed by integrating porosity, permeability, bulk density, thermal conductivity, diffusivity, heat capacity, acoustic velocities, and mineralogical data obtained from XRD and FTIR. The Buntsandstein, deposited in a semi-arid fluvio-lacustrine system of sand, silt, and clay, exhibits systematic porosity-dependent property trends. Thermal conductivity and diffusivity decrease with increasing porosity, while permeability increases, reflecting porosity as the first-order control. Acoustic velocities show strong negative correlations with porosity. Systematic deviations from this correlation are introduced by mineralogy and fabric. Detrital clays are hypothesised to tighten the grain framework and increase velocities, replacive clays derived from feldspar leaching are associated with enhanced thermal conductivity, dolomite cement lowers both porosity and conductivity, and nacrite-rich samples combine higher porosity with efficient heat transport. Sedimentary lamination produces orientation-dependent velocity variability, with horizontal lamination lowering and vertical lamination raising measured velocities. Principal component analysis shows similar structures in both formations, with porosity opposing density and velocities, while thermal transport properties define an independent direction of variability. Thermal conductivity links partly to the framework, whereas thermal diffusivity is largely independent. Detailed comparison of Buntsandstein with Rotliegend sandstones reveals systematic offsets. For acoustic velocities, Buntsandstein and Rotliegend samples remain consistently separated across the porosity range, with the Triassic showing higher V_p and V_s with similar trends. Thermal property differences vary with porosity, with separation of the data between formations is more pronounced at low porosity, while overlap increases at higher porosity. For bulk density, values are similar below 12% porosity, but Rotliegend samples become systematically denser than the Buntsandstein at higher porosities. These findings demonstrate that porosity provides the first-order control on thermo-physical behaviour, while mineralogy and fabric impose predictable deviations, establishing a framework for extrapolating laboratory results to well logs and reservoir models and supporting geothermal resource assessment in the Netherlands.

3.1. Introduction

The Main Buntsandstein Subgroup of the Lower Triassic is regarded as a potential target for geothermal development in the Dutch subsurface (Mijnlieff, 2020). The suitability of this formation for geothermal purposes has previously been assessed at a regional scale using seismic data to evaluate how structural factors control the distribution of Main Buntsandstein

sediments in the Roer Valley Graben (Cecchetti et al., 2024b; Cecchetti et al., 2024a; Mijnlief, 2020; PanTerra Geoconsultants B.V., 2012). Some research on Buntsandstein reservoir go to smaller scales. For example, applied detailed facies analysis and sedimentary logging at outcrop and core scale, supported by thin section petrography, to characterise lithofacies, grain size trends, and stratigraphic architecture within the Main Buntsandstein Subgroup in the Roer Valley Graben.

Heap et al. (2017) analysed 133 Buntsandstein sandstone samples from the Soultz-sous-Forêts geothermal site, studying their porosity, mineral composition, and pore structure. They reported porosities of 0.03–0.20 in borehole samples and 0.18–0.25 in quarry samples, with minimal isolated porosity. Low permeability, due to pore-filling minerals, was identified as a key factor limiting fluid flow and geothermal potential. Beyer et al. (2014) examined 73 sandstone samples from the Buntsandstein formation, sourced from deep drill cores in the Thuringian Syncline and surface outcrops at its margins. They analysed the petrophysical properties of Buntsandstein sandstones, emphasizing the role of depositional environment and diagenesis. They reported that outcrop sandstones have ~5% higher porosity than deep borehole samples, with permeability ranging from ~4 mD in lacustrine facies to 27–108 mD in fluvial and aeolian facies. Cementation significantly influenced porosity, with carbonate cement more common in lacustrine sandstones and sulphate cement in aeolian sandstones. Mechanical compaction accounted for ~26% porosity loss, exceeding cementation effects. Haffen et al. (2015) studied the petrophysical characteristics of Buntsandstein. They reported that the Buntsandstein formation in the Upper Rhine Graben exhibits highly heterogeneous petrophysical properties, with permeability and porosity largely controlled by sedimentary facies and structural features. Thermal conductivity variations and fluid flow pathways, influenced by fault zones and diagenetic processes, play a crucial role in determining its potential as a geothermal reservoir. Yousaf et al. (2023) assessed the reservoir quality and heterogeneity of the Middle Buntsandstein sandstones in the southern Netherlands for deep geothermal exploration. Their study combined petrographic analysis and core measurements to evaluate porosity, permeability, and diagenetic controls. They found that aeolian sandstones exhibit the highest reservoir quality, with porosity and permeability higher than 18% and 100 mD, respectively, while ephemeral fluvial sandstones have significantly lower porosity (below 10%) and permeability (below 1 mD). The study highlights grain size and quartz content as primary controls on reservoir properties, whereas carbonate and anhydrite cement act as local constraints.

These findings emphasise the heterogeneous nature of the Buntsandstein reservoirs and the importance of depositional environments, diagenesis and mineralogy in predicting geothermal potential. Comprehensive studies on Buntsandstein rock properties in the Dutch subsurface that combine thermal, acoustic, and other petrophysical measurements on a sufficiently large number of core plugs to capture heterogeneity and map trends are needed for geothermal development in the Netherlands. Therefore, the objective of this study is to focus on the Main Buntsandstein Subgroup by emphasizing the importance of this formation for geothermal

applications, as stated in previous studies, and to re-examine it from a petrophysical perspective by understanding the rock properties relevant for geothermal development and other subsurface projects. This will be accomplished by presenting the measured thermal, acoustic, and primary rock properties of Triassic Buntsandstein and investigating the relationships between these properties. The next goal of this study is to compare these Triassic data with a large, similar database produced for the Permian Upper Rotliegend Group (Kolah-Kaj et al., 2024; Kolah-Kaj et al., 2021). This comparison between the Rotliegend (Permian) and Triassic formations provides valuable insight into how rock properties such as thermal conductivity, acoustic velocity, porosity, density, and permeability vary across different geological periods. This approach helps identify fundamental trends and empirical relationships that govern rock behaviour under different depositional and diagenetic conditions. Establishing these relationships allows for a better understanding of how key properties correlate, highlighting potential systematic variations between formations. Such an approach is essential for refining rock property estimates in geothermal and subsurface applications, where the continuity and consistency of reservoir characteristics play a crucial role.

3.1.1. Thermo-physical properties

These thermal properties are influenced by a range of rock features (Sun et al., 2017) as well as surrounding conditions such as pressure and temperature (Abdulagatova et al., 2009; Emirov et al., 2021; Maqsood & Kamran, 2005), and due to the inherent complexity of rocks (Popov et al., 2016), interpreting the controls on these thermal properties is challenging.

Thermal conductivity is a fundamental property that governs heat transfer through the rock framework and is a key parameter in geothermal reservoir assessment. In sandstones, porosity is the primary control. Thermal conductivity decreases systematically with increasing porosity because pores act as thermal insulators, interrupting the pathways for heat conduction (Abdulagatova et al., 2009; Haffen et al., 2017; Sun et al., 2017). This negative relationship has been demonstrated in both bulk laboratory measurements and spatially resolved conductivity maps, which show that higher porosity zones correspond to lower conductivities (Haffen et al., 2017). The effect of pore fluid is also significant. Air, with a thermal conductivity of ~ 0.025 W/m·K, provides minimal heat transfer, whereas water or brine (~ 0.6 W/m·K) increases conductivity relative to air-filled pores (Popov et al., 2016). However, porosity remains the dominant factor under both dry and saturated conditions. Mineralogy sets the baseline level of conductivity. Quartz has a high intrinsic conductivity ($\sim 6\text{--}7$ W/m·K), while feldspars, clays, and calcite are typically lower ($2\text{--}4$ W/m·K) (Anand et al., 1973; Clauser & Huenges, 1995b; E. C. Robertson, 1988). Among carbonate minerals, calcite averages ~ 3.3 W/m·K, dolomite $\sim 5.1\text{--}5.3$ W/m·K, and magnesite ~ 5.0 W/m·K, highlighting their intermediate to high conductivity relative to other rock-forming minerals (Brigaud & Vasseur, 1989; Clauser & Huenges, 1995b). Additional rock characteristics such as grain size and cementation also play a role. Experimental work on synthetic quartz sands showed that finer

grain sizes reduce conductivity due to increased microporosity and scattering of conduction paths (Midttomme & Roaldset, 1998).

Volumetric heat capacity is another critical property, as it describes the ability of a given rock volume to store heat per unit temperature change. It is the product of bulk density and specific heat capacity (Clauser & Huenges, 1995a), and thus depends on both porosity and mineralogy. Increasing porosity generally lowers volumetric heat capacity in dry sandstones, because pore space contributes little storage (Hillel, 2003). The type of pore-filling fluid can significantly alter this property; fluid-filled pores raise volumetric heat capacity because water has much higher heat storage than air (Popov et al., 2016). Mineralogy also influences volumetric heat capacity. Quartz, for example, has a relatively low specific heat ($\sim 710 \text{ J/kg}\cdot\text{K}$) and high density, yielding values of $\sim 2.1\text{--}2.4 \text{ MJ/m}^3\cdot\text{K}$, whereas feldspar- and clay-rich rocks may store more heat at equal porosity (Clauser & Huenges, 1995b).

Thermal diffusivity, which quantifies the rate at which temperature changes in a material, is defined as the ratio of thermal conductivity to volumetric heat capacity. Because porosity reduces both conductivity and volumetric heat capacity, the correlation of diffusivity with porosity reflects the balance of these effects. In dry sandstones, conductivity decreases more strongly with porosity than volumetric heat capacity does, leading to an overall decline in diffusivity (Goto & Matsubayashi, 2009). Microcracks and fracture networks further lower diffusivity by strongly reducing conductivity while only minimally affecting volumetric heat capacity, since cracks add negligible volume (Sun et al., 2016). Deviations from the main porosity–diffusivity trend are often linked to mineralogical contrasts, diagenetic features, or facies heterogeneity, which can locally modify both conductivity and heat capacity as described above.

Specific heat capacity, the heat storage per unit mass of rock per unit temperature change, is controlled by mineral composition and pore fluid (Čermák & Rybach, 1982; Robertson, 1988; Schärli & Rybach, 2001). In dry conditions, porosity has little direct influence, and mineralogy becomes the main factor (Heap et al., 2020; Waples & Waples, 2004). Quartz-rich rocks tend to have slightly lower specific heats compared to rocks richer in feldspars, micas, or clays. However, when pores are filled with water or brine, the effective specific heat capacity of the bulk rock increases, since the pore fluid contributes substantially to the heat storage. Thus, porosity affects specific heat capacity primarily when fluids are present.

3.1.2. Geological background

The study area is the Q block of the Dutch North Sea, located within the West Netherlands Basin. The studied wells penetrated Buntsandstein formation in this area are Q11-03, Q01-25, Q04-10, and Q4-C2 (Figure 3.1b). These Triassic sandstone formations belong to the Early Triassic geological period (Induan stage) and form part of the Lower Germanic Triassic Group with the Lower Buntsandstein dated to approximately 249–251 million years ago (Figure 3.1a).

The formation is the second most prolific hydrocarbon-producing formation for the Netherlands (Korevaar et al., 2023; Van Hulten, 2006). Geluk and Röhling (1997) provide key insights into the depositional environment, stratigraphic variability, tectonic influences, and cyclicity of the Buntsandstein. The Buntsandstein was deposited in a fluvio-lacustrine setting, where alternating wet and dry climate cycles-controlled sedimentation. These climatic shifts produced cyclic variations in sediment characteristics, which in turn affected trends in porosity and permeability. Geluk and Röhling (1997) distinguish seven primary sequences, including the Volpriehausen, Detfurth, and Hardegsen sequences, which serve as key gas-bearing formations. The depositional evolution of the Lower to Middle Buntsandstein reflects a transition from dominantly fluvial to fluvio-lacustrine environments, resulting in laterally extensive sand bodies. These successions may provide more continuous reservoir intervals compared to the heterogeneous aeolian dune deposits typical of the Rotliegend. Tectonics exerted a strong control on Triassic sedimentation, with sequence boundaries interpreted at the bases of the Volpriehausen, Detfurth, and Solling sequences. The Hardegsen Unconformity, which marks the base of the Solling, reflects pronounced uplift and erosion following deposition of the Hardegsen sequence. These structural phases not only influenced accommodation and sediment distribution but also affected subsequent compaction and diagenesis, as expressed in variations in porosity and bulk density across the basin (Geluk & Röhling, 1997).

To place their properties in a broader context, comparisons are made with the Permian Rotliegend sandstones previously described in Chapter 1. The Upper Rotliegend reservoir in the Netherlands is another key hydrocarbon-bearing unit within the Southern Permian Basin, characterised by arid to semi-arid fluvio-aeolian depositional environments that influence its petrophysical properties (Busch et al., 2020; Henares et al., 2014). The depositional setting primarily comprises aeolian dune, interdune, and fluvial deposits, leading to heterogeneous facies distributions that impact reservoir quality (Monsees et al., 2020). Quartz overgrowth on detrital quartz grains is pervasively distributed throughout the Rotliegend sandstones and significantly impact petrophysical properties. The presence of quartz cement reduces porosity and permeability while also preventing further chemical compaction. Additionally, feldspar dissolution is a common process in these sandstones, generating secondary porosity. However, these newly formed pores are often filled with authigenic clays, which can limit their contribution to improved permeability (Molenaar & Felder, 2019). The reservoir is also affected by structural diagenesis, particularly in faulted areas, which can modify fluid flow behaviour and connectivity (Van Ojik et al., 2020). The impact of depositional environments and diagenetic overprint on petrophysical characteristics, such as porosity and permeability, is crucial for understanding reservoir performance and hydrocarbon recovery strategies (Busch et al., 2020; Reijers, 2012).

Porosity and Mineralogical Controls on Thermal and Acoustic Properties of Sandstones from the Triassic Main Buntsandstein Subgroup and Permian Upper Rotliegend Group in the Netherlands

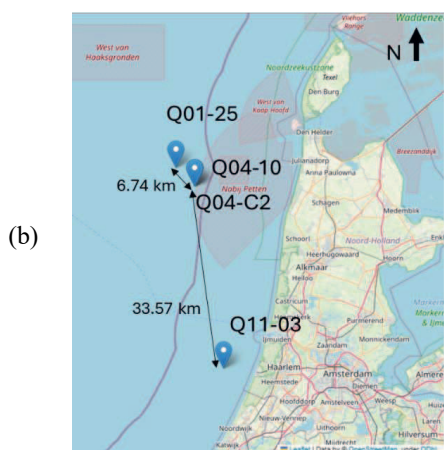
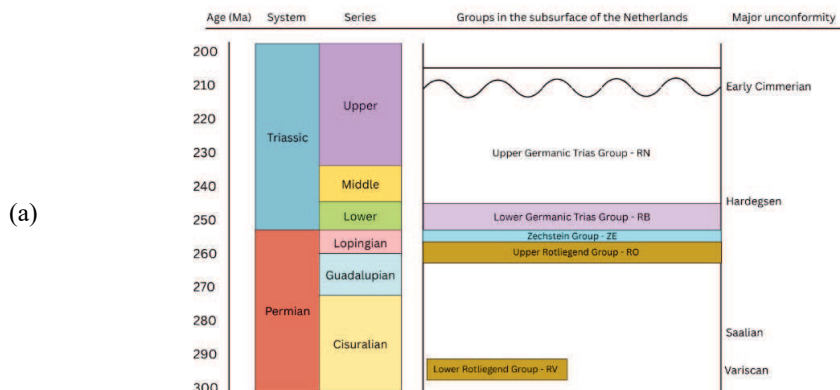


Figure 3.1 (a) Stratigraphy of the Buntsandstein and Rotliegend formations in the Dutch subsurface after ten Veen et al. (2025); (b) Wellbore locations with relative distances (in km) between based on their geographic coordinates provided on nlog.nl.

In the Permo-Triassic succession, the Upper Rotliegend and Lower Buntsandstein represent distinct depositional regimes and sedimentary processes. The Upper Rotliegend developed under arid to semi-arid conditions, where high-energy fluvial and aeolian systems produced coarser, well-sorted sandstones and conglomerates (Bouroullec & Geel, 2025). In contrast, the Lower Buntsandstein consists of cyclic alternations of fine-grained sandstones, siltstones, and claystones deposited in lower-energy lacustrine to fluvial settings that were influenced by recurring climatic oscillations (McKie & Kilhams, 2025). Although the Upper Rotliegend and Lower Buntsandstein differ in depositional environment and grain size, their diagenetic pathways show notable similarities. (Griffioen et al., 2025). Both units underwent mechanical compaction followed by cementation with quartz, dolomite, kaolinite, and illite. Feldspar dissolution in the Rotliegend generated secondary kaolinite and illite (Waldmann, 2012), while

in the Buntsandstein anhydrite and halite cements are more abundant and illite is less common. These differences in cement type and abundance, combined with their contrasting depositional histories, underpin the distinct reservoir behaviour of the two units in the Dutch subsurface: the Rotliegend sandstones have historically served as prolific gas reservoirs and are increasingly considered for geothermal applications, whereas the Buntsandstein sandstones more often function as low-productivity or water-bearing units. While clays in the Rotliegend are mainly authigenic, derived from feldspar dissolution, the Buntsandstein contains a greater proportion of detrital and diagenetic clays introduced during cyclic, fine-grained deposition (Geluk, 2005; Radies et al., 2005). Grain size and lithological uniformity further distinguish the two units. Rotliegend sandstones are coarser and more quartz-rich, whereas Buntsandstein sandstones exhibit finer, more uniform cyclic successions of sand, silt, and clay (Geluk, 2005; Martínek, 2008).

3.2. Material and methods

A total of 766 core plug samples were examined from the four offshore wells in the Q-block of the Dutch sector of the North Sea, located within the West Netherlands Basin. The samples were extracted from both conventional and sidewall cores. The Buntsandstein subgroup reaches a thickness of up to 150 meters (TNO-GDN, 2025). All material were provided by Wintershall Noordzee B.V., Rijswijk, Netherlands. These samples were divided into two groups based on their size including larger samples, with the approximate diameter of 37 mm (standard deviation = 0.57 mm) and length of 49 mm (standard deviation = 3.92 mm), and smaller samples, with an approximate diameter of 26 mm (standard deviation = 0.08 mm) and a length of 39 mm (standard deviation = 7.68 mm). These reported values are averages and the standard deviation reflects sample size variability, not measurement error. The total number of samples also included few side-wall cores from the well Q11-03. These samples were measured at room temperature and pressure under dry conditions.

All thermal properties, including thermal conductivity, thermal diffusivity, and volumetric heat capacity were measured using [HotDisk TPS2200](#) in the TU Delft geolaboratory, Delft, Netherlands. The acoustic properties, compressional (V_p) and shear (V_s) wave velocities, were also measured in the rock mechanics lab of TU Delft using an active acoustic set-up (Veltmeijer et al., 2022). The porosity values were retrieved from multiple reports on the website of Geological Survey of the Netherlands (TNO, 2024); detailed reference of individual measurements and complementary data and information about the studied samples are available at an online database presented by (Kolah-Kaj et al., 2024). The missing porosity values were measured using and [Ultrapyc 5000](#) at the TU Delft geolaboratory.

Mineralogy was measured using X-ray diffraction (XRD) and Fourier-transform infrared spectroscopy (FTIR) by Qmineral, Heverlee, Belgium. XRD is the standard and most reliable approach for quantitative mineral identification, particularly in petrophysics, and is frequently used to calibrate and validate other mineralogical methods in oilfield applications (Craddock

et al., 2017). FTIR spectroscopy is a widely applied technique in mineralogical studies, as it enables the identification and quantification of minerals by detecting characteristic vibrational modes of their crystal lattice and molecular bonds (Madejová, 2003).

Detrital fine-grained material was described macroscopically in plug samples from the Triassic dataset. At this scale, it was not possible to confidently distinguish between clay and very fine silt. For this reason, the term silt/clay is used throughout, although in some cases it may have been interpreted simply as clay. Instead, the descriptions were applied qualitatively to assess trends, for example by examining whether samples visually identified as richer in silt/clay corresponded to systematic changes in thermal properties (e.g., thermal conductivity versus porosity). This approach provides useful relative insight but has the limitation that macroscopic inspection alone cannot reliably quantify fine-grained content or discriminate between silt and clay. It may be beneficial to calibrate the macroscopic mineralogical observations on a sample-by-sample basis using XRD and FTIR data to enhance interpretation accuracy.

3.3. Results

3.3.1. Exploratory data analysis: Triassic versus Permian

In the following, the newly measured Buntsandstein samples with the Rotliegend dataset from Chapter 2 are compared, focusing on thermal conductivity, volumetric heat capacity, and acoustic velocities, to evaluate how depositional environment and diagenetic evolution have influenced their petrophysical characteristics. The results for the Buntsandstein samples are shown in Figure 3.2 and Figure 3.3, with comparisons to the Rotliegend samples presented in Figure 3.4.

For the Buntsandstein sandstone samples analysed in this study, bulk density and porosity show a clear negative relationship (Figure 3.2a), both overall (i) and within each well subset (ii–v). The few outliers result from irregularly shaped or chipped samples, which led to lower bulk density than the general trend. This is also displayed for both Permian and Triassic datasets (Figure 3.4a-i). The Rotliegend samples are concentrated in the lower porosity range (generally <22%) and higher bulk densities (2200–2800 kg/m³), whereas the Buntsandstein extends to higher porosities (up to ~30%) and lower densities (down to ~1800 kg/m³). While both datasets follow a similar overall trend, they diverge at higher porosities, where Buntsandstein shows a stronger decrease in density. Rotliegend samples maintain relatively high bulk densities due to quartz and dolomite cementation, whereas in the Buntsandstein the abundance of halite, with its lower grain density (~2.1–2.2 g/cm³), explains why the high-porosity plugs from the ZRP well are even lighter despite being unconsolidated.

Gas horizontal permeability and porosity exhibit a positive semi-log relationship (Figure 3.2b) indicating that an increase in porosity leads to higher permeability. Not the perfectly linear on the semi-log scale reflect that permeability depends not only on pore volume but also on pore-throat size, sorting, and diagenetic modification of connectivity. Such trend has been widely

Porosity and Mineralogical Controls on Thermal and Acoustic Properties of Sandstones from the Triassic Main Buntsandstein Subgroup and Permian Upper Rotliegend Group in the Netherlands

reported (Pape et al., 1999; Selley, 1998). V_p and porosity show a clear negative linear relationship across all wells and porosity ranges (Figure 3.2d), reflecting that as porosity increases, the rock becomes less effective in transmitting acoustic waves. Both Permian and Triassic datasets show this trend (Figure 3.4a-ii and Figure 3.4b-i). The Rotliegend samples cluster at lower velocities for a given porosity, whereas the Buntsandstein generally shows higher velocities at equivalent porosities. At porosities below 10%, Triassic samples often exceed 4500 m/s for V_p and 2500 m/s for V_s , values rarely reached by the Rotliegend.

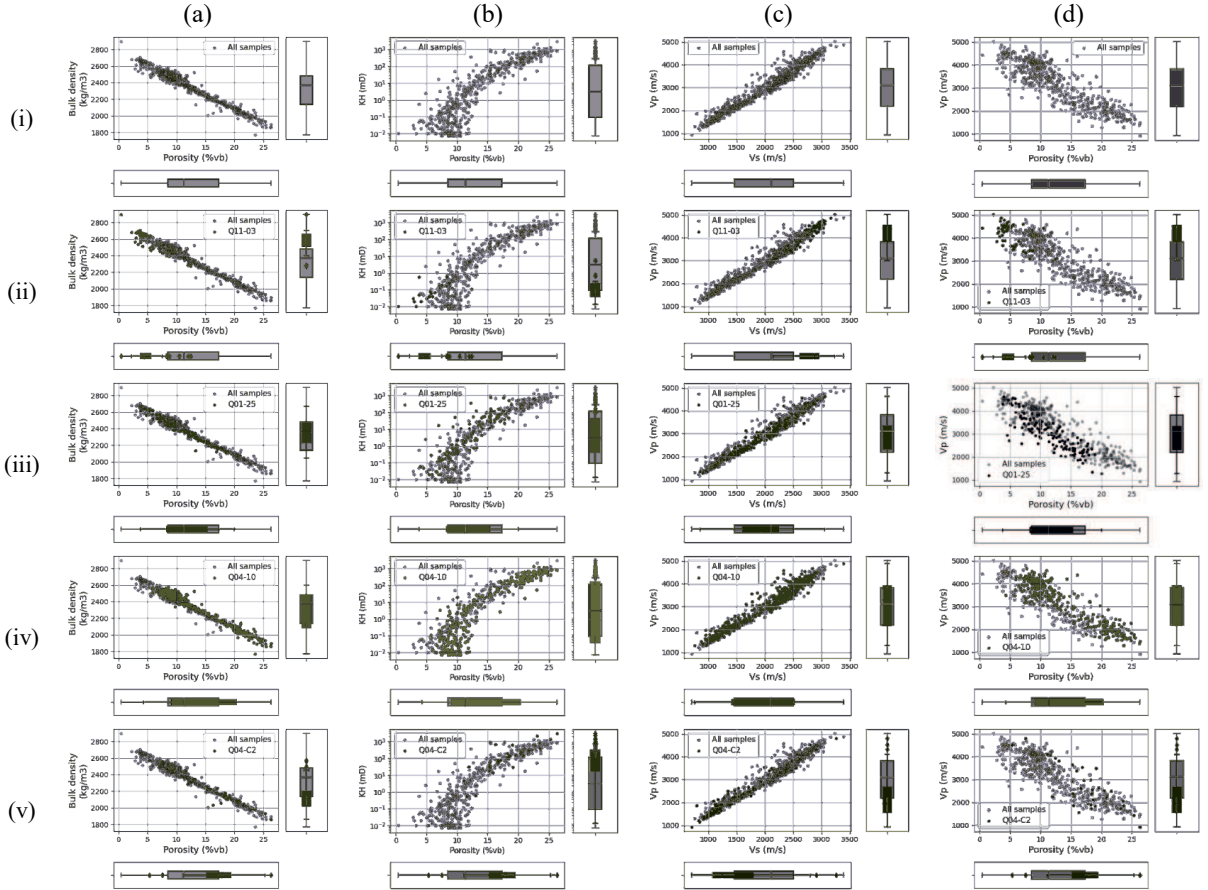


Figure 3.2. Measurements of the Main Buntsandstein core plugs showing (a) bulk density (kg/m^3) versus porosity (%vb), (b) horizontal permeability (mD) versus porosity (%vb) (semi-log), (c) V_p (m/s) versus V_s (m/s), and (d) V_p (m/s) versus porosity (%vb) for (i) all samples, (ii) well Q11-03, (iii) well Q01-25, (iv) well Q04-10, and (v) well Q04-C2. These plots illustrate the fundamental petrophysical relationships in the Buntsandstein, with clear trends between porosity, density, permeability, and acoustic velocities across all wells.

Porosity and Mineralogical Controls on Thermal and Acoustic Properties of Sandstones from the Triassic Main Buntsandstein Subgroup and Permian Upper Rotliegend Group in the Netherlands

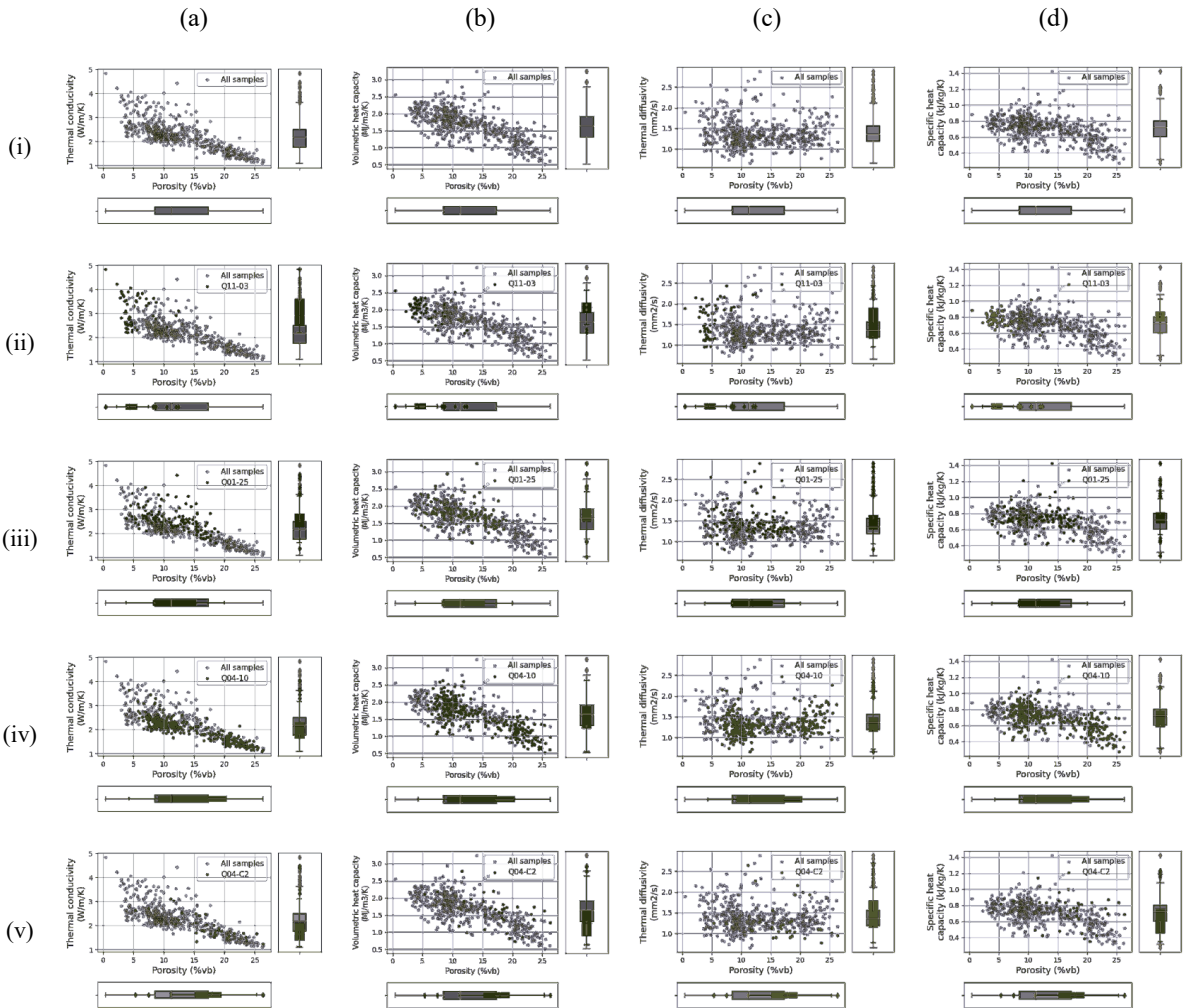


Figure 3.3. Cross plots of (a) thermal conductivity ($W/m\cdot K$), (b) volumetric heat capacity ($MJ/m^3\cdot K$), (c) thermal diffusivity (mm^2/s), and (d) specific heat capacity ($kJ/kg\cdot K$) versus porosity (%vb) for (i) all samples, (ii) well Q01-25, (iii) well Q04-10, (iv) well Q04-C2, and (v) well Q11-03. These plots highlight the systematic dependence of thermo-physical properties on porosity, showing strong negative correlations for thermal conductivity and diffusivity, while specific heat capacity exhibits weaker but consistent trends across wells.

Thermal conductivity and porosity show a clear negative linear relationship (Figure 3.3a) with a broader thermal conductivity range at lower porosity. This indicates that increasing porosity reduces the rock's ability to transfer heat. This finding remains valid for both formations (Figure 3.4b-ii). In the Rotliegend dataset, thermal conductivity ranges from ~ 1.0 to 5.0

W/m·K, with most samples clustering between 2.0 and 4.0 W/m·K at porosities below 15%. In contrast, the Buntsandstein samples exhibit a narrower spread, ranging from ~1.0 to 3.5 W/m·K, and extend to porosities approaching 30%. At equivalent porosity, Rotliegend samples generally maintain higher thermal conductivities compared to Buntsandstein, particularly in the low- to intermediate-porosity domain (<15%). At higher porosities (>20%), both datasets converge toward lower thermal conductivity values near 1.0–1.5 W/m·K.

Volumetric heat capacity and porosity also display a generally negative relationship (Figure 3.3b), although with some scatter, meaning that more porous samples require less heat to increase their temperature by 1°C. In Figure 3.4b-iii, both Rotliegend and Buntsandstein span broadly similar ranges in volumetric heat capacity (≈ 0.6 – 3.0 MJ/m³·K). Within the 5–15% porosity interval, Buntsandstein samples lie systematically above Rotliegend by about 0.2–0.3 MJ/m³·K. At higher porosities (>20%), the two datasets converge, with only minor differences of ~ 0.1 – 0.2 MJ/m³·K.

Thermal diffusivity and porosity exhibit strong scatter in the data at all porosities without significant trend. At porosities greater than 18% (Figure 3.3c) the samples from formations converge and become more limited to a narrower range. These high-porosity samples originate from wellbore Q04-10 (2650 m – 2670 m) and Q04-C2 (3691 m – 3719 m). In both wellbores, they originate from the Volpriehausen Formation. Thermal diffusivity varies between ≈ 0.8 and 4.0 mm²/s across both datasets (Figure 3.4a-iii). The Rotliegend samples (orange red) show a wider spread, with most values between 1.5 and 2.5 mm²/s and outliers reaching up to 4.0 mm²/s. The Buntsandstein samples (blue) are more tightly distributed, primarily between 1.0 and 1.8 mm²/s, and do not exceed 2.5 mm²/s. At porosities below 15%, Rotliegend generally exhibits higher diffusivities than Buntsandstein, whereas at porosities above 20% both datasets converge toward ~ 1.0 – 1.5 mm²/s.

Specific heat capacity and porosity variability around a mean without significant trend (Figure 3.3d). Samples with porosities above 18% exhibit slightly lower values than the rest. Specific heat capacity remains relatively constant with porosity across both formations (Figure 3.4a-iv). However, the Buntsandstein systematically shows higher values (≈ 0.9 – 1.1 kJ/kg·K) compared to the Rotliegend (≈ 0.8 – 1.0 kJ/kg·K).

Porosity and Mineralogical Controls on Thermal and Acoustic Properties of Sandstones from the Triassic Main Buntsandstein Subgroup and Permian Upper Rotliegend Group in the Netherlands

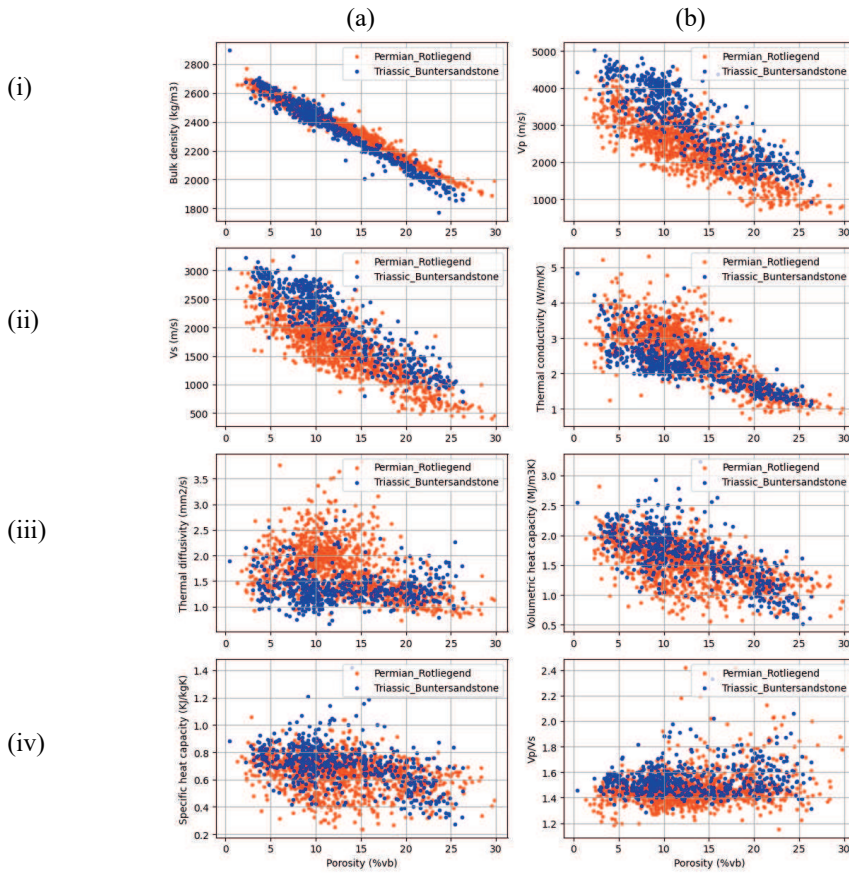


Figure 3.4 Petrophysical and thermo-physical properties versus porosity for the Permian Rotliegend (orange red) from Chapter 2 and Triassic Buntsandstein (blue). Shown are bulk density, V_p , V_s , thermal conductivity, thermal diffusivity, volumetric heat capacity, specific heat capacity, and V_p/V_s ratio. Both formations display systematic porosity-dependent trends, with distinct property ranges for each.

Similar scatter has been widely reported in siliciclastic reservoirs V_p and V_s display a strong positive linear correlation, with all samples following the same trendline (Figure 3.2c). The V_p/V_s ratio shows little dependence on porosity (Figure 3.4b-iv). Both formations fall between 1.5 and 2.0, with the Rotliegend clustering tightly around 1.6–1.8, while the Buntsandstein displays greater scatter and occasional values above 2.0.

3.3.2. Principal Component and Canonical Correlation Analysis

Principal component analysis (PCA) was applied to seven measured rock properties (porosity, bulk density, grain density, V_p , V_s , thermal conductivity, and thermal diffusivity) to identify how these variables co-vary. The PCA of seven measured rock properties (porosity, bulk

Porosity and Mineralogical Controls on Thermal and Acoustic Properties of Sandstones from the Triassic Main Buntsandstein Subgroup and Permian Upper Rotliegend Group in the Netherlands

density, grain density, V_p , V_s , thermal conductivity, and thermal diffusivity) shows that in both Triassic and Permian datasets the first two components explain ~90% of the total variance (Triassic: PC1 = 70.3%, PC2 = 19.6%; Permian: PC1 = 71.4%, PC2 = 18.5%), providing a robust basis for interpreting the loading plots in Figure 3.5.

In the Triassic dataset, bulk density, grain density, V_p , and V_s cluster together on the negative side of PC1, in line with their strong correlations seen in the exploratory data analysis. Porosity is positioned on the positive side of PC1, reflecting its clear inverse relation to density and velocity. Thermal conductivity contributes negatively to PC1 but positively to PC2, while thermal diffusivity loads mainly on PC2, largely independent from the other properties.

Permian PCA (same seven variables as Triassic: porosity, bulk density, grain density, V_p , V_s , thermal conductivity, thermal diffusivity): PC1 = 71.4%, PC2 = 18.5% (total = 89.9%). Porosity loads positively on PC1, whereas bulk density, grain density, V_p , V_s , and volumetric heat capacity load negatively on PC1, confirming the inverse relation seen in the EDA. Thermal conductivity also loads negatively on PC1 and slightly positively on PC2, so it is largely opposite to porosity and aligns with the density–velocity group, though less tightly than in the Triassic. Thermal diffusivity loads mainly on PC2 with a small negative PC1 component, indicating variance largely independent of the PC1 framework axis. Overall, the structure mirrors the Triassic (PC1: porosity versus framework properties; PC2: thermal-transport variance), with the main difference that thermal conductivity sits farther from porosity in the Permian case.

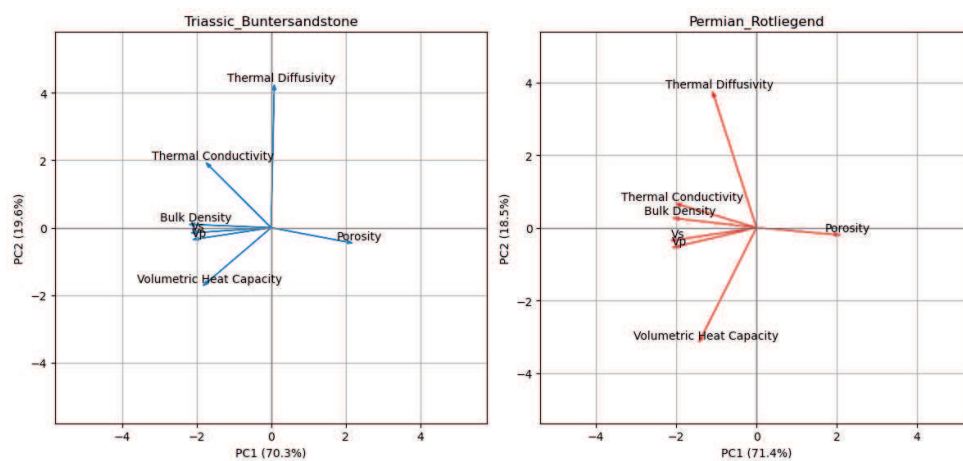


Figure 3.5 The PCA loading plots for the Triassic (left panel, red arrows) and Permian (right panel, blue arrows) datasets. Each arrow represents how strongly a given rock property contributes to the first two principal components (PC1 and PC2).

Canonical Correlation Analysis (CCA) is used to explore the relationship between two sets of variables by finding linear combinations that maximise the correlation between them. While PCA was applied to summarise variability within one set of properties, CCA focuses on quantifying how one group of properties relates to another.

From the PCA results, porosity, bulk density, V_p , and V_s formed a cluster that dominated the first principal component. These variables were therefore selected as a representative set of petrophysical and acoustic properties to be compared with the thermal property set (thermal conductivity, thermal diffusivity, volumetric heat capacity, and specific heat capacity). Applying CCA revealed very strong correlations between the two sets, with canonical correlation values of 0.987 for the Rotliegend and 0.981 for the Buntsandstein (Figure 3.6).

This result demonstrates that thermo-physical properties are strongly and systematically linked to petrophysical and acoustic parameters. It also confirms that porosity-related properties can serve as reliable predictors of thermal behaviour, thereby providing a solid statistical foundation for the predictive modelling approaches presented in the Chapter 5.

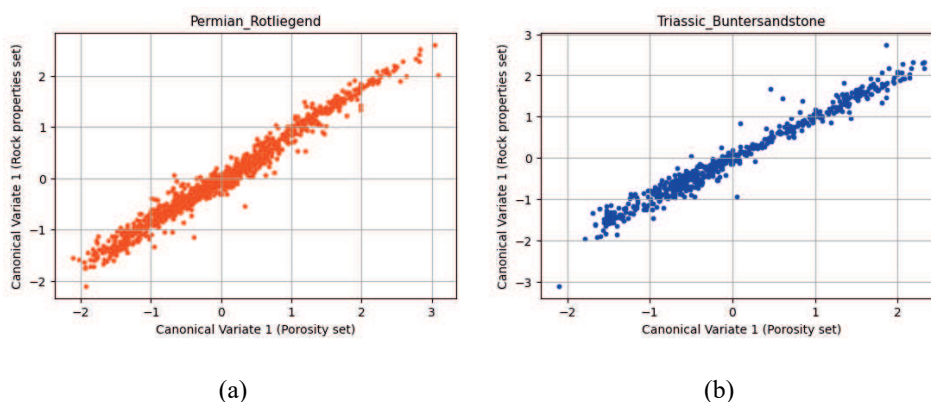


Figure 3.6 Canonical correlation analysis between *in situ* measurable properties (porosity, bulk density, and V_p , and V_s) and thermo-physical properties (thermal conductivity, thermal diffusivity, volumetric heat capacity, and specific heat capacity). Canonical correlation values are 0.987 for the Permian dataset and 0.981 for the Triassic dataset.

3.3.3. Core plug descriptions

In addition to the XRD-derived mineralogy, Triassic core plugs were macroscopically described for grain size, degree of sorting, lamination, colour, visual clay/silt content, and overall heterogeneity. Detrital fine-grained material is referred to as silt/clay, acknowledging that clay and very fine silt cannot be distinguished reliably macroscopically. These qualitative observations were used to assess potential links between lithological characteristics and the measured thermal and petrophysical properties.

The relationship between compressional and shear wave velocities (V_p – V_s) was examined for plug samples with visible lamination or bedding (Figure 3.7a). As with the full dataset, a strong positive linear correlation is observed, but laminated plugs cause clustering within this trend. Lamination orientation was defined independently of the core orientation: in horizontally laminated plugs, lamination is perpendicular to the main long axis, whereas in vertically laminated plugs, it is parallel. Plugs with horizontal lamination of sand and clay/silt (blue triangles) exhibit lower velocities ($V_s = 2000$ – 2600 m/s, $V_p = 3200$ – 4600 m/s), while vertically laminated samples (orange squares) show higher velocities ($V_s = 2100$ – 3000 m/s, $V_p = 2700$ – 3600 m/s). Despite this clustering, both horizontally and vertically laminated samples follow the same overall trend.

A strong positive linear correlation is observed between V_p and V_s for the Triassic samples (Figure 3.7b). Homogeneous and relatively clean sand samples (clay content $<10\%$) form a distinct cluster at lower velocities, with V_p values generally below 3500 m/s and V_s below 2500 m/s. These samples follow the same overall V_p – V_s trend as the full dataset.

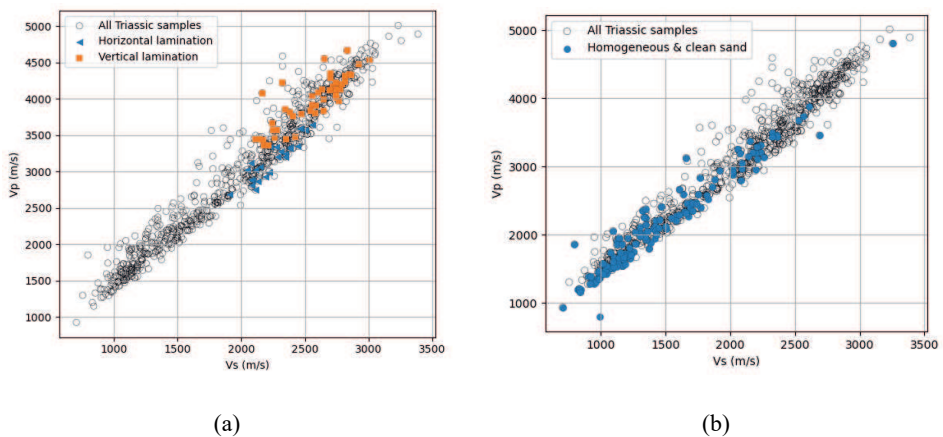


Figure 3.7 (a) Cross-plot of compressional velocity (V_p) versus shear velocity (V_s) for Triassic plug samples with visible lamination or bedding. While the overall positive linear correlation is preserved, plugs with horizontal lamination (blue triangles) show higher velocities than vertically laminated plugs, reflecting the influence of lamination orientation on wave propagation. This indicates that lamination introduces additional scatter and orientation-dependent variability in V_p – V_s behaviour. (b) Cross-plot of compressional velocity (V_p) versus shear wave velocity (V_s) for Triassic plug samples, color-coded by visually estimated detrital silt/clay content. Homogenous and relatively clean sands (clay content $<10\%$) cluster at relatively low velocities.

Figure 3.8 reproduces the thermal properties versus porosity cross plot for Buntsandstein samples, colour-coded by clay and silt content. Thermal diffusivity shows that high-clay samples ($>20\%$) are clustered at low porosities ($<10\%$) and display lower diffusivities (~ 1.0 – 1.2 mm²/s). This reflects the intrinsically low conductivity and higher heat capacity of clay

minerals, which together suppress diffusivity. In contrast, the remaining samples, which can be regarded as relatively clean sands, show a clearer tendency for diffusivity to increase as porosity decreases, consistent with the larger contribution of quartz and other high-conductivity minerals to heat transport. At higher porosities (>15%), diffusivity values consistently remain low (~1.0–1.2 mm²/s), reinforcing porosity as the dominant control, with fine-grained material acting as a secondary factor that dampens diffusivity in the clay-rich, low-porosity domain (Figure 3.8a).

At low porosities (<10%), samples with higher detrital silt/clay contents (>20%) tend to exhibit higher heat capacities (up to 2.5 MJ/m³·K), whereas low-clay samples (<5%) show more scattered and generally lower values. At higher porosities (>15%), where clay content is minimal, heat capacity decreases below ~1.5 MJ/m³·K (Figure 3.8b).

Samples with high clay fractions (>20%) are generally restricted to low porosities (<12%). Within this domain, their thermal conductivities fall within the porosity-controlled envelope, typically ~2.0–2.5 W/m·K, rather than being systematically higher. In contrast, low clay samples (<5%) span a much wider porosity range (up to ~25%) and extend to lower thermal conductivities, in some cases below 2.0 W/m·K. Increasing clay content tends to restrict the porosity range, but even at very high clay fractions (>60%), thermal conductivity follows the same porosity trend (Figure 3.8c).

A subset of homogeneous, low clay, i.e., clean sand, intervals span the full porosity range. These samples align closely with the regression trend and cluster between 2.0 and 3.0 W/m·K for intermediate porosities (10–20%) (Figure 3.8d). In both Triassic and Rotliegend samples, thermal conductivity decreases systematically with increasing porosity, as shown in Figure 3.9, regardless of variations in clay or mineral content derived from XRD and FTIR analyses.

Porosity and Mineralogical Controls on Thermal and Acoustic Properties of Sandstones from the Triassic Main Buntsandstein Subgroup and Permian Upper Rotliegend Group in the Netherlands

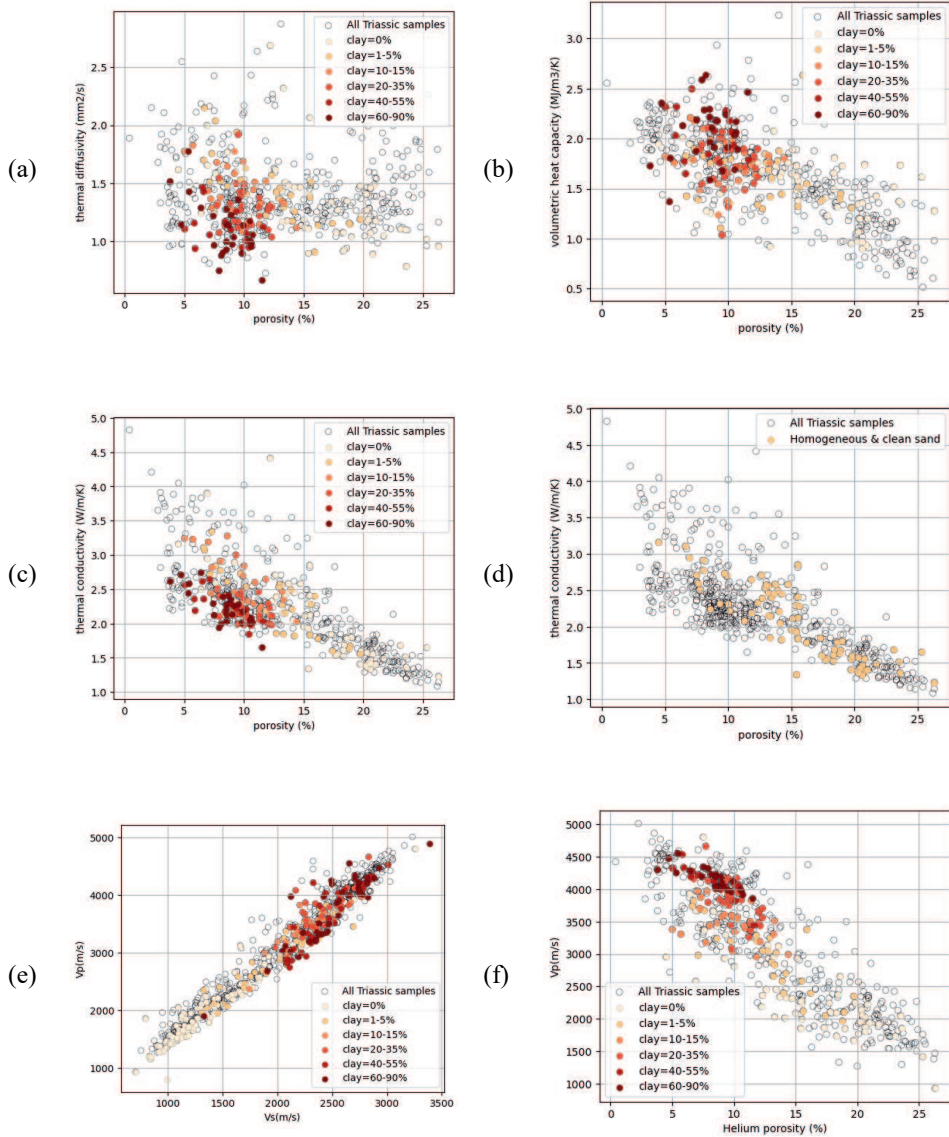


Figure 3.8 Cross-plots for Triassic Buntsandstein plug samples, color-coded by visually estimated detrital silt/clay content. (a) Thermal diffusivity versus porosities. (b) Volumetric heat capacity versus porosity (c) Thermal conductivity versus porosity (d) Thermal conductivity versus porosity (e) compressional wave velocity (V_p) versus shear wave velocity (V_s) and (f) compressional wave velocity (V_p) versus porosity.

For the Triassic samples (Figure 3.9a), high clay fractions (>40%) occur exclusively at low porosities (<10%) and are associated with relatively high thermal conductivities (>2.5 W/m·K). Samples with low clay contents extend to higher porosities and show lower thermal conductivities. Core Q11-03 appears as an outlier, characterised by extremely high clay content and very low porosity (<5%) but retaining high thermal conductivity.

In the Rotliegend dataset (Chapter 2), thermal conductivity decreases from values above 4.0 W/m·K at porosities below 5% to less than 2.0 W/m·K at porosities above 20%. Samples from well K18-08 (highlighted in blue) follow the main porosity– thermal conductivity trend but cluster toward the higher thermal conductivity envelope. These samples are distinguished by relatively low clay contents, with thermal conductivity values between 2.0 and 3.5 W/m·K for porosities of 5–15%, and display reduced scatter compared to the broader dataset.

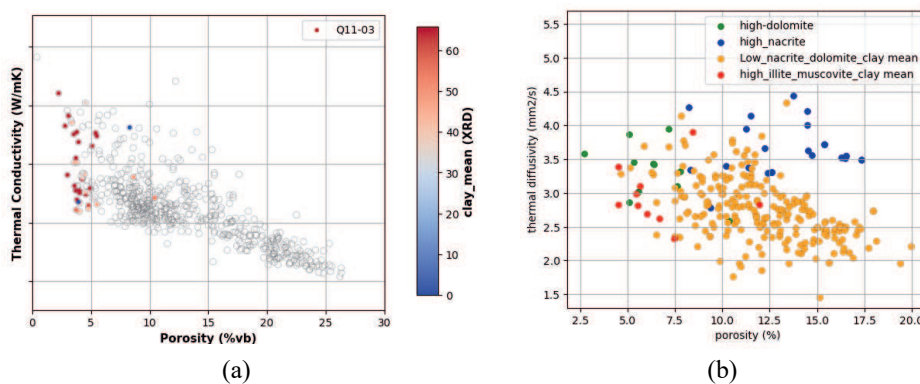


Figure 3.9 Thermal conductivity versus porosity cross-plots. (a) Triassic samples color-coded by XRD-derived clay content. High clay fractions (>40%) are restricted to low porosities (<10%) and show relatively high conductivities, whereas low-clay samples extend to higher porosities and display lower conductivities. This indicates porosity as the main control, with clay enhancing conductivity indirectly by reducing pore space. (b) Rotliegend samples from wells K18-08 and K18-07x grouped by FTIR/XRD-derived mineralogy. High illite/muscovite (clay-mean) samples show reduced conductivity, reflecting detrital clays. High dolomite samples occur at low porosities with reduced conductivity, consistent with dolomite cement. Nacrite-rich samples (kaolinite polymorph) combine high porosity with elevated conductivity, likely due to intergranular replacement clays. Remaining low nacrite–dolomite–clay samples cluster along the main trend.

Rotliegend samples from wells K18-08 and K18-07x (Figure 3.9b) span thermal conductivities of approximately 2.0–4.5 W/m·K and show a consistent negative porosity–thermal conductivity trend. Distinct mineralogical controls are evident. Samples with higher illite/muscovite contents display reduced thermal conductivities of about 2.5–3.0 W/m·K. Dolomite-rich samples occur at porosities below 10% and exhibit lower thermal conductivities, consistent with occlusion of pore space by dolomite cement. In contrast, nacrite-rich samples (a kaolinite polymorph) combine higher porosities of 10–15% with elevated thermal conductivities exceeding 4.0 W/m·K, suggesting replacement-related clay cement. Most

samples with low nacrite, dolomite, and clay contents cluster between 2.0 and 3.0 W/m·K across the porosity spectrum.

3.4. Discussion

The results section showed the trends between each pair of properties and compared them between Triassic and Permian sandstones. In addition, PCA and CCA were used to examine all properties together in both individual and grouped form. The core plug descriptions and mineralogical analyses further highlighted how specific minerals, and diagenetic processes influence these trends, alongside other rock characteristics and environmental factors. In the following discussion, these findings are integrated, compared with literature, and interpreted in terms of the controlling mechanisms and their implications for reservoir characterisation. The negative correlation between bulk density and porosity in Figure 3.2a i-v is well-documented in geological literature (Lin et al., 2015; Miller & Stewart, 1991; Salah et al., 2020). This relationship exists because increasing porosity causing a higher volume of void space relative to solid grains, which lowers the overall density of the rock. This trend is fundamental to petrophysical evaluations of reservoir rocks (Atapour & Mortazavi, 2017; Abdelaali. Rahmouni et al., 2014). The bulk density–porosity trends of the two formations in Figure 3.4a-i overlaps at low porosities but begin to diverge above ~12%. At equivalent porosities beyond this threshold, Rotliegend samples consistently show higher bulk densities (commonly 100–150 kg/m³ above Buntsandstein). This offset may reflect the greater abundance of detrital clays in the Triassic, which preserve microporosity and lower density, versus the authigenic and replacive phases in the Permian that infill pores or replace grains, maintaining a denser framework. At equal porosity and fluid saturation, the Rotliegend and Buntsandstein samples show distinct contrasts related to their mineralogical framework and cementation style. The Rotliegend, dominated by quartz grains with quartz overgrowths and leached feldspars, exhibits slightly higher bulk density and consistently higher thermal conductivity due to the high intrinsic conductivity of quartz and efficient grain-to-grain contacts. In contrast, the Buntsandstein, characterised by detrital clays and pervasive carbonate cement, shows lower bulk density and thermal conductivity but higher compressional wave velocity. The higher V_p in the Buntsandstein is attributed to the stiff load-bearing carbonate cement, which enhances the bulk modulus of the rock frame despite the presence of clay. Conversely, the Rotliegend, though quartz-rich, retains microcrack-like secondary porosity from feldspar leaching, which weakens frame stiffness and reduces V_p relative to the Buntsandstein. We interpret detrital clays to tighten the pore structure; however, this interpretation is tentative and requires verification at higher porosities.

The positive semi-logarithmic relationship between porosity and permeability (Figure 3.2b i-v) aligns with empirical findings from numerous studies (Abdelaali. Rahmouni et al., 2014). As porosity increases, interconnected pore networks improve fluid flow pathways, enhancing permeability. However, this relationship is not always linear, as factors such as diagenetic

cement (Dvorkin & Brevik, 1999) pore shape (Rahmouni et al., 2013), connectivity, and grain size distribution also influence permeability (Nelson, 1994).

3.4.1. Acoustic Properties

The results of this study reveal a strong positive correlation between V_p and V_s across all tested samples, consistent with previous findings in rock physics literature (Anselmetti & Eberli, 1999; Rafavich et al., 1984). The negative correlation between V_p and porosity in our study is consistent with Klimentos (1991), Yin and Nur (1993), Ahrens et al. (2018), Wang et al. (2021), and Salah et al. (2018), all of whom demonstrated that increasing porosity reduces both V_p and V_s . This trend arises because higher porosity reduces the solid framework that transmits acoustic waves, thereby lowering acoustic velocities. These relationships are indicated to be influenced by mineralogical composition, pore structure, and diagenetic alterations, which affect acoustic and petrophysical properties in sedimentary rocks (Christensen & Szymanski, 1991; Marion et al., 1992; Salah et al., 2020). Han (1986) demonstrated that both V_p and V_s decrease as porosity increases in sandstones, particularly when accompanied by variations in clay content. The magnitude and sense of this deviation depend on the type and abundance of clay. In our Buntsandstein samples (Figure 3.8f), plugs with high detrital clay and silt fractions cluster at higher velocities and lower porosities, whereas cleaner sands define the lower-velocity bound. Interestingly, samples with the highest clay fractions do not scatter widely but instead form compact clusters, with an apparent tendency toward higher velocities than samples with lower clay contents. This forms the hypothesis that in our dataset, fine-grained material is associated with compaction and cementation processes that stiffen the rock frame. An important point is that the Buntsandstein samples have high clay content. Reported mineral acoustic velocities show that although clays and quartz have different velocities, their ranges overlap (Xayavong et al., 2020). In addition, clay minerals vary in type and, therefore, in velocity. This means that identifying the exact type and arrangement of clays is essential for interpreting why Buntsandstein samples can exhibit higher V_p than Rotliegend sandstones, despite their higher clay content. Differences in clay mineralogy can plausibly explain the velocity contrast. This is information we do not have.

Han (1986) showed that bound clays, defined as pore-filling or grain-coating phases that directly soften grain contacts, are much more effective in reducing acoustic velocities because they decrease shear moduli, leading to larger reductions in shear velocity than in compressional velocity. In the context of our study, the Permian Rotliegend contains mainly authigenic and replacive clays derived from feldspar dissolution, which act as bound clays and therefore influence acoustic properties. By contrast, the Triassic Buntsandstein contains a higher proportion of detrital clays deposited with fine-grained sediments, which mainly reduce porosity but have a more limited effect on grain contact stiffness and acoustic velocities.

Our comparison of Permian and Triassic samples (Section 3.1) suggests systematic differences in clay type: Triassic Buntsandstein sandstones are characterised by higher proportions of

detrital (matrix) clays, whereas the Permian Rotliegend samples contain abundant authigenic replacive clays, derived mainly from alteration feldspar and mica alteration, that are concentrated along grain boundaries and pore walls. These phases locally replace framework grains and precipitate as pore-lining films, modifying grain contacts and restricting pore connectivity (Veeningen & Könitzer, 2016b). These could be a potential reason for the Triassic samples having higher velocities than Permian ones at a given porosity. The contrasting mechanical impact of detrital versus bound clays, and possibly the different clay types in Triassic and Buntsandstein samples could explain the velocity–porosity trends.

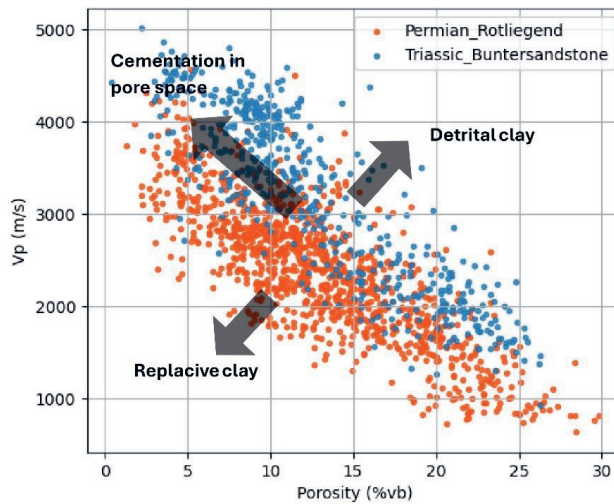


Figure 3.10 V_p –porosity cross-plot comparing Triassic Buntsandstein (orange) and Permian Rotliegend (blue) samples, showing systematic differences in velocity–porosity trends. Annotated arrows highlight the influence of cementation and different clay types (detrital versus replacive) on the velocity distribution.

The observed correlation between V_p and V_s suggests that both wave types are influenced by similar elastic properties of the rock matrix (Anselmetti & Eberli, 1999). Miller and Stewart (1991) observed that as porosity increased, the V_p/V_s ratio systematically decreased. For instance, they noted that a 1% increase in porosity was associated with roughly a 0.02 reduction in the V_p/V_s ratio. Figure 3.4b–iv shows that the V_p/V_s ratios of our sandstone samples remain largely constant across varying porosities. The V_p/V_s ratios of both Permian and Triassic samples predominantly fall within the 1.4–1.8 range, with an average of 1.51. The V_p/V_s ratio can be a key to determine lithology (Castagna et al., 1993; Mavko et al., 2020; Zhang & Bentley, 2003). Many researchers have concluded that variations in the V_p/V_s ratio are controlled more by pore geometry and fluid saturation than by porosity alone, which is consistent with our findings. Fortin et al. (2007) studied how pore collapse and grain crushing affect V_p and V_s of porous sandstone from Bleurswiller. They concluded that pore collapse and grain crushing result in a paradoxical increase in the V_p/V_s ratio, even as porosity

decreases. This phenomenon occurs because cracks, rather than absolute porosity, exert a dominant influence on elastic behaviour, making the V_p/V_s ratio more sensitive to pore geometry. This difference may reflect that in our Buntsandstein samples, compaction and cementation dominate over pore geometry effects, stabilizing the V_p/V_s ratio across porosities, whereas Miller and Stewart's dataset captured more compliant, clay-rich frameworks where porosity exerted a stronger influence.

In our Buntsandstein dataset, the samples were grouped according to clay and silt percentages determined from macroscopic inspection. The cross-plot (Figure 3.8 e) shows that samples with higher clay/silt content (41–80%) generally cluster at higher velocity ranges, whereas lower clay/silt samples (0–20%) exhibit a broader spread, extending to lower velocities.

In the Buntsandstein dataset, samples with higher clay/silt contents (41–80%) fall in the higher velocity range, while those with lower contents (0–20%) show a wider spread toward lower velocities (Figure 3.8f). This differs from Miller and Stewart (1991) finding, where increased clay content typically led to reduced velocities due to weaker grain contacts and increased attenuation. As mentioned before, this effect could change depending on the clay type and distribution within the porous media. This highlights the importance of mineralogical context when evaluating the effect of fine-grained content on acoustic properties.

Compared to the Permian Rotliegend, the Triassic Buntsandstein sandstones record distinct diagenetic changes linked to long-term fluid–rock interaction. In the Rotliegend, limited water flux under hydrocarbon charge tended to preserve feldspar with illite or quartz cement, whereas infiltration of surface-derived or carbon dioxide–rich waters locally enhanced feldspar dissolution and kaolinisation (Yuan et al., 2019). These alterations lowered V_p , while the quartz-rich Rotliegend matrix sustained relatively high thermal conductivity. By contrast, Buntsandstein samples in our dataset show higher V_p at a given porosity (dry), consistent with tighter packing and cement types such as anhydrite and dolomite.

Laminated plugs add orientation-dependent variability: horizontally laminated samples yield lower velocities, while vertically laminated ones show higher values, reflecting anisotropy in wave propagation (Figure 3.7a). For plugs with horizontal lamination, wave is forced to cross both sand and clay layers making it slower. In contrast, plugs with vertical lamination, aligned with the direction of acoustic wave propagation through the rock, tend to show higher velocities, as waves preferentially propagate through quartz-rich layers, which are faster than the intervening clay-rich bands (Han, 1986).

All acoustic measurements in this study were performed at room temperature and pressure, which implies that microcracks and other compliant pores (here referred to as crack-related porosity) remained open. Under in-situ reservoir conditions, higher confining pressures progressively close such features, resulting in systematically higher velocities than those measured in the laboratory.

3.4.2. Thermal Properties

The results of this study demonstrate correlations between porosity and thermal conductivity, volumetric heat capacity, and thermal diffusivity of sandstone. These relationships are evident not only in the individual cross-plots (Figure 3.3a–3d) but also in the broader statistical analyses (PCA and CCA). They arise because increasing porosity replaces solid mineral material with air, which fundamentally reduces the ability of the rock to conduct and store heat. At the same time, the data show that porosity alone does not account for all variability; mineral composition, cracks, cementation, and diagenetic overprint also modify the thermal properties. Below, the physical basis of these relationships and the influence of these secondary factors are discussed.

3.4.2.1. Thermal conductivity

All samples studied here were measured under dry conditions, so the effect of pore-filling fluids on thermal transport was negligible. The measured thermal conductivity therefore reflects the average contribution of the mineral framework and cement. The data demonstrate that porosity is the first-order control: thermal conductivity decreases systematically with increasing porosity (Figure 3a). This negative porosity–conductivity relationship is consistent with previous sandstone studies (Abdulagatova et al., 2009; Haffen et al., 2017; Sun et al., 2017). Pore space, particularly when air-filled, acts as a thermal insulator, reducing heat transport. Detrital clays exert a secondary effect by shifting samples into the low-porosity, high-conductivity regime. This is evident in clay-rich samples (<10% porosity), while further increases in clay fraction beyond 20% do not alter the overall conductivity–porosity envelope. In the Triassic dataset, clay-rich samples consistently show low porosity but relatively high conductivity, indicating that detrital clays reduce pore space and tighten packing. XRD data confirm that the Q11-03 samples contain exceptionally high clay contents, exemplifying this effect by forming compact fabrics that retain high conductivity despite very low porosity.

At higher porosities (>15%), where macroscopic clay is absent, thermal conductivity consistently drops below $\sim 2.0 \text{ W/m}\cdot\text{K}$. This indicates that the effect of detrital clay is restricted to the low-porosity range. Mineralogy sets the baseline as shown in Figure 3.9b where quartz-rich samples plot higher due to quartz's high intrinsic conductivity ($\sim 6\text{--}7 \text{ W/m}\cdot\text{K}$), whereas clay- and feldspar-rich samples show lower values due to their low thermal conductivity reported by (Clauser & Huenges, 1995b; Robertson, 1988). Thus, while porosity is the dominant control, deviations within the Buntsandstein dataset can be explained by mineralogical variations. The similarity between the conductivity–porosity and velocity–porosity relations confirms that porosity is the dominant factor controlling both properties. In both cases, detrital clay primarily modifies the porosity–conductivity relation by reducing pore space and tightening packing, which shifts samples toward the low-porosity, lower-conductivity regime. However, because clay minerals have intrinsically lower conductivities than quartz, an increase in the relative proportion of clay to quartz within the framework can

reduce the effective matrix conductivity, especially at higher clay fractions. Clean sandstone intervals, which define the main regression trend with minimal scatter, further support the interpretation that the porosity–conductivity relation in the Buntsandstein is primarily governed by the sandstone matrix, with clay content exerting only a secondary influence. The results confirm that porosity exerts the dominant control on thermal conductivity in both Triassic and Rotliegend samples, with conductivity decreasing systematically as porosity increases (Figure 3.9). However, mineralogical variations, particularly clay and dolomite contents, strongly influence the shifts and define characteristic subsets of the data.

For comparison, the Rotliegend results presented in Chapter 2 showed that mineralogical subsets exert distinct effects. Illite/muscovite reduces thermal conductivity by filling pores, dolomite cement lowers porosity and increase thermal conductivity through intergranular cementation, and nacrite increases thermal conductivity at moderate porosities through secondary clay replacement. These findings highlight that while porosity is the first-order control on thermal conductivity in both formations, the Triassic samples mainly reflect the role of detrital clays, whereas the Rotliegend shows stronger modification by replacive clays and carbonate cements.

Thermal conductivity in both the Permian Rotliegend (red) and Triassic Buntsandstein (blue) decreases with increasing porosity (Figure 3.11). The main regression trend is defined by clean, homogeneous sandstone samples, representing quartz-rich intervals with minimal clay or cement influence. Deviations from this trend reveal distinct populations. Samples plotting below the regression correspond to intervals with high detrital clay contents, associated with reduced conductivities. A second group, characterised by reduced porosity and intermediate conductivities, aligns with the influence of intergranular cements. A third subset, located at intermediate porosities but displaying elevated conductivities, corresponds to samples with replacive cements. The Rotliegend data show a broader spread in conductivity values relative to porosity, while the Buntsandstein dataset is more tightly constrained along the main regression trend.

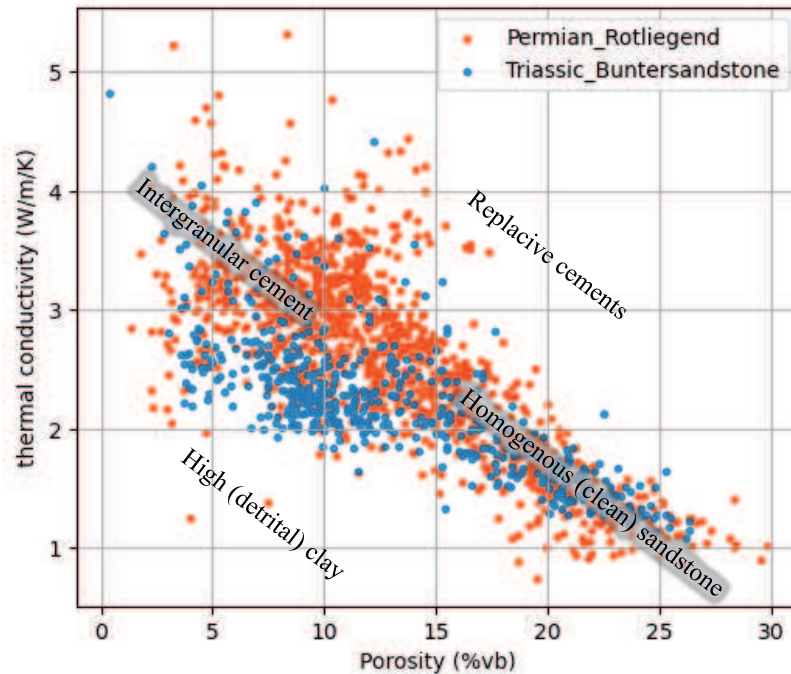


Figure 3.11 Cross-plot of thermal conductivity versus porosity for Permian Rotliegend (red) and Triassic Buntsandstein (blue) samples. The main porosity, conductivity trend is defined by homogenous, clean sandstones, while deviations from this trend reflect mineralogical and diagenetic influences. Samples shifted toward lower conductivities correspond to high detrital clay contents, while those with reduced porosity and moderate conductivities indicate intergranular cementation. Elevated conductivity at intermediate porosities is associated with replacive cements.

Clean sandstones define the fundamental porosity–conductivity relation, whereas deviations can be linked to specific processes. We interpret that detrital clays lower conductivity by introducing low-conductivity phases and enhancing pore-scale heterogeneity, intergranular cements reduce porosity and yield moderate conductivities by occluding pore space, and replacive cements strengthen grain contacts and solid-phase pathways, thereby supporting higher conductivities at intermediate porosities. These interpretations represent a conceptual model that explains the observed data trends, but they also constitute hypotheses that require further validation. For example, testing the role of replacive cements would benefit from additional mineralogical characterisation at the pore scale, while the influence of detrital clays could be further constrained by targeted sampling across different Buntsandstein regions. Importantly, all Buntsandstein samples analysed here are from the Q-block, and the results therefore reflect this specific setting. Regional studies (e.g., (Griffioen et al., 2025)) demonstrate that Buntsandstein properties vary across the Dutch subsurface, so the trends

reported here should be regarded as representative of the Q-block and not generalised to the entire formation.

3.4.2.2. Volumetric heat capacity

As observed in Figure 3.3b, volumetric heat capacity decreases with increasing porosity because a portion of the rock (with relatively high density and moderate specific heat) is replaced with air, which has almost no ability to store heat. The volumetric heat capacity of air is essentially negligible ($\sim 0.00124 \times 10^{-6}$ J/m³/K) compared to that of rock (Popov et al., 2016). Note, in reservoir conditions, the pores will be saturated with a different fluid(s) changing the bulk properties.

The results demonstrate that volumetric heat capacity reflects the combined influence of porosity and mineralogical composition. Fine-grained material increases volumetric heat capacity by contributing minerals with higher intrinsic heat storage capacity and by reducing pore volume (Figure 3.3b). Under dry conditions, volumetric heat capacity scales with the solid fraction and its specific. Adding fine-grained, clay-rich material both lowers porosity and raises specific heat capacity, so the volumetric heat capacity increases too (Robertson, 1988). This explains the elevated heat capacities observed in clay-rich, low-porosity samples, compared to lower values in clean sands. At higher porosities, where clay content is minimal, porosity again becomes the dominant control, leading to heat capacities consistently below ~ 1.5 MJ/m³·K.

The relationship with thermal diffusivity further clarifies these patterns. From Figure 3.3a, adding detrital silt/clay reduces porosity and lowers thermal conductivity. In Figure 3.3b, clay-rich samples cluster at low porosities (<10%) and display lower diffusivities (~ 1.0 – 1.2 mm²/s) compared to cleaner sands at similar porosities, which sometimes reach higher diffusivities. This apparent reversal arises because volumetric heat capacity, defined as thermal conductivity divided by thermal diffusivity, increases with clay content. Although clay lowers conductivity, it also has a relatively high specific heat capacity. The net effect is to raise volumetric heat capacity and thereby suppress diffusivity.

By contrast, clean, quartz-rich sands have higher conductivity but lower volumetric heat capacity, which results in relatively higher diffusivities at comparable porosities. At higher porosities (>15%), where clay content is negligible, diffusivity remains consistently low (~ 1.0 – 1.2 mm²/s). This highlights that porosity is the dominant control, while detrital clay modulates the balance between conductivity and heat capacity in the low-porosity regime.

Volumetric heat capacity most clearly differentiates the two formations. The Triassic consistently shows higher values, particularly above 15% porosity where many samples exceed 2.0 MJ/m³·K, whereas the Rotliegend typically remains below 1.8 MJ/m³·K. This contrast reflects mineralogical composition: the quartz-rich Rotliegend has lower capacities, while the Triassic, with more feldspar and clay, stores more heat and compensates for lower diffusivities.

Overall, volumetric heat capacity decreases linearly with porosity, confirming the validity of the observed trend.

3.4.2.3. Thermal diffusivity

Thermal diffusivity decreases with increasing porosity because thermal conductivity declines more steeply than volumetric heat capacity. Although density and heat capacity also decrease with porosity, they do not fully offset the conductivity loss, so diffusivity drops overall. However, with a lower relative range than either the thermal conductivity or volumetric heat capacity. This narrower variability partly explains the lower predictability of diffusivity, as smaller contrasts between samples reduce model sensitivity to compositional and textural variations (Chapter 5). Microcracks enhance this effect by interrupting heat pathways, consistent with experimental results.

Systematic differences between the formations are evident. Rotliegend samples generally show higher diffusivities (1.2–2.5 mm²/s) compared to the Triassic (1.0–2.0 mm²/s). This reflects mineralogy: quartz-rich Rotliegend sandstones combine relatively high conductivity with low heat capacity, whereas the Triassic, with more feldspar and clay, shows elevated heat capacity that suppresses diffusivity. In agreement with theoretical expectations, clay- and mica-rich Triassic samples at low porosities (<10%) have lower diffusivities (~1.0–1.2 mm²/s) than cleaner quartzose sands at similar porosities. This supports the idea that mineralogy modifies diffusivity indirectly by raising heat capacity and lowering conductivity.

A subset of samples from Q04-10 and Q04-C2, particularly those at porosities above 20%, deviate from the main trend. These outliers are likely clean, quartz-rich sandstones, as suggested by their low clay contents (<6%), low gamma-ray values (~50 API), and PCA results showing diffusivity inversely correlated with grain density and trending toward pure quartz. Nevertheless, scatter is high in these intervals (especially in Q04-10), so checking the plug description data for textural or structural features would help verify the clean-sandstone interpretation.

3.4.2.4. Specific heat capacity

Specific heat capacity shows no strong dependence on porosity due to the porosity not impacting the mass in the tested conditions, with most values clustering between 0.6 and 1.0 kJ/kg·K across both formations. The Triassic Buntsandstein generally exhibits slightly higher values than the Rotliegend, which is consistent with its greater feldspar and clay contents that possess intrinsically higher heat capacities than quartz. In contrast, the Rotliegend is more quartz-rich and therefore tends to display lower specific heat capacities, reflecting the low heat capacity of quartz. Despite this offset, there is substantial overlap between the two datasets, suggesting that mineralogy rather than porosity exerts the primary control on specific heat capacity. The absence of a clear porosity trend also contrasts with volumetric heat capacity,

where a strong negative correlation with porosity was observed, highlighting again the dominant role of mineral composition in controlling specific heat capacity.

3.5. Conclusion

The integration of thermal, acoustic, and petrophysical data from more than 700 Triassic Buntsandstein core plugs, complemented by comparison with the Permian Rotliegend, demonstrates that porosity is the primary control on rock properties relevant for geothermal exploitation. Thermal conductivity decreases systematically with porosity, spanning ~ 2.0 – 4.5 W/m \cdot K, while thermal diffusivity decreases from ~ 2.0 to 1.0 mm²/s. Volumetric heat capacity shows a strong negative correlation with porosity, reaching values above 2.5 MJ/m³ \cdot K in low-porosity intervals. Acoustic velocities (V_p 2500–5200 m/s; V_s 1500–3100 m/s) correlate positively with each other and negatively with porosity, while permeability increases semi-logarithmically with porosity.

Mineralogy and diagenesis govern systematic deviations from these trends. In the Triassic, detrital clays tighten the framework, yielding higher velocities at low porosity compared with the Permian, where replacive clays reduce stiffness. Dolomite cement decreases porosity and lowers conductivity, while nacrite-rich samples uniquely combine higher porosities with elevated thermal conductivities. Clean, quartz-rich sandstones define the main porosity–conductivity regression, with R^2 values up to 0.75, whereas clay- and cement-rich samples explain characteristic scatter. Lamination induces orientation-dependent velocity variability, confirming that rock fabric modifies elastic behaviour without altering the overall V_p – V_s relationship.

Systematic offsets between the Buntsandstein and Rotliegend highlight the role of depositional and diagenetic history: Buntsandstein samples exhibit broader porosity variability, higher volumetric heat capacity, and lower diffusivity, whereas the quartz-rich Rotliegend shows higher diffusivity but lower heat capacity. Principal component and canonical correlation analyses reveal very strong links between thermal, acoustic, and petrophysical parameters, with canonical correlation values of 0.987 (Permian) and 0.981 (Triassic), confirming the predictability of thermal properties from porosity and velocity.

Together, these results establish a robust empirical and physical framework for predicting subsurface rock properties in Dutch geothermal plays. They demonstrate that porosity is the dominant control, mineralogy and diagenesis define systematic deviations, and rock fabric introduces directional variability. The integration of these findings into reservoir models will improve well-log based property prediction and enhance the assessment of geothermal resources in the Netherlands and comparable sedimentary basins.

4. Coupled mechanical and thermo-physical characterisation of the lower Cretaceous Delft Sandstone Member for geothermal applications

Abstract: Reliable geomechanical reservoir models require depth-continuous static elastic moduli, yet standard downhole logs, i.e. sonic and density logs, supply high-frequency dynamic moduli that are known to over-estimate static rock stiffness. We therefore combined laboratory and log data acquired from well DEL-GT-01 of the TU Delft campus geothermal project to derive lithology-specific dynamic-to-static conversions. The focus was on the reservoir section where both shales and sands as part of the lower Cretaceous Delft Sandstone Member. Sixty cylindrical core plugs of both sandstone, shale, and mixes of these lithologies were measured for porosity, permeability, thermal properties, and ultrasonic velocities; 14 were loaded in uniaxial compression and 13 in triaxial compression (0–40 MPa) to determine the static Young’s modulus, E_s . Our result show that laboratory dynamic Young’s moduli correlate with log-derived values ($E_{d-lab} = 2.15 E_{d-log} - 51.17$, $R^2 = 0.75$) and that static moduli can be predicted from laboratory dynamics ($E_s = 0.94 E_{d-lab} - 1.7$, $R^2 = 0.33$). This indirect two-step workflow reproduces measured sandstone E_s values (5–22 GPa) within the experimental scatter along seven core sections with a total length of 84.74 m, whereas a simpler direct fit applied to logs alone ($E_s = 1.2 E_{d-log} - 24.63$, $R^2 = 0.12$) shows larger scatter. In shales, the dynamic–static gap is even wider (35–48 GPa vs. 10–25 GPa), confirming that correlations must be lithology-aware. The calibrated indirect workflow produces a continuous static-modulus log that is ready for input to wellbore-stability and reservoir-compaction models of the Delft sandstone. It offers a practical approach for developing framework that enables generating correlations for various rock type even when limited data are available.

4.1. Introduction

The performance and safety of geothermal reservoirs depend on reliable forecasts of rock deformation and stability (Zhang & Zhao, 2023). These forecasts are obtained through geomechanical models, which require static elastic moduli as key inputs. Reservoir-scale models rely on static elastic moduli, yet continuous downhole data, e.g. sonic and density logs, provides high-frequency dynamic moduli that systematically overestimate static rock moduli (Eissa & Kazi, 1988). The static Young’s modulus obtained directly from UCS test stress–strain curves reflects the rock’s deformation behaviour under uniaxial loading. Static moduli are generally lower than dynamic values due to strain amplitude effects, microcrack development, and time-dependent deformation (Kotsanis et al., 2021). For geomechanical applications, such as stress modelling and wellbore stability, static moduli are typically considered more representative of in-situ mechanical behaviour (Shen et al., 2024). Therefore, a robust, lithology-specific conversion from dynamic to static Young’s modulus is therefore essential to obtain realistic mechanical properties and to safeguard wellbore stability, cap-rock integrity, and overall reservoir performance.

Table 4.1 gives an overview of published equations that relate dynamic and static Young’s modulus for different rock types. It shows how these relationships vary depending on the rock properties, testing methods, and conditions.

Coupled mechanical and thermo-physical characterisation of the lower Cretaceous Delft Sandstone Member for geothermal applications

Table 4.1 list of correlations used to convert dynamic Young's modulus to static Young's modulus (Shen et al., 2024). The unit of dynamic (E_d) and static (E_s) Young's modulus is GPa in all equations.

No.	Equation	R ²	Rock type	Reference	Remarks
1	$E_s = 0.64E_d - 0.32$	0.84	All types	(McCann & Entwisle, 1992)	<ul style="list-style-type: none"> • Dynamic modulus values are generally higher than static modulus values (up to two orders of magnitude higher in soft mudrocks). • A linear equation applied to log data can provide a quick estimate of the static modulus, but only if lithology is properly considered.
2	$E_s = 0.74E_d - 0.82$	0.84	All types	(Eissa & Kazi, 1988)	<ul style="list-style-type: none"> • Cracks and non-linear elasticity affect static more than dynamic measurements. • Static modulus derived from uniaxial compressive strength tests. • Dynamic modulus measured using seismic methods.
3	$E_s = 1.05E_d - 3.16$	0.99	Sedimentary	(Christaras et al., 1994)	<ul style="list-style-type: none"> • Dynamic modulus was derived from sonic (V_p, V_s) and density logs. • In high-strength rocks, static and dynamic modulus values are more similar. In contrast, soft mudrocks show much higher dynamic-to-static modulus ratios, mainly due to plastic deformation and differences in strain levels between the two types of measurements.
4	$E_s = 0.867E_s - 2.085$	0.96	Sedimentary	(Brotons et al., 2014)	<ul style="list-style-type: none"> • S-wave velocity proved to be a reliable, non-destructive indicator of thermal damage. • Strength loss was primarily attributed to crack propagation, rather than mineralogical changes. • Dynamic moduli (from velocity tests) tend to overestimate stiffness, requiring correction or validation against static measurements after thermal exposure.
5	$E_s = 0.932E_s - 3.421$	0.97	All types	(Brotons et al., 2016)	<ul style="list-style-type: none"> • Porosity strongly influences the dynamic-to-static modulus ratio (k). As total porosity increases from less than 1% to about 35%, the ratio rises from approximately 1 to 2.3. As a result, ultrasonic tests tend to overestimate the stiffness of rocks with open or porous textures. • Compact rocks ($E_s \geq 80$ GPa) behave elastically – In dense limestones, marbles, and granites the two moduli converge ($k \approx 1$), making velocity-based estimates trustworthy. • Including bulk density (and uniaxial compressive strength, when available) in the model improves accuracy. Such models can achieve R² values up to

					<p>0.996 and keep static modulus errors within $\pm 5\%$, enabling reliable non-destructive evaluation on site.</p> <ul style="list-style-type: none"> • With similar pore structures, calcitic marbles and silicate igneous rocks show alike stiffness meaning that mineralogy has a minor influence; pore volume and geometry, not mineral mix, govern elastic response.
--	--	--	--	--	--

Dynamic moduli are measured at high frequencies (1 MHz in this present study) and small strains, where the rock framework responds elastically and microcrack closure does not significantly affect stiffness. In contrast, static moduli are determined under gradual and slow loading, where pore structure, microcrack propagation, and irreversible deformation are more pronounced (Zimmer et al., 2007). Zimmer et al. (2007) investigated the pressure dependence of seismic velocities in unconsolidated sands by conducting laboratory experiments under hydrostatic loading conditions from 0.1 to 20 MPa. They measured changes in porosity and volumetric strain during loading and unloading cycles. Their results showed that most of the porosity loss and volumetric strain did not recover upon unloading, indicating irreversible deformation in the grain structure. This behaviour reflects permanent compaction and microstructural rearrangement under quasi-static stress, highlighting the difference between how rocks respond under static and dynamic conditions. Fjær (2009) conducted a series of mechanical tests on dry Castlegate sandstone to investigate how stress levels and loading paths affect the difference between static and dynamic elastic moduli. The study found that static moduli are consistently lower than dynamic moduli, except immediately after a change in the loading direction. This difference is attributed primarily to the larger strain amplitudes and irreversible deformations (e.g. microcrack growth, frictional sliding) that occur during quasi-static loading but are not activated under the small-strain, high-frequency conditions of dynamic testing. As a result, dynamic moduli reflect the instantaneous elastic response of the rock matrix, while static moduli better represent its deformability under reservoir conditions.

McCann and Entwisle (1992) compared tangent static Young’s modulus from core tests with dynamic modulus from full-waveform sonic and density logs in British boreholes. Their dataset yielded the relation $E_s = 0.69E_d + 6.40$ GPa ($R^2 = 0.75$), with a log–log equivalent. They observed near equality of dynamic and static moduli in stiff, well-cemented rocks, but differences of up to two orders of magnitude in weak mudrocks, indicating that conversions must be lithology-specific.

Christaras et al. (1994) tested eight French rocks from six lithologies. Static Young’s modulus from core tests was compared with dynamic values from ultrasonic pulse velocity and mechanical resonance. Correlations were very high ($R^2 > 0.99$). Static values were about 3 GPa lower than dynamic ones, but the small dataset limits broader applicability.

Eissa and Kazi (1988) examined 342 pairs of dynamic and static Young’s moduli from different rock types (granites, limestones, sandstones, and schists) and proposed a first-order conversion,

$E_s = 0.74 E_d - 0.82 \text{ GPa}$ ($R^2 = 0.84$) between static and dynamic Young's moduli. They noted that it becomes unreliable when the dynamic modulus (E_d) drops below about 20 GPa. Using a smaller set of 76 samples that also included bulk-density data, they developed a stronger relation, $\log E_s = 0.02 + 0.77 \log(\rho \times E_d)$, which improved the R^2 to 0.96 and cut prediction scatter to roughly $\pm 10\%$.

Brotons et al. (2016) examined 57 rock samples and developed a linear relation $E_s = 0.932 E_d - 3.421 \text{ GPa}$ with $R^2 = 0.97$. A two-parameter log-linear form, $\log E_s = 0.967 \log(\rho \times E_d) - 3.306$, improved the fit to $R^2 = 0.99$. Expanding the model to include density, total porosity and UCS increased the coefficient of determination to 0.996. They concluded that single-parameter dynamic-to-static conversions are insufficient across varied rock types, and that including variables reflecting petrographic controls, notably porosity, along with bulk density and UCS, significantly improves predictions.

Zhang et al. (2024a) reviewed four decades of experiments on static–dynamic elastic moduli in rocks. They showed that P- and S-wave velocities, and the derived dynamic Young's and bulk moduli, vary strongly with frequency (10^{-6} – 10^6 Hz), especially in water-saturated samples. Two main approaches were identified: empirical correlations (linear, power-law, or quadratic) and the multifrequency ultrasonic method, which extrapolates velocities to low frequency. Zhang et al. (2024a) outlined the advantages, limitations, and key challenges of both, emphasizing that reliable static moduli require robust empirical conversion, low-frequency reference velocities, and corrections for strain, saturation, loading, and crack density.

Recently, Shen et al. (2024) reviewed 40 datasets covering igneous, metamorphic, and sedimentary rocks showing that most published $E_s - E_d$ correlations could be written in the form $E_s = a \times E_d + b$. By analysing the reported constants they derived a correlation between the two coefficients, i.e. $a = 0.67 + 0.101 b - 0.006 b^2 + 0.0001 b^3$, so that a single parameter (b) could be identified to allow the estimation of E_s from E_d . However, when fitting their compiled data directly, they found that power-law models best described the relationship for igneous and metamorphic rocks ($R^2 \approx 0.97$ and 0.93), whereas linear or log-linear models performed better for sedimentary rocks ($R^2 \approx 0.91$). They also noted that dynamic and static Poisson's ratios correlated poorly, highlighting that modulus conversions must be used with caution.

Shales have been seen to show the widest dynamic–static gap because of strain-rate sensitivity and bedding-plane slip. For example, Lozovyi and Bauer (2019) measured static and dynamic Young's moduli of brine-saturated shales from the Molasse Basin and Opalinus Clay. Young's modulus increased by 30–100% between seismic (1–150 Hz) and ultrasonic (500 kHz) frequencies, with corresponding P- and S-wave velocity increases of 10–20% and 20–40%. Static stiffness was strongly stress-dependent, and extrapolation to zero stress change aligned static and dynamic values at seismic frequency. They concluded that differences between

dynamic and static moduli in shales depend on both frequency and loading, so a single Ed–Es ratio is not generally applicable.

Later, Bian et al. (2023) performed triaxial tests with ultrasonic measurements on shale-oil cores from the Gulong area. They found that loading rate had little effect on Ed (<1%) but strongly influenced Es (up to 32%). Increasing axial stress raised Ed by up to threefold while reducing Es by 42% and unloading caused further Es reductions of up to 35%. The gap between Ed and Es narrowed under low-strain unloading. They concluded that loading rate, strain magnitude, and stress history control the Ed–Es relation, and recommended measuring Es during low-strain unloading before applying conversion formulas.

Sun et al. (2022) studied 20 shale core samples from the Qingshankou Formation using XRD and uniaxial/triaxial compression tests to assess the link between mineral composition and mechanical properties. They concluded that shale strength is highly dependent on mineral composition, bedding orientation, and confining pressure. Sand-rich shales exhibit higher compressive strength than clay-rich pure shales, especially in the parallel bedding direction. Under increasing confining stress, strength increases significantly, but shales remain prone to failure along weak planes and microcracks, leading to complex shear and splitting modes of deformation (Sun et al., 2022). In dynamic tests, the load is not high enough to allow for microstructural features of shales to respond. This leads to overestimating stiffness. Static tests, however, involve slower and significantly heavier loading rates, allowing for the activation of inelastic deformation mechanisms such as microcrack propagation and grain boundary sliding, resulting in lower measured stiffness.

Yang et al. (2025) examined three shale samples (Kimmeridge, Whitby Mudstone, and Marcellus) using triaxial deformation experiments under varying pressures and temperatures to investigate deformation mechanisms. Results show that at low pressure, shales deform along weak planes, while increasing confining pressure promotes ductile behaviour, crack closure, and deformation via creep and pressure solution along clay-rich layers. The mechanical response of shales is frequency-dependent. Delle Piane et al. (2014) investigated the frequency-dependent mechanical behaviour of Pierre shale by testing three core samples using resonant bar experiments over seismic frequencies (1 Hz to 10 kHz). Their results showed that both compressional and shear wave velocities increased with frequency, while attenuation decreased. This frequency dependence is due to shale's internal structure response to stress. At low frequencies, stress changes slowly, giving time for microcracks and grain boundaries to move or slide. This absorbs energy and reduces stiffness. At higher frequencies, the stress changes too quickly for these inelastic movements to occur, making the rock behave more like a stiff, elastic material and allowing waves to travel faster with less energy loss (Delle Piane et al., 2014).

Dynamic tests operate at higher frequencies, capturing the immediate elastic response of the material, while static tests assess the material's behaviour over longer durations, including time-

dependent (viscoelastic) effects. This frequency dependence means that dynamic tests may not account for creep and other long-term deformation behaviours inherent to shales. Zhang et al. (2025) quantified and related the static and dynamic Young's moduli of Cangdong Sag shale by conducting paired triaxial compression and ultrasonic velocity tests on core plugs oriented at 0°, 45°, and 90° to the bedding plane. Under both loading and unloading paths, static measurements, derived from axial and lateral strain in incremental confining-pressure steps, and dynamic measurements, from V_p , V_s , and bulk density, revealed that both moduli increase with pressure and are higher on unloading than loading. Across all orientations and pressures, dynamic Young's modulus exceeded static values by roughly 10–30%, with the greatest stiffness observed when loading was parallel to bedding and the lowest when perpendicular. By fitting a single linear regression ($R^2 \approx 0.93$) between dynamic and static moduli under reservoir-like pressures, the study provides a strong conversion model that enables engineers to predict the slower, large-strain elastic response of shale directly from rapid, small-strain ultrasonic data. This streamlines the characterisation of geomechanical properties for shale reservoir design and hydraulic fracturing. Empirical studies have consistently shown that dynamic Young's modulus values for shales are higher than their static counterparts. This overestimation can be significant, especially in formations with high clay content and pronounced anisotropy. Therefore, relying solely on dynamic measurements for geomechanical assessments can lead to inaccurate predictions of shale behaviour under stress. Eissa and Kazi (1988) studied how static and dynamic Young's moduli differ across a wide range of intact rocks by compiling 342 paired measurements from the literature, covering limestones, shales, schists, porphyries and more, and then performing statistical regression to relate the two. Static moduli (taken as the secant slope at 50% of uniaxial strength) were gathered from conventional loading-frame tests, while dynamic moduli came from both sonic-pulse and bar-resonance ultrasonic methods. Consistent with prior work, they found dynamic values to exceed static by up to a factor of two (E_d/E_s ranging ≈ 0.85 – 2.05) due to the high-frequency, small-strain nature of ultrasonic measurements being less sensitive to microcracks. A simple linear fit across all data yielded $E_s = 0.74 E_d - 0.82$ ($R^2 = 0.84$).

Bian et al. (2023) explained the difference between dynamic and static Young's modulus in shales by examining the influence of loading rate, strain amplitude, and loading history on the rock's mechanical response. The dynamic modulus, measured using ultrasonic waves, remains nearly constant regardless of loading conditions, while the static modulus, derived from stress–strain data, is highly sensitive to them. Slower loading allows microcracks and pores in the shale to close more effectively, increasing static stiffness, whereas faster loading leaves more open fractures, reducing it. Additionally, larger strain amplitudes in static tests lead to more internal friction and irreversible deformation, further lowering the measured modulus. In contrast, dynamic measurements involve very small strains and do not trigger frictional energy loss, capturing only the intrinsic stiffness of the rock matrix. Moreover, testing during unloading phases, when friction is reduced and particle contacts are stabilised, yields static modulus values closer to the dynamic ones. These effects are especially important in shales due to their fine-grained structure, bedding planes, and microcrack networks. They also explain

why dynamic Young's modulus is often 10–30% higher than static and highlight the importance of considering deformation history when converting between the two.

Lozovyi and Bauer (2019) examined the difference between static and dynamic Young's moduli in shales by testing four fully saturated shales using a custom triaxial setup capable of measuring stiffness at both seismic (1–150 Hz) and ultrasonic (500 kHz) frequencies. They found that dynamic Young's modulus increases with frequency, showing up to 100% difference between seismic and ultrasonic values. Meanwhile, static modulus was strongly affected by stress amplitude: higher loading amplitudes led to more non-elastic deformation and reduced static stiffness.

These dynamic parameters represent the elastic response of the rock under small-strain, high-frequency loading conditions, and are useful for evaluating intact rock behaviour and wave propagation characteristics. However, log-based values may be affected by borehole conditions, formation heterogeneity, and anisotropy, which can reduce accuracy compared to laboratory results (Brotons et al., 2016; Xu et al., 2016).

Soustelle et al. (2022) performed triaxial tests on water-saturated sandstone cores from four West Netherlands Basin wells to obtain mechanical and thermal properties relevant to geothermal design. Under reservoir-level pressures the static Young's modulus reached about 16–23 GPa, Poisson's ratio fell below 0.2, and thermal-expansion coefficients stayed near 10^{-5} °C⁻¹. Dynamic moduli from nearby dipole-sonic logs were consistently higher, confirming that log data alone overstate rock stiffness and should be corrected with laboratory measurements before geomechanical modelling. Soustelle et al. (2022) concluded that the Young's modulus of West Netherlands Basin sandstones increases quickly with increases in confining pressure yet still show static Young's moduli well below the values implied by dipole-sonic logs; with thermal-expansion and poroelastic parameters staying in a narrow range but likewise depending on pressure. Because these pressure-dependent static properties differ from log estimates, the authors stress that laboratory-measured moduli, Poisson's ratios, and thermal coefficients must be used, rather than raw log data, when modelling wellbore stability, reservoir compaction and induced-seismicity risk in Dutch geothermal projects.

In addition to elastic moduli, thermal, porosity, and permeability properties are essential for geothermal reservoir assessment. Thermal properties including thermal conductivity, thermal diffusivity, and volumetric heat capacity govern heat transport and influences heat recharge efficiency (Clauser & Huenges, 1995b; Fuchs & Förster, 2010). Porosity and permeability determine fluid storage and flow capacity, directly affecting reservoir productivity and long-term sustainability (Nelson, 1994). These properties are physically linked and are all strongly influenced by lithology, mineralogy, and pore structure. Sandstones typically show higher porosity and permeability, while shales tend to be denser, less porous, and more resistive to flow (He et al., 2021; Abdelaali, Rahmouni et al., 2014). Thermal conductivity is also sensitive to these factors, decreasing with porosity but increasing with bulk density and mineral content

(Clauser & Huenges, 1995b) Chapters 2 and 3 of this thesis). Understanding these links is essential for simulating coupled thermal–hydro–mechanical processes and for constraining reservoir behaviour under dynamic loading (Jianxin, 2009; Pimienta et al., 2018). This study integrates thermal, petrophysical, and mechanical properties to characterise the Delft Sandstone Member, with a particular focus on elastic moduli relevant for geomechanical modelling.

Building on these gaps, this work utilises data and samples from the geothermal project on the TU Delft campus which targets the lower Cretaceous Delft sandstone (Vardon et al., 2024b). Specifically, the present work (i) integrates core-scale triaxial and ultrasonic measurements from well DEL-GT-01 with co-located sonic and density logs, (ii) derives sandstone- and shale-specific relationships that convert log-based dynamic moduli to static values, and (iii) tests two workflows, a one-step direct fit and a two-step indirect fit that first harmonises dynamic data to laboratory conditions. By comparing both approaches against blind laboratory data, we quantify their accuracy and outline depth-continuous static-modulus profiles suitable for geomechanical models of the Delft Sandstone Member. These findings can improve and benefit wellbore stability analysis and reservoir integrity assessment on the TU Delft geothermal campus.

4.2. Study area and materials

This study focuses on rock property analysis from the DEL-GT-01 well, drilled as part of the geothermal project on the TU Delft campus (otherwise known as Geothermie Delft, GTD) located in the West Netherlands Basin (WNB) (Vardon et al., 2024b). The project targets the lower Cretaceous Delft Sandstone Member within a small, structurally-defined syncline bounded by inactive faults. Figure 4.1 illustrates the well trajectory, fault proximity, and geothermal influence area. The basin is a NW–SE trending subsiding structure that formed through several tectonic events, including Late Jurassic to Early Cretaceous rifting, which led to the deposition of thick clastic successions (Willems et al., 2020).

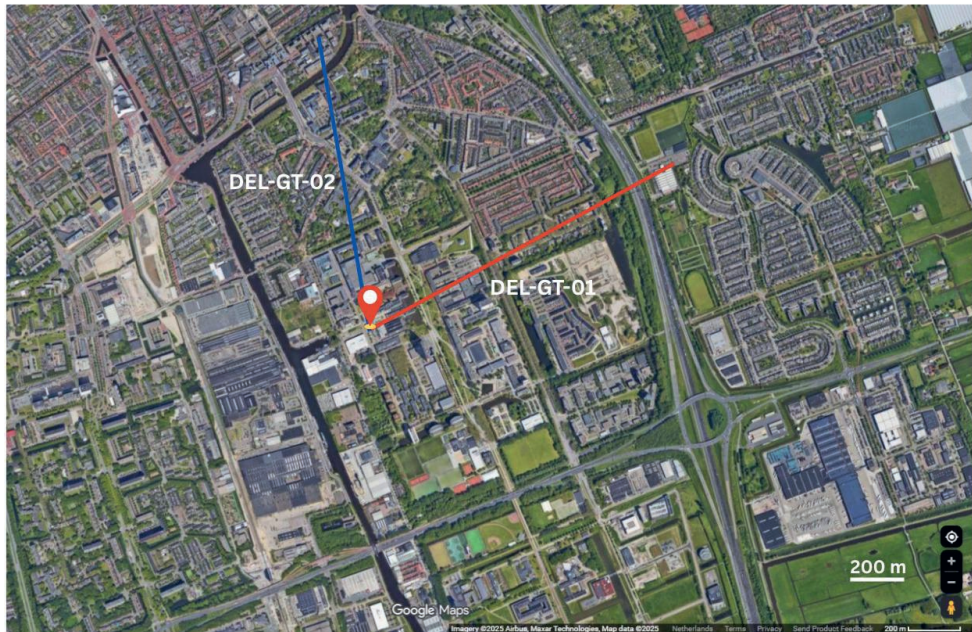


Figure 4.1 The approximate surface location of the DEL-GT-01 and DEL-GT-02 wells, their paths after (Vardon et al., 2024b). Background image from Google Maps (©2025 Google, Imagery ©2025 Airbus, Maxar Technologies).

The geothermal target for this project is part of the lower Cretaceous Nieuwerkerk Formation, specifically the upper part of the Alblasserdam Member and the Delft Sandstone Member (DSSM). These members consist primarily of fine- to coarse-grained sandstones and claystones deposited in fluvial to deltaic environments. The lithological alternation reflect rapid changes in depositional energy (Bruining, 2024). Approximately 85 m of 4” diameter core was retrieved from the producer well (DEL-GT-01), covering a representative section of both caprock and producing reservoir formations. The well trajectory (and therefore also the core) was approximately 45° to vertical and approximately 55° to the bedding plane. The available

material exhibits a range of lithologies, including cross-bedded and laminated sandstones, as well as interbedded siltstones and clay-rich layers (Bruining, 2024). These have been grouped into distinct facies types based on grain size, sedimentary structures, and matrix content. Cylindrical core plugs with a circa 30 mm diameter were taken from the 4” cores. 60 plugs were taken as detailed in Table 4.2. Plugs were extracted from odd-numbered core sections, usually at both the top and bottom of each section, to systematically capture stratigraphic variability at roughly 1-meter intervals throughout the Delft Sandstone. This approach ensured representation of textural and facies variation within the formation, including massive, cross-bedded sandstone (likely higher permeability and strength), fine-grained laminated sandstones, and heterolithic zones with shale interbeds. Based on 14 measured specimens, the average diameter was 29.74 mm (standard deviation = 0.076 mm), and the average length was 70.5 m (standard deviation = 16.32 mm), suitable for standard laboratory testing protocols.

Table 4.2 Overview of cores and extracted plugs from the DEL-GT-01 well, including formation assignments and reasoning for coring and sample selection. Cores 2 to 7 were taken from the Delft Sandstone Member, the primary geothermal reservoir, to capture vertical and lithological variability for thermo-mechanical and petrophysical analysis.

Core Number	Top Depth (m)	Bottom Depth (m)	Number of Extracted Plugs	Formation	member	Reasoning for coring and plugging
DELGT01-C1	2511.50	2526.50	5	Nieuwerkerk	Rodenrijs Claystone Member	not the primary focus for thermo-mechanical property analysis, as it lies above the reservoir and represents a caprock
DELGT01-C2	2576.00	2590.38	10		Delft Sandstone Member	target reservoir for the geothermal project.
DELGT01-C3	2594.50	2597.01	3			
DELGT01-C4	2597.50	2609.45	9			
DELGT01-C5	2610.50	2617.82	5			
DELGT01-C6	2618.00	2641.95	21			
DELGT01-C7	2642.00	2651.63	7			

Representative examples of the core plugs used in this study are shown in Figure 4.2. The plug in Figure 4.2a is a typical sandstone sample, characterised by a relatively homogeneous grain structure and light colour. Bedding can be observed at approximately 45° through the sample.

In contrast, the plug in Figure 4.2b is a shale sample, finer-grained and more compact, with subtle textural variability that may suggest bedding or internal layering. These two lithologies represent the primary rock types encountered in the DEL-GT-01 core, and both were included in the thermal and mechanical property analysis.



Figure 4.2 Core plug examples from the DEL-GT-01 wellbore: (a) sandstone and (b) shale.

4.3. Methodology

This study combines measurements conducted at geolaboratory of TU Delft, well log data, and regression-based modelling to characterise the elastic and mechanical behaviour of core samples from the DEL-GT-01 well. The workflow involves three main stages: (1) exploratory analysis of the measured petrophysical and thermal properties, (2) correlation and prediction of mechanical properties, and (3) conversion of dynamic elastic moduli to static values suitable for geomechanical applications.

All measurements, except for permeability, were performed at the laboratories of Delft University of Technology. Sample cleaning and the permeability measurements were performed at PanTerra Geoconsultants.

4.3.1. Laboratory measurements

Due to the use of oil-based mud during the drilling of DEL-GT-01, all samples required cleaning prior to measurements. All plugs were first visually inspected, and those which were seen to be affected by drilling fluids, residual salts, or structural damage were flagged for additional attention. To minimise alteration of clay-rich samples while still removing pore-filling salts, a low-temperature, mild cleaning procedure was applied. This involved soaking the samples in gentle cleaner to remove the existing salt in the pore space and subsequently placing them in an oven at 60 °C and 45% relative humidity for a week until a stable dry weight was achieved, which typically took around one week.

During cleaning, 15 samples were damaged due to pre-existing fractures or disintegration of weak clay-rich zones, likely held together by suction due to the formation brine or salt prior to drying. Samples were categorised based on their condition post-cleaning: intact and measurable (45), damaged but salvageable through trimming (4 samples), or fully failed and excluded from further testing (11).

4.3.1.1. Permeability

Permeability measurements were performed using a steady-state gas permeameter under 400 psi confining pressure. Helium was used as the permeant gas, and the resulting air permeability values were corrected to Klinkenberg permeability using the Klinkenberg equation (Klinkenberg, 1941). The confining pressure ensured adequate conformance between the sample surface and the rubber sleeve, reducing bypass flow.

4.3.1.2. Porosity and density

Each sample was weighed to determine its dry mass and measured with a calliper. As the samples had been stored at room temperature for several years without intentional saturation, they were considered effectively dry, and no additional oven-drying step was performed prior to weighing. These values were used to calculate the bulk volume (V_{bulk}) and bulk density, assuming cylindrical geometry and uniform sample geometry. To determine grain density and grain volume (V_{grain}), an Anton Paar Ultrapyc 5000 helium pycnometer was used.

4.3.1.3. Thermal properties

Thermal conductivity, thermal diffusivity, and volumetric heat capacity were measured using the transient plane source (TPS) technique with the Hot Disc TPS 2200 Thermal Constants Analyzer (Hot Disk method). The one-sided TPS technique is used, which involves placing a thin sensor between a flat surface of the measured material and an insulating material. The sensor acts as both a heat source and a temperature monitor during the measurement. These measurements were conducted under ambient laboratory conditions. For each sample, thermal conductivity, thermal diffusivity, and volumetric heat capacity are determined.

4.3.1.4. Acoustic velocities

To determine acoustic properties, we measured the compressional (P-wave) and shear (S-wave) velocities using a wave generator- oscilloscope, and amplifier, which allowed for the generation and recording of ultrasonic signals. Acoustic measurements were performed using the Sonic Micro Acoustic (SMA) system with transducers operating at a central frequency of 1 MHz. One transducer, connected to the wave generator, transmitted the signal through the sample, while a second transducer, placed on the opposite end and connected to the oscilloscope, received the signal. The travel time of the ultrasonic waves was recorded and used to calculate the acoustic velocities. This frequency, in the ultrasonic range, enables high-resolution characterisation of elastic wave propagation in small-scale rock samples. A similar setup and frequency have been used by Veltmeijer et al. (2022) in active acoustic monitoring of sandstone deformation under varying confining pressures.

For each test, the arrival times of the respective waveforms were identified on the oscilloscope. The acoustic velocities were then calculated by dividing the measured travel time by the known sample length, previously determined during the density measurements.

4.3.1.5. Derived dynamic elastic moduli

The dynamic elastic moduli can be calculated as a function of shear and compressional wave velocities and bulk density (Mavko et al., 2009; Shakouri et al., 2019; Zhang et al., 2024a). Although these equations are physically derived for isotropic and homogeneous media, their application to real rocks is empirical in nature, as rocks often exhibit anisotropy and heterogeneity. Therefore, other empirical formulations may also exist. Equation 4.1 shows the expression used to calculate the dynamic Young's modulus (E_{dyn}):

$$E_{dyn} = \rho V_s^2 \left(3 \frac{V_p^2}{V_s^2} - 2 \right) \quad \text{Equation 4.1}$$

where ρ is the bulk density, V_p is the compressional wave velocity, and V_s is the shear wave velocity. Additional elastic parameters derived include the dynamic bulk modulus (K_{dyn}):

$$K_{dyn} = \rho \left(V_p^2 - \frac{4}{3} V_s^2 \right) \quad \text{Equation 4.2}$$

the shear modulus (G_{dyn}):

$$G_{dyn} = \mu = \rho V_s^2 \quad \text{Equation 4.3}$$

and the Poisson's ratio (ν):

$$\nu_{dyn} = \frac{V_p^2 - 2V_s^2}{2(V_p^2 - V_s^2)} \quad \text{Equation 4.4}$$

4.3.1.6. Mechanical behaviour (static)

The static mechanical behaviour of the plugs was evaluated through a series of uniaxial and triaxial compression tests conducted by Postema (2025). A total of 14 uniaxial compressive strength (UCS) tests and 13 triaxial tests were performed. The sandstone samples were saturated with water prior to testing to replicate in-situ reservoir conditions. In contrast, the shale samples were tested in dry conditions, as they tended to disintegrate upon saturation due to their clay-rich composition and swelling upon saturation in unconfined conditions.

Triaxial tests were conducted at confining pressures up to 40 MPa, simulating subsurface effective stress environments found at several km depth. Each sample was loaded axially to failure under constant lateral pressure, and the resulting stress-strain data were used to determine peak strength, Young's modulus, and Poisson's ratio. The combination of the peak strengths is combined to determine the failure envelope. All mechanical test specimens were CT scanned in advance to identify internal defects or fractures and ensure reliable results.

4.3.2. Downhole petrophysical log data

This study used conventional well logs from the Dutch subsurface repository (www.nlog.nl), including gamma ray (GR), bulk density (ZDNC), neutron porosity (NPHI), and compressional and shear sonic logs (DTCQI and DTSQI, respectively). All logs were quality-checked, shifted, and depth-aligned to core data to ensure accurate comparison and interpretation. Compressional and shear wave velocities were derived from sonic logs using the equations $V_p (m/s) = 304800 / DTCQI$ and $V_s (m/s) = 304800 / DTSQI$, where DTCQI and DTSQI are recorded in microseconds per foot ($\mu s/ft$). Bulk density in SI units was calculated as $\rho (kg/m^3) = ZDNC \times 1000$, with ZDNC provided in g/cm^3 .

These computed V_p , V_s , and ρ values were used to derive dynamic elastic properties. Static moduli were then estimated using empirical correlations calibrated against laboratory measurements (see Section 4.3.1.5). Such evaluation is essential, as core measurements and log-derived data are obtained at different resolutions and spatial scales. While core data reflect discrete samples on the centimetre scale, log data represent continuous records averaged over decimetre to meter scales, potentially leading to smoothing effects or averaging of

heterogeneities. Furthermore, most laboratory measurements were conducted on dry samples under ambient conditions, whereas the log recordings reflect in-situ conditions, specifically, saturated formations under reservoir pressure and temperature. In addition, differences in measurement environments, controlled laboratory settings versus borehole conditions can further contribute to discrepancies. By identifying and quantifying these differences, the limitations and strengths of each dataset can be better understood and appropriately accounted for in subsequent modelling efforts.

4.3.3. Data analysis and modelling workflow

The analysis began with an exploratory non-destructive evaluation of porosity, permeability, density, acoustic velocity, and thermal properties on core plugs. The results were separated for sandstones and shales and analysed separately, allowing for lithology-dependent ranges and trends to be identified. Basic statistics and visual inspections of the data distributions were carried out, and outliers were interpreted in the context of mineralogy and sample condition. Mechanical properties were collected via dynamic (non-destructive) tests and static (destructive) tests. The mechanical analysis focuses on Young's modulus (E) that was evaluated using data from both dynamic and static tests. The dynamic Young's modulus was estimated from P-wave and S-wave velocities together with density, using both laboratory measurements and log-derived data.

The static Young's modulus was derived from uniaxial compressive strength (UCS) tests and triaxial tests. The objective was to establish a reliable method to convert dynamic moduli to static equivalents, which are more relevant for reservoir geomechanical modelling. The mechanical dataset used in this study originates from laboratory experiments described in Postema (2025). Three standard rock mechanics tests were performed on Delft Sandstone and Rodenrijs Claystone specimens: unconfined compressive strength (UCS), triaxial compression, and Brazilian disc tests. Core plugs were prepared to the required geometries, with sample ends ground flat and parallel; some broken ends were stabilised with gypsum to ensure uniform loading. Sandstone samples were brine-saturated prior to testing, whereas shale samples were left dry to prevent disintegration.

During UCS tests, axial load was applied at a controlled strain rate while both axial and radial strains were monitored using LVDTs and chain sensors. Young's modulus and Poisson's ratio were obtained from the linear part of the stress-strain curves. Triaxial compression tests were conducted in a Hoek cell under drained conditions, with confining pressures up to 40 MPa, while the axial load was increased under strain control. Brazilian disc tests were performed on shorter specimens at a fixed displacement rate (0.0005 mm/s) to derive tensile strength in line with ISRM recommendations.

To monitor velocity evolution under stress, P- and S-wave arrivals were recorded at regular intervals during UCS and triaxial experiments using active acoustic sensors integrated into the loading system. Instrumental deformation was quantified through calibration with aluminium

standards, and the resulting compliance was subtracted from the raw measurements. No replicate tests were performed; therefore, reproducibility was addressed through careful calibration, strain correction, and cross-checks against literature values and expected property ranges.

To estimate the static Young's modulus for all samples, first, the static Young's modulus values measured under different confining pressures during triaxial tests were extrapolated to zero confining pressure to allow fair merging with uniaxial tests (see Figure 4.11). Next, dynamic Young's modulus was calculated for each plug using laboratory-measured values of V_p , V_s , and bulk density. Then, samples with both static and dynamic data were used to build a linear regression model as ($E_{s_lab} = a \times E_{d_lab} + b$). Using this equation, we predicted static Young's modulus for all other plugs based on their dynamic values. The schematic workflow is illustrated in Figure 4.3, where the final panel shows an example depth-dependent comparison of E_{d_lab} , E_{s_lab} , and predicted E_s . The predicted values were then compared with measured static values and with common equations from the literature that are used to convert dynamic to static moduli. This allowed us to check how well our data aligned with established correlations and to estimate E_s for samples lacking direct measurements (Figure 4.3).

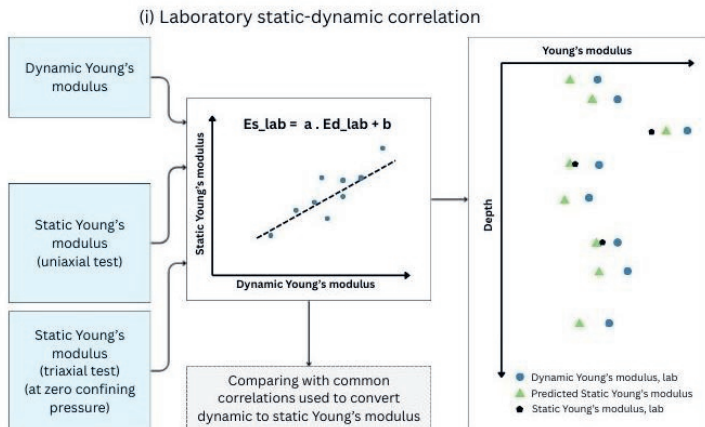


Figure 4.3 Schematic workflow for estimating and predicting static Young's modulus for Delft Sandstone plugs. Static Young's modulus was obtained from uniaxial and triaxial compression tests, with triaxial values extrapolated to zero confining pressure. These values (E_{s_lab}) were compared with dynamic Young's modulus (E_{d_lab}) derived from ultrasonic velocity measurements. A linear regression ($E_{s_lab} = a \cdot E_{d_lab} + b$) was established to relate static and dynamic moduli and was evaluated against common empirical correlations. The resulting relationship was applied to predict static Young's modulus for plugs with only dynamic data, as illustrated in the final depth-dependent comparison of E_{d_lab} , E_{s_lab} , and predicted E_s .

In the next step, the derived correlations between dynamic and static Young's modulus were compared with commonly used empirical relationships reported in the literature. This comparison was performed to assess the consistency of the conversion factors obtained in this study with those previously proposed for sedimentary rocks. By benchmarking the results against established models, the robustness and applicability of the derived equations, both from the direct and indirect approaches, were evaluated in the context of the lithological variability and testing conditions specific to the DEL-GT-01 well.

To convert the log dynamic Young's modulus to static, two regression-based strategies were developed and applied, as summarised in Figure 4.4. In the direct approach, each core plug was matched with its log-derived dynamic modulus (E_{d_log}) and its corresponding UCS-based static modulus (E_s). A linear regression was performed, yielding a calibration (e.g., $E_s = e \times E_{d_log} + f$) that was then applied across the full E_{d_log} curve to generate a continuous static Young's modulus profile. To account for differences between sandstones and shales, the same procedure was repeated separately by lithology, using gamma ray values (for instance, sandstone if $GR \leq 50$ API; shale if $GR > 50$ API). The resulting lithology-specific static logs were then recombined into a single masked static modulus profile.

In the indirect approach, the full set of ultrasonic laboratory dynamic moduli (E_{d_lab}) was first correlated with interpolated E_{d_log} values at plug depths, producing a transformation to bring the log-derived moduli into laboratory conditions ($E_{d_lab} = c \times E_{d_log} + d$). This log to laboratory dynamic modulus correlation was then converted to a static profile using the UCS-based correlation derived earlier in Figure 4.3 ($E_{s_lab} = a \times E_{d_lab} + b$).

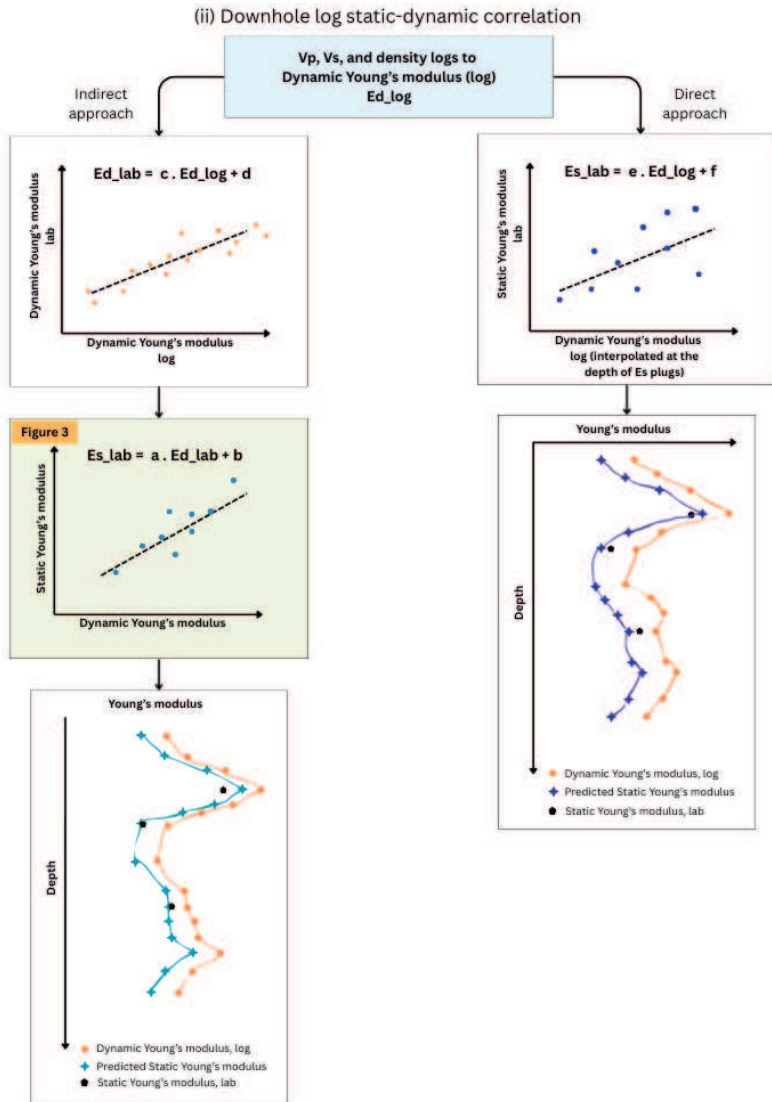


Figure 4.4 Schematic workflow for estimating static Young's modulus from well-log-derived dynamic modulus using two approaches: indirect and direct. In the indirect approach (left branch), the dynamic Young's modulus from logs (E_d_log) interpolated at plug depths is correlated with lab-measured dynamic modulus (E_d_lab). A linear regression ($E_d_lab = c \cdot E_d_log + d$) is established to convert interpolated log-based values to lab conditions. This is then combined with the laboratory-derived relationship between dynamic and static modulus ($E_s_lab = a \cdot E_d_lab + b$) to estimate static Young's modulus under lab conditions. In the direct approach (right branch), dynamic Young's modulus from logs (E_d_log) is correlated directly with static Young's modulus from mechanical testing (E_s_lab), yielding a regression of the form $E_s_lab = e \cdot E_d_log + f$. Both approaches are used to predict static

Young's modulus, with the depth-dependent comparisons of E_{d_lab} , E_{s_lab} , and predicted E_s shown in the lower panels.

Both workflows provide a method to translate log-derived dynamic Young's modulus to a static modulus appropriate for mechanical modelling. The direct approach is straightforward but relies on UCS coverage, whereas the indirect route benefits from the broader availability of plug-scale dynamic measurements.

4.4. Results

4.4.1. Exploratory data analysis

The outcomes of the laboratory analyses, including the full property ranges, are summarised in Figure 4.5. Among the thermal properties, both thermal conductivity and volumetric heat capacity have higher values in shale compared to sandstone, so their ranges also lie at relatively higher levels, in contrast to thermal diffusivity. Sandstone has higher porosity, permeability, and grain density compared to shale, while shale has higher bulk density. The shale has higher P-wave velocity, S-wave velocity, and all dynamic elastic moduli (Young's, shear, and bulk) compared to sandstone.

It should be noted that shale UCS and CCS tests were performed on dry samples, whereas the sandstone tests were conducted under saturated conditions. This choice was made to preserve the integrity of the shale samples, but it may have contributed to the elevated dynamic stiffness values. Lithologies and the broad variability in elastic behaviour across the cored interval.

The following initial overall observations are made:

- The thermal conductivity is seen to range from 2.13 to 4.75 W/m·K across all samples. The mean thermal conductivity is higher in shale (3.55 W/m·K) than in sandstone (3.13 W/m·K), with a combined average of 3.31 W/m·K
- The volumetric heat capacity being higher in shale (1.96 MJ/m³·K) than in sandstone (1.43 MJ/m³·K). These both reflect shale's greater bulk density and lower porosity.
- The thermal diffusivity shows an opposite trend, averaging 2.22 mm²/s in sandstone and 1.85 mm²/s in shale, but a lower range.
- Porosity strongly distinguishes the lithologies: sandstones average 15% (median 14.3%), while shales average only 5.9%, with a maximum of 7.1%.
- Bulk density is higher in shale (mean: 2580 kg/m³) compared to sandstone (2176 kg/m³). Grain density is slightly lower in shale (2.64 g/cm³) versus sandstone (2.68 g/cm³), though the variation is small.
- Gas horizontal permeability is significantly higher in sandstones (mean: 1128 mD) than in shales (mean: 169 mD), with values in sandstone reaching up to 3708 mD. The Klinkenberg-corrected permeability follows the same pattern (mean: 1083 mD for sandstone vs. 158 mD for shale). These differences are consistent with the higher pore connectivity in sandstone.

- In sandstone, the average P-wave velocity (V_p) is 2810 m/s, and the average S-wave velocity (V_s) is 1891 m/s. For shale, the corresponding mean values are 3870 m/s for V_p and 2477 m/s for V_s .
- The dynamic elastic moduli of the core plugs from the DEL-GT-01 well show significant variation between lithologies. For sandstone samples, the dynamic Young's modulus ranges from 4.1 to 32.7 GPa, with an average of 17.1 GPa. The shear modulus varies between 3.1 and 15.5 GPa (mean: 8.0 GPa), while the bulk modulus ranges from 0.8 to 12.3 GPa, with a mean of 7.0 GPa. These values reflect the generally lower stiffness and higher porosity of sandstone. In contrast, shale samples exhibit significantly higher stiffness. Young's modulus ranges from 16.5 to 48.6 GPa, with an average of 36.9 GPa. The shear and bulk moduli also follow this trend, averaging 16.2 GPa and 18.0 GPa, respectively. The higher moduli in shales are consistent with their greater density, lower porosity, and higher P- and S-wave velocities
- When considering all samples combined, Young's modulus ranges from 4.1 to 50.3 GPa, with a mean of 25.0 GPa. Shear modulus spans 3.0 to 23.6 GPa (mean: 11.3 GPa), and bulk modulus ranges from 0.8 to 28.0 GPa (mean: 11.3 GPa).

Coupled mechanical and thermo-physical characterisation of the lower Cretaceous Delft Sandstone Member for geothermal applications

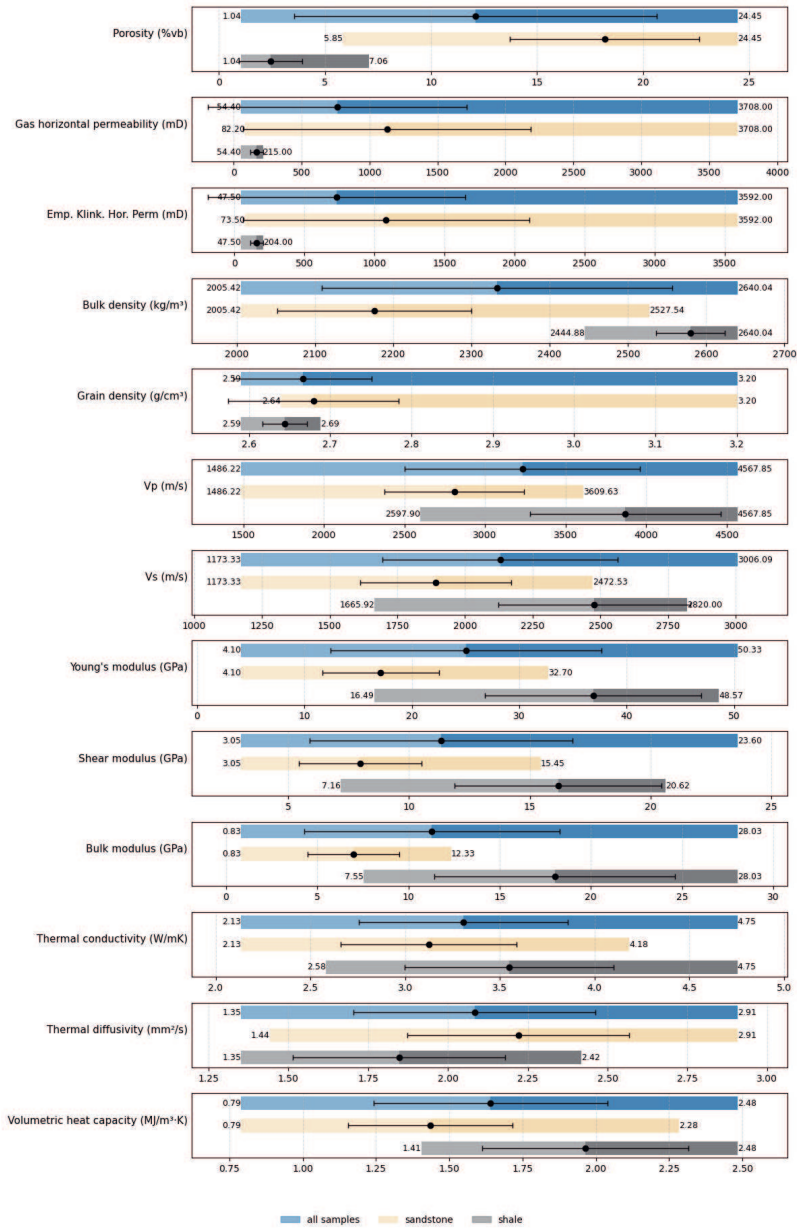


Figure 4.5 Ranges, mean values, and standard deviations of thermal, petrophysical, and elastic properties measured on 60 core plugs from the DEL-GT-01 well. Each bar represents the minimum-to-maximum range within a group, with a black dot indicating the mean and horizontal black whiskers showing ± 1 standard deviation. Colours denote rock types: blue for all samples, cream for sandstone, and grey for shale. Properties include thermal conductivity, thermal diffusivity, volumetric heat

capacity, gas permeability (direct and Klinkenberg-corrected), bulk and grain density, porosity, P- and S-wave velocities, and elastic moduli (Young's, shear, and bulk modulus).

Figure 4.6 shows the thermal conductivity versus porosity cross-plot (top left), where an overall negative correlation is observed consistent with a higher thermal conductivity of the solid material than the pore filling fluid (air in this case). For the full dataset, the best-fit line shows a clear but moderate negative correlation between the two properties ($Th_Cond = -0.4 \times 10^{-1} \times \varphi + 3.75, R^2 = 0.33$). When sandstone samples are isolated, the trend becomes slightly steeper and better defined ($Th_Cond = -0.7 \times 10^{-1} \times \varphi + 4.38, R^2 = 0.44$). The moderate R^2 values suggest a modest predictive relationship, particularly when analysing all samples. This likely reflects the influence of mineralogical variability and the limited porosity range and the number of available samples in the dataset (see Chapter 2 and 3 for further analysis of this aspect for other samples).

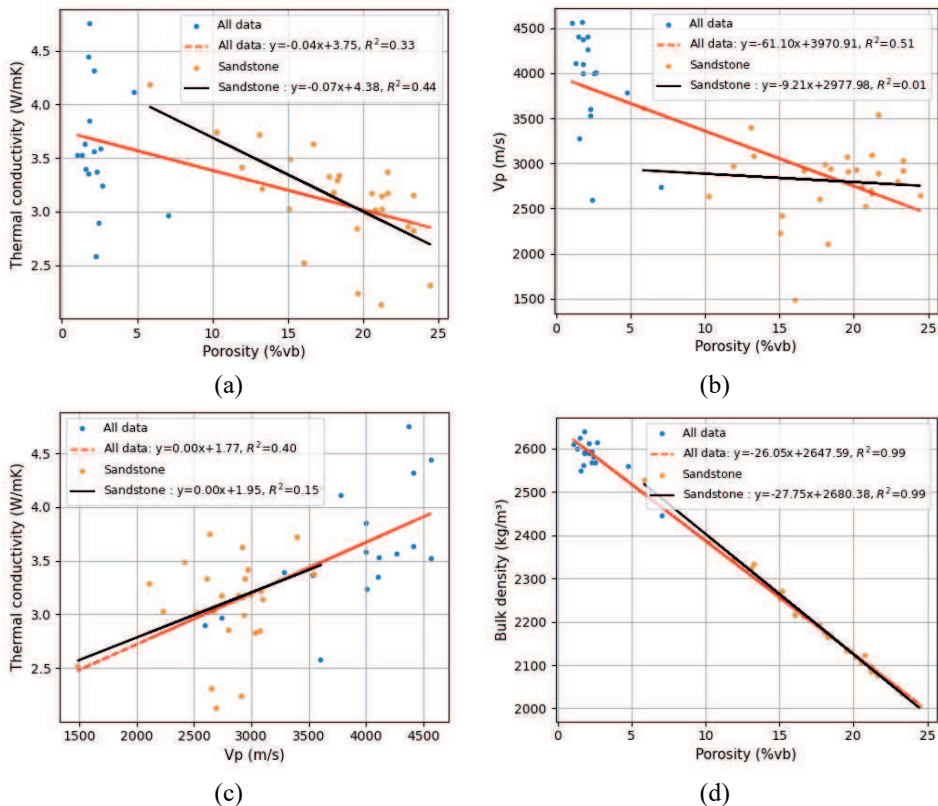


Figure 4.6 Cross-plots showing empirical relationships between selected rock properties from the DELGT-01 dataset. (a) thermal conductivity vs. porosity and (b) P-wave velocity (V_p) vs. porosity. (c) thermal conductivity vs. V_p and (d) bulk density vs. porosity. Fits are shown for the full dataset (red dashed line) and sandstone-only data (black line), with corresponding regression equations and R^2 values provided.

The V_p versus porosity cross-plot (top right) also reveal a moderate negative correlation for the full dataset ($V_p = -6.11 \times 10^1 \times \varphi + 3.971 \times 10^3, R^2 = 0.51$), with regression showing a stronger correlation than for sandstone only ($V_p = -9.21 \times \varphi + 2.978 \times 10^3, R^2 = 0.01$). The low R^2 for sandstones suggests that V_p is relatively insensitive to porosity variation within this group, while the full dataset reflects a stronger negative correlation, largely influenced by shale data.

In the thermal conductivity vs. V_p plot (bottom left), the overall trend for all samples ($\text{Th_Cond} = 4.75 \times 10^{-4} \times V_p + 1.772, R^2 = 0.40$) and for sandstones ($\text{Th_Cond} = 4.2 \times 10^{-4} \times V_p + 1.95, R^2 = 0.15$) is positive. Though the slopes are near zero due to unit scaling, the trend and determination coefficients (R^2) confirms that samples with higher V_p tend to have higher thermal conductivity, though the relationship is modest, especially within the sandstone group.

A moderate negative correlation is observed between thermal conductivity and the logarithm of gas horizontal permeability (Figure 4.7). The regression equation, $y = -0.565 \cdot \log_{10}(x) + 4.746$, indicates that higher permeability tends to be associated with lower thermal conductivity. The coefficient of determination ($R^2 = 0.285$) suggests that although there is a general trend, permeability alone does not fully explain the variability in thermal conductivity, implying that other factors such as mineral composition, porosity, or texture may also play a significant role.

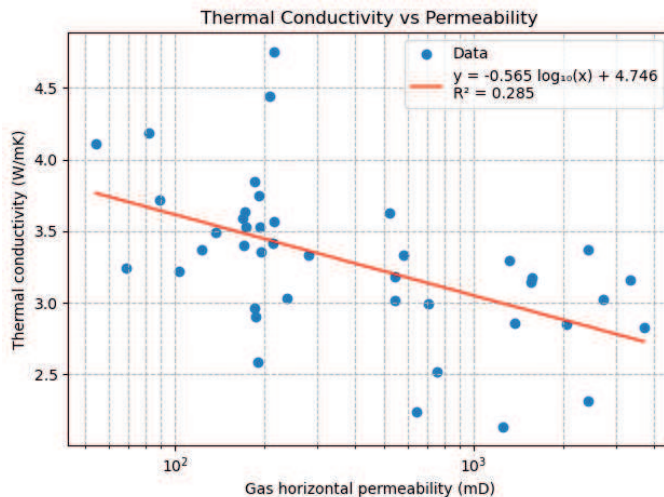


Figure 4.7 Relationship between thermal conductivity and gas horizontal permeability for all available samples. A logarithmic scale is applied to the permeability axis. The red line represents the linear regression fitted to the data in $\log_{10}(\text{permeability})$ space, with the corresponding regression equation and coefficient of determination (R^2) shown in the legend.

Figure 4.8 presents strong positive correlations are observed among acoustic velocities (V_p and V_s) and dynamic elastic moduli (Young's, shear, and bulk), with the Pearson correlation coefficient (R) values exceeding 0.95. These strong associations reflect their shared dependence on rock stiffness and density. Porosity exhibits consistently strong negative correlations with acoustic velocities ($R = -0.72$ to -0.81) and elastic moduli ($R = -0.76$ to -0.81), reinforcing the role of pore space in reducing wave propagation speed and mechanical strength. Thermal conductivity shows a moderate positive correlation with V_p ($R = 0.63$) and Young's modulus ($R = 0.66$), but a weaker negative correlation with porosity ($R = -0.57$), consistent with the trends observed in the cross-plots. Heat capacity shows a strong positive correlation with bulk density ($R = 0.65$), but a negative correlation with thermal diffusivity ($R = -0.72$), reflecting its inverse relationship with diffusivity when thermal conductivity is held constant. These correlations provide a comprehensive overview of how thermal and mechanical properties co-vary and underscore the dominant influence of porosity and lithology on the physical behaviour of the studied rocks.

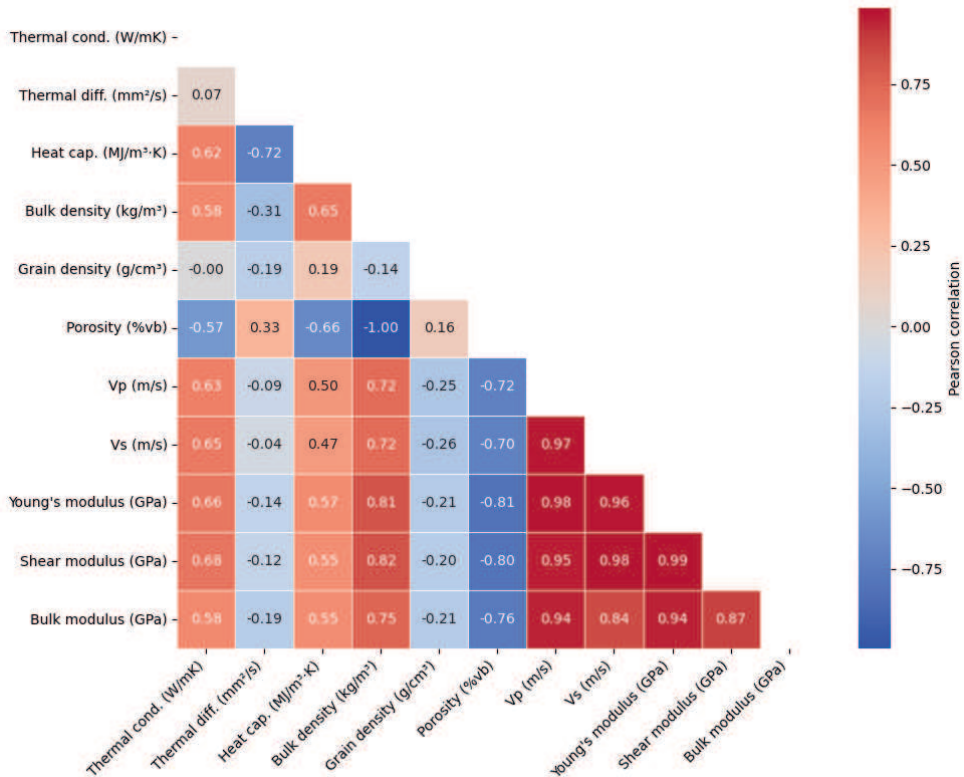


Figure 4.8 Pearson correlation matrix showing relationships between thermal, petrophysical, acoustic, and elastic properties measured on core plugs from the DEL-GT-01 well. Strong positive correlations are observed among dynamic elastic moduli (Young's, shear, and bulk moduli) and acoustic velocities

(V_p , V_s), as well as between bulk density and heat capacity. Porosity shows strong negative correlations with most elastic and velocity-related properties, and a moderate negative correlation with thermal conductivity. These trends reflect the physical interdependence between pore structure, density, and wave propagation in the rock samples.

4.4.1.1. Comparison of laboratory and log-derived mechanical properties

To evaluate the consistency between laboratory core measurements and well-log data, and to ensure their reliable integration in the subsequent analysis of static and dynamic elastic moduli, a systematic comparison of key petrophysical and elastic properties has been carried out. Figure 4.9 presents depth profiles of key petrophysical and elastic properties along the wellbore. In general, the log data exhibit smooth and continuous trends, capturing formation-scale heterogeneities with depth. The laboratory data, on the other hand, reflect localised plug-scale variability and appear more scattered due to the shorter sampling length compared to the averaging effect in downhole logs. The GR log reflects the expected stratigraphic variations and provides a useful context for interpreting lithological transitions. Higher GR values correlate with intervals of lower porosity and higher velocities, indicative of finer-grained, clay-rich layers. This observation is consistent with the ranges shown in Figure 4.5. For V_p and V_s , the log-derived profiles show a stacked layer of high and low velocities. These trends are broadly consistent with the laboratory data, particularly in the 2600–2700 m interval where core plugs are most densely sampled. However, the lab measurements tend to yield slightly lower velocities in some intervals, possibly due to the absence of reservoir pressure and saturation during measurement, especially at low GR zones, which are commonly associated with sands. The bulk density log slightly increases with depth and correlates well with the lab data in overlapping intervals. Minor deviations are observed in low GR (sandy) zones, with the log values occasionally higher than core measurements likely due to borehole environmental effects or partial mud invasion. This discrepancy may be attributed to environmental effects such as borehole mudcake buildup or partial mud invasion. In clean, porous sandstones, the invasion of higher-density drilling fluids into the pore space or the accumulation of a dense mudcake on the borehole wall can lead to elevated log responses. These effects may result in higher apparent densities in the logs compared to the true matrix density measured on clean samples and under controlled laboratory conditions. Porosity, derived from logs and core plugs, also correlated well, which is expected given the clear correlation shown in Figure 4.6 and the good correlation of bulk density. Both bulk density and porosity values at the low GR intervals differ slightly between laboratory and log measurements. This discrepancy is expected, as plug-scale heterogeneity and micro-fracturing can affect core porosity, while logs provide smoothed averages over larger volumes.

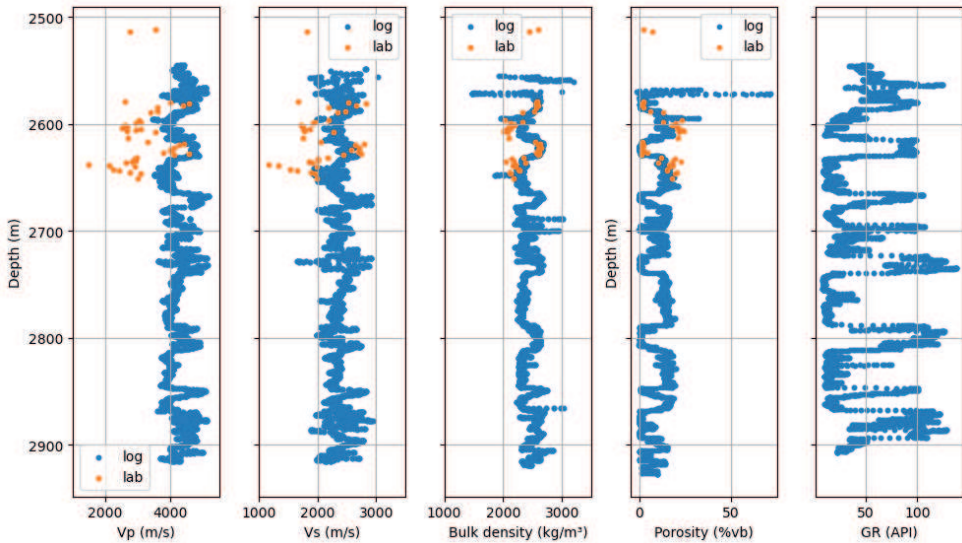


Figure 4.9 Depth profiles of compressional velocity (V_p), shear velocity (V_s), bulk density, and porosity from both well-log recordings (blue) and laboratory core measurements (orange), alongside the gamma-ray (GR) log for lithological context. The log data represent continuous measurements along the borehole, while the laboratory data correspond to discrete core plug measurements. Differences between the two sources reflect variations in measurement scale, resolution, and conditions—logs being recorded under in-situ reservoir pressure and fluid saturation, and lab data generally obtained on dry samples under ambient conditions.

Figure 4.10 supplements the visual inspection in Figure 4.9 by presenting cross-plots of lab and log derived acoustic velocities and bulk density. We extract the log values at the exact core plug depths using interpolation.

In Figure 4.10a, the V_p , shown in blue, exhibits a strong linear correlation with an R^2 value of 0.64, following the relationship $V_{p_lab} = 1.68 \times V_{p_log} - 3.932e3$. The scatter is moderate, indicating that while the general trend holds, local variability and measurement conditions contribute to some deviation. The V_s cluster shows a weaker correlation with an R^2 value of 0.39 and a best-fit line $V_{s_lab} = 2.66 \times V_{s_log} - 4.247e3$. The slope significantly greater than 1 and the large negative intercept indicate that log-derived V_s values tend to be overestimated compared to laboratory measurements for low values. The greater scatter could reflect either higher uncertainty in V_s log estimation or enhanced sensitivity to heterogeneities not captured by logs at the plug scale. Furthermore, since V_s only travels through the rock matrix, log-derived values tend to be higher than laboratory measurements because, in situ, the rock framework is subjected to confining pressure and saturation, which enhance grain contacts and reduce the effects of microcracks.

Figure 4.10b displays a strong linear correlation between bulk density measured in the lab and recorded in the wellbore, with an R^2 of 0.81, indicating a high degree of consistency. The best-fit regression equation is $\rho_{bulk_lab} = 1.5012 \times \rho_{bulk_log} - 1.366e3$. The slope greater than unity suggests that lab values are slightly and consistently smaller than log values, which may be attributed to differences in saturation state and borehole environmental effects, particularly the influence of in-situ confining stresses that increase the density of formations under reservoir conditions. A distinct separation is apparent in the data, broadly separating shale, and sandstone samples, likely reflecting their different compaction behaviours and mineralogical compositions.

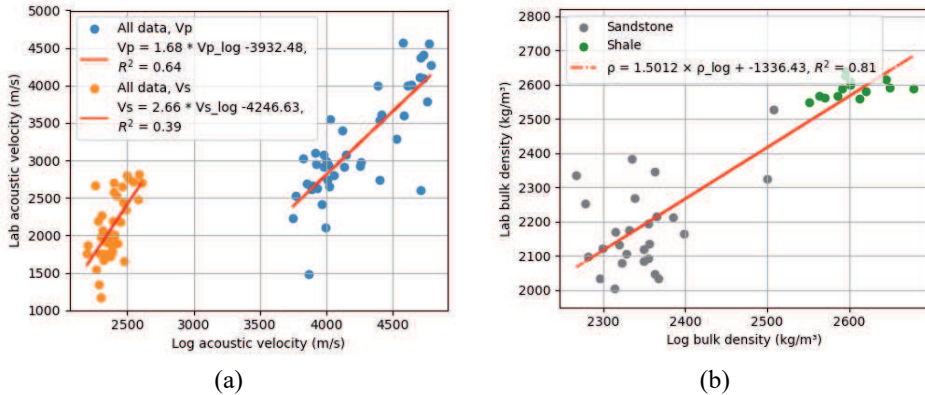


Figure 4.10 (a) lab versus log measurement of V_s (in green) and V_p (in blue), and (b) bulk density for all the 45 samples of the DEL-GT-01.

Overall, the obtained correlations, especially for V_p and bulk density, will be used in the following sections to integrate static and dynamic data for elastic properties prediction.

4.4.2. Static versus dynamic Young's modulus

Figure 4.11 presents the results of triaxial test (CCS) tests conducted on a subset of core plug samples at confining pressures of 0.5, 5, 10, 20, 30, and 40 MPa by (Postema, 2025). As expected, the modulus increases with confining pressure due to enhanced grain contact stiffness and fewer open cracks. To allow meaningful comparison with static measurements, both uniaxial and triaxial, with dynamic data, the triaxial modulus values were extrapolated to zero confining pressure.

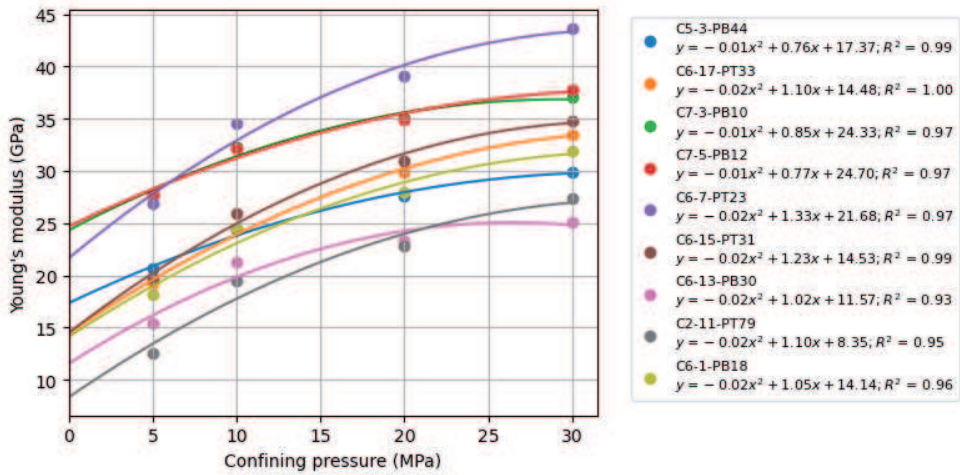


Figure 4.11 Static Young's modulus measured under triaxial conditions at confining pressures of 0.5, 5, 10, 20, 30, and 40 MPa for selected core plug samples. Polynomial trendlines were fitted to each dataset and used to extrapolate Young's modulus to zero confining pressure. These extrapolated values were used for comparison with uniaxial measurements and dynamic moduli obtained under ambient conditions. Sample naming follows the format: Core–Section–Position–Sample number (e.g., C1-2-PT-12 = Core 1, Section 2, Top part, Sample 12)

4.4.2.1. Lab data

Figure 4.12a reveals distinct mechanical behaviours between shale and sandstone samples. Shales, with porosities below 5%, consistently exhibit high dynamic Young's modulus values compared to sandstones. The clustering of both static and dynamic values in this group indicates significant difference and high sensitivity to the measurement method. This means that Equation 4.1 overestimated the dynamic Young's modulus. Sandstone samples which spread wider across porosity range, have dynamic and static Young's moduli in similar ranges indicating less sensitivity to measurement technique. All datasets follow a broadly decreasing trend of dynamic stiffness with increasing porosity, consistent with effective medium behaviour. In contrast, static stiffness displays no consistent trend and exhibits significant scatter. These results emphasise the need for calibration when using dynamic moduli in geomechanical assessments, particularly for shales and clay-rich zones.

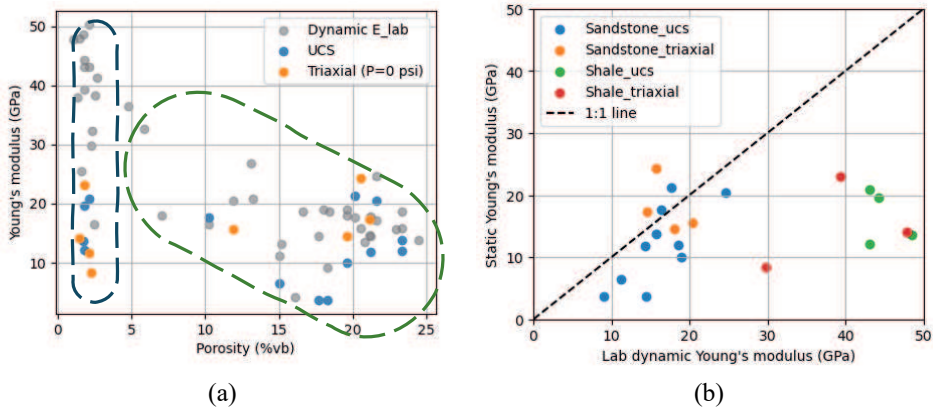
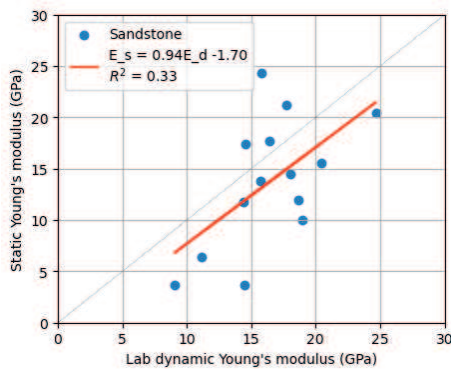


Figure 4.12 (a) Cross-plot of Young's modulus versus porosity, showing dynamic modulus (grey), static modulus from UCS tests (blue), and static modulus from triaxial tests extrapolated to zero confining pressure (orange). Two compositional groups are highlighted: a low-porosity, high-modulus shale cluster, and a broader sandstone cluster with moderate-to-high porosity and a wide range of stiffness values. (b) Comparison of dynamic Young's modulus (GPa), calculated from ultrasonic measurements, and static Young's modulus (GPa), derived from UCS and triaxial tests. Data are grouped by lithology and test type: sandstone UCS (blue), sandstone triaxial (orange), shale UCS (green), and shale triaxial (red). The dashed line represents a 1:1 reference, where dynamic and static moduli would be equal.

Figure 4.12b shows that across all test types and lithologies, almost all the static values are lower than their dynamic equivalents, with most data points falling below the 1:1 line. In sandstones, dynamic moduli range primarily between 8 and 25 GPa, while static moduli from UCS and triaxial tests cluster between 5 and 22 GPa. A general deviation from the 1:1 line is observed, indicating an overestimation of stiffness by dynamic measurements. Shale samples occupy the higher end of the dynamic modulus range (35–48 GPa) that compared to their corresponding static values (10-25GPa). Filtering the data based on rock type and only keeping sandstone results in Figure 4.12a. It shows a clear positive trend between the static and dynamic Young's modulus, although the scatter indicates moderate variability. Lower values of Young's modulus are underestimated by the dynamic Young's modulus, while higher values seem to be reasonably estimated. While the correlation is not very strong, reflected by the $R^2 = 0.33$, it suggests that a proportional relationship exists between dynamic and static moduli for sandstone, with dynamic values consistently overestimating stiffness. The slope close to unity implies that the dynamic and static values scale similarly, though the negative intercept reflects an offset.



(a)

Figure 4.13 (a) Comparison between static and dynamic Young's modulus for white sandstone samples. The red line represents the linear regression fit ($E_s = 0.94E_d - 1.70$) with $R^2 = 0.33$ and $MSE = 25.12\text{GPa}$. The grey dashed line indicates the 1:1 relationship. (b) Depth profile of Young's modulus for sandstone samples from the DEL-GT-01 well. Blue markers represent dynamic modulus values ($E_{d,lab}$), orange markers show calculated static values ($E_{s,lab,calculated}$) using the regression $E_s = 0.94 \cdot E_d - 1.70$, and black stars indicate measured static values from UCS and CCS tests. The plot demonstrates consistency between predicted and measured static moduli across the sampled interval.



(b)

The distinction between lithologies is evident in both the magnitude and variability of the results. Sandstone data show more coherent groupings (Figure 4.13 a, $R^2 = 0.33$), whereas shale data appear more dispersed (Figure A 3 a, $R^2 = 0.08$), particularly for triaxial measurements. These patterns reinforce the need for lithology-specific treatment in the conversion from dynamic to static modulus.

The regression line in Figure 4.13a provides a basis for converting dynamic to static Young's modulus in cases where only acoustic data are available, acknowledging that some uncertainty remains due to lithological heterogeneity, test conditions, and a limited number of tested samples. Figure 4.13b displays the depth distribution of dynamic Young's modulus ($E_{d,lab}$) and the corresponding static Young's modulus ($E_{s,lab,calculated}$), calculated using the linear regression $E_s = 0.94 \times E_{d,lab} - 1.7$ derived in the previous step. Black stars represent the measured static moduli from either UCS or triaxial tests at zero confining pressure to directly compare values at each depth. The calculated static Young's modulus follows the depth trend

of the dynamic values but consistently show lower magnitudes, in agreement with the expected offset between dynamic and static stiffness. In most cases, the predicted values (orange) align closely with measured static moduli (black), supporting the applicability of the derived regression for sandstone plugs across the sampled interval. Although some scatter remains, especially at shallower depths, the overall agreement confirms the validity of this approach for estimating static modulus from ultrasonic measurements in the absence of direct mechanical tests.

4.4.3. Dynamic elastic moduli from log and laboratory data

Dynamic elastic moduli were calculated using V_p , V_s , and bulk density from both well-log recordings and laboratory measurements using Equation 4.1 to Equation 4.4. The log-derived dynamic Young's modulus ranges from approximately 20 GPa to 50 GPa. Laboratory-measured dynamic elastic moduli for rocks within the overlapping depth range mostly lie between 10 GPa and 50 GPa, exhibiting consistent trends with the log data (Figure 4.14a). The shear modulus from well logs varies mostly between 8 GPa and 25 GPa. Laboratory values, observed only in the shallower interval, also fall within this range, with only two data points with shear modulus lower than 5 GPa (Figure 4.14b). Log-derived bulk modulus values range from approximately 15 GPa to 40 GPa. While most laboratory values fall between 5 GPa and 30 GPa. The laboratory and log-derived show similar trends with the laboratory-derived values general being below those determined from logs (Figure 4.14c).

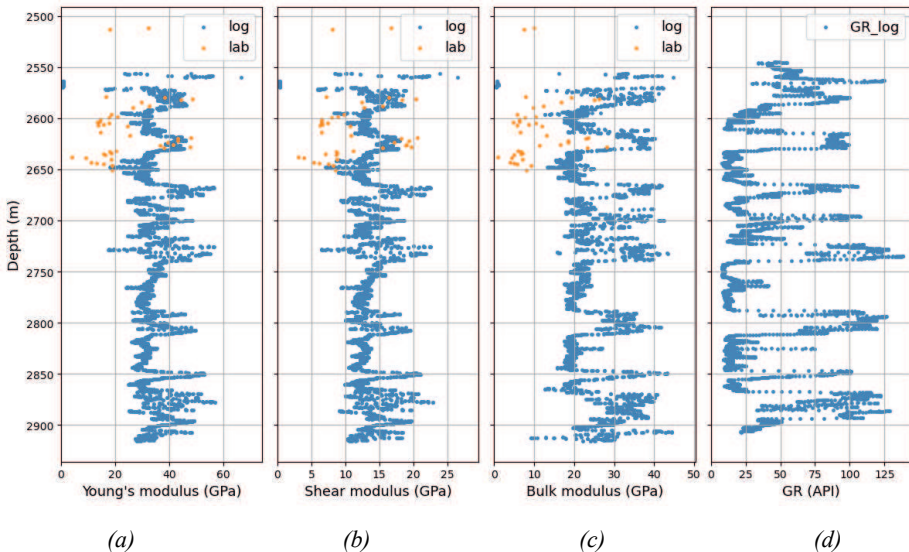


Figure 4.14 Depth profiles comparing elastic moduli derived from well logs (blue) and laboratory measurements (orange) for (a) Young's modulus (dynamic), (b) shear modulus, and (c) bulk modulus, next to (d) gamma ray values. Laboratory measurements are concentrated in the 2550–2670 m interval, while log-derived values span the full depth range from 2500 to 2950 m.

Coupled mechanical and thermo-physical characterisation of the lower Cretaceous Delft Sandstone Member for geothermal applications

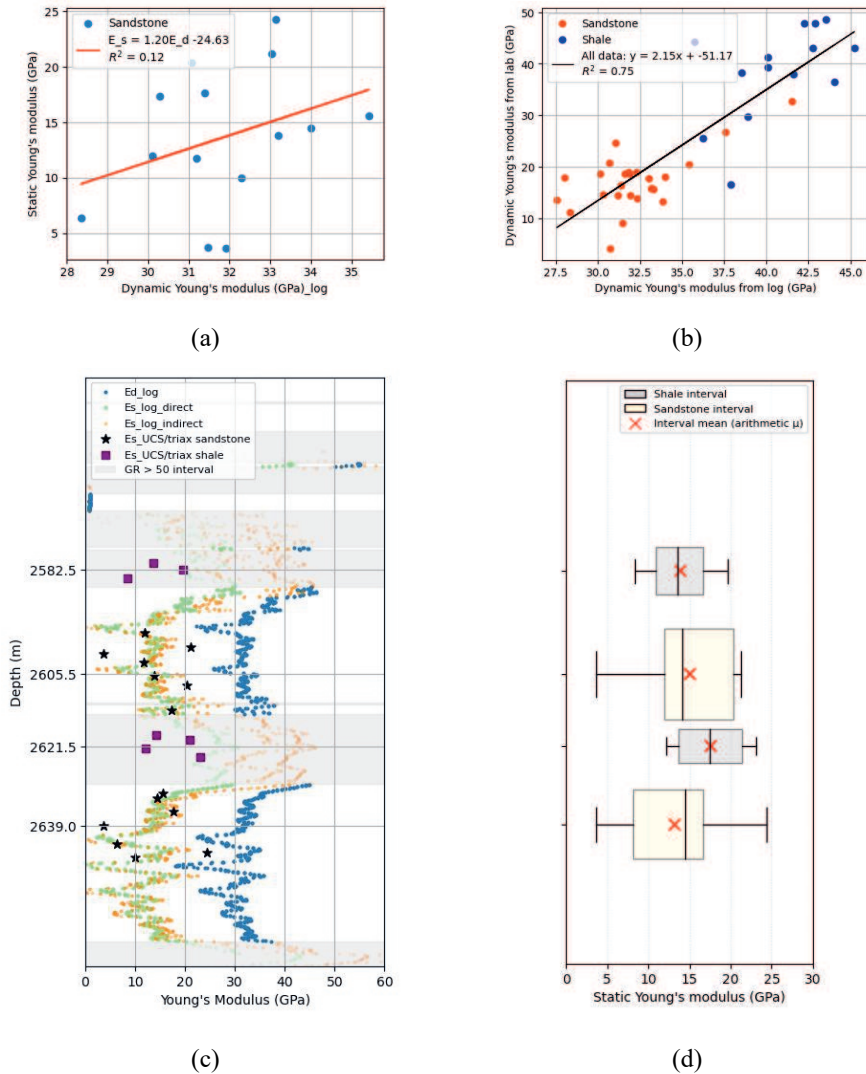


Figure 4.15 (a) Cross-plot of static Young's modulus estimated from UCS/triaxial tests versus dynamic Young's modulus derived from well logs. The red line represents the best-fit linear regression used to convert log-based dynamic moduli to estimated static values, (b) Dynamic Young's modulus from the lab data versus dynamic Young's modulus from the log data, (c) dynamic Young's modulus from the sonic log (blue) with two log-based static estimates (green = direct, orange = indirect) and lab-measured static values for sandstone (black stars) and shale (purple squares), and (d) box-plots of all lab points inside four depth layers; yellow boxes mark sandstone and grey boxes shale, black lines show the median, whiskers the full range, and red \times the layer mean.

4.4.3.1. Integrating lab and log data (direct approach)

In the direct approach, the goal is to convert dynamic Young's modulus derived from well-log data to static values by deriving a regression line between them. By using the interpolating log dynamic Young's modulus at the plug's depth, we made a direct comparison between those values and measured static Young's modulus at corresponding depths. A regression is then established between these two datasets, which then was applied to the entire dynamic Young's modulus log, producing a continuous static Young's modulus log. It is important to note, however, that the fit between the measured static moduli and the dynamic values was relatively poor, as indicated by the low R^2 value (Figure 4.15a). This reflects the inherent complexity and scatter in the relationship, likely due to variations in rock fabric, microstructure, and the limited number of samples.

The predicted static Young's modulus curve, derived from the direct conversion approach, tracks the dynamic trend but at consistently lower magnitudes, as expected due to the strain-dependent nature of static measurements. This offset is approximately constant through the entire depth range suggesting that the derived regression captures lithological variation. However, it does not adjust for absolute stiffness. In other words, it treats clay-rich and sandy intervals the same while Figure 4.15c shows that this is not a correct assumption. The measured static values (black stars) align well with the green curve in several depth intervals, especially between 2630 and 2650 m. However, localised deviations are observed, for example at ~2645 m, where a sudden increase in GR indicates higher natural radioactivity and therefore clay content. Since the workflow is tailored for sandy layers, elevated clay content may reduce its accuracy in such intervals.

4.4.3.2. Integrating lab and log data (indirect approach)

In the indirect method, there is an intermediate step to improve the consistency between dynamic moduli from well logs and laboratory conditions before converting to static values. First the log dynamic Young's modulus at the plug's depth and the lab dynamic Young's modulus were correlated (see Figure 4.15b). This regression provides a calibration function to account for the effects of frequency, resolution, and depth mismatch between logging tools and laboratory conditions. Once the dynamic log values have been adjusted to lab conditions, they are converted to static modulus using the regression ($E_s = 0.94 \times E_{d,lab} - 1.7$) developed earlier from lab data (Section 4.4.2.1), which results in the correlation $E_s = 2.02 \times E_{d,log} - 46.4$. As shown in Figure 4.15c, the static Young's modulus estimated through the indirect method (orange) tracks the overall depth trend of the dynamic log (blue) but in a good agreement with lab-measured values (black stars). The dynamic modulus spans nearly twice the range of the static values, and the indirect method effectively corrects this through both a scaling and an offset.

Combining both steps allows the original log-derived modulus to be indirectly transformed into a static Young's modulus log that reflects both the dynamic-to-static relationship and the calibration between logging and lab environments.

The indirect method (Figure 4.15c) demonstrates a stronger overall match to the black star markers, which represent static modulus values measured from UCS and triaxial tests. In fact, the indirect curve tracks both the magnitude and variability of the laboratory data with higher consistency. This suggests that correcting the log-derived dynamic modulus to laboratory conditions before applying the dynamic-to-static conversion improves accuracy, especially in intervals of more complex lithology or variation. This improvement likely results from compensating for in-situ effects, such as confining stress and saturation, which cause dynamic moduli to overestimate stiffness compared to static lab measurements. By adjusting for these effects, the indirect method brings the values closer to true static behaviour. The direct method (Figure 4.15c) follows the overall trend of the dynamic log and offers reasonable estimates, but tends to diverge more from measured values, both in the upper and lower portions of the profile. The indirect method occasionally overestimates modulus in softer, clay-rich intervals and underestimates it in stiffer, sandy zones. A more detailed comparison in clay-rich layers was not possible due to the limited availability of static measurements in those intervals. Nevertheless, a preliminary attempt to estimate static Young's modulus for shale using petrophysical logs is presented in Appendix 1, highlighting the challenges and limitations of applying the same approach to shales. Despite this, a comparison between the directly measured static Young's modulus and the indirectly derived continuous log shows that the values are reasonably consistent, suggesting that, although the prediction could be improved by including more samples when generating the correlation, the current relationship captures the overall trend and can still be used for approximate estimation.

4.5. Discussion

4.5.1. Cross property analysis

The broad ranges presented in Figure 4.5 illustrate and emphasise that lithology exerts a primary control on the thermo-physical and petrophysical behaviour of the Delft Sandstone and associated shales. The contrast between porous, permeable sandstones and dense, low-porosity shales explains the systematic differences in thermal and elastic properties, and highlights how lithological heterogeneity governs the coupled flow, heat transport, and mechanical response of the formation. The permeability difference between sandstone and shale aligns the well-established control of porosity and pore structure on fluid flow, as described by (Nelson, 1994; Abdelaali Rahmouni et al., 2014).

Although sandstone forming minerals are more thermally conductive than clay minerals (shale) (Clauser & Huenges, 1995a), the higher thermal conductivity and volumetric heat capacity observed in shale is generally due to higher density. Other rock features, including the type of clay present, the distribution of clay within the pore network, lamination orientation,

heterogeneity, and, most importantly, porosity, exert strong control on thermal and acoustic properties (Chapter 2 and 3).

Turning to acoustic velocities, these are controlled by porosity and mineralogy. The shale samples have very low porosity (<5%), and porosity strongly controls velocity. Although shale shows higher velocities (Hamada & Joseph, 2020; Han, 1986), clay content also reduces velocity because clays are softer, absorb more water, and weaken the grain framework. The combined effect of porosity and clay, including clay type, determines the overall acoustic properties of the rock.

The cross-property correlations observed in Figure 4.8 is aligned with the well-established physical relationships between porosity, density, acoustic velocity, and thermal conductivity in sedimentary rocks. The inverse correlation between porosity and bulk density is mechanically clear; a pore volume increases, it directly lowers the rock's mass per unit volume (Chang et al., 2006).

The negative correlation between thermal conductivity and porosity also aligns with prior studies showing that increasing void space disrupts grain-to-grain heat conduction paths, reducing effective conductivity (Clauser & Huenges, 1995a; Sumirat et al., 2006) (Chapter 2 and 3 of this thesis). This correlation becomes stronger if we only look at sandstone samples. Since the shale samples have very variable thermal conductivity value over a small porosity range, the correlation between thermal conductivity and porosity is not as statically strong as for sandstone. A plot of thermal conductivity versus permeability shows a moderate negative trend (Figure 4.7).

A stronger correlation between V_p and porosity is observed when considering all samples together (Figure 4.6b). This suggests that V_p may also correlate with other porosity-dependent properties such as thermal conductivity and permeability. Other factor, beside porosity, that can impact V_p is mineralogy. Minerals can play a significant role in controlling acoustic response since they convey acoustic waves. Our results show that clay-rich samples are higher V_p than the sandstones. While He et al. (2021) investigated shaly sandstones with porosities below 0.30 and clay fractions below 0.35. They showed that by increasing clay fraction reduces both V_p and V_s . They also shows that between porosity and clay fraction, the impact of porosity is much more dominant. Bailly et al. (2019) investigated the impact of sedimentological features (primary microstructures) and early diagenetic processes on the physical and seismic properties of lacustrine and palustrine carbonates from the Upper Miocene Hora Formation on Samos Island, Greece. By analysing porosity, V_p , and density in relation to sedimentary facies and diagenetic modifications, the study reveals that primary textures alone cannot explain variations in V_p . Two key diagenetic processes, neomorphism (which reduces porosity and increases V_p) and dissolution (which increases porosity and decreases V_p), are critical in shaping seismic reflectors. Eberli et al. (2003) show that in carbonate rocks, elastic properties like V_p are mainly controlled by porosity and especially pore type, not just total porosity. Early

diagenetic processes, such as cementation and dissolution, significantly alter pore structure and thus velocity. Rocks with mouldic or intraframe porosity can have very high velocities even at high porosity, while those with interparticle or microporosity show much lower velocities. These complex relationships cause large velocity variations at the same porosity, making standard porosity-velocity equations unreliable for seismic inversion in carbonates. These studies demonstrate that rock properties influence both V_p and V_s in interconnected ways. To accurately explain observed trends, these properties must be considered collectively rather than in isolation.

The correlation between thermal conductivity and V_p for the entire dataset and for the sandstone group is very similar (Figure 4.6c). The shale samples mainly clustered at the higher V_p and higher thermal conductivity zone show although clay minerals are known for their low capability for transferring heat and acoustic velocity (Xie et al., 2023; Xie et al., 2025), their very low porosity has created a very continuous matrix with minimum disruptions for heat and sound waves to travel through them.

The cross plot between bulk density and porosity simply shows the reason behind the observed separation between the sandstone and shale samples in the previous figures (Figure 4.6d). The shale samples are at the higher end of bulk density range, and at the lowest range of porosity. This suggests when studying this present group of shale samples, we were facing a very compacted medium with high grain density.

The comparison between core and log data in Figure 4.9 shows general consistency in property trends. There are offsets for some properties and at some intervals that reflect fundamental differences in measurement scale and conditions. The maximum offset is for the V_p , and that is because the samples tested in the lab were dry. Saturation plays an important role because compressional wave travels through both pores and matrix, and in this case, where the pores are filled with air, they attenuate the compressional wave (Castagna et al., 1985). In addition to the saturation difference, the pressure and temperature of the subsurface are significantly higher than in the lab. Higher pressure impact the rock structure in a way that makes the rock bed a more continuous medium (Kolah-Kaj et al., 2021), which boosts the compressional and shear wave transmission (Fjær & Holt, 1994). This difference between conditions is also the reason behind the slight offset for the V_s measurements. Since shear waves only travel through the rock matrix, the saturation condition does not play an important role, and only the higher pressure in the subsurface lead to higher V_s values in the log. However, Elevated temperatures tend to decrease V_s and V_p . Higher temperatures tend to soften the mineral structures within rocks, decreasing their elastic moduli and thus lowering seismic velocities (King, 1983). In contrast, lab measurements on dry cores at ambient pressure are more susceptible to scattering due to local heterogeneities, differences in scale, and testing direction with respect to sample lamination.

The offset between the measured V_s and V_p in the lab and those recorded by log is higher in low-GR intervals. In other words, the low-GR intervals, which represent sandstones (i.e., clay-poor sand), were more vulnerable to the measurement conditions than shaly (i.e., clay-rich) intervals. To explain this, porosity and bulk density data must be included in this analysis too. The shaly intervals have a very low porosity value. This, as explained for Figure 4.6, plays an important role in V_p and V_s value, and porosity has a dominant effect on the V_p and V_s values rather than mineralogy. The observed offset in bulk density is very small, and when comparing the sandy and shaly intervals, the sandy intervals measured in the lab show smaller values. That is because of the saturation condition, and the values in the lab do not account for the fluid content, unlike the log recordings. However, for the shaly intervals, since porosity is very small, this difference is negligible. Porosity is also in line with known artefacts related to mud invasion, cementation effects, or the different vertical resolution of core plugs versus logging tools. Another factor could be stress relaxation, pores and cracks may have opened as the overburden pressure was released after coring.

The compatibility between the lab and log data is also confirmed by the regression analysis in Figure 4.10a. The scatter in the data points arises from differences in measurement conditions, resolution, and associated uncertainties. The higher R^2 for V_p compared to V_s reflects the more stable response of compressional waves across both measurement environments. In contrast, the lower determination coefficient for V_s suggests greater variability, likely amplified by the difficulty of accurately picking the shear wave arrival time in the laboratory, particularly in layered or heterogeneous samples. This difference in behaviours aligns with findings by King (1983) and Prasad and Manghnani (1997), who studied the effects of pressure and temperature on V_p and V_s across various rock types, including metamorphic, igneous, and sandstones. They reported that pressure tends to have a more pronounced effect on V_p than on V_s , primarily because it increases elastic stiffness through the closure of pores and microcracks. Temperature affects both velocities but typically reduces them by weakening the rock frame. In other words, V_s is more sensitive to temperature, while V_p is strongly influenced by pressure. Both studies emphasise the importance of considering these factors simultaneously when interpreting seismic velocities in geological applications. This explains the larger gap between lab and log measurements of V_p observed in Figure 4.9.

The density comparison (Figure 4.10b) shows a strong and consistent relationship ($R^2 = 0.81$). Although the slope is greater than one, the negative intercept results in lower bulk density values in the lab compared to those from logs. This is expected, as the lab measurements were performed on dry samples and therefore do not account for the mass contribution of pore fluids. Despite small-scale variability and differences in saturation, the close agreement between the datasets supports the integration of core and log data for quantitative analysis, provided that the effects of measurement scale and fluid content are properly considered. This alignment between lab and log data, once corrected for measurement conditions, allows for more confident use of both datasets in combination. It supports the use of core data to calibrate log-based interpretations and, where core coverage is limited, enables interpolation or estimation

of properties across unsampled intervals. It also provides a basis for evaluating the reliability of log responses in different lithologies, particularly when direct measurements are not available.

Building on the previous comparison of core and log data, the dynamic elastic moduli derived from both datasets (Figure 4.14) demonstrate consistent trends as well. The absolute values from laboratory measurements are lower than those from logs, which is consistent with the earlier explanation regarding the impact of measurement conditions on acoustic velocities and bulk density. Among the moduli, shear modulus shows the smallest separation between lab and log values. This is because shear modulus depends on bulk density and V_s , and among the two velocities, V_s is less affected by pressure conditions compared to V_p . As a result, saturation and confining pressure have a limited effect on shear modulus differences between the lab and log datasets.

4.5.2. Correlating static and dynamic Young's modulus

While dynamic elastic moduli derived from acoustic velocities and bulk density are useful for comparing the mechanical behaviour of different rock types, they often overestimate in-situ stiffness when compared to static moduli obtained from stress–strain measurements. This difference is because Given the lithological variation across the depth interval, as indicated by the GR log in Figure 4.9 and Figure 4.14, a single dynamic-to-static correlation (section 4.3.1.5) must be evaluated carefully because applying a general empirical relationship without considering rock type could introduce substantial errors.

Figure 4.12 show that dynamic moduli decrease with increasing porosity, primarily because the modulus calculation (Equation 2) is directly dependent on both acoustic velocities and bulk density, both of which reduce as porosity increases. Static Young's modulus, obtained from UCS and triaxial tests extrapolated to zero confining pressure, remains more constrained, with values generally not exceeding 25 GPa regardless of porosity. This difference becomes most vivid in the clay-rich group (low-porosity shales), where dynamic modulus values are often more than twice as high as static values. This large gap reflects the high sensitivity of dynamic measurements to small-strain, high-frequency responses that do not capture time-dependent and irreversible deformations, which are common in fine-grained, low-strength rocks like shales (Fjær, 2009; Zimmer et al., 2007). The similar range of static and dynamic Young's modulus for the sandstone group is because the sandstone samples exhibit a stiffer, grain-supported framework with reduced microcrack compliance, and are less affected by inelastic deformation mechanisms during static loading. As a result, the pressure dependency and strain-rate sensitivity in these rocks are lower, leading to better agreement between dynamic and static stiffness. Figure 4.13a further supports this interpretation, where most sandstone points cluster near the 1:1 reference line, indicating comparable static and dynamic responses. Shale samples, however, consistently plot well below the line, confirming that their static stiffness is

significantly lower due to enhanced irreversible deformation, microcrack opening, and time-dependent effects under low-frequency loading (H. Bhuiyan & M. Holt, 2012).

One reason could be that shales have higher bulk density, and V_p , and V_s due to their low porosity range, therefore, in Equation 4.1, it leads to a higher number compared to the sandstone. From a structural perspective, Shales often contain microcracks and weak planes that can close or slip under stress.

We conclude from our observations in this present study and literature that lumping sandstone and shale when correlating dynamic and elastic Young's modulus introduce systematic errors and the results will not be applicable as these rock types behave differently. On the other hand, since the number of shale samples and their distribution over the porosity range is not sufficient to cover a range of porosity therefore be analysed separately, we exclude them and proceeded with only the sandstone group. Figure 4.13a shows a correlation between the dynamic and static Young's modulus of sandstone samples that can be used for other sandstone samples which have not been used tested mechanically with UCS or triaxial. We predicted the static Young's modulus values for these samples and the results are displayed in Figure 4.13b. The correlation between the static and dynamic Young's modulus derived in this present study ($E_s = 0.94 \times E_d - 1.7$) is close to Equation $E_s = 0.867 \times E_d - 2.08$ belong to the study of Brotons et al. (2014) where they measured the dynamic Young's modulus (E_d) ultrasonic tests, while the static modulus (E_s) was obtained from uniaxial compression tests on five of the samples. The high correlation ($R^2 = 0.961$) suggests that this formula is reliable for estimating static modulus in soft, porous calcarenites.

Another close correlation to ours is $E_s = 0.932 \times E_d - 3.42$ also derived by Brotons et al. (2016). They revised and reanalysed the previous equation by adding 33 core samples results to the previously examines 24 additional samples. This dataset included rocks with dynamic modulus values ranging from 5 to 80 GPa. Based on the measured Young's moduli on dry samples at ambient conditions and fitting both linear and nonlinear models to their data, they concluded that the linear regression equation ($E_s = 0.932 \times E_d - 3.42$) produced a very strong correlation with $R^2 = 0.99$, showing excellent agreement across rock types.

The close match between our correlation and those from Brotons et al. (2014); (2016) confirms the reliability of using dynamic measurements to estimate static Young's modulus in moderately stiff, non-shale rocks. This consistency across datasets suggests that, for such rocks, a simple linear conversion is valid and can be applied in geomechanical models when only dynamic data are available. Extending this approach to the wellbore scale by incorporating dynamic properties from sonic and bulk density logs led to the estimation of static modulus beyond core data (Figure 4.15c). Figure 4.15c also highlights that using dynamic modulus directly can significantly overestimate the true stiffness of the rock, especially in the sandstone intervals. This may lead to misleading interpretations, suggesting that the formation is stronger and stiffer than it is, which can result in unsafe geomechanical designs. Between the direct and

indirect methods, the differences are generally small in the lower GR (sandstone-rich) intervals. However, the indirect method provides a wider range of predicted values that better encompasses the laboratory measurements. Another key advantage of the indirect method is its ability to account for the difference between lab and subsurface conditions by calibrating log data against experimental results before applying the conversion. This correction improves the reliability of static modulus estimates under reservoir conditions.

It is important to note that this entire workflow was developed and validated for sandstone samples. If shale samples were included without adjustment, applying the same equation (Equation 4.1), the mismatch between measured and predicted static moduli would likely be even greater. In such cases, it is more reasonable to use an average static modulus value for the low GR intervals (clay-poor sandstones) than to apply the derived equation to shale, where the mechanical behaviour is significantly different.

4.5.2.1. Comparison with literature

To further validate the methodology and assess its broader applicability, the dynamic-to-static Young's modulus relationship derived in this study was compared with published correlations (Table 4.1). A recent and comprehensive list compiled by Shen et al. (2024) was used as the reference. To ensure relevance and minimise lithological bias, only linear correlations developed for sedimentary rocks, sandstones, or broadly applicable to all rock types were selected. This filtering ensures consistency with the geological context of the DEL-GT-01 samples and enhances the credibility of the comparison.

The comparison of the correlation derived in this work with those from McCann and Entwisle (1992) and Eissa and Kazi (1988) shows larger differences. These correlations were developed for a wide range of rock types, including mixed lithologies and rocks with greater heterogeneity or clay content, which are not representative of the Delft sandstone. This impacts their applicability to formations with more uniform properties, such as those in this study. Overall, the better match with correlations for sedimentary rocks highlights the importance of considering lithology, porosity, and pore structure when selecting or developing relationships between static and dynamic modulus.

To evaluate how well the dynamic-to-static Young's modulus relationship derived in this study compares with those reported in the literature, seven published linear correlations were selected and plotted alongside the regression from this work (Figure 4.16). For each, the mean absolute error (MAE) was computed over a range of E_d values (0–80 GPa) relative to the current study's trend. Equation 5 ($E_s = 0.932 \times E_d - 3.42$) and Equation 4 ($E_s = 0.867 \times E_d - 2.08$) yielded the lowest MAEs (2.04 and 4.76, respectively), indicating strong agreement. In contrast, some equations such as Equation 1 ($E_s = 0.64 \times E_d - 0.32$) deviate significantly, with an MAE exceeding 16 GPa, suggesting limited applicability to the current dataset.

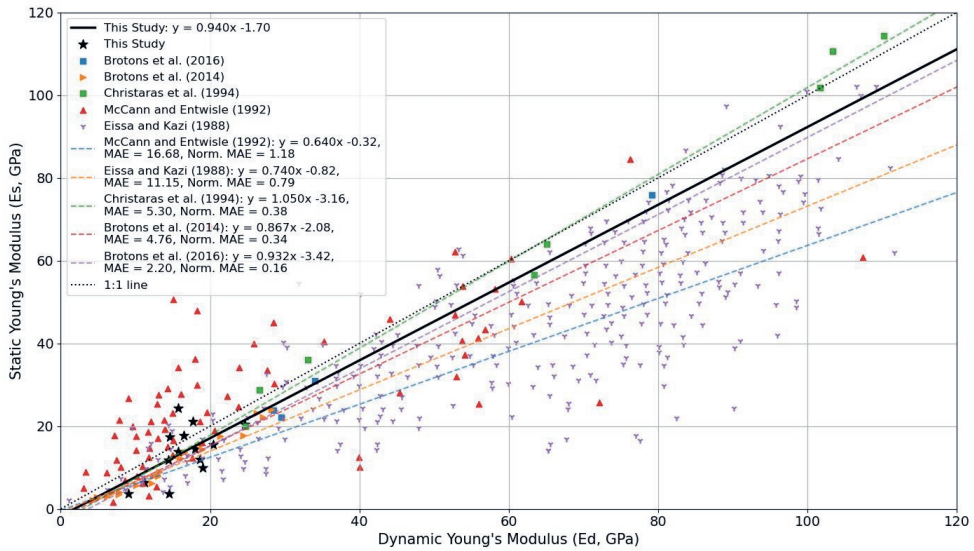


Figure 4.16 Comparison of the dynamic-to-static Young's modulus relationship derived in this study (solid black line) with seven published empirical equations (dashed lines), alongside the underlying data. MAE and normalised MAE values were computed by comparing each published regression line to the static Young's modulus values from this study. Disclaimer1: The literature data points were digitised and may differ slightly from the original values in the papers. Disclaimer2: The literature correlations are plotted exactly as reported in their respective papers and were not refitted to the digitised data points.

Figure 4.16 also highlights the considerable scatter present in some datasets, particularly those from weak mudrocks or mixed lithologies (e.g., Eissa and Kazi (1988); McCann and Entwisle (1992)). This underscores that dynamic-to-static relationships are highly formation-dependent, and the predictive accuracy can vary significantly depending on rock type, measurement scale, and physical conditions. Our dataset, focused on relatively homogeneous sandstone samples under consistent testing conditions, shows tighter clustering and thus benefits from a better-defined correlation. These results emphasise the importance of calibration using formation-specific data when applying dynamic-to-static conversions. Our dataset covers a narrower range than the reviewed studies. Although not an initial aim, this outcome underlines the value of expanding measurements to better capture variability across lithologies.

4.6. Conclusion

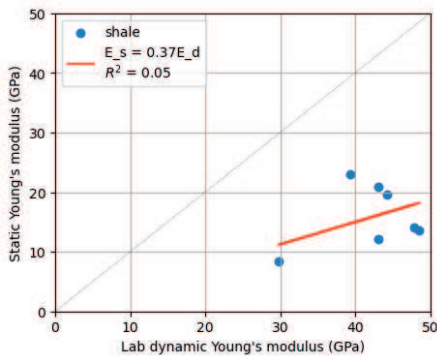
This study investigated the mechanical and thermo-physical properties of the Delft Sandstone Member and associated shales from the DEL-GT-01 well. Laboratory measurements revealed clear differences between sandstones and shales in terms of porosity, permeability, density, thermal properties, and elastic moduli. Dynamic Young's modulus derived from well logs consistently overestimated rock stiffness compared to laboratory static measurements, with the largest overestimation observed in clay-rich, low-porosity shales. A two-step calibration

approach was developed to improve the estimation of static Young's modulus from log data. This method first adjusted log-derived dynamic modulus to match laboratory dynamic conditions and then applied a dynamic-to-static conversion based on laboratory data. The approach reproduced measured static moduli within experimental scatter and captured depth-dependent trends in stiffness. In contrast, direct conversion from log dynamic modulus to static modulus showed poor correlation and higher prediction errors, especially where lithology changed. The resulting static modulus profile offers a reliable input for geomechanical models supporting wellbore stability and reservoir integrity in geothermal development.

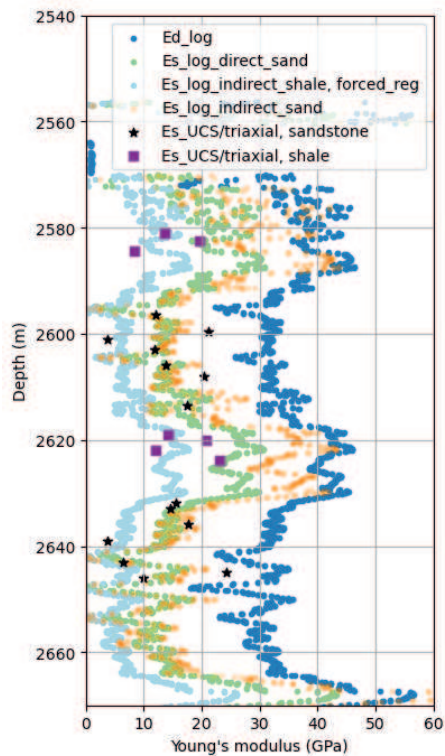
4.7. Appendix 1

4.7.1. Static Young's modulus for shale, indirect method

Despite the limited number of shale samples available for laboratory testing, an attempt was made to predict the static Young's modulus of shales using downhole petrophysical logs. Figure A2a shows the cross-plot of static versus dynamic Young's modulus from lab measurements on shale samples. The data exhibit a weak positive correlation, with an R^2 of only 0.08, indicating that dynamic moduli poorly capture the static behaviour in shale. This result highlights the challenge of applying a dynamic-to-static correlation in shales, likely due to their anisotropy, clay content, and sensitivity to saturation and stress conditions.



(a)



(b)

Figure A 3 (a) Static versus dynamic Young's modulus of shale samples measured on dry core plugs in the laboratory. The weak correlation ($R^2 = 0.05$) of the forced regression line (intercept=0) highlights the challenge of predicting static modulus directly from dynamic values in shales. (b) Depth profile of dynamic and static Young's modulus across the reservoir. The static modulus for shale was estimated using an indirect method based on log data (light blue), while lab-measured values from triaxial tests are shown in purple. Despite the limited number of shale samples, the predicted static modulus values capture the general trend and variability of shale stiffness across the interval.

Nonetheless, as shown in Figure A 3, the indirect estimation method was applied to shale intervals using available dynamic log data. While the fit is not as robust as for sandstones, the predicted static Young's moduli (light blue markers) provide a reasonable depth trend that complements the sparse lab measurements (purple squares). The predicted values are generally within the expected range of static modulus for shales and reflect the overall mechanical heterogeneity of the reservoir.

4.7.2. Dynamic shear and bulk moduli, and Poisson's ratio

Using Equation 4.3 and Equation 4.4, the dynamic shear and bulk moduli based on downhole petrophysical logs were calculated. Figure A 4 shows a strong linear correlation in both panels, with $R^2 = 0.75$ for the full dataset and $R^2 = 0.77$ for sandstones (GR < 50 API). The slope of the regression increases from 0.93 (full dataset) to 1.11 (sandstones), suggesting a slightly stronger dependency in cleaner lithologies. Despite this shift, the spread around the guide regression line highlights the effect of different conditions and resolutions between logs and lab setups.

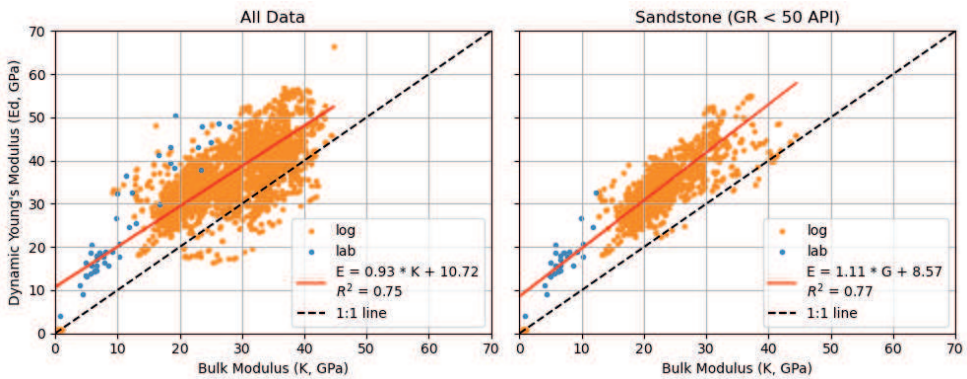


Figure A 4 Dynamic Young's modulus versus bulk modulus calculated from lab (blue) and log (orange) data. Left: Full dataset. Right: Sandstone-only data (GR < 50 API). Red line: regression fit; black dashed line: 1:1 reference. The correlation improves slightly when restricting the analysis to sandstone-rich intervals

Figure A 5 shows similar cross-plot by incorporating dynamic shear modulus where the results demonstrate an exceptionally strong linear correlation, with R^2 values of 0.99 in both cases. The regression slopes are approximately 2.54 (full dataset) and 2.48 (sandstone), closely matching the expected theoretical ratio for dynamic modulus relationships. The close clustering of data points along the regression line confirms the consistency between shear modulus and dynamic Young's modulus, regardless of the source.

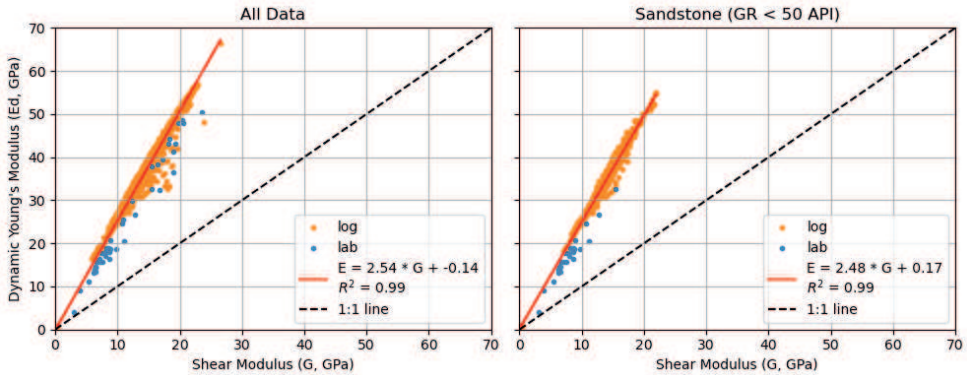


Figure A 5 Dynamic Young's modulus versus shear modulus calculated from lab (blue) and log (orange) data. Left: Full dataset. Right: Sandstone-only data (GR < 50 API). Red line: regression fit; black dashed line: 1:1 reference. The tight clustering and high correlation confirm the strong coupling between dynamic shear and Young's moduli.

Figure A 6 shows the relationship between Poisson's ratio and dynamic Young's modulus (E_d) for both the complete dataset (left) and the sandstone-dominated interval (right; GR < 50 API). In both cases, dynamic modulus was calculated from log-derived P- and S-wave velocities and density. A weak negative trend is observed between E_d and Poisson's ratio in both panels. The linear regression for all data gives a slope of -21.62 and $R^2 = 0.01$, suggesting no meaningful relationship. When filtered for the sandstone-rich interval, the negative slope becomes steeper (-53.53), and the R^2 slightly improves to 0.05 , but still suggests a weak relationship. These results indicate that Poisson's ratio, on its own, is not a strong predictor of dynamic Young's modulus in this dataset, although the trend is more pronounced within the cleaner sandstone zone. In dry rocks, the Poisson's ratio is low because both compressional and shear waves propagate through the mineral skeleton without support from pore fluids (blue dots in Figure A 6). In saturated rocks that V_p increases, due to stiffer response from pore fluids, while V_s remains mostly unchanged, leading to a higher V_p/V_s ratio and higher Poisson's ratio (Castagna et al., 1985).

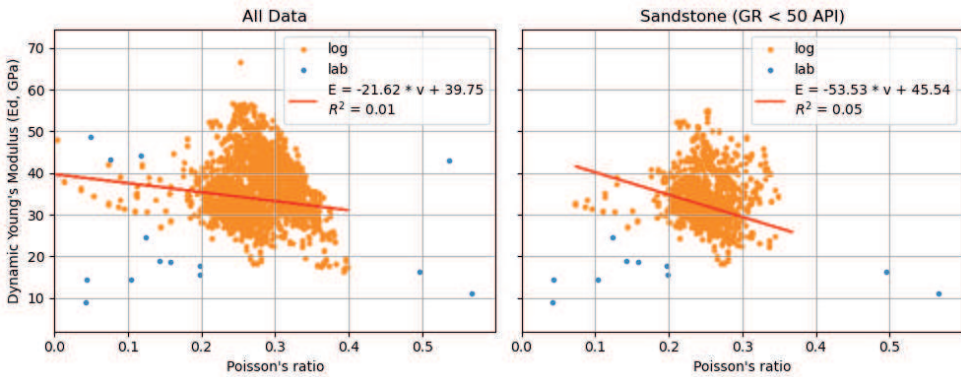


Figure A 6 Relationship between Poisson's ratio and dynamic Young's modulus (E_d) derived from log data. Left: full dataset. Right: sandstone-rich interval ($GR < 50$ API). Orange dots represent log-derived values; blue dots represent lab measurements. A weak negative correlation is observed, with a slightly stronger trend in the sandstone interval.

5. Integrating experimental and log data to predict thermal rock properties in geothermal plays using machine learning

Abstract: The efficiency of geothermal projects depends strongly on the properties of reservoir rocks, which govern both fluid flow and heat transfer. To maximise efficiency and minimise risk, a thorough understanding of reservoir rock properties is necessary, and ideally the ability to predict parameters from limited information. An exploratory data analysis and principal component analysis (PCA) was carried out using an extensive database of laboratory experiments on Permian and Triassic sandstone samples from the Dutch subsurface. Our results from Chapter 2 and 3 showed that thermal conductivity correlates moderately with bulk density, porosity, and elastic velocities, whereas thermal diffusivity shows weakly correlated with only bulk density and porosity. Two predictive approaches were evaluated. In both cases, the target thermal properties (thermal conductivity and diffusivity) were measured in the laboratory. In the first approach (i), laboratory-measured physical properties were used as inputs for linear regression models. In the second approach (ii), down-hole petrophysical logs served as inputs for machine learning models.

The first workflow (i) showed that using more properties as predictors improve predictions of thermal properties and increase the R^2 such gains are inconsistent and lack a systematic trend. The second workflow (ii) showed that for both thermal conductivity and thermal diffusivity, XGBoostRegressor with Optuna hyperparameter tuning achieved the best performance when evaluated using one-well-held-out cross-validation. For thermal conductivity, the model reached an R^2 of about 0.57, demonstrating moderate ability to generalise to entirely unseen wells in both Permian and Triassic. For thermal diffusivity, predictive power remained very limited, but XGBoostRegressor still outperformed the other models, reaching a slightly positive R^2 .

In both workflows, thermal conductivity predictions were moderately accurate (average $R^2 > 0.5$). In contrast, thermal diffusivity is poorly predictable across all models and configurations, suggesting that while standard logs may capture variations associated with microstructural and mineralogical factors, they are not sensitive to the specific interaction between these factors that determines thermal diffusivity. In addition, since thermal diffusivity depends on saturation, measurements obtained from dry samples represent a limited range of values, which restricts the model's capacity to predict this property accurately. This observation was valid in the feature importance analyses, revealing strong model reliance on density and elastic features for conductivity, and no dominant features for diffusivity.

5.1. Introduction

The efficient design and operation of geothermal systems require accurate characterisation of the thermal regime of the subsurface. Thermal conductivity is a critical parameter that governs heat transfer within geological formations, directly influencing temperature distribution, heat flow calculations, and reservoir performance (Blackwell & Steele, 1989). In sedimentary basins targeted for geothermal exploitation, thermal conductivity varies due to changes in lithology, mineral composition, porosity, and fluid content. Direct measurement of thermal conductivity in the subsurface is practically extremely difficult (Fuchs & Förster, 2014). Direct

measurements of thermal conductivity from core samples in laboratory provide the most reliable data, however such measurements are often limited in availability. This limitation arises from the cost and logistical constraints associated with core acquisition and laboratory testing. Petrophysical well logs, on the other hand, can be acquired in wells and provide continuous depth-resolved information on rock and fluid properties. These logs, including sonic velocity, density, gamma ray, and neutron porosity, contain information that can be related to thermal properties either directly or indirectly. This approach can also be followed for predicting other thermal properties. As a function of both thermal conductivity and heat capacity, thermal diffusivity controls the transient temperature changes due to conduction in the subsurface and is therefore critical for dynamic heat transfer modelling in geothermal applications.

Given the role of thermal conductivity and thermal diffusivity in geothermal reservoir assessment, there is a need for methods that can reliably predict these properties where laboratory plug measurements are absent or sparse. Some researchers have employed empirical correlations and theoretical models based on lithology or porosity, however, such empirical correlations have been shown not to generalise well across different formations, as their applicability can be limited by lithological variability and diagenetic conditions. Therefore, while developing formation-specific correlations is necessary for accurate local predictions, as done in this thesis, improving the general understanding of the controlling factors remains essential for broader applicability.

As is shown in Chapters 2 and 3, developing empirical correlations is challenging because they are often based on simple regression methods. The limited use of large multivariate datasets further prevents the identification of underlying patterns in the data. Machine learning, therefore, offers a potential approach for improving the prediction of thermal properties using well logs. Machine learning could enable the development of data-driven models that can learn from experimental data and well logs to predict thermal properties. By integrating experimental measurements of thermal and acoustic properties with standard petrophysical logs, machine learning models can potentially provide accurate, continuous predictions of thermal conductivity across different formations (Brigaud et al., 1990; Fuchs & Förster, 2014; Griffiths et al., 1992; Hartmann et al., 2005).

In this study, we therefore explore and evaluate machine learning approaches for predicting thermal conductivity and thermal diffusivity using experimental data and petrophysical logs. We train the models using the data collected from 8 wells that penetrated Rotliegend (Permian) and Buntsandstein (Triassic) formations in the Dutch subsurface, presented in Chapter 2 and 3 of this thesis. The integration of experimental and downhole petrophysical logs from these stratigraphic intervals provides a valuable case for developing predictive models applicable to geothermal exploration and production.

5.1.1. Literature review

Several empirical and semi-theoretical models have historically been used to estimate thermal conductivity from porosity and mineral composition. Clauser and Huenges (1995b) introduced mixing laws that consider volumetric fractions of mineral phases and pore fluids, developed primarily from literature-based mineral and fluid thermal property datasets, and validated against laboratory measurements of core samples. Birch (1960) further explored the temperature dependence and anisotropy of thermal conductivity, using laboratory measurements on sedimentary rocks. In more recent applications, Fuchs and Förster (2014) evaluated empirical models against extensive laboratory core datasets, confirming moderate correlations between thermal conductivity, bulk density, and sonic velocity in siliciclastic successions.

Beyond simple regression, multivariate approaches have been widely applied to quantify interdependencies between thermal and petrophysical properties. Brigaud et al. (1990) and Hartmann et al. (2005) used simple and multi linear regression models to predict thermal conductivity from wireline acoustic and density logs. They showed that combining multiple inputs, such as porosity, velocity, and mineral content, enhanced predictive accuracy although the performance varied by formation and diagenetic state. In contrast, thermal diffusivity has proven more difficult to predict. As it depends on both thermal conductivity and volumetric heat capacity, it is sensitive to mineral-specific and microstructural factors that are not captured well by standard log measurements (Fuchs et al., 2015; Griffiths et al., 1992).

Dimensionality reduction techniques such as Principal Component Analysis (PCA) have also been employed to examine relationships between elastic, thermal, and petrophysical variables. For example, Chehili et al. (2025) applied Principal Components Analysis (PCA) to petrophysical data from the Illizi Basin, Algeria, to identify reservoir units with high hydrocarbon potential. Among the studied intervals, unit IV-3 showed the most favourable properties, with high porosity and low water saturation. PCA effectively highlighted relationships between petrophysical parameters and guided the identification of productive zones. Their study demonstrates PCA's value in reservoir characterisation and supports its integration with machine learning for improved prediction in complex settings. Weibel et al. (2012) applied PCA to data from the Gassum Formation (sandstones from the Norwegian–Danish Basin) to investigate porosity–permeability relationships. Their PCA showed that the first principal component (PC1) largely represents variation in porosity and permeability versus burial depth and diagenesis, i.e., compaction processes. Rezaeyan et al. (2023) used neutron scattering data and multivariate statistical methods (PCA and regression) to study porosity in mudrocks. It helped them to conclude that compaction is the strongest control on porosity, especially for larger pores, while clay content mainly affects nano porosity and surface area. The first principal component (PC1) reflects the combined influence of clay content and

compaction on the pore structure. Their results showed that porosity in mudrocks is governed by multiple factors and cannot be reliably explained by any single parameter.

In this context, machine learning (ML) has gained attention for its ability to model complex, nonlinear relationships among petrophysical properties. Applications in geosciences have included porosity and permeability prediction (Chaki, 2015; Matinkia et al., 2023), rock typing (Hussain et al., 2022; Mohammadian et al., 2022; Xing et al., 2023), and reservoir characterisation (Anifowose et al., 2017; Chaki, 2015; Mishra et al., 2022). Ridge regression offers a robust linear baseline model, particularly effective when input features exhibit multicollinearity. Ensemble methods such as Random Forest, LGBMRegressor, and XGBRegressor, when properly tuned, have been seen to outperform simpler models in capturing nonlinear trends and feature interactions (Bijan & Al-Rahim, 2024; Pan et al., 2022; Probst et al., 2019). Meshalkin et al. (2020) applied eight machine learning models to predict thermal conductivity from well-log data in a heavy oil reservoir. Random Forest achieved the highest accuracy ($R^2 = 0.85$, $RMSE = 0.15 \text{ W} \cdot \text{m}^{-1} \cdot \text{K}^{-1}$, and total relative error = 12.54%), outperforming both multiple linear regression and the Lichtenecker–Asaad model. Their results highlight the effectiveness of ML, particularly ensemble methods, in capturing nonlinear relationships between petrophysical logs and thermal properties.

The main challenge is that thermal conductivity and diffusivity cannot be measured directly in most wells, and empirical correlations do not generalise across formations. This chapter evaluates whether machine learning applied to integrated laboratory and log data can provide more reliable predictions of these properties.

5.2. Methodology

5.2.1. Study area and material

This study focuses on two key stratigraphic units in the Dutch subsurface. The Permian Upper Rotliegend Formation, and the Triassic Buntsandstein Subgroup. These formations represent important targets for geothermal energy development and other subsurface applications in the Netherlands (Cecchetti et al., 2023; Cecchetti et al., 2024a; Heijnen et al., 2015; Mijnlief, 2020; Pluymaekers et al., 2012; Willems et al., 2020). The Permian Upper Rotliegend Group and the Triassic Main Buntsandstein Subgroup differ to some extent in their depositional environments, diagenetic histories, and mineralogy (Kombrink et al., 2012; Mijnlief, 2020) though many similarities also exist (Griffioen et al. 2025). These differences potentially affect how thermal and petrophysical properties are related and could raise the need for formation-specific models or model validation across stratigraphic boundaries.

The Permian data were collected in Chapter 2 from wells located in the Dutch offshore sector in the North Sea as well as one onshore location in the Groningen area, sampling the Upper Rotliegend Slochteren Formation and associated Silverpit Formation (see Figure 5.1 for the

locations and Table 5.1 for the well names). These formations consist mainly of aeolian and fluvial sandstones with local conglomeratic interbeds (de Jager & Geluk, 2007; Kombrink et al., 2012). Over 1130 plugs were collected from existing cored material and tested for petrophysical and thermo-acoustic properties as described in Chapter 2. Thermal conductivity, thermal diffusivity, and volumetric heat capacity were measured based on transient plane source method using a HotDisk TPS2200 device. Compressional and shear wave velocities were determined via ultrasonic transmission device, and porosity and bulk density were measured using a pycnometer by injecting helium gas. All measurements were performed under consistent dry and ambient laboratory conditions

The Triassic dataset comprises samples from the Buntsandstein Subgroup, obtained from Q-block wells in the Dutch North Sea sector (see Figure 5.1 for the locations and Table 5.1 for the well names). The Buntsandstein in this region consists of stacked fluvial and lacustrine sandstones with interbedded finer-grained layers (de Jager & Geluk, 2007; Kombrink et al., 2012). The same suite of measurements was undertaken, and again all measurements were performed under consistent dry and ambient laboratory conditions which was discussed in Chapter 3.

Across these datasets, consistent procedures and the same devices were used to ensure comparability of the measured properties. The dataset consists of laboratory-measured properties, V_p , V_s , bulk density, porosity, thermal conductivity, thermal diffusivity, and volumetric heat capacity obtained from core plug samples. Methodological details are presented in Chapter 2 and 3.

In addition to retrieving laboratory measurements on core plugs, downhole petrophysical log data were obtained from the publicly available database of the Geological Survey of the Netherlands (www.nlog.nl) from the wells for which core plug samples were available. These logs include standard measurements such as gamma ray, bulk density, neutron porosity, and sonic velocities. Unlike core data, the logs provide continuous depth coverage across the reservoir intervals and sometimes beyond. They were used to complement the laboratory measurements by enabling a comparison between log-derived and lab-derived properties and served as input for predictive modelling.

Table 5.1 Overview of wells and number of core plug samples studied in this work, grouped by geological period and formation. The table lists well codes penetrated each period and the total number of core plugs analysed per period (Kolah-Kaj et al., 2024).

	Permian (Rotliegend)	Triassic (Buntsandstein)
Well names	K18-08	Q01-25
	K18-07x	Q04-10
	E18-05	Q04-C2
	ZRP-03a	Q11-03
Number of Studied core plug	1130	770

- Permian
- Triassic

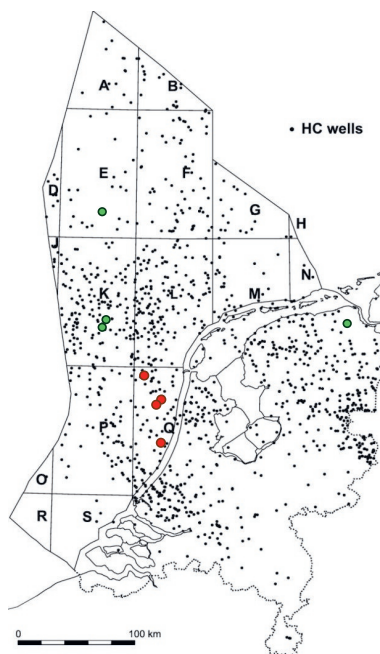


Figure 5.1 Geographical distribution of the wells studied in this work within Dutch boundaries. The map shows the locations of wells targeting Triassic (red), and Permian (green) formations. Black dots represent other hydrocarbon wells. Map is retrieved from the work of de Jager and Geluk (2007).

5.2.2. Data preparation

Before developing the models, a series of data preparation steps were applied to ensure the quality and integrity of the dataset. The completeness of the data was assessed using missing data visualisation, including bar plots and heatmaps, to examine the distribution and patterns of missing values across the input features. Records with missing values in any of the selected input features or the target variable were excluded from further analysis to prevent potential biases or errors during model training and evaluation.

No imputation methods were used, as the objective was to train models only on fully observed data points. Likewise, no outlier detection or removal techniques were applied, and the dataset was used in its original form without generating any derived or engineered features. This minimalist preprocessing approach ensures transparency and allows the predictive performance of the models to be assessed based solely on the available measured data, without introducing assumptions through data manipulation.

Following this, the available petrophysical logs and laboratory measurements were inspected for consistency and plausibility. The distributions of input variables were checked using summary statistics and scatter plots. Well-log data were aligned with the depth intervals of laboratory measurements to ensure that the input features corresponded to the depths at which thermal properties were measured. The input features were retained in physical units for interpretability. Tree-based models (Random Forest, LGBMRegressor, XGBRegressor) were trained without scaling, as they are insensitive to feature scaling. Linear regression models were fitted on unscaled features. For Ridge regression, predictors were standardised using a StandardScaler within the training pipeline. Variables were also standardised prior to PCA.

5.2.3. Prediction workflows

To make predictions, two workflows were designed, as illustrated in Figure 5.2. The first workflow, empirical regression models were developed to predict thermal conductivity and thermal diffusivity. This workflow relied entirely on laboratory-measured parameters, namely compressional wave velocity (V_p), shear wave velocity (V_s), bulk density, and porosity. These parameters were selected because they are known to be physically linked to the thermal behaviour of rocks through mineral composition, porosity structure, and elastic properties, and are reasonably standard to measure in a laboratory. It is important to note that the target variables in workflow, thermal conductivity and thermal diffusivity, were also measured in the laboratory. The workflow began with a comprehensive exploratory analysis to assess data distribution and normalise variables where necessary. Principal Component Analysis (PCA) was then performed to investigate the interrelationships among the measured parameters, with the aim of reducing dimensionality and identifying the most informative combinations of predictors. Multiple predictor combinations were tested to assess how different input sets influenced prediction accuracy, and model performance was evaluated using statistical metrics such as the coefficient of determination (R^2), mean absolute error (MAE), and root mean square error (RMSE).

The second workflow evaluated the feasibility of predicting thermal conductivity and diffusivity from wireline petrophysical logs, which are more widely available than laboratory measurements in subsurface studies. In this approach, sonic (compressional wave), bulk density, porosity, and gamma ray logs were used as predictors in supervised machine learning models. After models were trained, cross-validation was carried out to ensure robust performance assessment. In addition, feature importance analysis was also conducted to determine which log-derived parameters most strongly influenced the predictions. Predictions from these models were compared against the laboratory-measured thermal properties to evaluate their accuracy and generalisability.

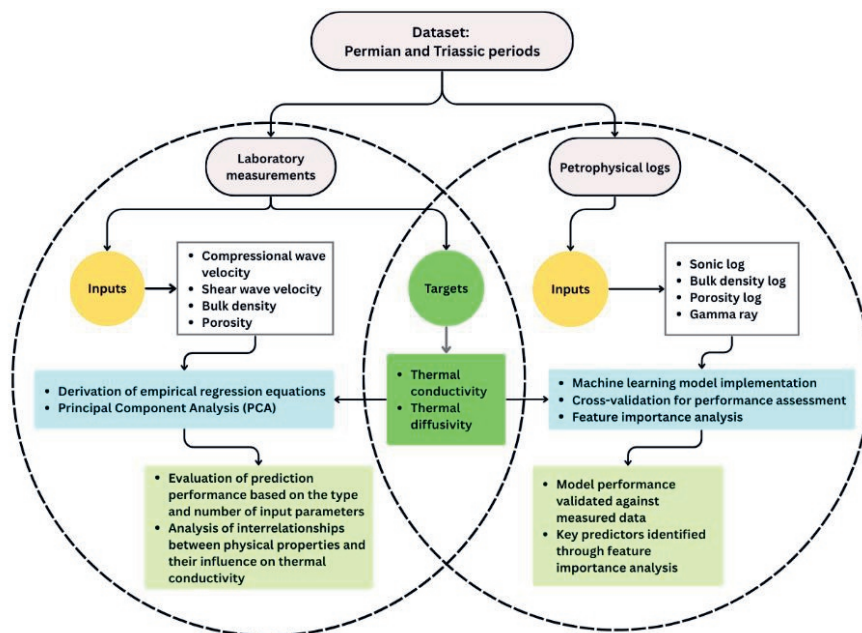


Figure 5.2 Workflow for predicting thermal conductivity using experimental data and petrophysical logs. The left circle illustrates the use of experimentally measured acoustic and petrophysical properties (V_p , V_s , bulk density, and porosity) as input features, while the right branch shows the use of petrophysical well logs (sonic log, bulk density log, porosity log, and gamma ray log) as inputs. In both workflows, thermal conductivity and thermal diffusivity were the target.

5.2.3.1. Machine learning algorithms

Four regression algorithms were employed to predict thermal conductivity and thermal diffusivity. Those included [Ridge Regression](#), [Random Forest Regressor](#), from scikit-learn developed by Pedregosa et al. (2011), as well as [LGBMRegressor](#) by Ke et al. (2017) and [XGBRegressor](#) from the work of Chen and Guestrin (2016). Each algorithm was selected for its specific characteristics and suitability for handling structured geoscientific data (Fan et al., 2021; Li et al., 2024; Zhang et al., 2024b).

Ridge Regression is a linear model that adds regularisation to control overfitting, particularly when predictors are correlated. It is useful for capturing linear trends and offers stable, interpretable outputs. Random Forest Regressor is an ensemble method that constructs multiple decision trees and averages their predictions. It effectively captures nonlinear relationships and reduces overfitting by relying on a diverse set of trees. LGBMRegressor is a gradient boosting algorithm designed for fast computation and efficient handling of large datasets. It builds decision trees sequentially, where each tree corrects the errors of the previous ones, and performs well when tuned properly. XGBRegressor is a powerful gradient boosting model

known for its ability to handle complex relationships between features. It incorporates advanced regularisation techniques, which help prevent overfitting and improve predictive accuracy, especially when fine-tuned.

Model validation was performed using two grouped cross-validation strategies. The first was a shuffled holdout, in which all data, regardless of the well from which they originated, were divided into five folds. In each of five rounds, four folds were used for training, and the remaining fold was kept out for testing.

Given that the ultimate goal was to predict thermal properties throughout a well, we continued with a k-fold strategy by treating each well as a fold. In each round, one well was left out for testing while the model was trained on the remaining wells. This ensured that the models were always evaluated on unseen wells, providing a realistic assessment of their generalisation ability across different geological settings. We call this cross-validation a one-well-held-out approach.

Each selected machine learning model has a set of parameters that control its performance, i.e. hyperparameters. Three levels of model implementation were investigated by training models with different hyperparameters. First, models were trained using default parameters. Next, we applied hyperparameter tuning to identify the most effective values. Two tuning strategies used were grid search and Optuna-based Bayesian optimisation (Akiba et al., 2019).

The following models were implemented:

- Baseline models
 - Algorithms: Random Forest, Ridge Regression, XGBRegressor, LGBMRegressor
 - Cross-validation: Shuffled k-fold
 - Parameters: Default
- Tuned models
 - Set 1
 - Algorithms: Ridge Regression, XGBRegressor, LGBMRegressor
 - Cross-validation: One-well-held-out
 - Parameters: Grid search
 - Set 2
 - Algorithms: Ridge Regression, XGBRegressor, LGBMRegressor
 - Cross-validation: One-well-held-out
 - Parameters: Optuna-based Bayesian optimisation

5.2.3.2. Performance evaluation

Model performance was assessed using the coefficient of determination (R^2), mean absolute error (MAE), normalised mean squared error (NMSE), and mean absolute percentage error

(MAPE). These metrics were calculated per well and aggregated to provide an overall evaluation of predictive performance and model consistency. In addition to numerical metrics, residual plots were generated to visualise the differences between predicted and measured values and to identify possible systematic errors or bias in the predictions.

5.3. Results

5.3.1. Experimental data

5.3.1.1. Exploratory data analysis

The relationships among the physical and thermal properties of the samples were examined using pair-plots (Figure 5.3). As expected, there is a very strong negative correlation between bulk density and porosity ($R^2 = 0.95$), given the reasonably consistent solid material density and strong contrast to the pore filling air density.

Similarly, V_p and V_s are strongly correlated ($R^2 = 0.95$), reflecting their joint dependence on the rock's elastic properties (as mentioned by (Castagna et al., 1985)). Both velocities also show moderate to strong positive relationships with bulk density and negative relationships with porosity (Klimentos, 1991; Tatham, 1982). For example, V_s -porosity and V_p -porosity yield R^2 values of 0.69 and 0.61, respectively. The scatter is as expected due to dependence of the velocities on the rock structure.

Thermal conductivity correlates moderately with both porosity ($R^2 = 0.56$) and bulk density ($R^2 = 0.53$). These results suggest that denser and less porous rocks tend to conduct heat more efficiently, consistent with higher thermal conductivities of the solid material components than the pore fluid (in this case, air as the studied samples here are dry). A weaker correlation is observed between thermal conductivity and wave velocities. The thermal conductivity versus V_s has an $R^2 = 0.36$, and for V_p it is 0.29. This indicates some elastic control on thermal conductivity and suggests that the influence of rock structure is different for wave velocities and thermal conductivity. Thermal diffusivity shows poor correlations with V_s ($R^2 = 0.0054$) and V_p ($R^2 = 0.0003$), and slightly better correlations with porosity ($R^2 = 0.0849$) and bulk density ($R^2 = 0.0657$). Its correlation with thermal conductivity is relatively stronger ($R^2 = 0.3110$). The correlation with thermal conductivity is expected as thermal diffusivity is defined as thermal conductivity divided by the volumetric heat capacity.

The histograms on the diagonal indicate that most variables are approximately normally distributed, with respectively positive and negative skewness in porosity and bulk density.

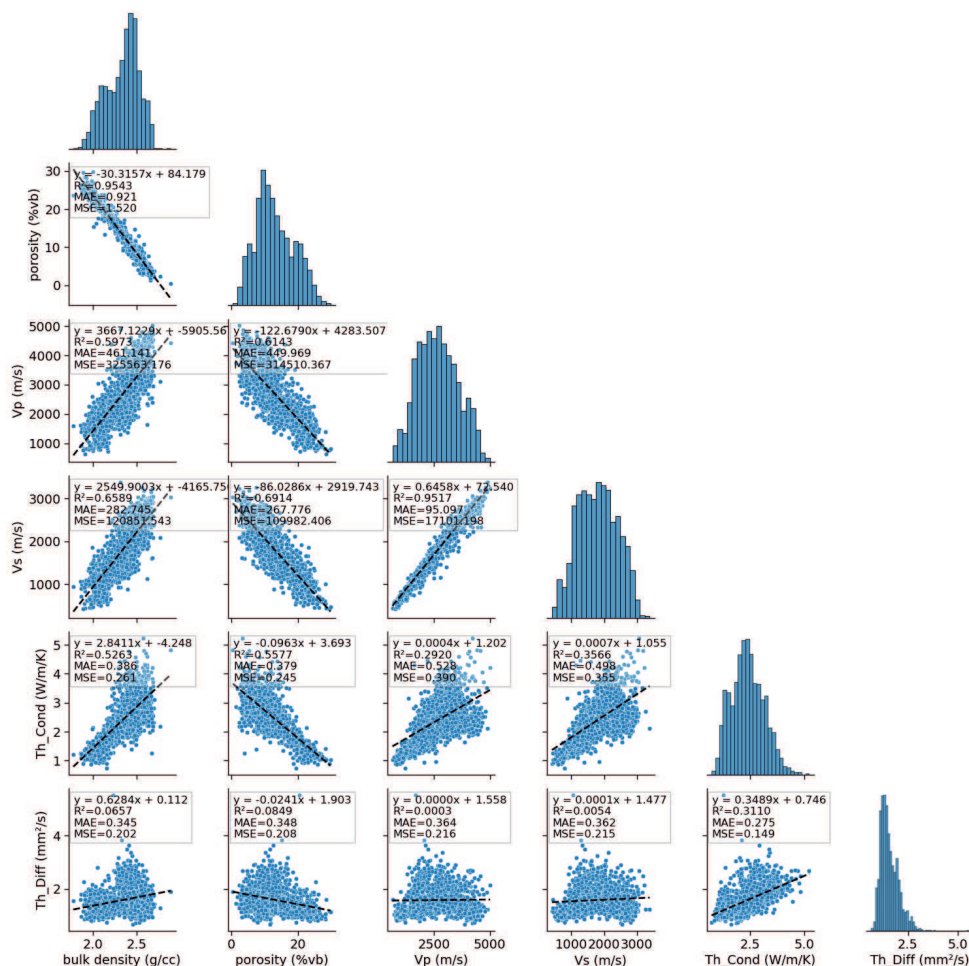


Figure 5.3 Pair-plot showing the distributions and relationships among key physical and thermal properties of the Permian and Triassic core plug dataset. Each subplot in the lower triangle displays scatter plots with fitted linear regression lines (in black), highlighting trends between variables. Histograms on the diagonal show the distribution of individual variables. Positive correlations are observed between bulk density, Vp, Vs, thermal diffusivity, and thermal conductivity, while porosity exhibits negative correlations with those properties.

The equations and their metrics presented in Figure 5.3 are presented in Table 5.2 only for target properties. Porosity is the strongest predictor of both thermal conductivity ($R^2 = 0.557$) and thermal diffusivity ($R^2 = 0.0849$). Bulk density is the next-best predictor, with a slightly lower R^2 , which reflects the near one-to-one correlation between porosity and bulk density.

Table 5.2 Coefficients of determination (R^2) from simple linear regression models of thermal conductivity (Th_Cond) and thermal diffusivity (Th_Diff) as a function of petrophysical properties (porosity, bulk density, V_p and V_s). Data are from over 2000 core plugs from both Permian and Triassic wells in the Dutch subsurface.

Equation	R^2	MAE	MSE
$Th_Cond = 2.8411 \times \rho_b - 4.2483$	0.5263	0.3857	0.2608
$Th_Cond = -0.0963 \times \varphi + 3.6930$	0.5577	0.3786	0.2447
$Th_Cond = 0.0004 \times V_p + 1.2024$	0.292	0.5275	0.3902
$Th_Cond = 0.0007 \times V_s + 1.0555$	0.3566	0.4979	0.3546
$Th_Diff = 0.6284 \times \rho_b + 0.1118$	0.0657	0.3449	0.2017
$Th_Diff = -0.0241 \times \varphi + 1.9027$	0.0849	0.3480	0.2078
$Th_Diff = 8 \times 10^{-6} \times V_p + 1.5577$	0.0027	0.3640	0.2157
$Th_Diff = 0.0001 \times V_s + 1.4774$	0.0054	0.3625	0.2146

5.3.1.2. Principal Component Analysis (PCA)

The PCA results presented in Figure 5.4 reveal that the first principal component (PC1), which accounts for 70.5% of the total variance, primarily reflects a strong inverse relationship between porosity and the other measured properties. Variables including V_p , V_s , bulk density, and thermal conductivity all project positively onto PC1, indicating that they co-vary and are inversely related to porosity. This agrees with established petrophysical understanding that as porosity increases, the rock matrix becomes less consolidated, leading to lower density, seismic velocities, and thermal conductivity.

Thermal diffusivity, however, aligns more strongly with the second principal component (PC2), which explains 20.3% of the variance. Its separation from the cluster of V_p , V_s , density, and thermal conductivity suggests that diffusivity is influenced by additional factors, such as heat capacity, that are not directly captured by the porosity-density framework.

Overall, the PCA shows that most of the variability (90.8% of the variance) can be explained by two principal components. PC1 represents the main porosity-controlled trend in elastic and thermal conductivity behaviour, while PC2 captures the distinct contribution of thermal diffusivity. This dimensional structure provides a robust basis for multivariate prediction of thermal properties using petrophysical inputs.

Bulk density, V_p , V_s , and thermal conductivity cluster together along PC1, highlighting their shared dependence on the rock framework and compaction. Porosity plots in the opposite direction, consistent with its inverse relationship to density and stiffness. Thermal diffusivity, in contrast, defines a separate axis along PC2, indicating that it varies independently of the porosity–density trend and is likely governed by additional influences such as heat capacity. Thermal diffusivity, in contrast, aligns mainly with PC2 and shows little covariance with V_p , V_s , bulk density, or porosity. This indicates that its variability is not governed by the

compaction-related trend captured by PC1 but instead reflects a distinct control on thermal behaviour separate from the elastic and density properties.

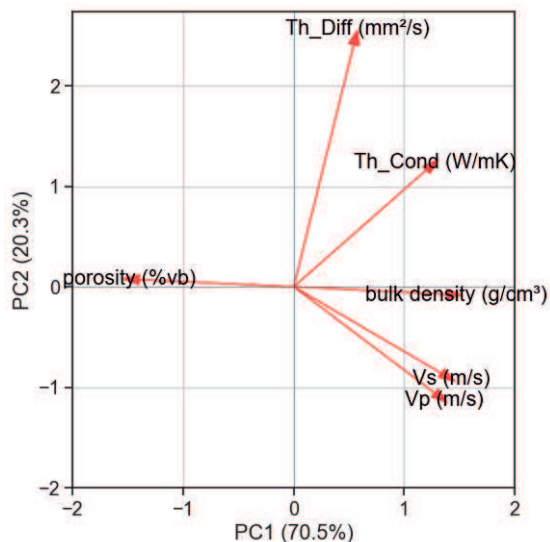


Figure 5.4 Biplot of the first two principal components (PC1 and PC2) derived from PCA on six rock properties: V_p , V_s , bulk density, porosity, thermal conductivity, and thermal diffusivity. PC1 explains 70.5% of the variance and PC2 explains 20.3%, together capturing 90.8% of the total variance in the dataset. The direction and length of each arrow represent the contribution of each variable to the components. Bulk density, V_p , V_s , and thermal conductivity align strongly with PC1, indicating shared variance associated with rock framework and compaction. Thermal diffusivity projects mainly along PC2, while porosity loads negatively on PC1, opposite to density and velocities.

5.3.1.3. Regression-based prediction of thermal properties

The strong to moderate linear correlations of thermal properties (thermal conductivity and thermal diffusivity) with several physical rock properties (V_p , V_s , bulk density, and porosity) suggest that regression models are valid here and could be suitable for estimating these thermal parameters. To do so, a series of simple linear regression models were constructed. We used holdout validation by combining all data, regardless of the well of origin. The regression models were fitted on 80% of the data and evaluated on the remaining 20% (Table 5.3).

In all models, 93–96 percent of test observations fell within a residual-based $\pm 1.96\sigma$ band around the predictions. This empirical coverage is close to the nominal 95 percent expected under approximately normal residuals, but it does not by itself demonstrate strong predictive performance. We therefore interpret results primarily from out-of-sample R^2 , MAE, and MSE. These metrics indicate that thermal conductivity is more predictable from V_p , V_s , bulk density, and porosity than thermal diffusivity, and that multivariate models provide only modest

improvements, suggesting that additional predictors or alternative model forms may be needed for substantial gains.

For thermal conductivity, both bulk density and porosity showed sufficiently strong linear relationships to justify regression modelling. The model using porosity as the sole predictor achieved the highest performance among single-feature models, with an $R^2 = 0.585$, a MAE of $0.385 \text{ W/m}\cdot\text{K}$, and a MSE of $0.234 \text{ (W/m}\cdot\text{K)}^2$. The negative regression coefficient confirms that thermal conductivity decreases with increasing porosity, as explained before. The bulk density-based model also performed comparably well ($R^2 = 0.560$), with a strong positive coefficient, indicating higher thermal conductivity in denser, less porous rocks.

For thermal diffusivity, the highest-performing single-feature model used porosity ($R^2 = 0.115$), followed closely by bulk density ($R^2 = 0.112$); models using V_s and V_p performed poorly ($R^2 = 0.021$ and 0.0038).

Model performance improved when multiple predictors were included. Across two-, three-, and four-variable combinations drawn from V_p , V_s , bulk density, and porosity, R^2 increased, reaching 0.609 for thermal conductivity and 0.246 for thermal diffusivity. For thermal conductivity, the three-variable model combining V_p , V_s , and porosity provided the best performance ($R^2 = 0.609$); adding bulk density gave a similar but slightly lower R^2 (0.595). For thermal diffusivity, the highest R^2 with these physical predictors was 0.246 using all four variables; the best two- and three-variable combinations were about 0.22 , indicating only modest improvement over single-feature models. In both cases, the gains over the best single predictor are moderate.

Table 5.3 Summary of statistical performance for regression models predicting thermal conductivity (Th_Cond) and thermal diffusivity (Th_Diff) as a function of bulk density (ρ_b), porosity (ϕ), V_p and V_s . The table presents single-feature, two-feature, three-feature, and four-feature linear regression models. For each model, the predictor(s), regression equation, coefficient of determination (R^2), mean squared error (MSE), mean absolute error (MAE), and the percentage of test samples falling within the 95% confidence interval are reported. Multilinear models using all available features are also included for comparison.

Model Type	Equation	MAE	MSE	R^2	Percentage within 95% CI
Simple linear Regression (1 feature)	$Th_Cond = 2.855 \times \rho_b - 4.258$	0.39	0.25	0.56	95.60
	$Th_Cond = -0.096 \times \phi + 3.689$	0.39	0.23	0.59	95.30
	$Th_Cond = 4.4 \times 10^{-4} \times V_p + 1.246$	0.53	0.39	0.30	96.30
	$Th_Cond = 7.6 \times 10^{-4} \times V_s + 1.073$	0.49	0.35	0.38	95.30
Multiple linear Regression (2 features)	$Th_Cond = -9.32 \times 10^{-4} \times V_p + 2.131 \times 10^{-3} \times V_s + 1.10897$	0.46	0.32	0.44	95.30

Integrating experimental and log data to predict thermal rock properties in geothermal plays using machine learning

	$Th_Cond = -1.4 \times 10^{-5} \times Vp$ $+ 2.906477 \times \rho_b$ $- 4.340704$	0.39	0.25	0.56	95.30
	$Th_Cond = -7.5 \times 10^{-5} \times Vp$ $- 0.104677 \times \varphi$ $+ 4.008245$	0.38	0.23	0.60	95.60
	$Th_Cond = 1.05 \times 10^{-4} \times Vs$ $+ 2.584573 \times \rho_b$ $- 3.812699$	0.40	0.25	0.56	95.60
	$Th_Cond = -5 \times 10^{-6} \times Vs$ $- 0.096073 \times \varphi$ $+ 3.704413$	0.38	0.23	0.59	95.30
	$Th_Cond = -0.45386 \times \rho_b$ $- 0.110023 \times \varphi$ $+ 4.941788$	0.39	0.23	0.58	95.30
Multiple linear Regression (3 features)	$Th_Cond = -6.59 \times 10^{-4} \times Vp$ $+ 1.14 \times 10^{-3} \times Vs$ $+ 2.328348 \times \rho_b$ $- 3.302875$	0.38	0.24	0.58	94.60
	$Th_Cond = -6.09 \times 10^{-4} \times Vp$ $+ 9.59 \times 10^{-4} \times Vs$ $- 0.087517 \times \varphi$ $+ 3.493625$	0.37	0.22	0.61	94.30
	$Th_Cond = -7.4 \times 10^{-5} \times Vp$ $- 0.442281 \times \rho_b$ $- 0.112142 \times \varphi$ $+ 5.227703$	0.38	0.23	0.60	95.60
	$Th_Cond = -5 \times 10^{-6} \times Vs$ $- 0.453354 \times \rho_b$ $- 0.110108 \times \varphi$ $+ 4.953862$	0.39	0.23	0.58	95.30
Multiple linear Regression (All features)	$Th_Cond = -5.71 \times 10^{-4} \times Vp$ $+ 8.6 \times 10^{-4} \times Vs$ $- 0.407534 \times \rho_b$ $- 0.104904 \times \varphi$ $+ 4.745832$	0.36	0.24	0.59	96.30
Simple linear Regression (1 feature)	$Th_Diff = 7.1 \times 10^{-5} \times Vs$ $+ 1.4601$	0.37	0.22	0.02	94.30
	$Th_Diff = 9 \times 10^{-6} \times Vp$ $+ 1.5627$	0.38	0.22	0.004	94.30
	$Th_Diff = -0.0241 \times \varphi + 1.9009$	0.34	0.20	0.11	94.30
	$Th_Diff = 0.7302 \times \rho_b - 0.1279$	0.34	0.20	0.11	94.00
Multiple linear Regression (2 features)	$Th_Diff = -7 \times 10^{-4} \times Vp$ $+ 1.1 \times 10^{-3} \times Vs$ $+ 1.4736$	0.36	0.20	0.07	95.30

Integrating experimental and log data to predict thermal rock properties in geothermal plays using machine learning

	$Th_{Diff} = -2 \times 10^{-4} \times Vp + 1.5679 \times \rho_b - 1.4698$	0.33	0.18	0.20	95.60
	$Th_{Diff} = -3 \times 10^{-4} \times Vp - 0.0558 \times \varphi + 3.0173$	0.33	0.17	0.22	95.30
	$Th_{Diff} = -3 \times 10^{-4} \times Vs \cdot 1.5017 \times \rho_b - 1.3916$	0.34	0.18	0.18	94.60
	$Th_{Diff} = -4 \times 10^{-4} \times Vs - 0.0549 \times \varphi + 2.9512$	0.33	0.18	0.19	94.63
	$Th_{Diff} = -0.1127 \times \rho_b - 0.0279 \times \varphi + 2.217$	0.35	0.20	0.10	93.62
Multiple linear Regression (3 features)	$Th_{Diff} = -5 \times 10^{-4} \times Vp + 5 \times 10^{-4} \times Vs + 1.2927 \times \rho_b - 0.9759$	0.33	0.18	0.20	95.64
	$Th_{Diff} = 5 \times 10^{-4} \times Vp + 5 \times 10^{-4} \times Vs - 0.0477 \times \varphi + 2.7737$	0.33	0.17	0.22	95.64
	$Th_{Diff} = -3 \times 10^{-4} \times Vp - 0.0722 \times \rho_b - 0.0581 \times \varphi + 3.2163$	0.33	0.17	0.22	95.30
	$Th_{Diff} = -4 \times 10^{-4} \times Vs - 0.0734 \times \rho_b - 0.0572 \times \varphi + 3.1536$	0.33	0.18	0.19	94.63
Multiple linear Regression (All features)	$Th_{Diff} = -5 \times 10^{-4} \times Vp + 4 \times 10^{-4} \times Vs + 0.0587 \times \rho_b - 0.0487 \times \varphi + 2.6872$	0.29	0.15	0.25	95.83

Predicting thermal conductivity using multilinear regression with Vp, Vs, bulk density, and porosity resulted in an R² of 0.60, which shows only a marginal improvement compared to using three predictors (Figure 5.5a). In comparison, predicting thermal diffusivity with the same set of predictors yielded an R² of 0.25, indicating a considerably weaker relationship (Figure 5.5b).

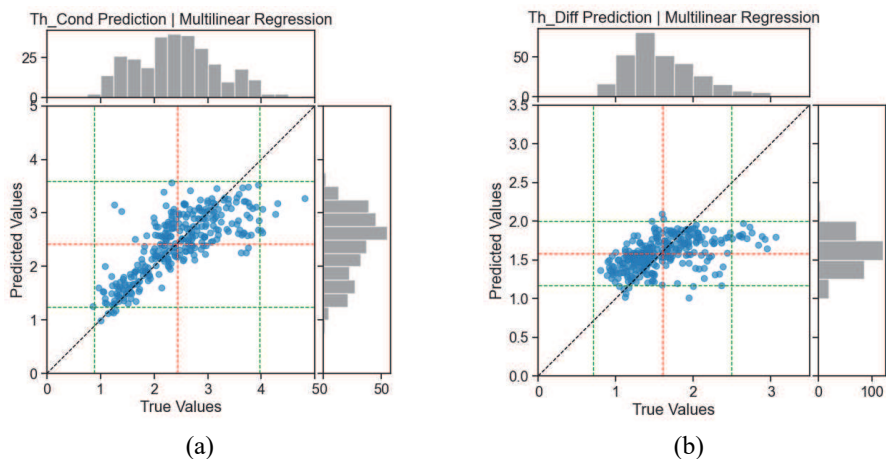


Figure 5.5 Predicted versus measured values for (a) thermal conductivity modelled using multilinear regression with V_p , V_s , bulk density, and porosity ($R^2 = 0.60$), and (b) thermal diffusivity modelled using multilinear regression with the same set of predictors ($R^2 = 0.25$). Both models were trained and tested using a random train–test split (80% training, 20% testing). The dashed line represents the 1:1 reference line. Marginal histograms show the distribution of true and predicted values. The displayed R^2 value represents the performance of the correlation when all predictors, V_p , V_s , porosity, and bulk density, are included.

To complement the regression results, a summary plot was prepared to show how R^2 changes with the number of predictors (Figure 5.6).

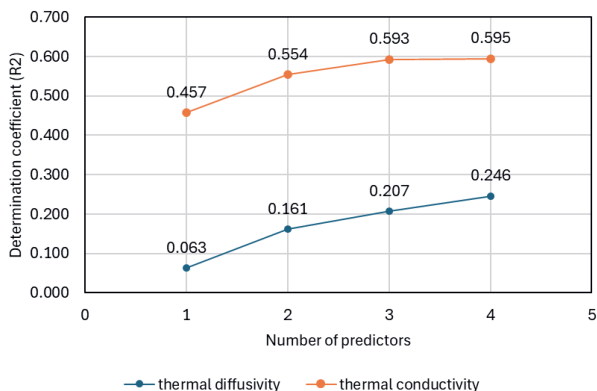


Figure 5.6 Coefficient of determination (R^2) for thermal conductivity (Th_Cond) and thermal diffusivity (Th_Diff) predictions using one to four predictors. The values illustrate how model performance changes with the increasing number of features. Thermal conductivity improves with additional predictors and stabilises after three, while thermal diffusivity increases gradually with each added predictor. The displayed R^2 values represent the average performance across different predictor combinations at each step of adding variables.

For thermal conductivity, the R^2 values increase with the number of predictors. Starting from 0.457 with a single predictor, the R^2 rises to 0.554 with two predictors, 0.593 with three predictors, and reaches 0.595 with four predictors. This trend indicates that combining multiple input features helps the model better explain the variation in thermal conductivity. Although the improvement is marginal beyond the third predictor, each additional feature still contributes some complementary information. It should be noted that the pairs porosity–bulk density and V_p – V_s are strongly correlated and therefore do not necessarily provide additional independent information to the correlation.

Thermal diffusivity, the R^2 increases gradually from 0.063 with a single predictor to 0.161 with two predictors, 0.207 with three predictors, and 0.246 with four predictors. This shows that while adding predictors does improve diffusivity predictions, the overall explanatory power remains relatively low compared to conductivity. The weaker correlations between diffusivity and the available predictors likely limit the model performance.

5.3.2. Integration of experimental data and petrophysical logs

5.3.2.1. Model performance trends

Validation strategy, model choice, and hyperparameter tuning jointly influence predictive skill and generalizability of machine learning models. In this section, the predictive performance of all tested model configurations are systematically compared for both thermal conductivity and thermal diffusivity. The evaluation considers two cross-validation strategies (shuffled k-fold and one-well-out), four regression models (Ridge, Random Forest, LGBMRegressor, and XGBRegressor), and three parameter settings (default parameters, grid search optimisation, and Bayesian optimisation implemented with Optuna). Model performance is reported in terms of mean R^2 across folds, its standard deviation as a measure of stability, and error metrics. The mean R^2 reflects the proportion of variance explained by the model, providing a measure of predictive accuracy, while the standard deviation of R^2 quantifies the stability of this performance across different wells. A model with a high R^2 but large variability may perform well in some folds but poorly in others, indicating limited generalizability, whereas a model with a slightly lower R^2 but a small standard deviation is more consistent and therefore more reliable. The comparison of cross-validation strategies, shown in Table 5.4, revealed that model performance was strongly influenced by the way data were partitioned. The relatively high R^2 values obtained under shuffled K-fold validation, together with low error metrics, indicated that the models were exposed to well-specific patterns during training, which inflated their predictive skill. This leakage effect explained why ensemble models such as Random Forest and LGBMRegressor achieved values above 0.67 for thermal conductivity under shuffled folds, despite their weaker performance under stricter testing conditions.

In the one-well-out cross validation, predictive accuracy declined. The R^2 values for thermal conductivity dropped from 0.68 to 0.48 in the case of Random Forest, and diffusivity models

often yielded negative values. Because the objective of this study was to predict thermal properties in entirely new wells, well-based validation provided the most realistic measure of predictive performance. In contrast, the high accuracy observed under shuffled folds was inflated by information leakage and did not reflect true generalisation. The increased difficulty encountered under this stricter framework highlighted the challenge of transferring models across wells with distinct geological signatures. For example, Terry et al. (2021) tested Random Regression Forest models to predict total volatile organic compound (TVOC) concentrations from borehole geophysical logs at three contaminated sites (California, Wisconsin, New Jersey). Random k-fold cross-validation suggested strong predictive performance ($R^2 \approx 0.83$ – 0.86). However, when evaluated for transferability across sites, boreholes, or depth intervals, the models failed ($R^2 \approx 0$). This discrepancy was caused by spatial autocorrelation: random shuffling places samples close in space in both training and test set, inflating accuracy. The study demonstrates that while cross-validation is a critical tool, its design must account for spatial structure and reflect how the model will be applied in practice. In geothermal exploration, the practical goal is to predict thermal conductivity and thermal diffusivity in new wells where no core measurements are available. This is why, in our study, we deliberately excluded any information from the target well during training. By doing so, we ensured that validation reflected true predictive performance across wells, rather than being artificially inflated by spatial autocorrelation effects.

Hyperparameter optimisation with the one-well-out cross validation partially mitigated this reduction in performance. Grid search improved model calibration by refining structural parameters, and further using Bayesian optimisation (implemented with the Optuna framework) achieved marginal gains by exploring the parameter space more adaptively. Nevertheless, the extent of these improvements was limited, and performance did not approach the inflated levels observed under shuffled validation. The convergence of results across tuning approaches suggested the presence of a predictive ceiling, imposed by both the quality of the available features and the geological variability of the dataset.

Taken together, these observations emphasise that rigorous validation frameworks are essential for avoiding overestimation of model performance. While hyperparameter tuning strengthened model robustness, it did not fully overcome the constraints associated with predicting thermal properties in unseen wells. The results therefore point to the need for additional or alternative predictors, particularly geological or mineralogical descriptors, if further improvements in predictive accuracy are to be achieved.

Model (Cross-validation)	R ² (std)	NMSE	MAE	MAPE
Th_Cond (W/m/K)				
RandomForestRegressor (Kfold (5,shuffled))	0.679 ± 0.022	0.32	0.3	13.34
LGBMRegressor (Kfold (5,shuffled))	0.671 ± 0.022	0.33	0.31	13.42
XGBRegressor (Kfold (5,shuffled))	0.609 ± 0.043	0.39	0.33	14.51
Ridge (Kfold (5,shuffled))	0.595 ± 0.033	0.41	0.35	15.46
Ridge (Well-based CV)	0.514 ± 0.211	0.49	0.39	17.86
Random Forest (Well-based CV)	0.482 ± 0.303	0.52	0.41	18.73
LightGBM (Well-based CV)	0.447 ± 0.429	0.55	0.43	19.31
XGBoost (Well-based CV)	0.397 ± 0.425	0.6	0.44	19.72
Ridge (Grid Search)	0.514 ± 0.211	0.49	0.34	17.6
LightGBM (Grid Search)	0.538 ± 0.346	0.42	0.32	16.9
XGBoost (Grid Search)	0.515 ± 0.294	0.45	0.35	18.3
Ridge (Optuna)	0.515 ± 0.208	0.49	0.35	17.9
LightGBM (Optuna)	0.570 ± 0.253	0.42	0.32	16.8
XGBoost (Optuna)	0.573 ± 0.329	0.45	0.34	17.5
Th_Diff (mm²/s)				
RandomForestRegressor (Kfold (5,shuffled))	0.4113 ± 0.0329	0.59	0.26	16.45
LGBMRegressor (Kfold (5,shuffled))	0.5893 ± 0.0359	0.61	0.26	16.68
XGBRegressor (Kfold (5,shuffled))	0.3290 ± 0.0497	0.67	0.27	17.56
Ridge (Kfold (5,shuffled))	0.2652 ± 0.0483	0.71	0.29	18.51
Ridge (Well-based CV)	0.057 ± 0.514	0.94	0.34	22.23
Random Forest (Well-based CV)	-0.02 ± 0.709	1.02	0.36	23.57
LightGBM (Well-based CV)	-0.026 ± 0.732	1.03	0.36	23.34
XGBoost (Well-based CV)	-0.178 ± 1.094	1.18	0.38	25.27
Ridge (Grid Search)	0.066 ± 0.548	0.98	0.29	23.5
LightGBM (Grid Search)	0.003 ± 0.596	1.02	0.32	25.8
XGBoost (Grid Search)	0.038 ± 0.621	0.96	0.3	24.7
Ridge (Optuna)	0.072 ± 0.562	0.93	0.29	23.3
LightGBM (Optuna)	0.057 ± 0.611	0.96	0.3	24.8
XGBoost (Optuna)	0.082 ± 0.504	0.92	0.29	23
	Good	Neutral	Bad	
R2	≥0.5	0-0.5	≤0	
NMSE	≤0.5	0.5-1	≥1	
MAE (Th_Cond (W/m/K))	≤0.15	0.15-0.35	>0.35	
MAE(Th_Diff (mm ² /s))	≤0.1×10 ⁻⁶		>0.1×10 ⁻⁶	
MAPE	≤10%	10-20%	≥20%	

Table 5.4 Cross-validation results for thermal conductivity (Th_Cond) and thermal diffusivity (Th_Diff) prediction using Ridge Regression, Random Forest, LGBMRegressor, and XGBRegressor models under different hyperparameter optimisation strategies (Random group k-fold, well-based grouped k-fold, Grid Search, and Optuna). Performance metrics include coefficient of determination (R^2) and standard deviation, normalised mean squared error (NMSE), mean absolute error (MAE), and mean absolute percentage error (MAPE). Colour coding highlights model performance based on defined thresholds: green for good, yellow for neutral, and red for poor performance.

Default parameters

Shuffled k-fold

For thermal conductivity, all models achieved reasonably high performance. Random Forest performed best ($R^2 = 0.68$, MAE = 0.30 W/m·K, MAPE = 13.3%), followed closely by LGBMRegressor ($R^2 = 0.67$, MAE = 0.31 W/m·K). Ridge and XGBRegressor also performed consistently ($R^2 \approx 0.59-0.61$). For thermal diffusivity, results were weaker. Random Forest ($R^2 = 0.41$) and LGBMRegressor ($R^2 = 0.39$) performed best, while XGBRegressor and Ridge yielded lower $R^2 (\leq 0.33)$.

One-well-held-out

Figure 5.7 shows that Ridge has the narrowest residual spread across depth and the tightest clustering about the 1:1 line, indicating the best fit, whereas XGBRegressor exhibits the widest scatter. Ridge gives the best accuracy ($R^2 = 0.51$, NMSE = 0.49, MAE = 0.39 W/m·K), followed by Random Forest ($R^2 = 0.48$) and LGBMRegressor ($R^2 = 0.45$), with XGBRegressor lowest ($R^2 = 0.40$). Relative to the others, XGBRegressor shows markedly larger dispersion around the one-to-one line and a residual range of about -2 to $+2$ W/m·K, roughly twice that of the other models.

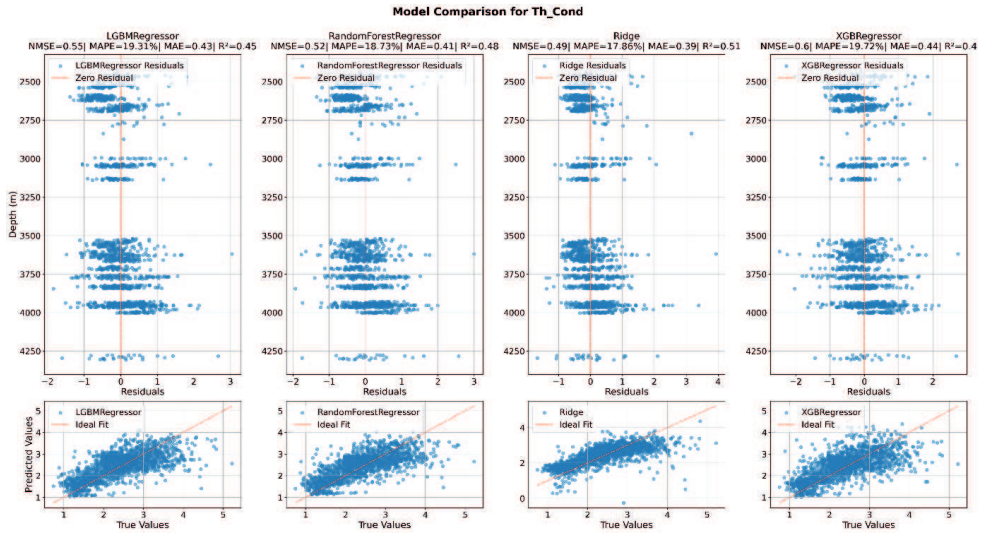


Figure 5.7 Residual plots (top row) and predicted vs. true value plots (bottom row) comparing the performance of LGBMRegressor, Random Forest Regressor, Ridge Regression, and XGBRegressor for predicting thermal conductivity. Each model’s NMSE, MAPE, MAE, and R^2 are indicated. The residual plots highlight the error distribution across depth, while the scatter plots visualise the agreement between predicted and true values.

For thermal diffusivity, the models showed negligible predictive capability. Ridge achieved only $R^2 = 0.06$ (NMSE = 0.94), whereas Random Forest, LGBMRegressor, and XGBRegressor

all yielded negative R^2 values. In this case, machine learning performance fell below than a simple mean predictor (Figure 5.8).

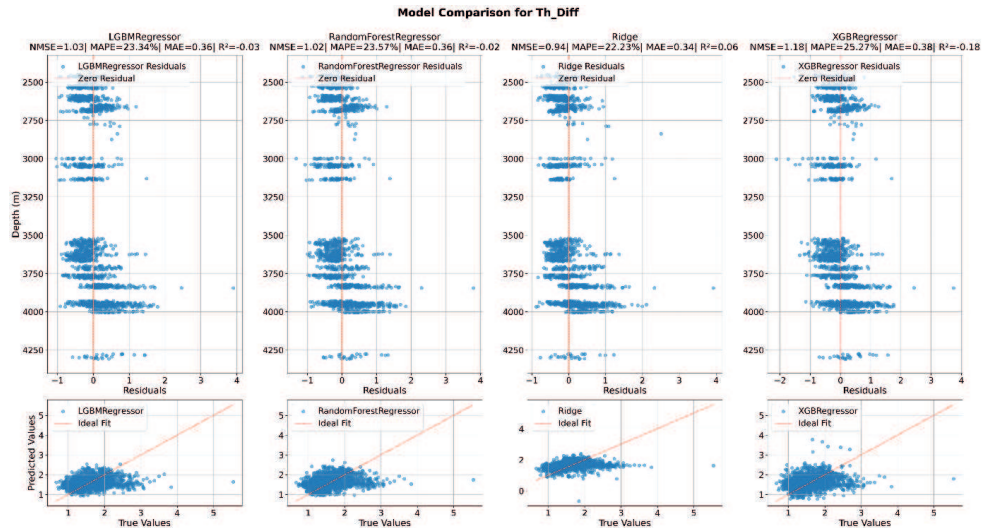


Figure 5.8 Residual and predicted vs. true value plots for the machine learning models applied to thermal diffusivity. The same models tested for thermal conductivity prediction are evaluated here, with corresponding NMSE, MAPE, MAE, and R^2 values displayed. The residual plots highlight the error distribution across depth, while the scatter plots visualise the agreement between predicted and true values.

Ridge regression, with its robustness against multicollinearity, produced residuals that were more symmetrically distributed around zero and predictions that aligned closely with the 1:1 line, indicating stable performance in capturing the dominant linear trends. However, since none of the models were tuned at this stage, these results cannot be interpreted as evidence that linear models are inherently superior. A more reliable assessment of linearity comes from the exploratory correlation analysis presented earlier. LGBMRegressor also offered comparable performance in a fraction of the training time compared to other ensemble methods. Given its comparatively longer computation time, the Random Forest Regressor was excluded from further analysis to prioritise models with higher computational efficiency. Consistent with the findings of Probst and Boulesteix (2018), who showed that the number of trees in a random forest should be set to a sufficiently large but computationally feasible value rather than tuned extensively, it was observed that exhaustive tuning of this parameter mainly increased runtime without yielding proportional gains in predictive accuracy. In contrast, while the XGBRegressor, did not outperform the other models in this study, was retained for its speed and potential for improvement through hyperparameter tuning. This refined selection ensures a balance between predictive accuracy and computational efficiency in the integration of laboratory and logging data for thermal properties estimation.

Hyperparameter tuning

Grid search

Grid search fine-tuned model parameters to improve baseline performance in predicting thermal conductivity. To do so, grid search hyperparameter tuning was conducted for Ridge Regression, LGBMRegressor, and XGBRegressor. The cross-validation method was one-well-held-out. The grid search results are summarised in Table 5.5. For each model, the optimal hyperparameter set was selected based on the lowest average mean absolute error (MAE) across the wells. The differences in optimal hyperparameter configurations across the models highlight how each algorithm balances complexity and generalisation when predicting thermal properties.

Table 5.5 Best hyperparameters and average mean absolute error (MAE) obtained from grid search for LightGBM, Ridge regression, and XGBoost models in predicting thermal conductivity and thermal diffusivity.

Model	Target Property	Best Parameters	Avg. MAE
LGBM	Thermal Conductivity	n_estimators=250, max_depth=5, learning_rate=0.01, objective=fair, boosting_type=goss	0.3861
	Thermal Diffusivity	n_estimators=100, max_depth=5, learning_rate=0.1, objective=fair, boosting_type=dart	0.3358
Ridge	Thermal Conductivity	alpha=0.1, fit_intercept=True, max_iter=None, tol=0.001, solver=saga	0.3901
	Thermal Diffusivity	alpha=100, fit_intercept=True, max_iter=None, tol=0.001, solver=sag	0.3416
XGBRegressor	Thermal Conductivity	n_estimators=250, max_depth=3, learning_rate=0.01, objective=reg:squarederror	0.4005
	Thermal Diffusivity	n_estimators=100, max_depth=3, learning_rate=0.1, objective=reg:squarederror	0.3443

The results confirmed that all three models benefited from hyperparameter tuning, though the degree of improvement varied. LGBMRegressor, which had the poorest baseline performance,

achieved the best overall results after tuning. It reached the highest coefficient of determination ($R^2 = 0.54$), and the lowest normalised mean squared error (NMSE = 0.46), along with a slight reduction in mean absolute percentage error (Figure 5.9a). This improvement reflects the model's ability to capture non-linear relationships more effectively when its complexity parameters, such as the number of leaves and learning rate, are carefully balanced.

Ridge also showed significant gains, with an increase in R^2 to 0.54 and a reduction in both NMSE and MAE compared to its default configuration (Figure 5.9b). While inherently limited to modelling linear relationships, Ridge benefited from tuning its regularisation parameter (alpha), which helped optimise the trade-off between bias and variance.

XGBRegressor, despite starting from a lower baseline performance, improved its R^2 to 0.52 post-tuning (Figure 5.9Figure 5.8c). The grid search helped identify parameter combinations that mitigated overfitting and enhanced generalisation. After LGBMRegressor as the best performer in predicting thermal conductivity, XGBRegressor and then Ridge Regression, with all tuned models outperforming their default settings.

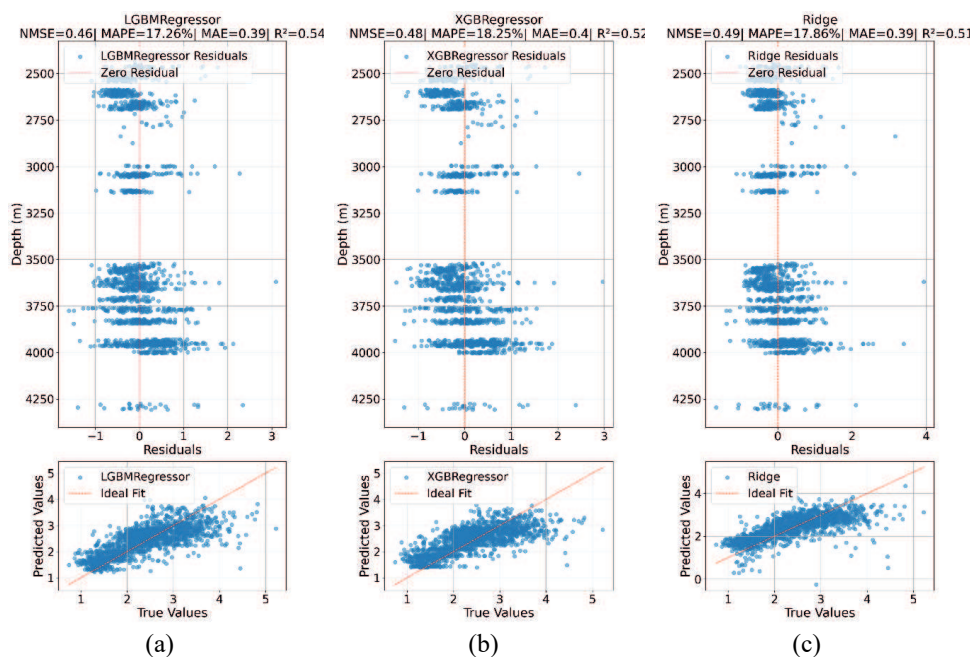


Figure 5.9 Residual and predicted versus true value plots for thermal conductivity models after hyperparameter tuning: (a) LGBMRegressor, (b) XGBRegressor, and (c) Ridge regression. Top panels show residuals versus depth with the zero-residual reference line; bottom panels show predicted versus true values with the one-to-one reference line. Each panel reports NMSE, MAPE, MAE, and R^2 .

Compared to the conductivity results, the improvements for thermal diffusivity were marginal, as shown in Figure 5.10. Ridge Regression, as the most consistent performer in the base model, showed the same R^2 of 0.07 and slightly higher NMSE of 0.98. XGBRegressor exhibited a small performance increase post-tuning, reaching an R^2 of 0.04, which remained lower than Ridge but represented an improvement over its default run. The model's tendency toward overfitting was slightly mitigated by tuning depth-related parameters, yet it still struggled to capture the variability in thermal diffusivity. LGBMRegressor, despite being the top performer for thermal conductivity, did not achieve a meaningful improvement in thermal diffusivity prediction after tuning. Its R^2 remained negative (-0.02), reflecting the persistent difficulty of capturing diffusivity trends from the available input features.

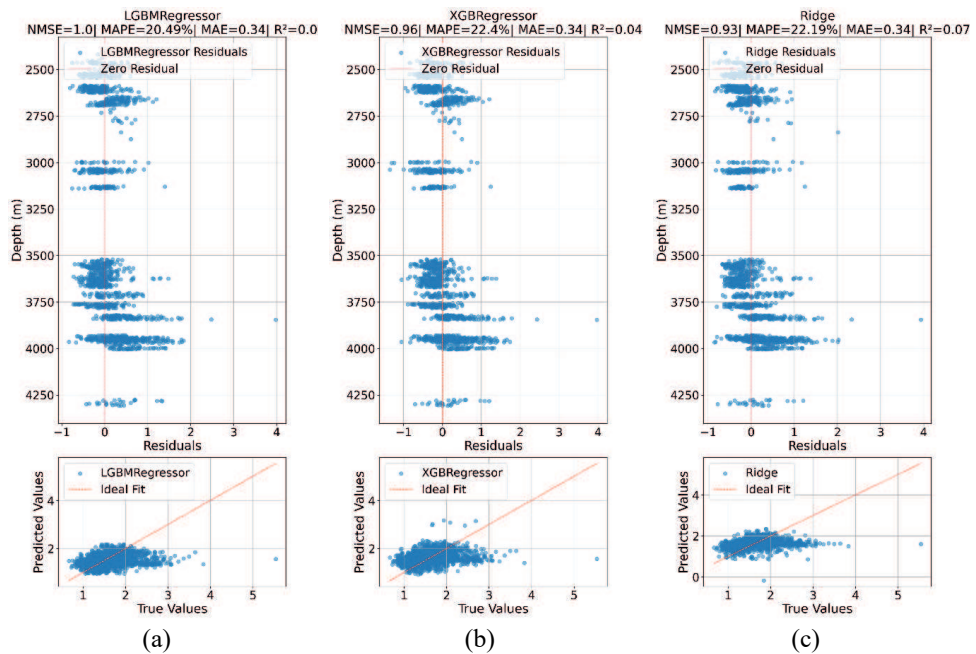


Figure 5.10 Performance of machine learning models after hyperparameter tuning for thermal diffusivity prediction. (a) LGBMRegressor after tuning shows limited improvement, with residuals remaining widely scattered and low model fit. (b) XGBRegressor after tuning exhibits slight enhancement in residual distribution and predictive alignment compared to the default configuration. (c) Ridge Regression after tuning maintains the most stable behaviour among the tested models, with minor gains in predictive accuracy and residual spread.

These outcomes underscore the inherent challenge of modelling thermal diffusivity with the given data. Even after optimisation, all models displayed limited predictive power, reinforcing the conclusion that thermal diffusivity is weakly correlated with the measured petrophysical properties. However, hyperparameter tuning proved useful in reducing overfitting tendencies and refining the models' stability, especially for Ridge Regression and XGBRegressor, which

maintained their role as the more reliable options among the tested algorithms. As detailed in Table 5.4, models tuned via grid search and Optuna generally achieve higher R^2 and lower NMSE, MAE, and MAPE than their default counterparts.

Bayesian optimisation Optuna

To further optimise model performance, automated hyperparameter tuning was performed using Optuna, a Bayesian optimisation framework designed to efficiently explore large parameter spaces, with the results shown in Table 5.6 and Figure 5.11. The goal was to push the performance of the previously selected models, LGBMRegressor, XGBRegressor, and Ridge, beyond what was achievable with grid search. The tuning with Optuna resulted in incremental yet meaningful improvements for thermal conductivity prediction.

LGBMRegressor retained its position as the best performer, achieving an R^2 of 0.57 and the lowest NMSE among the tested models. Optuna's adaptive search enabled finer adjustments to learning rate, tree depth, and regularisation parameters, enhancing both predictive accuracy and model generalisation. The tuned parameters for all models are presented in Table 5.6.

Table 5.6 Best hyperparameters and average mean absolute error (MAE) obtained from Optuna tuning for Ridge regression, LightGBM, and XGBoost models in predicting thermal conductivity and thermal diffusivity from downhole petrophysical logs.

Model	Target Property	Best Parameters	Avg. MAE
Ridge	Thermal Conductivity	alpha=0.0001	0.3899
	Thermal Diffusivity	alpha=81.97	0.3380
LGBM	Thermal Conductivity	num_leaves=191, max_depth=16, learning_rate=0.0068, n_estimators=963, min_child_samples=194, subsample=0.5214, boosting_type=gbdt, objective=fair	0.3732
	Thermal Diffusivity	num_leaves=81, max_depth=9, learning_rate=0.0160, n_estimators=1093, min_child_samples=166, subsample=0.8375, boosting_type=dart, objective=regression	0.3255

XGBRegressor	Thermal Conductivity	learning_rate=0.0120, max_depth=4, n_estimators=1345, subsample=0.7241, colsample_bytree=0.9806, gamma=1.8947, reg_alpha=0.2544, reg_lambda=0.1900, min_child_weight=17, objective=reg:squarederror	0.3820
	Thermal Diffusivity	learning_rate=0.0267, max_depth=3, n_estimators=1207, subsample=0.8460, colsample_bytree=0.8108, gamma=0.2367, reg_alpha=0.4944, reg_lambda=0.0731, min_child_weight=9, objective=reg:squarederror	0.3352

XGBRegressor followed closely with an R^2 of 0.55, benefiting from targeted tuning of its learning rate, max depth, and subsample ratio. Although slightly behind LGBMRegressor in terms of error metrics, XGBRegressor demonstrated more stable residual distributions compared to its previous tuned versions.

Ridge Regression showed moderate gains, reaching an R^2 of 0.51, confirming its robustness and consistency despite its simpler linear nature. This indicates that the linear model quickly reaches its performance ceiling and cannot capture more complex relationships, limiting its practical value. Fine-tuning the regularisation strength via Optuna only reduced bias marginally, without substantial improvement in predictive accuracy.

These results demonstrate that Optuna-based hyperparameter tuning produced performance comparable, and in some cases slightly superior, to grid search. However, this came at a higher computational cost, and the benefits were only meaningful for the more complex ensemble models (LGBMRegressor, XGBRegressor). Among all tested models, LGBMRegressor consistently offered the best trade-off between prediction accuracy and efficiency, making it the preferred choice for predicting thermal conductivity from integrated laboratory and well-log data.

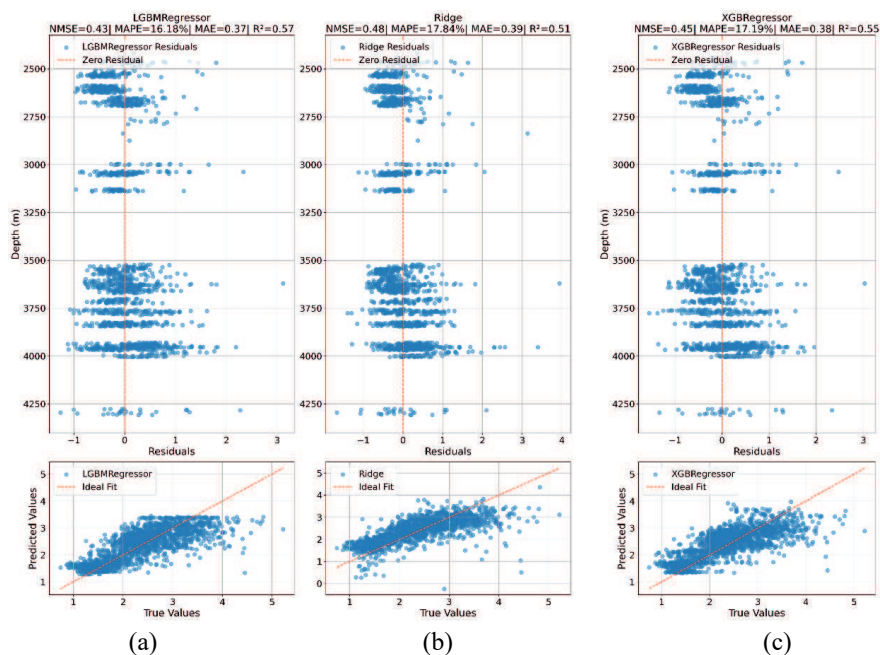


Figure 5.11 Performance of machine learning models after Optuna-based hyperparameter tuning for thermal conductivity prediction. (a) LGBMRegressor delivers the best overall predictive performance with optimised learning rate, tree depth, and regularisation settings. (b) Ridge Regression exhibits stable behaviour with modest gains in fit following optimisation of the regularisation parameter. (c) XGBRegressor shows improved residual distribution and prediction accuracy after adaptive tuning of model complexity and regularisation parameters.

As anticipated from earlier analyses, the improvements in thermal diffusivity prediction were subtle. XGBRegressor showed the best post-tuning performance, reaching an R^2 of 0.08 and slightly lower error metrics compared to its default and grid search versions. Although modest, this improvement indicates that XGBRegressor responded well to targeted tuning of its depth, learning rate, and subsampling parameters.

LGBMRegressor followed closely with an R^2 of 0.04, maintaining its characteristic computational efficiency but still failing to establish a strong correlation with thermal diffusivity. The limited impact of tuning suggests that, for this target, LGBMRegressor structural advantages do not translate into significant predictive gains.

Ridge, while remaining the most stable linear model in our selection, achieved an R^2 of 0.07, mirroring its prior behaviour with only marginal improvement. Its main strength lies in its robustness to multicollinearity among predictors and to violations of linear regression assumptions, although it lacked the flexibility to capture the weak underlying patterns in the data.

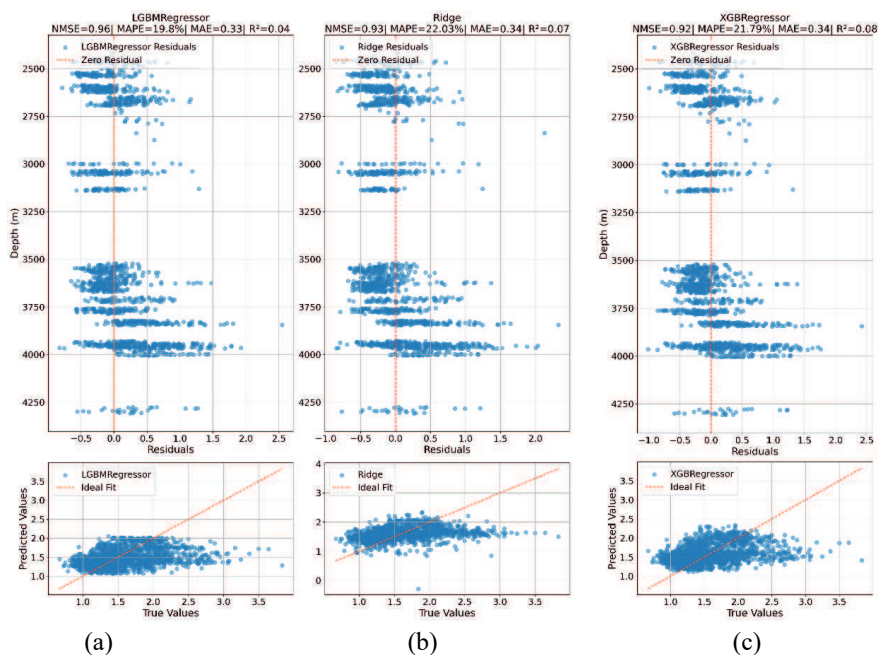


Figure 5.12 Results of Optuna-based hyperparameter tuning for thermal diffusivity prediction using (a) LGBMRegressor, (b) Ridge Regression, and (c) XGBRegressor. Residuals are shown as a function of depth, and scatter plots compare predicted and measured values for each model.

In summary, Optuna-based hyperparameter tuning confirmed the inherent difficulty of predicting thermal diffusivity from the selected petrophysical features. While XGBRegressor and LGBMRegressor offered slight enhancements, none of the models achieved substantial accuracy gains. These findings reinforce the earlier conclusion that thermal diffusivity is weakly linked to the available measurements and may require either additional predictors or alternative modelling strategies for improved estimation.

Further evaluation of the model performance of individual wells showed that for Q04-C2 the tuned ensembles (particularly LGBMRegressor and XGBRegressor) provide the best visual agreement with measurements, with Ridge offering a stable but slightly biased linear reference. For well Q04-C2, the side-by-side panels show a clear progression from default to tuned models (Figure 5.13). In the default panel, Ridge Regression follows the measured thermal-conductivity trend most closely, while the tree-based models, especially Random Forest, display a wider scatter and a tendency to miss the extremes. After grid-search tuning, the ensemble methods tighten markedly around the measurements. LGBMRegressor and XGBRegressor reproduce both the shallow interval with higher thermal conductivity and the deeper interval with lower thermal conductivity with a slope and spread that visually match the observations better than the default runs, while Ridge remains a strong linear baseline but still

clips some extremes. The Optuna-tuned panel is broadly consistent with the grid-search results, yielding incremental refinements rather than large changes; LGBMRegressor and XGBRegressor continue to align closely with the measured points, and residual scatter is reduced relative to the default case. The accompanying sonic travel time (DT), Gamma Ray (GR), Bulk Density (RHOB) and Porosity (POR) tracks indicate depth intervals where petrophysical contrasts coincide with changes in thermal conductivity, and the tuned ensemble models are the most responsive to these log-derived variations, whereas Ridge remains more conservative.

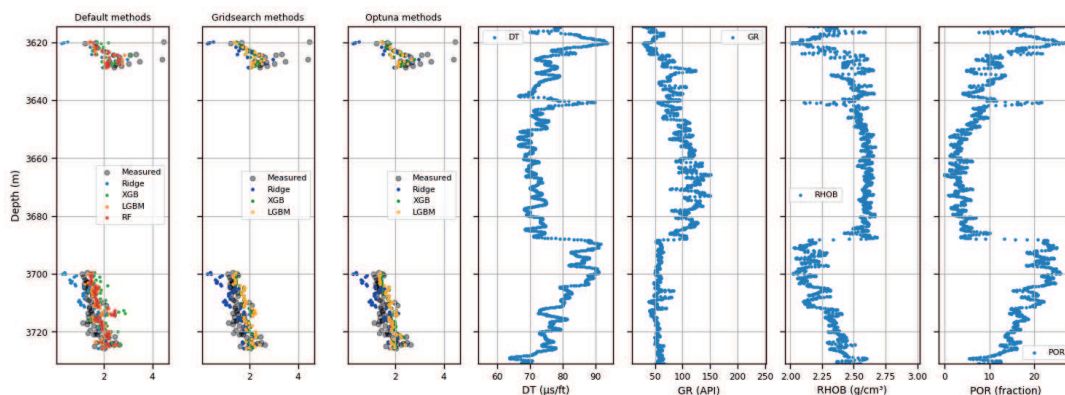


Figure 5.13 Predicted thermal conductivity ($W/m\cdot K$) versus depth for the Q04-C2 well using Ridge, Random Forest, LGBMRegressor, and XGBRegressor under three setups (Default, Grid-search, Optuna), plotted against measured values; depth increases downward. DT, GR, RHOB, and POR logs are shown for context.

These findings were further reinforced by grouped cross-validation by well, which confirmed that thermal conductivity models generalised reasonably across different wells after tuning, whereas thermal diffusivity predictions remained inconsistent and unreliable. The analysis underscores that while model choice, tuning strategy, and cross-validation are critical for optimizing predictive performance, their success ultimately depends on the presence of meaningful relationships between the input features and the target properties. In the case of thermal conductivity, such a relationship exists and can be exploited with careful modelling. In contrast, for thermal diffusivity, the lack of a strong link to the available petrophysical features limited the effectiveness of all tested models, regardless of algorithm or optimisation method.

Feature importance analysis

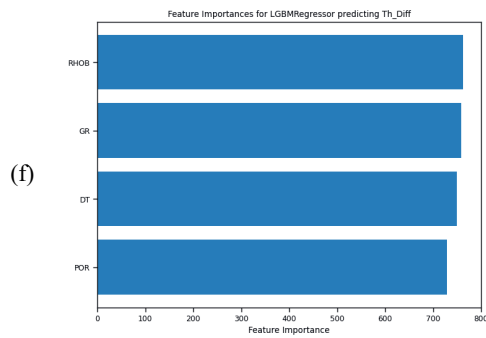
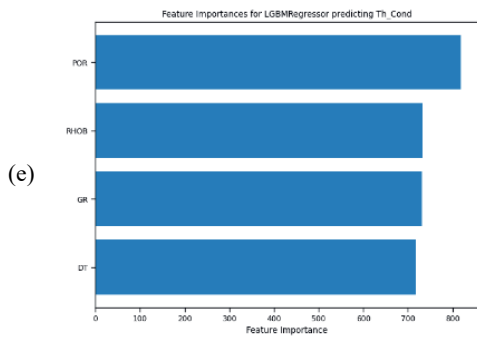
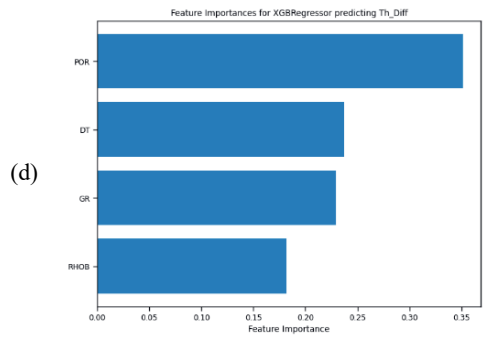
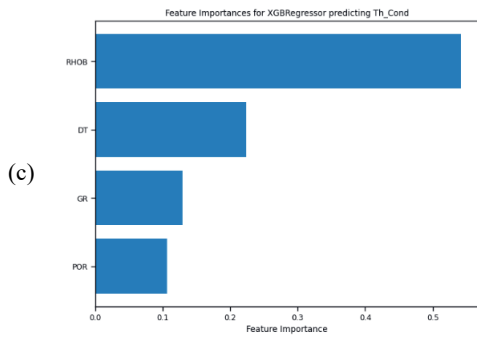
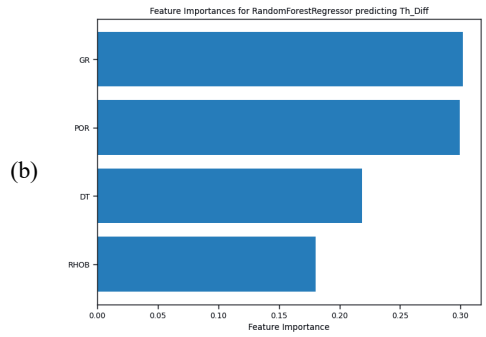
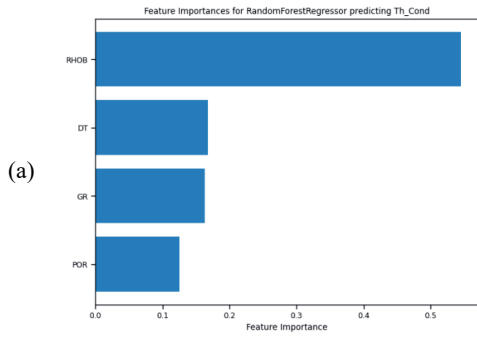
The feature importance analysis based on the default machine learning models highlighted distinct trends between thermal conductivity and thermal diffusivity prediction attempts.

For thermal conductivity, the models largely agreed on the key contributing features (Figure 5.14a, c, e, and g). Bulk density (RHOB) emerged as the most influential predictor across all

models, particularly in Random Forest and XGBRegressor, where it accounted for more than half of the predictive importance. This aligns well with the expected physical relationship, as bulk density reflects compaction and mineral framework, both critical to heat conduction in sedimentary rocks. Sonic travel time (DT) consistently ranked as the second most important feature, likely due to its link with elastic properties, which are also influenced by compaction and lithology. Porosity (POR) and Gamma Ray (GR) had comparatively lower importance, with porosity ranking last in XGBRegressor and Random Forest but gaining importance in LGBMRegressor, where feature scores were more balanced. LGBMRegressor, in contrast to the other ensemble models, showed a more even distribution of feature importance among all predictors, including gamma ray and porosity, suggesting that its tree structure may have captured interactions between features better. Ridge Regression reinforced this pattern, assigning a strong positive coefficient to bulk density and negative coefficients to DT, GR, and POR, reflecting their inverse relationships with thermal conductivity in a linear model framework.

In the case of thermal diffusivity, the feature importance distributions were noticeably different. Unlike for thermal conductivity, no single feature dominated the prediction (Figure 5.14b, d, f, and h). Instead, the importance was spread almost equally among all four predictors in both Random Forest and LGBMRegressor, indicating that none of the input features provided a consistently strong signal for predicting thermal diffusivity. XGBRegressor showed slightly higher importance for porosity and DT but still lacked a clear leading predictor. Ridge Regression confirmed this observation, assigning small negative coefficients to all features, with bulk density contributing almost negligibly. This spread of importance suggests that thermal diffusivity may not be directly controlled by any of the logged petrophysical parameters, supporting the earlier finding that diffusivity could be influenced by factors beyond the scope of standard well logs.

Integrating experimental and log data to predict thermal rock properties in geothermal plays using machine learning



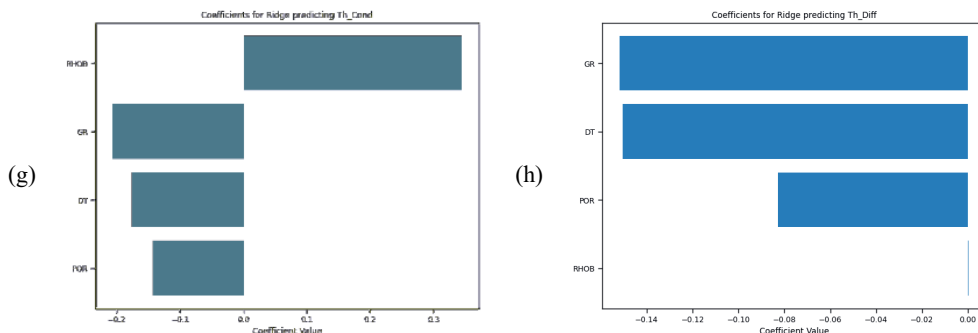


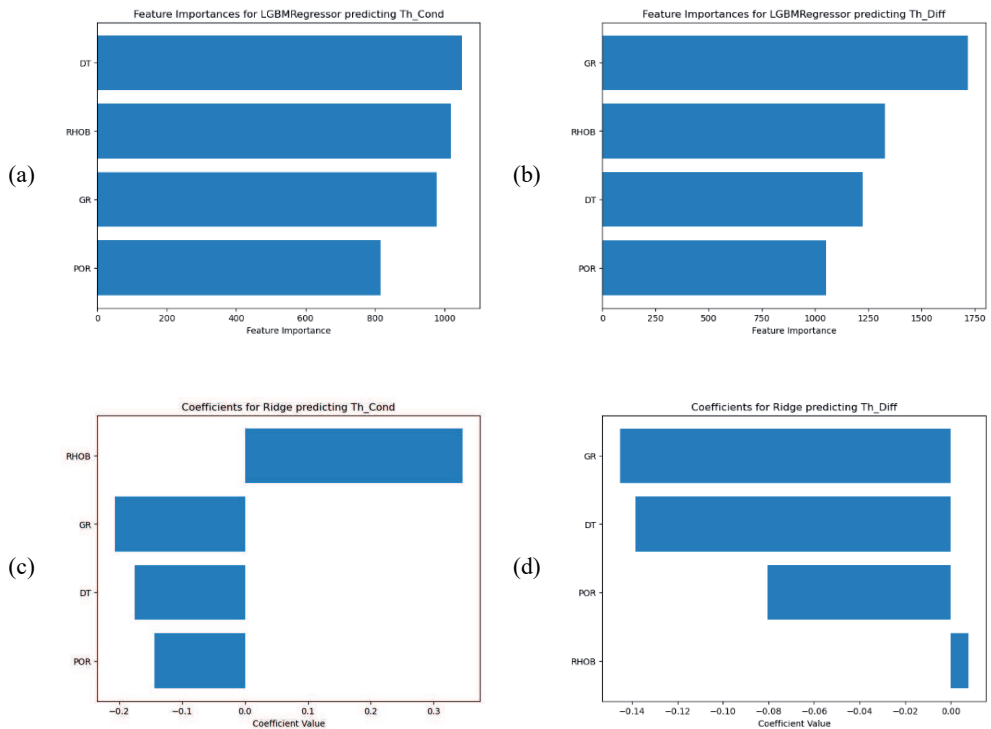
Figure 5.14 Feature importance and coefficient analysis of models predicting thermal conductivity and thermal diffusivity. (a, b) Random Forest Regressor feature importances for thermal conductivity and thermal diffusivity, respectively. (c, d) XGBRegressor feature importances for thermal conductivity and thermal diffusivity. (e, f) LGBMRegressor feature importances for thermal conductivity and thermal diffusivity. (g, h) Ridge regression coefficients for thermal conductivity and thermal diffusivity. The results highlight the relative contribution of each input parameter, bulk density (RHOB), gamma ray (GR), sonic (DT), and porosity (POR), to the model predictions.

For thermal conductivity, Optuna tuning resulted in more balanced and consistent feature importance across models, particularly for the ensemble methods (Figure 5.15a, c, and e). In the LGBMRegressor model, feature importances were closely distributed among sonic travel time (DT), bulk density (RHOB), and gamma ray (GR), with porosity (POR) slightly less but still contributing. Unlike the default setting, where RHOB dominated, the Optuna-tuned LGBMRegressor model suggests that sonic velocity and gamma ray gained predictive relevance after optimisation. This implies that while bulk density remains critical, the model benefited from capturing complex interactions between multiple petrophysical parameters when tuned. The Ridge Regression model maintained its characteristic pattern with a strong positive coefficient for RHOB and negative coefficients for DT, GR, and POR, consistent with the linear trends observed in the data. XGBRegressor, post-Optuna tuning, continued to assign the highest importance to RHOB, followed by DT, with GR and POR contributing less, mirroring the pattern seen in the grid search-tuned models. Overall, Optuna tuning did not drastically alter the fundamental relationships identified in the earlier stages but fine-tuned the weighting of features, especially in LGBMRegressor, making their contributions more balanced. This balance likely contributed to the observed performance gains in cross-validation metrics.

For thermal diffusivity, Optuna tuning reinforced the earlier finding of weak and diffuse feature contributions (Figure 5.15b, d, and f). In the LGBMRegressor model, gamma ray (GR) emerged as the most important feature, followed by bulk density, sonic travel time, and porosity, all with relatively comparable importance scores. This uniform spread of importance

suggests that no single predictor had a dominant influence on thermal diffusivity estimation, even after tuning. The XGBRegressor model showed a similar trend, with GR, porosity, and DT contributing almost equally, and RHOB slightly less. Ridge Regression again displayed negligible coefficients for all features, further indicating the absence of strong linear relationships.

The persistent lack of dominant features for thermal diffusivity, even after tuning, highlights the intrinsic limitations of the dataset in capturing the controlling factors of this property. While Optuna tuning helped stabilise feature importance patterns and possibly reduced model variance, it did not lead to any clear identification of key predictors, supporting the conclusion that thermal diffusivity cannot be reliably modelled using standard petrophysical logs alone.



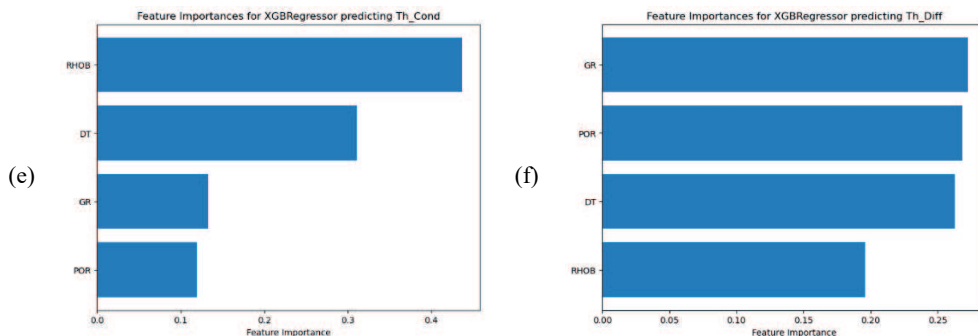


Figure 5.15 Feature importance and coefficient analysis of Optuna-optimised models predicting thermal conductivity and thermal diffusivity. (a, b) LGBMRegressor feature importances for thermal conductivity and thermal diffusivity, respectively. (c, d) Ridge regression coefficients for thermal conductivity and thermal diffusivity. (e, f) XGBRegressor feature importances for thermal conductivity and thermal diffusivity. The analysis highlights the relative contribution of each input parameter, bulk density (RHOB), gamma ray (GR), sonic (DT), and porosity (POR), to the prediction of thermal properties after hyperparameter tuning using Optuna.

For thermal conductivity, the feature importance patterns showed both consistency and adjustment after Optuna tuning. In the default ensemble models, particularly Random Forest and XGBRegressor, bulk density (RHOB) clearly dominated the rankings, often contributing more than half of the total importance. Sonic travel time (DT) and gamma ray (GR) followed with moderate influence, while porosity (POR) remained consistently the least important predictor. This reflects a strong dependence on RHOB in untuned models, likely due to their tendency to prioritise straightforward linear relationships in the data.

After tuning, the distribution of feature importance changed, most particularly in the LGBMRegressor models. In the Optuna-tuned LGBMRegressor, RHOB, DT, and GR shared similar importance scores, and POR also contributed more substantially. This suggests that tuning enabled the model to incorporate multi-feature interactions rather than relying predominantly on a single variable. A similar, though less pronounced, pattern was observed in XGBRegressor, where RHOB remained the most important feature, but the gap between predictors narrowed. Ridge Regression, as expected for a linear model, showed stable coefficients before and after tuning, consistently identifying RHOB as positively related to thermal conductivity, with DT, GR, and POR contributing negatively. Overall, Optuna tuning reduced the dominance of RHOB and allowed ensemble models, particularly LGBMRegressor, to make better use of the available predictors. This improved balance corresponds with the increase in model performance, supporting the interpretation that improved predictions stem from capturing complementary information across multiple features rather than over-relying on a single input. In contrast, feature importance patterns for thermal diffusivity remained

weakly structured in both default and tuned models. In the untuned versions of Random Forest and XGBRegressor, importance was almost evenly distributed across all predictors, with no single feature standing out. LGBMRegressor showed a slight tendency for gamma ray and porosity to contribute more, but the pattern lacked consistency.

After tuning, this diffuse distribution persisted. In LGBMRegressor, GR became marginally more important, with RHOB, DT, and POR contributing at similar levels. XGBRegressor showed a comparable spread, with minor changes in ranking but no clear shift in dominance. Ridge Regression continued to assign low and relatively uniform coefficients to all predictors, with no significant change after tuning. These results indicate that hyperparameter tuning had a clear impact on feature importance in the thermal conductivity models, supporting a more balanced use of predictors and likely improving generalisation. For thermal diffusivity, however, tuning did not substantially alter the weak and scattered feature contributions, reinforcing the conclusion that none of the logged parameters adequately explain its variability.

The feature importance results presented in this section confirm that DT, GR and bulk density are the most influential predictors of thermal conductivity across all machine learning models. These findings are consistent with the physical interpretation of rock properties, where porosity controls both the solid framework and fluid content, thereby affecting both elastic and thermal responses. However, it is important to note that high feature importance does not imply causality. For example, although Vs ranks highly as a predictor, it does not directly influence thermal conductivity. Instead, both properties respond similarly to shared geological factors such as porosity, mineralogy, and compaction. This distinction is further clarified by the PCA results, which show Vp, Vs, and thermal conductivity clustering together and opposing porosity. Therefore, the relationships captured by the models reflect common physical controls rather than direct cause-and-effect mechanisms. In contrast, thermal diffusivity shows lower predictability and weaker feature associations, highlighting its dependence on additional parameters, such as heat capacity, not fully captured by standard petrophysical logs. This effect is expected to be even more pronounced under downhole conditions, where the presence of water with its high heat capacity and low thermal conductivity reduces the strength of correlations with bulk density and porosity observed under dry laboratory conditions.

Feature importance analysis revealed that RHOB and GR were the most influential input features for predicting thermal conductivity. Based on this, a second set of models was trained using only these two logs to evaluate whether acceptable predictive performance could still be achieved with a reduced input set. The results showed a slight decrease in R^2 values across all models compared to using the full set of four features (DT, GR, RHOB, and porosity), with Ridge Regression dropping from 0.51 to 0.48, LGBMRegressor from 0.57 to 0.53, and XGBRegressor from 0.55 to 0.54. Although the performance declined marginally, the GR and RHOB models still produced reasonably accurate predictions. This confirms that these two features alone carry substantial predictive power, making them suitable for use in scenarios

where log availability is limited. The limited performance loss after removing DT and porosity can be explained by the strong correlations observed in the exploratory analysis: porosity and bulk density showed an almost one-to-one inverse relationship, and both porosity and sonic velocity exhibited a linear dependence. As a result, bulk density effectively carries the information contained in porosity and DT into the training process, reducing the impact of their removal. Nonetheless, the improved performance observed when including DT and porosity suggests that these additional features provide complementary information that helps capture more variability in thermal conductivity.

From a practical standpoint, these results suggest a stepwise approach for end-users. In data-rich settings, where all four key logs are available, incorporating DT and porosity alongside RHOB and GR is recommended to achieve the most accurate predictions. In data-limited wells, RHOB and GR alone can still yield useful estimates, allowing thermal conductivity to be approximated even in older wells or in areas with incomplete logging suites. In all cases, model outputs should be interpreted considering the geological context, ensuring that predictions are cross-checked against formation-specific trends and available core data before being used for geothermal modelling or reservoir simulations.

Overall, the results highlight several key observations. Ridge Regression proves to be a robust baseline model, offering consistent performance despite its simplicity and often performing competitively with more complex ensemble models. Among the models tested, the LGBMRegressor, when properly tuned, consistently achieved the best combination of high R^2 , low NMSE, and low MAE, making it the most effective model for predicting thermal conductivity from integrated laboratory and well-log data for in this dataset. The importance of hyperparameter tuning is particularly evident for ensemble models, whose performance otherwise tends to fall behind that of Ridge Regression.

5.4. Discussion

The results gathered in this chapter demonstrated that machine learning models can capture relationships between thermal and petrophysical properties when evaluated under realistic validation settings. Thermal conductivity was predicted with moderate success, particularly by the ensemble model XGBRegressor, while thermal diffusivity remained poorly constrained. A range of approaches was tested, including four models, two hyperparameter tuning strategies, and two cross-validation schemes, and the best-performing configurations based on their evaluation metrics were identified to be XGBRegressor with Optuna hyperparameter tuning and one-well-held-out cross validation. Building on these findings, the discussion now turns to the underlying physical relationships observed in the experimental data. Clear interdependencies were identified among porosity, bulk density, V_p , and V_s , which in turn influence the thermal behaviour of the rocks. These links between porosity, compaction, and rock framework properties provide the basis for interpreting the predictive performance of thermal conductivity and thermal diffusivity models.

5.4.1. Interpretation of experimental data

The nearly perfect inverse correlation between porosity and bulk density ($R^2 = 0.95$; Figure 5.4a) is consistent with the basic principle that bulk density scales directly with the fraction of solid mineral matter and inversely with pore volume. In sedimentary rocks, porosity reduction typically results from compaction and cementation, processes that progressively close pore spaces and increase solid contact between grains (Bjørlykke et al., 2009; Hiatt, 2000). This porosity–bulk density relationship underscores the dominance of mechanical compaction in shaping the properties of the Rotliegend and Triassic sandstones examined.

The strong correlation between V_p and V_s ($R^2 = 0.95$; Figure 5.4b) reflects their shared sensitivity to elastic moduli, particularly bulk and shear moduli, which depend on both mineral composition and the integrity of grain contacts. As porosity decreases, grain contacts mainly improved, although this depends on sorting, and the rock behaves more as a coherent elastic medium, thereby increasing both V_p and V_s . This behaviour aligns with rock physics models describing elastic wave propagation in porous media (Dvorkin & Nur, 1996), where the elastic moduli, and hence wave velocities, are primarily governed by the solid framework rather than the pore fluid at seismic frequencies.

Thermal conductivity exhibited a moderate but significant correlation with porosity ($R^2 = 0.56$; Figure 5.5a) and bulk density ($R^2 = 0.53$; Figure 5.5b). These relationships are expected, considering that heat conduction in rocks occurs mainly through the solid matrix, with pore spaces, particularly when air-filled, acting as thermal insulators. As porosity decreases, the connectivity within the solid matrix improves, enhancing heat conduction pathways. This observation is in line with established theoretical models, such as the geometric mean model for composite media (Clauser & Huenges, 1995b), which predict that bulk thermal conductivity increases as the fraction of the highly conductive solid phase rises.

The correlation between thermal conductivity and elastic wave velocities (e.g., Figure 5.6) was moderate, despite both properties showing strong individual relationships with porosity and bulk density. This result highlights that, although both thermal and elastic properties are affected by porosity and compaction, they are governed by distinct physical mechanisms. Elastic wave velocities primarily reflect the stiffness of grain-to-grain contacts and are sensitive to the presence of fractures or microcracks that affect mechanical coupling (Mavko et al., 2009). In contrast, thermal conductivity depends on the continuity and connectivity of the solid mineral phase, and is less affected by the stiffness of grain contacts (Clauser & Huenges, 1995b). The presence of microcracks influences both the mechanical and thermal properties of rocks, but through distinct mechanisms, while elastic properties are primarily affected by the weakening of grain contacts and changes in stiffness, thermal conductivity is altered by the disruption of continuous heat conduction pathways within the mineral framework (Fredrich & Wong, 1986). Their systematic SEM observations and fracture mechanics analysis confirmed

these effects, linking elastic property degradation to grain contact damage and reduced thermal conductivity to interrupted heat transfer in the solid matrix.

Principal component analysis provided additional insight into the dataset's structure. The first principal component explained 70.5% of the variance and was heavily loaded on bulk density, velocities, and thermal conductivity, and porosity (Figure 5.4). This result confirms that these properties are governed by a common underlying factor, likely the degree of compaction and consolidation, and that porosity acts inversely along this trend. Anovitz and Cole (2015) demonstrated that geological processes such as compaction, cementation, dissolution, and fracturing significantly modify pore structures in rocks, which in turn influence fluid transport and various bulk physical properties.

Finally, although these relationships are robust within the studied dataset, their predictive power may be limited when applied to other geological settings. The heterogeneity of sedimentary rocks, particularly variations in mineralogy and diagenetic history, can significantly influence these trends. Therefore, although the findings confirm theoretical expectations and are consistent with previous empirical observations (Clauser & Huenges, 1995b), caution is advised when extrapolating to other formations without further calibration.

5.4.2. Evaluation of the ML models

5.4.2.1. Thermal conductivity prediction

The machine learning models applied to predict thermal conductivity from well-log-derived features revealed distinct trends depending on the algorithm and the tuning strategy. Across all workflows, Ridge Regression, and tree-based ensemble models (Random Forest, LGBMRegressor, and XGBRegressor) showed varying degrees of success, with model performance consistently improving after hyperparameter optimisation.

In the base models, Ridge outperformed all ensemble models, yielding an R^2 of 0.51, an NMSE of 0.49, and an MAE of 0.39 W/m·K. These results fall within the good performance range for all three metrics according to the adopted thresholds. Ridge's stability in the default run is likely due to its linear nature, which suits the mostly linear relationships observed between thermal conductivity and petrophysical features in the experimental data.

Conversely, the default ensemble models performed worse than Ridge Regression. Random Forest, LGBMRegressor, and XGBRegressor produced lower R^2 values (0.48, 0.45, and 0.40, respectively), with NMSE between 0.52 and 0.56 and MAE between 0.41 and 0.44 W/m·K, placing them mainly in the "neutral" to "bad" categories for R^2 and NMSE, and in the neutral category for MAE. This suggests that, when applied without parameter tuning, tree-based methods capture some non-linear trends but fail to generalise optimally in the presence of inter-well variability and the limited size of the dataset.

With grid search hyperparameter tuning, all models improved. Ridge Regression's R^2 increased slightly to 0.54, NMSE remained at 0.49, and MAE improved to 0.34 W/m·K, maintaining “good” performance across metrics. LGBMRegressor achieved the highest R^2 (0.57) and the lowest NMSE (0.42) and MAE (0.32 W/m·K), ranking as the top performer. XGBRegressor also performed well post-tuning, with an R^2 of 0.55, NMSE of 0.45, and MAE of 0.35 W/m·K. These results confirm that hyperparameter tuning is particularly beneficial for ensemble models, enabling them to better capture the non-linear relationships in the data.

Further refinement using Optuna-based tuning led to marginal or negligible gains compared to grid search. LGBMRegressor maintained its leading performance ($R^2 = 0.57$, NMSE = 0.42, MAE = 0.32 W/m·K), while XGBRegressor and Ridge Regression achieved similar results to their grid search configurations. Ridge Regression, for example, had an R^2 of 0.51, NMSE of 0.49, and MAE of 0.35 W/m·K, indicating that its optimal performance was already reached during earlier tuning.

The performance of all tuned models converges within a narrow range of R^2 values (0.51–0.57) and MAE (0.32–0.35 W/m·K), indicating a common predictive ceiling likely imposed by limited variability and resolution of the input logs, as well as by the geological heterogeneity among the samples. These results underscore that thermal conductivity can be predicted with moderate confidence from standard petrophysical logs, particularly when leveraging ensemble models with carefully optimised parameters. However, even under optimal tuning, the achievable R^2 values suggest that additional geological or mineralogical parameters may be needed to further enhance model accuracy.

5.4.2.2. Thermal diffusivity prediction

The prediction of thermal diffusivity from well-log-derived features presented a consistent challenge across all machine learning workflows. Unlike thermal conductivity, which showed moderate predictability after tuning, thermal diffusivity models performed poorly, with R^2 values remaining low or even negative, regardless of the algorithm or optimisation strategy used.

In the default configuration, all models failed to capture strong relationships between the input features and thermal diffusivity. Ridge Regression achieved the highest R^2 among the defaults (0.06), but NMSE was 0.94 and MAE was 0.34 m²/s, placing it in the neutral category for R^2 and bad for NMSE. Ensemble models performed even weaker, with Random Forest, LGBMRegressor, and XGBRegressor showing negative R^2 values (-0.02, -0.03, and -0.18, respectively), NMSE above 0.92, and MAE between 0.32 and 0.38 m²/s. These results indicate that, without tuning, none of the tested models could generalise patterns within the data, likely due to weak inherent correlations between thermal diffusivity and standard petrophysical logs.

With grid search hyperparameter tuning, slight improvements were observed. Ridge Regression achieved a neutral R^2 of 0.07, while LGBMRegressor and XGBRegressor reached -0.02 and 0.04, respectively. NMSE values remained close to or above 0.92, and MAE values ranged from 0.32 to 0.43 m²/s, suggesting that while tuning reduced some variance, it did not uncover meaningful predictive patterns.

Optuna-based tuning yielded similarly marginal gains. XGBRegressor reached its highest R^2 of 0.08, slightly outperforming Ridge (0.07) and LGBMRegressor (0.04), but all models remained well below the good performance threshold. NMSE values stayed between 0.92 and 0.98, and MAE values between 0.29 and 0.33 m²/s, confirming that even advanced tuning strategies cannot overcome the fundamental predictive limitations. For Ridge Regression, Bayesian optimisation may appear excessive given the small number of hyperparameters and the speed of training. A simpler approach such as random or grid search would have been sufficient. However, Optuna was retained across all models to ensure a consistent optimisation framework and comparable treatment of model complexity.

These results indicate that thermal diffusivity exhibits a weak relationship with petrophysical properties derived from well logs, such as gamma ray, bulk density, porosity, and sonic velocity. This observation is consistent with experimental data interpretation, where thermal diffusivity showed lower correlation coefficients with these parameters compared to thermal conductivity. The findings suggest that diffusivity is influenced by additional factors not captured by conventional logging tools, but also on complex, possibly non-linear interactions among known properties. Furthermore, laboratory-derived diffusivity values may reflect microstructural or mineralogical characteristics, and potentially measurement variability, which are not represented at the resolution or scale of well-log measurements.

Future work should focus on incorporating parameters that better capture the effects of water saturation, mineral composition, and microstructure on thermal diffusivity. The feature importance analysis showed that gamma ray (GR) was the most influential predictor of thermal diffusivity in most models. This indicates that variations in mineral composition, probably in clay, have a measurable impact on diffusivity. This highlights the need to refine mineralogical descriptors beyond GR, for example, using spectral gamma-ray (Caldwell et al., 1963) or elemental capture spectroscopy logs. The photoelectric factor (PE) could also be used to distinguish mineral types, particularly carbonate versus clay content, due to its sensitivity to mineral composition differences (Hu et al., 2023). Since diffusivity also depends on water saturation, integrating saturation estimates from resistivity or NMR logs could further improve predictions. Complementary laboratory measurements under varying saturation, temperature, and pressure conditions would help establish quantitative relationships under reservoir-relevant conditions.

5.5. Conclusions

This study explored the use of machine learning models to predict thermal conductivity and thermal diffusivity of sedimentary rocks using laboratory measurements and petrophysical well-log data. The results confirm that thermal conductivity is moderately correlated with bulk density, porosity, and sonic velocity, and can be predicted with reasonable accuracy using multivariate models. Among the tested algorithms, LGBMRegressor, when properly tuned, consistently provided the best balance between accuracy and stability. Ridge Regression produced more stable but generally lower R^2 values, while XGBRegressor achieved slightly higher mean R^2 but with larger variability, making it less reliable. Hyperparameter tuning was critical for improving ensemble model performance, enabling a more balanced use of input features, and reducing over-reliance on bulk density. Overall, Optuna and grid search produced comparable results, but Bayesian optimisation required substantially more computation, making its use justifiable mainly for the more complex ensemble models. Between the two validation strategies, one-well-held-out cross-validation proved to be the most reliable framework. While k-fold validation across samples gave higher apparent accuracy, it suffered from information leakage, whereas the well-based approach provided a more realistic assessment of model generalisation to unseen wells.

For model selection, both the mean R^2 and its standard deviation were considered since a high R^2 alone is not sufficient if the performance varies strongly across folds. A model with a slightly lower mean R^2 but a smaller standard deviation is more reliable and therefore preferable. Based on this criterion, the best model for predicting thermal conductivity is XGBRegressor with Optuna hyperparameter tuning, which achieved a mean R^2 of 0.570 with a comparatively low standard deviation of 0.233, indicating both good accuracy and stable performance across folds. In contrast, thermal diffusivity proved far more challenging to predict. All models yielded very low mean R^2 values (generally < 0.1) with large standard deviations (~ 0.5 – 0.6), meaning their performance was unstable and often close to random. Even the top performer, XGBRegressor (Optuna, $R^2 = 0.082 \pm 0.504$), lacked robustness, showing that diffusivity cannot be predicted reliably with the available dataset and features.

Overall, the findings highlight both the potential and limitations of data-driven models in geothermal applications. While machine learning can support the prediction of thermal conductivity using conventional well-log data, improving predictions for thermal diffusivity will likely require the integration of additional geological or imaging data. A key advantage of the machine learning approach demonstrated in this study is its ability to estimate thermal conductivity directly from standard well-log data, reducing reliance on laboratory measurements from core samples, which are often sparse or unavailable. The results underscore the importance of understanding the physical controls behind each property and the need for careful feature selection and model calibration in data-driven subsurface prediction.

6.Synthesis and Conclusions

This thesis presents an investigation into the thermal and mechanical behaviour of key geothermal formations in the Dutch subsurface, including the Permian Upper Rotliegend Group, the Triassic Main Buntsandstein Subgroup, and the lower Cretaceous Delft Sandstone Member, through a combination of laboratory measurements, petrophysical well-log analysis, and data-driven predictive modelling. The work advances our understanding of subsurface property variability and demonstrates new methodologies for improving geothermal reservoir characterisation in data-scarce settings. This chapter synthesises the principal outcomes of the thesis and reflects on their implications for geothermal development and broader subsurface applications.

6.1. Integrated dataset and experimental insights

The foundation of this research lies in the compilation and analysis of the most extensive integrated dataset to date of thermal, acoustic, and other petrophysical properties of Dutch geothermal reservoir formations, which also represents the largest open sandstone-based dataset in a broader geothermal context and other subsurface projects. This dataset was developed through systematic laboratory testing of more than 1100 core plug samples from the Permian Rotliegend group, over 700 samples from the Triassic Main Buntsandstein Subgroup (see Chapters 2 and 3). Measurements included porosity, bulk density, permeability, thermal conductivity, thermal diffusivity, volumetric heat capacity, and compressional and shear wave velocities, all conducted under consistent dry and ambient conditions (Kolah-Kaj et al., 2024).

In addition to these extensive Permian and Triassic datasets, 60 cylindrical core plugs from the lower Cretaceous Delft Sandstone Member were analysed to determine their static mechanical properties, as well as porosity, permeability, density and thermal properties. The mechanical properties were measured using uniaxial and triaxial compression tests at varying confining pressures to simulate in-situ stress conditions (Chapter 4). Together, these datasets provide a robust basis for assessing cross-formational trends in rock behaviour and support the development of property estimation workflows that are both formation-specific and data-driven.

These datasets result in a set of empirical correlations between rock properties. Across formations, thermal conductivity and V_p both displayed strong negative correlations with porosity, highlighting porosity's fundamental control on thermal and acoustic behaviour. The results also reveal a clear divergence in controls: while thermal conductivity is found to be dominantly influenced by porosity and mineralogical composition, acoustic properties are more sensitive to rock texture, compaction state, and grain contact character. Porosity is the main control on thermal and acoustic properties, while detrital clay content and cementing minerals introduce systematic deviations. In the Triassic, high detrital clay fractions at low porosity create a more continuous medium that raises acoustic velocities while lowers thermal diffusivity through increased heat capacity. The Permian is more dominated by quartz cement and replacive clays that reduce acoustic velocities but maintain higher thermal conductivity.

Dolomite lowers porosity and increases conductivity, whereas nacrite locally enhances conductivity at moderate porosity.

6.2. Formation-specific observations and comparisons

The Rotliegend group, as the most extensively studied and sampled unit in this thesis, served as a benchmark for evaluating petrophysical behaviour in both the Triassic Buntsandstein and the lower Cretaceous Delft Sandstone formations. As described in Chapter 2, the Rotliegend samples are quartz-rich and extensively cemented by quartz overgrowths, with additional diagenetic modification through feldspar dissolution and authigenic clay formation. These textural and mineralogical attributes contributed to consistently higher values of thermal conductivity.

Thermal conductivity and thermal diffusivity decrease with porosity (Chapter 2 and 3). Clean sands anchor the porosity–thermal conductivity regression ($R^2 \approx 0.75$). Clay-rich, low-porosity samples show higher volumetric heat capacity and lower diffusivity. This was observed for the Triassic samples that were rich in detrital clay. At equal porosity, the thermal conductivity of Buntsandstein samples are generally lower than those of the Rotliegend, especially below ~15% porosity. Higher porosity ranges were determined to belong to relatively clean sandstone, therefore, for those, porosity is the primary control on thermal conductivity. However, for lower porosities, where clay content increases, the clay types and percentage of are thought to cause separation between Permian and Triassic groups. Further mineralogical analyses have shown that accumulation of certain minerals or mineral subsets can create clusters. For instance, the Rotliegend samples show that the presence of illite and muscovite is associated with lower thermal conductivity. In contrast, dolomite-rich samples exhibit higher thermal conductivity. These samples cluster in the low-porosity range of the thermal conductivity–porosity cross plot. This pattern indicates that mineralogical composition can locally override the primary porosity control on thermal conductivity. Permian samples rich in nacrite, as a clay mineral from the kaolin group, display elevated conductivity at moderate porosity range.

Relative to the Triassic, the Rotliegend samples exhibit lower volumetric heat capacity. The clay minerals have higher heat capacity and as explained before, the difference in clay content and type between samples from Rotliegend and Buntsandstein confirms this observation.

The V_p and V_s of the Buntsandstein samples are strongly correlated and both decrease with porosity. Samples identified as high in detrital clay content also occur at low porosity (<10%) and sit in the upper velocity range. In these samples, clean sands define the lower-velocity bound at comparable porosity (Section 3.3.1).

In addition to porosity and mineralogy, lithological lamination controls V_p and V_s . Horizontally laminated samples (with lamination perpendicular to the measurement direction, i.e., along the long axis of the sample) yields systematically lower velocities, while vertical lamination yields higher velocities. This occurs because waves crossing alternating layers

might have been slowed down by individual layers that have low wave velocities. On the other hand, vertically laminated samples with waves propagating along the length of samples shows higher V_p and V_s . This is because acoustic waves travel through the lamina with the highest velocity (Section 3.4.1).

The V_p/V_s ratio shows low dependence on porosity. Triassic ratios exhibit greater scatter, approaching ~ 2 , compared to the Permian, which are tightly clustered around ~ 1.6 – 1.8 . This reflects the combined influence of compaction, cementation, and mineralogy, which stabilises the V_p/V_s ratio despite porosity variability. The same trend between V_p , V_s , and porosity is valid for the Rotliegend samples. This is because increasing pore volume reduces the solid high-velocity pathways for acoustic waves to travel through the porous medium.

Replacive clays from feldspar dissolution act as bound clays at grain contacts and reduce stiffness, lowering velocities relative to clean framework sands at the same porosity. This occurs because bound clays soften grain contacts and reduce shear modulus, which disproportionately decreases V_s .

At a given porosity, Triassic samples have lower thermal conductivity and higher V_p and V_s than Permian samples (Section 3.4.2). The contrast aligns with clay type and distribution. The type and placement of clay can have both positive and negative impacts on thermal conductivity and V_p . Based on our observations and available data, we conjecture that detrital clays in the Triassic could tighten the framework and are associated with higher velocities at low porosity. The type of clays, which are unknown to us, could also be of high velocity. Replacive bound clays in the Rotliegend could have softened grain contacts and lowered velocities. This highlights that not only clay content but also clay type and distribution dictate acoustic behaviour (Section 3.3.3).

The Delft Sandstone, investigated in detail in Chapter 4, provides a distinct case study where both thermal and mechanical rock properties were evaluated in an integrated manner. Static elastic moduli were determined through uniaxial and triaxial compression tests on full-diameter core plugs, and these results were compared against dynamic moduli derived from ultrasonic laboratory measurements and petrophysical logs. The analysis confirms that dynamic moduli, particularly those derived from sonic and density logs, systematically overestimate rock stiffness, an effect that was especially pronounced in shale-rich intervals and lithologies with significant heterogeneity (Chapter 4).

To address this discrepancy, a two-step empirical calibration workflow is developed. The first step harmonises dynamic moduli from logs with laboratory ultrasonic data, while the second converts the harmonised dynamic moduli into static values using lithology-specific relationships. This calibrated workflow significantly outperforms direct log-to-static conversions in both accuracy and bias reduction and enables the construction of continuous depth profiles of static Young's modulus. These profiles are directly applicable to wellbore stability and reservoir compaction models. As such, the Delft Sandstone serves as a practical

example of how calibrated core-log integration can improve the mechanical characterisation of geothermal reservoirs. This workflow may also be applied to other formations where static mechanical testing is unavailable or limited, as discussed in the predictive modelling framework of Chapter 5.

6.3. Log-based estimation and machine learning approaches

A critical component of this thesis is the development and validation of methods to extend core-derived insights to intervals lacking direct laboratory measurements. As demonstrated in Chapter 4, static elastic moduli for the Delft Sandstone were estimated using a calibrated two-step conversion workflow. In the first step, dynamic moduli derived from sonic and density logs are aligned with ultrasonic laboratory measurements to correct for frequency and scale effects. In the second step, lithology-specific empirical relationships are applied to convert the harmonised dynamic moduli into static values. This workflow reduces error and bias when compared to conventional direct dynamic-to-static conversions and allows the construction of continuous static modulus profiles for geomechanical applications (Chapter 4).

In a broader predictive context, Chapter 5 explores the use of ensemble machine learning models, particularly LightGBM and XGBoost, to estimate thermal conductivity from standard petrophysical logs including density, sonic velocity, porosity, and gamma ray. While some individual regression models achieve higher R^2 values (up to 0.68), the machine learning models consistently outperform linear baselines across multiple wells and formations, demonstrating superior generalizability and robustness, with cross-validated R^2 values reaching up to 0.57. The predictive performance is highest when models are trained on multi-formation datasets, reflecting the benefit of data diversity and coverage. However, predictions of thermal diffusivity are significantly less accurate, which is consistent with the known sensitivity of this property to microstructural and mineralogical variations that are not captured by routine well-log measurements (Fuchs & Förster, 2014; Woodside & Messmer, 1961).

Although an R^2 of 0.57 may appear moderate, it is reasonable for heterogeneous geological datasets where thermal properties are influenced by factors not captured by conventional logs. Previous studies, such as Meshalkin et al. (2020), Ekeopara et al. (2023), and Pang et al. (2023), reported higher coefficients of determination when predicting thermal conductivity from log data; however, their models were validated using within-well k-fold or random stratified cross-validation. In contrast, this study applies a stricter leave-one-well-out validation, ensuring that each test well was completely unseen during training, which provides a more realistic measure of model generalizability across spatially independent wells. When a grouped k-fold cross-validation with fixed fold numbers without accounting for well separation is applied, the R^2 increases to 0.68, consistent with those reported in the literature. However, such an approach does not represent true predictive performance on unseen wells. Therefore, the achieved R^2 of 0.57 is considered a robust and defensible result under more stringent validation conditions. Further improvement could be achieved by incorporating mineralogical and textural

parameters and developing hybrid models that combine petrophysical knowledge with machine learning.

The integration of well-log interpretation with machine learning thus provides a useful model for estimating thermal properties in intervals where core data are unavailable. As shown in Chapter 5, these models can generalise across formations when properly trained and validated, although their reliability ultimately depends on the quality, range, and representativeness of the input features, because machine learning relies on repeated training and validation cycles where the partitioning of data can influence how well the model generalises across formations with differing characteristics. This approach complements laboratory-based characterisation and offers a scalable solution for improving the resolution and completeness of thermal property models in geothermal and other subsurface applications.

6.4. Broader contributions and applications

The combined findings of this thesis contribute to both the scientific understanding of sedimentary rock behaviour and the practical development of subsurface resource projects in the Netherlands and beyond. This work demonstrates how depositional processes, diagenetic evolution, and mineral composition govern the coupled thermal and mechanical properties of reservoir rocks. The integrated dataset and cross-formational comparisons establish a consistent framework for evaluating how properties such as thermal conductivity, acoustic velocities, and elastic moduli relate to porosity, microstructure, and mineralogy. These findings help refine rock physics models, localise empirical formulas, and support the calibration of predictive tools used across geoscientific disciplines.

When compared to prior studies, this work differs in both scale and scope. Many previous investigations into subsurface formations have focused on a single formation or used small datasets. In contrast, this thesis compiles a multi-formation dataset of over 1100 core plug samples from the Rotliegend and over 700 from the Buntsandstein, with additional mechanical data from the Delft Sandstone. The result is a national-scale dataset that includes thermal, acoustic, mechanical, and mineralogical data across the main geothermal target formations in the Netherlands. As such, this thesis not only deepens the understanding of individual formations but also compares different formation to find similarities and differences.

A key advance offered by this larger dataset is the ability to distinguish robust property trends from well-specific artefacts. Smaller datasets are more prone to overfitting and may fail to capture natural heterogeneity in rock texture, mineralogy, or diagenetic alteration. In contrast, the scale of the dataset in this thesis allows for the identification of statistically significant trends, such as the observed negative correlation between porosity and both thermal conductivity and V_p , across hundreds of samples and multiple wells and different formations. These relationships hold consistently in clean quartz-rich intervals and deviations in clay-rich or samples with different grain size or laminations that affected their predictably, validating their physical basis. The XRD and FTIR data, together with macroscopic descriptions of the

core plugs, help to interpret these deviations and support the grouping of samples based on mineralogical and textural characteristics.

The size of the dataset also allows for an in-depth comparison between core plug measurements and well-log responses. While prior studies have established that dynamic moduli from logs overestimate static stiffness, most of these works relied on a handful of overlapping core and log intervals. In this thesis, particularly in Chapter 4, a calibrated two-step workflow is developed and validated using a sizable number of matched dynamic and static moduli, with strong formation-specific performance. The robustness of this calibration stems directly from the dataset's depth, which includes variations in lithology, depth, and diagenetic state. This makes the derived conversion formulas more generalizable and applicable beyond a single project.

In the context of machine learning (Chapter 5), the benefits of a large and diverse dataset become even more apparent. Machine learning algorithms require representative, high-coverage datasets to effectively learn complex, non-linear relationships. The model performance achieved in this thesis, particularly for thermal conductivity, reflects not only careful feature selection and tuning but also the richness of the input data. This thesis demonstrates that models trained on multi-formation datasets perform better across unseen wells, highlighting the value of dataset diversity in model training and deployment. At the same time, increasing dataset size and diversity can introduce additional layers of complexity. A broader dataset often contains a wider range of geological trends, measurement conditions, and potential outliers, which may require more extensive preprocessing, robust modelling strategies, and careful interpretation to avoid misleading correlations. These challenges, while adding to the analytical effort, also provide an opportunity to better understand data variability and improve the model's resilience to real-world heterogeneity.

These advances are not only of academic interest but carry direct implications for subsurface energy development in the Netherlands and beyond. The country's ambitions for expanding geothermal energy, as well as its efforts in carbon storage and hydrogen storage, require accurate and site-specific characterisation of the subsurface. However, acquiring new core data at each site is rarely feasible due to cost and logistical constraints. The ability to draw on a national-scale property dataset, as compiled in this thesis, offers a pragmatic solution. By enabling empirical relationships, log calibrations, and machine learning models that are grounded in hundreds of lab measurements, this work provides a ready-to-use foundation for predicting properties at new geothermal prospects with limited or no core data.

In geothermal exploration, thermal conductivity, heat capacity, and diffusivity are crucial inputs for heat transport modelling, as they directly influence calculations of subsurface temperature distribution, heat extraction rates, and long-term production sustainability. Willems et al. (2017) modelled the long-term thermal performance of the Dogger geothermal reservoir in the Paris Basin, producing water at ~ 72 °C from depths of 1.6–2 km. The simulations, based on a 50-year operational horizon for a typical doublet, show that thermal

conductivity and heat capacity of both the reservoir and confining beds strongly influence production temperature decline, thermal breakthrough timing, and overall doublet lifetime. For example, increasing confining-bed thermal conductivity delays thermal breakthrough by several years and maintains higher production temperatures, directly improving system viability. The results demonstrate that even moderate changes in assumed thermal properties can significantly alter performance forecasts, highlighting the need for accurate, site-specific measurements when designing and operating geothermal projects. Using the Transient Plane Source (TPS) method, Fuchs and Förster (2013) measured thermal conductivity, diffusivity, and heat capacity of rock samples with known mineralogy, porosity, and saturation, and compared them with values from geothermal modelling guidelines and prior studies. Field-specific measurements differed by up to 30–40 % from literature estimates, mainly due to variations in mineral composition, porosity, and moisture content. Such discrepancies can significantly distort heat-in-place calculations and production forecasts, underscoring that laboratory and in-situ testing should be standard practice to ensure geothermal designs reflect true formation behaviour.

Machine learning approaches can support this process by upscaling sparse laboratory measurements to continuous depth profiles and reservoir scale property distributions. By capturing non-linear relationships between thermal properties, petrophysical data, and well logs, these methods enable more consistent prediction of thermal behaviour in heterogeneous reservoirs and reduce uncertainty in geothermal modelling and scenario evaluation.

Beyond initial project screening, the ability to derive continuous depth profiles of thermal properties enables more detailed and spatially consistent subsurface models, improving the resolution of reservoir simulations and enhancing the accuracy of well-placement strategies. These continuous profiles also facilitate scenario testing, allowing planners to evaluate how variations in rock thermal behaviour may impact system performance over time, including during peak demand periods or under changing operational conditions.

Moreover, incorporating property estimates into regional-scale geothermal assessments can help identify the most promising target zones and prioritise areas for further exploration. This is particularly relevant in the Dutch context, where heterogeneous lithologies and variable diagenetic histories can cause significant differences in thermal behaviour across relatively short distances. By integrating the workflows and datasets developed in this thesis, possibly helped by machine learning protocols, into national geothermal databases, operators can refine their regional heat resource maps and more accurately evaluate economic viability before committing to costly drilling campaigns. In the Bavarian Molasse Basin case study assessed by Mihályka et al. (2023), cores from 1650–3820 m depth with in-situ temperatures up to 140 °C were tested for thermal conductivity, diffusivity, and heat capacity. Measured thermal conductivity ranged from 1.9 to 3.6 W/m·K, with variations linked to mineralogy (quartz-rich vs. clay-rich carbonates) and porosity. These values deviated by up to 25–30 % from common literature estimates. Reservoir simulations showed that such differences can shift predicted thermal breakthrough by up to 5 years and change recoverable heat estimates by ± 15 %, directly

impacting doublet spacing, production rate design, and lifetime forecasts. The study demonstrates that site-specific thermal property measurements are indispensable for accurate geothermal modelling.

Finally, the prediction tools demonstrated here are adaptable to ongoing monitoring and operational phases. For example, updated well-log data from newly drilled or side-tracked wells can be processed through the same workflows to refine reservoir models during field development, supporting adaptive management strategies. This iterative approach, in which models are progressively updated as new data become available, can reduce operational risk and improve the long-term efficiency of geothermal systems.

In carbon capture and storage (CCS), mechanical property prediction is essential for evaluating caprock integrity and stress redistribution under CO₂ injection. The methodologies developed in this thesis for estimating static elastic moduli from dynamic logs, especially the two-step conversion validated on the Delft Sandstone, can be readily applied to CCS contexts. For example, the understanding of lithology-specific correction factors helps avoid the common pitfall of overestimating caprock stiffness based on sonic logs alone. Furthermore, knowledge of thermal properties is also relevant in CCS for evaluating the thermally induced stresses and caprock sealing capacity over time.

Similarly, in subsurface hydrogen storage, which is gaining momentum in depleted gas fields and porous reservoirs in the Netherlands, thermal and mechanical properties play a critical role. Reservoirs used for hydrogen storage must withstand cyclic injection and withdrawal, leading to thermal and pressure fluctuations. The thermal behaviour of the rock, how quickly it warms or cools, how much heat it stores, and how its mechanical properties respond to these changes, must be well understood. The work in this thesis, particularly its attention to thermal diffusivity and the limits of its prediction from logs, informs how such reservoirs may behave under these dynamic conditions.

Beyond energy applications, this work supports underground construction and civil engineering. For tunnelling, waste isolation, and underground infrastructure planning, accurate static elastic moduli are required for ground stability assessments. The workflow developed in this thesis offers a practical method for estimating these parameters even when only well-log data are available, which is particularly relevant for deeper subsurface projects where coring is often difficult or expensive. For shallow projects, however, core acquisition may be a more straightforward and economical. This is particularly important for early-stage feasibility studies, where core acquisition has not yet occurred, but design calculations must begin.

The thesis also contributes to the growing field of data-driven geoscience. As digital subsurface twins and predictive models become standard practice in energy and infrastructure projects, there is an increasing need for high-quality training data. The ProperBase dataset, and the empirical and machine learning models developed here, provide such a resource. In contrast to synthetic or literature-derived datasets, this work draws on actual measurements from key

Dutch geothermal formations, improving the credibility and usability of resulting models. Furthermore, the detailed documentation and formation-level resolution of the dataset facilitate its integration into national databases, such as www.nlog.nl.

Finally, by addressing both thermal and mechanical aspects of reservoir characterisation, and doing so across multiple formations, this thesis offers a comprehensive framework that goes beyond single-parameter or single-formation studies. It bridges gaps between academic research and applied geoscience, between data-rich and data-scarce environments, and between traditional empirical methods and modern machine learning techniques. It creates a foundation for how subsurface research can be both technically rigorous and practically relevant, serving the broader goal of supporting safe, efficient, and sustainable subsurface energy development in the Netherlands and beyond.

6.5. Final remarks and recommendations

This thesis demonstrates that systematic experimental analysis, combined with calibrated log interpretation and predictive modelling, can significantly enhance the characterisation of geothermal reservoir properties. The presented findings and methods form a foundation for improving the efficiency and safety of geothermal projects by enabling better-informed drilling, completion, and reservoir simulation strategies.

Future work could expand on these contributions in several directions. Additional mechanical testing of Triassic and Permian formations under in-situ subsurface conditions would allow broader application of dynamic-to-static modulus conversions and improve the reliability of other property estimations derived from laboratory data. During sample preparation, cores should be preserved under conditions that better represent the in-situ state. Using steady-state methods for thermal property measurements and simulating subsurface pressure and temperature in the laboratory would yield more representative results. Improved thermal diffusivity prediction could be achieved by incorporating mineralogical data from FTIR and XRD and grain-scale features from CT or SEM imaging to identify the type and distribution of critical minerals such as nacrite. Developing automated calibration routines for dynamic-to-static conversion would enhance model transferability between datasets. Measuring thermal expansion coefficients would further constrain thermo-mechanical behaviour, as thermal stresses strongly influence reservoir integrity and longevity. Coupling the presented property models with heat flow simulations and stress modelling would provide a more integrated view of reservoir behaviour under dynamic production conditions. Finally, establishing standardised laboratory and logging protocols would ensure data consistency and facilitate integration into national rock property databases.

References

- Abdulagaov, I. M., Abdulagatova, Z. Z., Kallaev, S. N., & Omarov, Z. M. (2019). Heat-capacity measurements of sandstone at high temperatures. *Geomechanics and Geophysics for Geo-Energy and Geo-Resources*, 5(1), 65-85. <https://doi.org/10.1007/s40948-018-0099-1>
- Abdulagatova, Z., Abdulagatov, I. M., & Emirov, V. N. (2009). Effect of temperature and pressure on the thermal conductivity of sandstone. *International Journal of Rock Mechanics and Mining Sciences*, 46(6), 1055-1071. <https://doi.org/10.1016/j.ijrmms.2009.04.011>
- Adrichem-Boogaert, H. A., & Kouwe, W. (1993). *Stratigraphic nomenclature of the Netherlands; revision and update by RGD and NOGPA*. TNO-NITG, Mededelingen Rijks Geologische Dienst. Haarlem, 50.
- Ahrens, B., Duda, M., & Renner, J. (2018). Relations between hydraulic properties and ultrasonic velocities during brittle failure of a low-porosity sandstone in laboratory experiments. *Geophysical Journal International*, 212(1), 627-645. <https://doi.org/10.1093/gji/ggx419>
- Akiba, T., Sano, S., Yanase, T., Ohta, T., & Koyama, M. (2019). Optuna: A next-generation hyperparameter optimization framework. *Proceedings of the 25th ACM SIGKDD international conference on knowledge discovery & data mining*, Anchorage, AK, USA.
- Al-Dousari, M., Garrouch, A. A., & Al-Omair, O. (2016). Investigating the dependence of shear wave velocity on petrophysical parameters. *Journal of Petroleum Science and Engineering*, 146, 286-296. <https://doi.org/10.1016/j.petrol.2016.04.036>
- Al-Jaroudi, S. S., Ul-Hamid, A., Mohammed, A.-R. I., & Saner, S. (2007). Use of X-ray powder diffraction for quantitative analysis of carbonate rock reservoir samples. *Powder Technology*, 175(3), 115-121. <https://doi.org/10.1016/j.powtec.2007.01.013>
- Anand, J., Somerton, W., & Gomaa, E. (1973). Predicting thermal conductivities of formations from other known properties. *Society of Petroleum Engineers Journal*, 13(05), 267-273. <https://doi.org/10.2118/4171-PA>
- Anees, M., Sosa, G., Van den Kerkhof, A., Leiss, B., Kley, J., Shah, M. M., & Weydt, L. (2024). Granitoids of the western Himalaya and Karakoram as potential geothermal reservoirs – A petrological, geochemical and petrophysical study. *Geothermics*, 121, 103040. <https://doi.org/10.1016/j.geothermics.2024.103040>
- Anifowose, F. A., Labadin, J., & Abdulraheem, A. (2017). Ensemble machine learning: An untapped modeling paradigm for petroleum reservoir characterization. *Journal of Petroleum Science and Engineering*, 151, 480-487. <https://doi.org/10.1016/j.petrol.2017.01.024>
- Anovitz, L. M., & Cole, D. R. (2015). Characterization and Analysis of Porosity and Pore Structures. *Reviews in Mineralogy and Geochemistry*, 80(1), 61-164. <https://doi.org/10.2138/rmg.2015.80.04>

- Anselmetti, F., & Eberli, G. (1999). The Velocity-Deviation Log: A Tool to Predict Pore Type and Permeability Trends in Carbonate Drill Holes from Sonic and Porosity or Density Logs. *AAPG Bulletin - AAPG BULL*, 83, 450-466.
- Assefa, S., McCann, C., & Sothcott, J. (2003). Velocities of compressional and shear waves in limestones. *Geophysical Prospecting*, 51(1), 1-13. <https://doi.org/10.1046/j.1365-2478.2003.00349.x>
- Atapour, H., & Mortazavi, A. (2017). The Effect of Grain Size and Cement Content on Index Properties of Weakly Solidified Artificial Sandstones. *Journal of Geophysics and Engineering*, 15 (2), 613-619. <https://doi.org/10.1088/1742-2140/aaa14a>
- Athy, L. F. (1930). Density, porosity, and compaction of sedimentary rocks. *AAPG Bulletin*, 14(1), 1-24. <https://doi.org/10.1306/3D93289E-16B1-11D7-8645000102C1865D>
- Bailly, C., Adelinet, M., Hamon, Y., & Fortin, J. (2019). Combined controls of sedimentology and diagenesis on seismic properties in lacustrine and palustrine carbonates (Upper Miocene, Samos Island, Greece). *Geophysical Journal International*, 219, 1300–1315. <https://doi.org/10.1093/gji/ggz365>
- Bär, K., Felder, M., Götz, A. E., Molenaar, N., & Sass, I. (2011). The Rotliegend reservoir system of the northern Upper Rhine Graben (Germany): from pores to production. *Geophysical Research Abstracts*, AAPG International Conference and Exhibition, Milan, Italy.
- Békési, E., Struijk, M., Bonté, D., Veldkamp, H., Limberger, J., Fokker, P. A., Vrijlandt, M., & van Wees, J.-D. (2020). An updated geothermal model of the Dutch subsurface based on inversion of temperature data. *Geothermics*, 88, 101880. <https://doi.org/10.1016/j.geothermics.2020.101880>
- Beyer, D., Kunkel, C., Aehnelt, M., Pudlo, D., Voigt, T., Nover, G., & Gaupp, R. (2014). Influence of depositional environment and diagenesis on petrophysical properties of elastic sediments (Buntsandstein of the Thuringian Syncline, Central Germany), 165 (3), 345 - 365. <https://doi.org/10.1127/1860-1804/2014/0072>
- Bian, H., Wang, F., Chen, W., & Wang, H. (2023). Study on dynamic and static elastic moduli of shale oil by different loading methods. *Unconventional Resources*, 3, 183-191. <https://doi.org/10.1016/j.unres.2023.03.002>
- Bijan, A., & Al-Rahim, A. M. (2024). Random Forest and Decision Tree Facies Classification Models for Well Log Data of the Mishrif Formation from Basrah Oil Company, Southern Iraq. *The Iraqi Geological Journal*, 57(2E), 14-32. <https://doi.org/10.46717/igj.57.2E.2ms-2024-11-11>
- Bjørlykke, K., Jahren, J., Mondol, N., Marcussen, O., Croize, D., Peltonen, C., & Thyberg, B. (2009). Sediment Compaction and Rock Properties, Adapted from poster presentation at AAPG International Conference and Exhibition, Cape Town, South Africa, October 26-29, 2008.
- Blackwell, D. D., & Steele, J. L. (1989). Thermal Conductivity of Sedimentary Rocks: Measurement and Significance. *Thermal History of Sedimentary Basins*, 13-36, New York, NY.

- Bouroullec, R., & Geel, C. R. (2025). Chapter 4: Permian. In J. ten Veen, G.-J. Vis, J. Jager, & T. Wong (Eds.), *Geology of the Netherlands*. Amsterdam University Press. 127-153, https://doi.org/DOI:10.5117/9789463728362_ch04
- Brigaud, F., Chapman, D. S., & Douaran, S. L. (1990). Estimating thermal conductivity in sedimentary basins using lithologic data and geophysical well logs. *AAPG Bulletin*, 74(9), 1459-1477.
- Brigaud, F., & Vasseur, G. (1989). Mineralogy, porosity and fluid control on thermal conductivity of sedimentary rocks. *Geophysical Journal International*, 98(3), 525-542. <https://doi.org/10.1111/j.1365-246X.1989.tb02287.x>
- Brotons, V., Tomás, R., Ivorra, S., & Grediaga, A. (2014). Relationship between static and dynamic elastic modulus of calcarenite heated at different temperatures: the San Julián's stone. *Bulletin of Engineering Geology and the Environment*, 73(3), 791-799. <https://doi.org/10.1007/s10064-014-0583-y>
- Brotons, V., Tomás, R., Ivorra, S., Grediaga, A., Martínez-Martínez, J., Benavente, D., & Gómez-Heras, M. (2016). Improved correlation between the static and dynamic elastic modulus of different types of rocks. *Materials and Structures*, 49(8), 3021-3037. <https://doi.org/10.1617/s11527-015-0702-7>
- Bruining, J. K. (2024). Sedimentological analysis of the well-logs, cores, plugs, and sidewall cores of the DEL-GT wells, MSc thesis, Delft University of Technology, Delft, The Netherlands. <https://resolver.tudelft.nl/uuid:c7b1ce3a-7e27-4bba-b007-bef69df924b1>
- Buijze, L., Veldkamp, H., & Wassing, B. (2023). Comparison of hydrocarbon and geothermal energy production in the Netherlands: reservoir characteristics, pressure and temperature changes, and implications for fault reactivation. *Netherlands Journal of Geosciences*, 102, e7, Article e7. <https://doi.org/10.1017/njg.2023.6>
- Busch, B., Hilgers, C., & Adelman, D. (2020). Reservoir quality controls on Rotliegend fluvio-aeolian wells in Germany and the Netherlands, Southern Permian Basin—Impact of grain coatings and cements. *Marine and Petroleum Geology*, 112, 104075. <https://doi.org/10.1016/j.marpetgeo.2019.104075>
- Caldwell, R. L., Baldwin, W. F., Bargainer, J. D., Berry, J. E., Salaita, G. N., & Sloan, R. W. (1963). Gamma-ray spectroscopy in well logging. *Geophysics*, 28(4), 617-632.
- Castagna, J., Batzle, M., Kan, T., & Backus, M. (1993). Rock physics—The link between rock properties and AVO response. Offset-dependent reflectivity—Theory and practice of AVO analysis: SEG, 8, 135-171.
- Castagna, J. P., Batzle, M. L., & Eastwood, R. L. (1985). Relationships between compressional-wave and shear-wave velocities in clastic silicate rocks. *Geophysics*, 50(4), 571-581.
- Cathles, L. (1999). Permeability of shaly sands. *Water Resources Research*, 35, 651-662. <https://doi.org/10.1029/98WR02700>

-
- Cecchetti, E., Martinius, A., Donselaar, M. E., Felder, M., & Abels, H. (2024b). Sedimentology, Stratigraphy and Reservoir Architecture of the Lower Triassic Main Buntsandstein in the Roer Valley Graben, the Netherlands, 182. <https://doi.org/10.2139/ssrn.4744988>
- Cecchetti, E., Martinius, A., Felder, M., Donselaar, M. E., & Abels, H. (2023). Reservoir heterogeneities in the Buntsandstein Subgroup: investigating the role of sedimentary facies, 84-84. Abstract from 12th International Conference on Fluvial Sedimentology 2023, Riva del Garda, Italy. <https://resolver.tudelft.nl/uuid:1004e212-fe19-4c72-a342-38884f22b1cf>
- Cecchetti, E., Martinius, A. W., Bruna, P.-O., Bender, A., & Abels, H. A. (2024a). Structural controls on the Triassic Main Buntsandstein sediment distribution in the Roer Valley Graben, the Netherlands. *Netherlands Journal of Geosciences*, 103. <https://doi.org/10.1017/njg.2024.17>
- Čermák, V., & Rybach, L. (1982). Thermal conductivity and specific heat of minerals and rocks. *Landolt-Börnstein: Numerical Data and Functional Relationships in Science and Technology, New Series, Group V (Geophysics and Space Research), Volume Ia, (Physical Properties of Rocks)*, edited by G. Angenheister, Springer, Berlin-Heidelberg, 305-343. https://doi.org/10.1007/10201894_62
- Chaki, S. (2015). Reservoir characterization: A machine learning approach. MSc thesis, Indian Institute of Technology, Kharagpur, <https://doi.org/10.48550/arXiv.1506.05070>
- Chaki, S., Routray, A., & Mohanty, W. (2018). Well-Log and Seismic Data Integration for Reservoir Characterization: A Signal Processing and Machine-Learning Perspective. *IEEE Signal Processing Magazine*, 35, 72-81. <https://doi.org/10.1109/MSP.2017.2776602>
- Chang, C., Zoback, M. D., & Khaksar, A. (2006). Empirical relations between rock strength and physical properties in sedimentary rocks. *Journal of Petroleum Science and Engineering*, 51(3), 223-237. <https://doi.org/10.1016/j.petrol.2006.01.003>
- Chehili, D., Sadek, K., Rahmani, B. E., Aour, B., Bendali, M., Bacetti, A., & Serhane, B. (2025). Evaluation of Algerian Reservoir Petrophysics Properties by Principal Components Analysis: Case Study of Illizi Basin. *Natural Resources Research*, 34(4), 2067-2088. <https://doi.org/10.1007/s11053-025-10502-0>
- Chen, T., & Guestrin, C. (2016). XGBoost: A Scalable Tree Boosting System Proceedings of the 22nd ACM SIGKDD International Conference on Knowledge Discovery and Data Mining, San Francisco, California, USA. <https://doi.org/10.1145/2939672.2939785>
- Christaras, B., Auger, F., & Mosse, E. (1994). Determination of the moduli of elasticity of rocks. Comparison of the ultrasonic velocity and mechanical resonance frequency methods with direct static methods. *Materials and Structures*, 27(4), 222-228. <https://doi.org/10.1007/BF02473036>
- Christensen, N. I., & Szymanski, D. L. (1991). Seismic properties and the origin of reflectivity from a classic Paleozoic sedimentary sequence, Valley and Ridge province, southern Appalachians. *Geological Society of America Bulletin*, 103(2), 277-289.
- Clauser, C. (2011). Thermal Storage and Transport Properties of Rocks, I: Heat Capacity and Latent Heat. In (pp. 1423-1431). https://doi.org/10.1007/978-90-481-8702-7_238

- Clauser, C., & Huenges, E. (1995a). Rock Physics and Phase Relations. A Handbook of Physical Constants. 3, 105-126. American Geophysical Union.
- Clauser, C., & Huenges, E. (1995b). Thermal Conductivity of Rocks and Minerals, American Geophysical Union (AGU), 3, 105-126. <https://doi.org/10.1029/RF003p0105>
- Craddock, P., Herron, M., & Herron, S. (2017). Comparison of Quantitative Mineral Analysis By X-Ray Diffraction and Fourier Transform Infrared Spectroscopy. *Journal of Sedimentary Research*, 87, 630-652. <https://doi.org/10.2110/jsr.2017.34>
- de Jager, J., & Geluk, M. C. (2007). Petroleum geology. In (Eds) *Geology of the Netherlands*. Royal Dutch Academy of Arts and Sciences, Amsterdam, 237-260, chapter 14.
- De Simone, S., Vilarrasa, V., Carrera, J., Alcolea, A., & Meier, P. (2013). Thermal coupling may control mechanical stability of geothermal reservoirs during cold water injection. *Physics and Chemistry of the Earth, Parts A/B/C*, 64, 117-126. <https://doi.org/10.1016/j.pce.2013.01.001>
- Delle Piane, C., Sarout, J., Madonna, C., Saenger, E. H., Dewhurst, D. N., & Raven, M. (2014). Frequency-dependent seismic attenuation in shales: experimental results and theoretical analysis. *Geophysical Journal International*, 198(1), 504-515. <https://doi.org/10.1093/gji/ggu148>
- DINOLoket. Stratigraphic nomenclature grouped by age. <https://www.dinoloket.nl/en/stratigraphic-nomenclature/via-diagram/group-by-age>
- Dvorkin, J., & Brevik, I. (1999). Diagnosing high-porosity sandstones: Strength and permeability from porosity and velocity. *Geophysics*, 64(3), 795-799. <https://doi.org/10.1190/1.1444589>
- Dvorkin, J., & Nur, A. (1996). Elasticity of high-porosity sandstones: Theory for two North Sea data sets. *Geophysics*, 61(5), 1363-1370. <https://api.semanticscholar.org/CorpusID:38348547>
- Eberli, G., Baechle, G., Anselmetti, F., & Incze, M. (2003). Factors Controlling Elastic Properties in Carbonate Sediments and Rocks. *The Leading Edge*, 22, 654-660. <https://doi.org/10.1190/1.1599691>
- Eissa, E. A., & Kazi, A. (1988). Relation between static and dynamic Young's moduli of rocks. *International Journal of Rock Mechanics and Mining Sciences & Geomechanics Abstracts*, 25(6), 479-482. [https://doi.org/10.1016/0148-9062\(88\)90987-4](https://doi.org/10.1016/0148-9062(88)90987-4)
- Ekeopara, P., Nwosu, C., Kelechi, F., Nwadiaro, C., & ThankGod, K. (2023). Prediction of Thermal Conductivity of Rocks in Geothermal Field Using Machine Learning Methods: a Comparative Approach, SPE Nigeria Annual International Conference and Exhibition, Lagos, Nigeria. <https://doi.org/10.2118/217217-MS>
- El Sayed, A. M. A., & El Sayed, N. A. (2019). Thermal conductivity calculation from P-wave velocity and porosity assessment for sandstone reservoir rocks. *Geothermics*, 82, 91-96. <https://doi.org/10.1016/j.geothermics.2019.06.001>

- El Sayed, A. M. A., & El Sayed, N. A. (2024). Thermal Diffusivity Prediction From P-Wave Velocity and Porosity Assessment for Sandstone Reservoirs. *Inżynieria Mineralna* 1 (1), <https://doi.org/10.29227/IM-2024-01-14>.
- Emirov, S. N., Aliverdiev, A. A., Zarichnyak, Y. P., & Emirov, R. M. (2021). Studies of the Effective Thermal Conductivity of Sandstone Under High Pressure and Temperature. *Rock Mechanics and Rock Engineering*, 54(6), 3165-3174. <https://doi.org/10.1007/s00603-020-02353-3>
- Esteban, L., Pimienta, L., Sarout, J., Plane, C. D., Haffen, S., Geraud, Y., & Timms, N. E. (2015). Study cases of thermal conductivity prediction from P-wave velocity and porosity. *Geothermics*, 53, 255-269. <https://doi.org/10.1016/j.geothermics.2014.06.003>
- Fan, P., Deng, R., Qiu, J., Zhao, Z., & Wu, S. (2021). Well logging curve reconstruction based on kernel ridge regression. *Arabian Journal of Geosciences*, 14, 1559. <https://doi.org/10.1007/s12517-021-07792-y>
- Fjær, E. (2009). Static and dynamic moduli of a weak sandstone. *Geophysics*, 74(2), WA103-WA112. <https://doi.org/10.1190/1.3052113>
- Fjær, E., & Holt, R. M. (1994). Rock acoustics and rock mechanics: Their link in petroleum engineering. *The Leading Edge*, 13(4), 255-258. <https://doi.org/10.1190/1.1437017>
- Fortin, J., Guéguen, Y., & Schubnel, A. (2007). Effects of pore collapse and grain crushing on ultrasonic velocities and V/V. *Journal of Geophysical Research: Solid Earth*, 112(B8). <https://doi.org/10.1029/2005JB004005>
- Fredrich, J. T., & Wong, T.-f. (1986). Micromechanics of thermally induced cracking in three crustal rocks. *Journal of Geophysical Research: Solid Earth*, 91(B12), 12743-12764. <https://doi.org/10.1029/JB091iB12p12743>
- Fuchs, S., & Balling, N. (2016). Improving the temperature predictions of subsurface thermal models by using high-quality input data. Part 1: Uncertainty analysis of the thermal-conductivity parameterization. *Geothermics*, 64, 42-54. <https://doi.org/10.1016/j.geothermics.2016.04.010>
- Fuchs, S., Balling, N., & Förster, A. (2015). Calculation of thermal conductivity, thermal diffusivity and specific heat capacity of sedimentary rocks using petrophysical well logs. *Geophysical Journal International*, 203(3), 1977-2000. <https://doi.org/10.1093/gji/ggv403>
- Fuchs, S., & Förster, A. (2010). Rock thermal conductivity of Mesozoic geothermal aquifers in the Northeast German Basin. *Geochemistry*, 70, 13-22. <https://doi.org/10.1016/j.chemer.2010.05.010>
- Fuchs, S., & Förster, A. (2013). Well-log based prediction of thermal conductivity of sedimentary successions: a case study from the North German Basin. *Geophysical Journal International*, 196(1), 291-311. <https://doi.org/10.1093/gji/ggt382>

- Fuchs, S., & Förster, A. (2014). Well-log based prediction of thermal conductivity of sedimentary successions: a case study from the North German Basin. *Geophysical Journal International*, 196(1), 291-311. <https://doi.org/10.1093/gji/ggt382>
- Fuchs, S., Förster, H.-J., Norden, B., Balling, N., Miele, R., Heckenbach, E., & Förster, A. (2021). The Thermal Diffusivity of Sedimentary Rocks: Empirical Validation of a Physically Based $\alpha - \phi$ Relation. *Journal of Geophysical Research: Solid Earth*, 126(3), e2020JB020595. <https://doi.org/10.1029/2020JB020595>
- Geluk, M. C. (2005). Stratigraphy and tectonics of Permo-Triassic basins in the Netherlands and surrounding areas. PhD thesis, Utrecht University, the Netherlands.
- Geluk, M. C., & Röhlings, H.-G. (1997). High-resolution sequence stratigraphy of the Lower Triassic Buntsandstein in the Netherlands and Northwestern Germany. *Geologie en Mijnbouw*, 76, 227-246. <https://doi.org/10.1023/A:1003062521373>
- Ghassemi, A. (2012). A Review of Some Rock Mechanics Issues in Geothermal Reservoir Development. *Geotechnical and Geological Engineering*, 30(3), 647-664. <https://doi.org/10.1007/s10706-012-9508-3>
- Glover, P. (2012). The Effect of Clay on Porosity and Resistivity Logs, Petrophysics, MSc Course, 270-281. <https://shorturl.at/fYypm>
- Goto, S., & Matsubayashi, O. (2009). Relations between the thermal properties and porosity of sediments in the eastern flank of the Juan de Fuca Ridge. *Earth, Planets and Space*, 61(7), 863-870. <https://doi.org/10.1186/BF03353197>
- Griffioen, J., Felder, M., Molenaar, N., Spijker, J., & Hoving, A. (2025). Chapter 13: Sediment mineralogy and geochemistry. In J. ten Veen, G.-J. Vis, J. Jager, & T. Wong (Eds.), *Geology of the Netherlands*. Amsterdam University Press. https://doi.org/DOI:10.5117/9789463728362_ch13
- Griffiths, C., Brereton, N., Beausillon, R., & Castillo, D. (1992). Thermal conductivity prediction from petrophysical data: a case study. *Geological Society, London, Special Publications*, 65(1), 299-315.
- H. Bhuiyan, M., & M. Holt, R. (2012). Vp-Vs Ratio as a Lithological Indicator for Shallow Reservoir. [74th EAGE Conference and Exhibition incorporating EUROPEC 2012](https://doi.org/10.3997/2214-4609.20148650), P313, <https://doi.org/10.3997/2214-4609.20148650>
- Haffen, S., Géraud, Y., & Diraison, M. (2015). Geothermal, structural and petrophysical characteristics of Buntsandstein sandstone reservoir (Upper Rhine Graben, France), Proceedings world geothermal congress, Melbourne, Australia.
- Haffen, S., Géraud, Y., Rosener, M., & Diraison, M. (2017). Thermal conductivity and porosity maps for different materials: A combined case study of granite and sandstone. *Geothermics*, 66, 143-150. <https://doi.org/10.1016/j.geothermics.2016.12.005>

-
- Hamada, G., & Joseph, V. (2020). Developed correlations between sound wave velocity and porosity, permeability and mechanical properties of sandstone core samples. *Petroleum Research*, 5(4), 326-338. <https://doi.org/10.1016/j.ptlrs.2020.07.001>
- Han, D.-H. (1986). Effects of porosity and clay content on acoustic properties of sandstones and unconsolidated sediments. PhD thesis, Stanford University, Department of Geophysics, School of Earth Sciences. <https://www.osti.gov/biblio/5477973>
- Harings, M. (2023). EBN and geothermal energy. *Energie Beheer Nederland (EBN)*. <https://www.ebn.nl/en/ebn-and-geothermal-energy/>
- Hartmann, A., Rath, V., & Clauser, C. (2005). Thermal conductivity from core and well log data. *International Journal of Rock Mechanics and Mining Sciences*, 42(7), 1042-1055. <https://doi.org/10.1016/j.ijrmms.2005.05.015>
- He, W., Chen, Z., Shi, H., Liu, C., & Li, S. (2021). Prediction of acoustic wave velocities by incorporating effects of water saturation and effective pressure. *Engineering Geology*, 280, 105890. <https://doi.org/10.1016/j.enggeo.2020.105890>
- Heap, M. J., Kushnir, A. R. L., Gilg, H. A., Wadsworth, F. B., Reuschlé, T., & Baud, P. (2017). Microstructural and petrophysical properties of the Permo-Triassic sandstones (Buntsandstein) from the Soultz-sous-Forêts geothermal site (France). *Geothermal Energy*, 5(1), 26. <https://doi.org/10.1186/s40517-017-0085-9>
- Heap, M. J., Kushnir, A. R. L., Vasseur, J., Wadsworth, F. B., Harlé, P., Baud, P., Kennedy, B. M., Troll, V. R., & Deegan, F. M. (2020). The thermal properties of porous andesite. *Journal of Volcanology and Geothermal Research*, 398, 106901. <https://doi.org/10.1016/j.jvolgeores.2020.106901>
- Heijnen, L., Buik, N., & te Gussinklo Ohmann, R. (2015). Management of geological and drilling risks of geothermal projects in the Netherlands, World Geothermal Congress, Melbourne, Australia
- Henares, S., Bloemsma, M. R., Donselaar, M. E., Mijnlieff, H. F., Redjosentono, A. E., Veldkamp, H. G., & Weltje, G. J. (2014). The role of detrital anhydrite in diagenesis of aeolian sandstones (Upper Rotliegend, The Netherlands): Implications for reservoir-quality prediction. *Sedimentary Geology*, 314, 60-74. <https://doi.org/10.1016/j.sedgeo.2014.10.001>
- Hiatt, E. (2000). Links between Depositional and Diagenetic Processes in Basin Analysis: Porosity and Permeability Evolution in Sedimentary Rocks: p. 63-92 in Kyser, K., (ed.) *Fluids and Basin Evolution*, Mineralogical Association of Canada, Ottawa, Canada, 262 p.
- Hill, J., Rogers, T., & Sever, M. (2025). Gaps, challenges, and pathways forward for superhot rock geothermal: summary report, proceedings, 50th Workshop on Geothermal Reservoir Engineering Stanford University, Stanford, California, USA.
- Hillel, D. (2003). Soil Physics. In R. A. Meyers (Ed.), *Encyclopedia of Physical Science and Technology (Third Edition)* (pp. 77-97). Academic Press. <https://doi.org/10.1016/B0-12-227410-5/00936-4>

- Hu, K., Liu, X., Chen, Z., & Grasby, S. E. (2023). Mineralogical Characterization From Geophysical Well Logs Using a Machine Learning Approach: Case Study for the Horn River Basin, Canada. *Earth and Space Science*, 10(12), e2023EA003084. <https://doi.org/10.1029/2023EA003084>
- Hussain, M., Liu, S., Ashraf, U., Ali, M., Hussain, W., Ali, N., & Anees, A. (2022). Application of machine learning for lithofacies prediction and cluster analysis approach to identify rock type. *Energies*, 15(12), 4501.
- Iranfar, S., Karbala, M. M., Shakiba, M., & Shahsavari, M. H. (2023). Effects of type and distribution of clay minerals on the physico-chemical and geomechanical properties of engineered porous rocks. *Scientific Reports*, 13(1), 5837. <https://doi.org/10.1038/s41598-023-33103-4>
- Jarzyna, J. A., Baudzis, S., Janowski, M., & Puskarczyk, E. (2021). Geothermal resources recognition and characterization on the basis of well logging and petrophysical laboratory data, polish case studies. *Energies*, 14(4), 850. <https://doi.org/10.3390/en14040850>
- Jeong, C. (2010). Integrated data analysis using electrofacies and seismic attribute for reservoir modeling, SCRF technical report (part of SCRF Report 23, 2010), Department of Energy Resources Engineering, Stanford University.
- Jianxin, L. (2009). Porosity-Based Model for Coupled Thermal-Hydraulic-Mechanical Processes. Ph D thesis, The University of Western Australia, Australia.
- Jin, G., Kwak, H. T., Yousef, A. A., & Banaja, H. H. (2024). Determination of Production Potentials of Geothermal Resources for Rapid Exploration and Development Decisions SPE Annual Technical Conference and Exhibition, New Orleans, Louisiana, USA <https://doi.org/10.2118/220812-MS>
- Jozanikohan, G., & Abarghoeei, M. N. (2022). The Fourier transform infrared spectroscopy (FTIR) analysis for the clay mineralogy studies in a clastic reservoir. *Journal of Petroleum Exploration and Production Technology*, 12(8), 2093-2106. <https://doi.org/10.1007/s13202-021-01449-y>
- Kämmlein, M., & Stollhofen, H. (2019). Pore-fluid-dependent controls of matrix and bulk thermal conductivity of mineralogically heterogeneous sandstones. *Geothermal Energy*, 7(1), 13. <https://doi.org/10.1186/s40517-019-0129-4>
- Ke, G., Meng, Q., Finley, T., Wang, T., Chen, W., Ma, W., Ye, Q., & Liu, T.-Y. (2017). Lightgbm: A highly efficient gradient boosting decision tree. 31st Conference on Neural Information Processing Systems (NIPS 2017), Long Beach, CA, USA.
- Kibikas, W. M., Ghassemi, A., Choens, R. C., Bauer, S. J., Shalev, E., & Lyakhovskiy, V. (2025). Thermophysical properties of the Ghareb formation relevant for nuclear waste disposal. *Acta Geotechnica* 20, 2799-2816. <https://doi.org/10.1007/s11440-025-02535-9>
- Kim, D.-C., Manghnani, M. H., & Schlanger, S. O. (1985). The role of diagenesis in the development of physical properties of deep-sea carbonate sediments. *Marine Geology*, 69(1), 69-91. [https://doi.org/10.1016/0025-3227\(85\)90134-3](https://doi.org/10.1016/0025-3227(85)90134-3)

- King, M. S. (1983). Static and dynamic elastic properties of igneous and metamorphic rocks from the Canadian shield, Lawrence Berkeley National Laboratory. LBNL Report #: LBL-15823. Retrieved from <https://escholarship.org/uc/item/6nz4t59d>.
- Klimentos, T. (1991). The effects of porosity-permeability-clay content on the velocity of compressional waves. *Geophysics*, 56(12), 1930-1939. <https://doi.org/10.1190/1.1443004>
- Klinkenberge, L. (1941). The permeability of porous media to liquids and gases. American Petroleum Institute, *Drilling and Productions Practices*, 1941, pp. 200-213.
- Kolah-Kaj, P., Abels, H. A., Barnhoorn, A., Vargas Meleza, L., & Vardon, P. J. (2024). Database of Experimental Data on Three Geothermal Plays in the Netherlands from the ProperBase Project. <https://doi.org/10.4121/63c28ba2-fbde-486f-9d82-660ab3a5c990>
- Kolah-Kaj, P., Kord, S., & Soleymanzadeh, A. (2021). The effect of pressure on electrical rock typing, formation resistivity factor, and cementation factor. *Journal of Petroleum Science and Engineering*, 204, 108757. <https://doi.org/10.1016/j.petrol.2021.108757>
- Kombrink, H., Doornenbal, J., Duin, E., Den Dulk, M., Ten Veen, J., & Witmans, N. (2012). New insights into the geological structure of the Netherlands; results of a detailed mapping project. *Netherlands Journal of Geosciences*, 91(4), 419-446. <https://doi.org/10.1017/S0016774600000329>.
- Korevaar, S., Dalman, R., Nelskamp, S., Atkins, S., Boter, E., Wiarda, E., Nolten, M., & Beintema, K. (2023). Play 5 Triassic. www.nlog.nl. Retrieved 05-03-2025 from <https://www.geodeatlas.nl/pages/play-5-triassic>.
- Kotsanis, D., Nomikos, P., & Rozos, D. (2021). Comparison of Static and Dynamic Young's Modulus of Prasinites. *Materials Proceedings*, 5(1).
- Kuijper, R. P. (2003). Petrography of igneous rocks in well E18-5. <https://www.nlog.nl/brh-web/rest/brh/document/3831683293>
- Lasheen, E. S. R., Rashwan, M. A., & Azer, M. K. (2023). Effect of mineralogical variations on physico-mechanical and thermal properties of granitic rocks. *Scientific Reports*, 13(1), 10320. <https://doi.org/10.1038/s41598-023-36459-9>
- Lei, G., Liao, Q., Patil, S., & Zhao, Y. (2019). Effect of clay content on permeability behavior of argillaceous porous media under stress dependence: A theoretical and experimental work. *Journal of Petroleum Science and Engineering*, 179, 787-795. <https://doi.org/10.1016/j.petrol.2019.05.011>
- Li, Y., Li, X., Guo, M., Chen, C., Ni, P., & Huang, Z. (2024). Regression analysis and its application to oil and gas exploration: A case study of hydrocarbon loss recovery and porosity prediction, China. *Energy Geoscience*, 5(4), 100333. <https://doi.org/10.1016/j.engeos.2024.100333>
- Lin, W., Tadai, O., Takahashi, M., Sato, D., Hirose, T., Tanikawa, W., Hamada, Y., & Hatakeda, K. (2015). An experimental study on measurement methods of bulk density and porosity of rock samples. *Journal of Geoscience and Environment Protection*, 3(5), 72-79.

-
- Lozovyi, S., & Bauer, A. (2019). From static to dynamic stiffness of shales: frequency and stress dependence. *Rock Mechanics and Rock Engineering*, 52(12), 5085-5098.
- Luo, J., Jia, J., Zhao, H., Zhu, Y., Guo, Q., Cheng, C., Tan, L., Xiang, W., Rohn, J., & Blum, P. (2016). Determination of the thermal conductivity of sandstones from laboratory to field scale. *Environmental Earth Sciences*, 75(16), 1158. <https://doi.org/10.1007/s12665-016-5939-0>
- Luo, Y., Li, M., Yuan, H., Liu, H., & Fang, Y. (2023). Predicting lattice thermal conductivity via machine learning: a mini review. *NPJ Computational Materials*, 9(1), 4. <https://doi.org/10.1038/s41524-023-00964-2>
- Madejová, J. (2003). FTIR techniques in clay mineral studies. *Vibrational Spectroscopy*, 31(1), 1-10. [https://doi.org/10.1016/S0924-2031\(02\)00065-6](https://doi.org/10.1016/S0924-2031(02)00065-6)
- Mahmoodpour, S., Singh, M., Turan, A., Bär, K., & Sass, I. (2021). Key parameters affecting the performance of fractured geothermal reservoirs: a sensitivity analysis by thermo-hydraulic-mechanical simulation. *arXiv preprint arXiv:2107.02277*. <https://doi.org/10.48550/arXiv.2107.02277>
- Maqsood, A., & Kamran, K. (2005). Thermophysical Properties of Porous Sandstones: Measurements and Comparative Study of Some Representative Thermal Conductivity Models. *International Journal of Thermophysics*, 26(5), 1617-1632. <https://doi.org/10.1007/s10765-005-8108-3>
- Marion, D., Nur, A., Yin, H., & Han, D.-H. (1992). Compressional velocity and porosity in sand-clay mixtures. *Geophysics*, 57(4), 554-563. <https://doi.org/10.1190/1.1443269>
- Martínek, K. (2008). Climatic, tectonic and provenance record of the Permian non-marine deposits of the Krkonoše Piedmont Basin. PhD thesis. Charles University, Prague, Czech Republic.
- Matinkia, M., Hashami, R., Mehrad, M., Hajsaeedi, M. R., & Velayati, A. (2023). Prediction of permeability from well logs using a new hybrid machine learning algorithm. *Petroleum*, 9(1), 108-123. <https://doi.org/10.1016/j.petlm.2022.03.003>
- Mavko, G., Mukerji, T., & Dvorkin, J. (2009). *The Rock Physics Handbook*, Cambridge University Press, ISBN:9780511626753. <https://doi.org/10.1017/CBO9780511626753>
- Mavko, G., Mukerji, T., & Dvorkin, J. (2020). *The rock physics handbook. The rock physics handbook (3rd ed.)*. Cambridge University Press. <https://doi.org/10.1017/9781108333016>
- McCann, D., & Entwisle, D. (1992). Determination of Young's modulus of the rock mass from geophysical well logs. *Geological Society, London, Special Publications*, 65(1), 317-325. <https://doi.org/10.1144/gsl.sp.1992.065.01.24>
- McKie, T., & Kilhams, B. (2025). Chapter 5: Triassic. In J. ten Veen, G.-J. Vis, J. Jager, & T. Wong (Eds.), *Geology of the Netherlands*. Amsterdam University Press. https://doi.org/DOI:10.5117/9789463728362_ch05

-
- Meshalkin, Y., Shakirov, A., Popov, E., Koroteev, D., & Gurbatova, I. (2020). Robust well-log based determination of rock thermal conductivity through machine learning. *Geophysical Journal International*, 222(2), 978-988. <https://doi.org/10.1093/gji/ggaa209>
- Miao, S., & Zhou, Y. (2018). Temperature dependence of thermal diffusivity and conductivity for sandstone and carbonate rocks. *Journal of Thermal Analysis and Calorimetry*, 131(2), 1647-1652. <https://doi.org/10.1007/s10973-017-6631-7>
- Midttomme, K., & Roaldset, E. (1998). The effect of grain size on thermal conductivity of quartz sands and silts. *Petroleum Geoscience*, 4(2), 165-172. <https://doi.org/doi:10.1144/petgeo.4.2.165>
- Midttomme, K., Roaldset, E., & Aagaard, P. (1998). Thermal conductivity of selected claystones and mudstones from England. *Clay Minerals*, 33(1), 131-145. <https://doi.org/10.1180/000985598545327>
- Mielke, P., Bär, K., & Sass, I. (2017a). Determining the relationship of thermal conductivity and compressional wave velocity of common rock types. *Pangaea: Data Publisher for Earth & Environmental Science*. <https://doi.org/10.1594/PANGAEA.874146>
- Mielke, P., Bär, K., & Sass, I. (2017b). Determining the relationship of thermal conductivity and compressional wave velocity of common rock types as a basis for reservoir characterization. *Journal of Applied Geophysics*, 140, 135-144. <https://doi.org/10.1016/j.jappgeo.2017.04.002>
- Mihályka, J., Paróczy, P., Balázs, L., Drahos, D., & Lenkey, L. (2023). Thermal conductivity of sediments from well-logs and its application to determine heat flow density in the Pannonian Basin, Hungary. *Tectonophysics*, 868, 230095. <https://doi.org/10.1016/j.tecto.2023.230095>
- Mijnlieff, H. (2020). Introduction to the geothermal play and reservoir geology of the Netherlands. *Netherlands Journal of Geosciences*, 99 (E2). <https://doi.org/10.1017/njg.2020.2>
- Miller, S. L., & Stewart, R. R. (1991). The relationship between elastic-wave velocities and density in sedimentary rocks: A proposal. *Crewes Res. Rep*, 260-273. <https://www.crewes.org/Documents/ResearchReports/1991/1991-17.pdf>
- Mishra, A., Sharma, A., & Patidar, A. K. (2022). Evaluation and Development of a Predictive Model for Geophysical Well Log Data Analysis and Reservoir Characterization: Machine Learning Applications to Lithology Prediction. *Natural Resources Research*, 31(6), 3195-3222. <https://doi.org/10.1007/s11053-022-10121-z>
- Mohammadian, E., Kheirollahi, M., Liu, B., Ostadhassan, M., & Sabet, M. (2022). A case study of petrophysical rock typing and permeability prediction using machine learning in a heterogeneous carbonate reservoir in Iran. *Scientific Reports*, 12(1), 4505. <https://doi.org/10.1038/s41598-022-08575-5>
- Molenaar, N., & Felder, M. (2018). Clay Cutans and the Origin of Illite Rim Cement: An Example from the Siliciclastic Rotliegend Sandstone in the Dutch Southern Permian Basin. *Journal of Sedimentary Research*, 88(5), 641-658. <https://doi.org/10.2110/jsr.2018.33>

-
- Monsees, A. C., Busch, B., Schöner, N., & Hilgers, C. (2020). Rock typing of diagenetically induced heterogeneities—a case study from a deeply-buried clastic Rotliegend reservoir of the Northern German Basin. *Marine and Petroleum Geology*, 113, 104163. <https://doi.org/10.1016/j.marpetgeo.2019.104163>
- Morgan, S., & Stam, C. (2025). CLEW Guide – How the European Union is trying to legislate a path to net-zero. https://www.cleanenergywire.org/factsheets/clew-guide-how-european-union-trying-to-legislate-path-net-zero?utm_source=chatgpt.com
- Mroczkowska-Szerszeń, M., & Orzechowski, M. (2018). Infrared spectroscopy methods in reservoir rocks analysis - semiquantitative approach for carbonate rocks. 11, 802. <https://doi.org/10.18668/NG.2018.11.04>
- Nelson, P. H. (1994). Permeability-porosity relationships in sedimentary rocks. *The Log Analyst*, 35(03), 38-62.
- Nortier, J. W., Baunack, C., & Juhasz-Bodnar, K. (2005). Sedimentology, petrography and reservoir quality of cores 1-4 of well K18-7X and petrography of sidewall samples from Well K18-7. Report retrieved from nlog.nl.
- Olutoki, J. O., Zhao, J.-g., Siddiqui, N. A., Elsaadany, M., Haque, A. K. M. E., Akinyemi, O. D., Said, A. H., & Zhao, Z. (2024). Shear wave velocity prediction: A review of recent progress and future opportunities. *Energy Geoscience*, 5(4), 100338. <https://doi.org/10.1016/j.engeos.2024.100338>
- Pan, S., Zheng, Z., Guo, Z., & Luo, H. (2022). An optimized XGBoost method for predicting reservoir porosity using petrophysical logs. *Journal of Petroleum Science and Engineering*, 208, 109520. <https://doi.org/10.1016/j.petrol.2021.109520>
- Pang, Y., Shi, B., Guo, X., Zhang, X., Wen, Y., Yang, G., & Sun, X. (2023). Machine learning algorithm optimization for intelligent prediction of rock thermal conductivity: A case study from a whole-cored scientific drilling borehole. *Geothermics*, 111, 102711. <https://doi.org/10.1016/j.geothermics.2023.102711>
- PanTerra Geoconsultants B.V. (2012). GeoMEC-4P Geothermal Energy Brielle. Report retrieved from https://www.rvo.nl/files/file/2018/03/Report_final_Triassic%20Brielle.pdf
- Pape, H., Clauser, C., & Iffland, J. (1999). Permeability prediction based on fractal pore-space geometry. *Geophysics*, 64(5), 1447-1460. <https://doi.org/10.1190/1.1444649>
- Pedregosa, F., Varoquaux, G., Gramfort, A., Michel, V., Thirion, B., Grisel, O., Blondel, M., Prettenhofer, P., Weiss, R., & Dubourg, V. (2011). Scikit-learn: Machine learning in Python. *the Journal of Machine Learning Research*, 12, 2825-2830.
- Pelletier, H. (2009). AVO Crossplotting II: Examining Vp/Vs Behavior. *Innovation*, no. 1998, 105-110.
- Peltonen, C., Marcussen, Ø., Bjørlykke, K., & Jahren, J. (2009). Clay mineral diagenesis and quartz cementation in mudstones: The effects of smectite to illite reaction on rock properties. *Marine and Petroleum Geology*, 26(6), 887-898. <https://doi.org/10.1016/j.marpetgeo.2008.01.021>

-
- Pimienta, L., Klitzsch, N., & Clauser, C. (2018). Comparison of thermal and elastic properties of sandstones: Experiments and theoretical insights. *Geothermics*, 76, 60-73. <https://doi.org/10.1016/j.geothermics.2018.06.005>
- Pimienta, L., Sarout, J., Esteban, L., & Piane, C. D. (2014). Prediction of rocks thermal conductivity from elastic wave velocities, mineralogy and microstructure. *Geophysical Journal International*, 197(2), 860-874. <https://doi.org/10.1093/gji/ggu034>
- Pluymaekers, M. P. D., Kramers, L., van Wees, J. D., Kronimus, A., Nelskamp, S., Boxem, T., & Bonté, D. (2012). Reservoir characterisation of aquifers for direct heat production: Methodology and screening of the potential reservoirs for the Netherlands. *Netherlands Journal of Geosciences - Geologie en Mijnbouw*, 91(4), 621-636. <https://doi.org/10.1017/S001677460000041X>
- Popov, Y., Beardsmore, G., Clauser, C., & Roy, S. (2016). ISRM Suggested Methods for Determining Thermal Properties of Rocks from Laboratory Tests at Atmospheric Pressure. *Rock Mechanics and Rock Engineering*, 49, 4179-4207. <https://doi.org/10.1007/s00603-016-1070-5>
- Popov, Y., Romushkevich, R., Korobkov, D., Mayr, S., Bayuk, I., Burkhardt, H., & Wilhelm, H. (2011). Thermal properties of rocks of the borehole Yaxcopoil-1 (Impact Crater Chicxulub, Mexico). *Geophysical Journal International*, 184(2), 729-745. <https://doi.org/10.1111/j.1365-246X.2010.04839.x>
- Popov, Y., Tertychnyi, V., Romushkevich, R., Korobkov, D., & Pohl, J. (2003). Interrelations Between Thermal Conductivity and Other Physical Properties of Rocks: Experimental Data. *Pure and Applied Geophysics*, 160(5), 1137-1161. <https://doi.org/10.1007/PL00012565>
- Postema, G. (2025). A Geomechanical Research on the Delft Sandstone and the Rodenrijs Claystone.
- Prasad, M., & Manghnani, M. H. (1997). Effects of pore and differential pressure on compressional wave velocity and quality factor in Berea and Michigan sandstones. *Geophysics*, 62(4), 1163-1176. <https://doi.org/10.1190/1.1444217>
- Probst, P., & Boulesteix, A.-L. (2018). To tune or not to tune the number of trees in random forest. *Journal of Machine Learning Research*, 18(181), 1-18. <https://doi.org/10.48550/arXiv.1705.05654>
- Probst, P., Boulesteix, A.-L., & Bischl, B. (2019). Tunability: Importance of hyperparameters of machine learning algorithms. *Journal of Machine Learning Research*, 20(53), 1-32. <https://doi.org/10.48550/arXiv.1802.09596>
- Radies, D., Stollhofen, H., Hollmann, G., & Kukla, P. (2005). Synsedimentary faults and amalgamated unconformities: Insights from 3D-seismic and core analysis of the Lower Triassic Middle Buntsandstein, Ems Trough, north-western Germany. *International Journal of Earth Sciences*, 94(5), 863-875. <https://doi.org/10.1007/s00531-005-0009-y>
- Rafavich, F., Kendall, C. S. C., & Todd, T. (1984). The relationship between acoustic properties and the petrographic character of carbonate rocks. *Geophysics*, 49(10), 1622-1636. <https://doi.org/10.1190/1.1441570>

-
- Rahmouni, A., Boulanouar, A., Boukalouch, M., Géraud, Y., Samaouali, A., Harnafi, M., & Sebbani, J. (2013). Prediction of porosity and density of calcarenite rocks from P-wave velocity measurements. *International Journal of Geosciences*, 4, 1292-1299. <https://doi.org/10.4236/ijg.2013.49124>
- Rahmouni, A., Boulanouar, A., Boukalouch, M., Géraud, Y., Samaouali, A., Harnafi, M., & Sebbani, J. (2014). Relationships between porosity and permeability of calcarenite rocks based on laboratory measurements. *J. Mater. Environ. Sci*, 5(3), 931-936, ISSN : 2028-2508.
- Rahmouni, A., Boulanouar, A., Boukalouch, M., Samaouali, A., Géraud, Y., & Sebbani, J. (2014). Porosity, permeability and bulk density of rocks and their relationships based on laboratory measurements. *Revista Romana de Materiale/ Romanian Journal of Materials*, 44, 147-152. <https://hal.science/hal-01303808v1>
- Reijers, T. (2012). Sedimentology and diagenesis as 'hydrocarbon exploration tools' in the Late Permian Zechstein-2 Carbonate Member (NE Netherlands). *Geologos*, 18(3), 163-195. <https://doi.org/10.2478/v10118-012-0009-x>
- Rezaeyan, A., Kampman, N., Pipich, V., Barnsley, L., Rother, G., Magill, C., Ma, J., & Busch, A. (2023). Compaction and clay content control mudrock porosity. *Energy*, 289, 129966. <https://doi.org/10.1016/j.energy.2023.129966>
- Rezk, M. G., & Ibrahim, A. F. (2025). Impact of rock mineralogy on reactive transport of CO₂ during carbon sequestration in a saline aquifer. *Journal of Petroleum Exploration and Production Technology*, 15(1), 10. <https://doi.org/10.1007/s13202-025-01927-7>
- Richard, P. D., Bazalgette, L., Volery, C., & Toukhi, A. (2022). Scale discrepancy paradox between observation and modelling in fractured reservoir models in oil and gas industry. *Geological Magazine*, 159(11-12), 1914-1935. <https://doi.org/10.1017/S0016756822000620>
- Robertson. (1988). *Thermal Properties of Rocks*. United States Department of the Interior Geological Survey. Open-File Report 88-441. <https://pubs.usgs.gov/of/1988/0441/report.pdf>
- Salah, M. K., Alqudah, M., El-Aal, A. K. A., & Barnes, C. (2018). Effects of porosity and composition on seismic wave velocities and elastic moduli of lower cretaceous rocks, central Lebanon. *Acta Geophysica*, 66, 867-894. <https://doi.org/10.1007/s11600-018-0187-1>
- Salah, M. K., Alqudah, M., Monzer, A. J., & David, C. (2020). Petrophysical and acoustic characteristics of Jurassic and Cretaceous rocks from Central Lebanon. *Carbonates and Evaporites*, 35(1), 12. <https://doi.org/10.1007/s13146-019-00536-w>
- Schärli, U., & Rybach, L. (2001). Determination of specific heat capacity on rock fragments. *Geothermics*, 30(1), 93-110. [https://doi.org/10.1016/S0375-6505\(00\)00035-3](https://doi.org/10.1016/S0375-6505(00)00035-3)
- Selley, R. C. and Sonnenberg, S.A. (1998). *Elements of petroleum geology*. Gulf Professional Publishing. <https://doi.org/DOI:10.1016/c2010-0-67090-8>
- Setyowiyoto, J., & Samsuri, A. (2012). Characterization, Pressure, and Temperature Influence on the Compressional and Shear Wave Velocity in Carbonate Rock.

-
- Sha, S., Rong, G., Chen, Z., Li, B., & Zhang, Z. (2020). Experimental Evaluation of Physical and Mechanical Properties of Geothermal Reservoir Rock after Different Cooling Treatments. *Rock Mechanics and Rock Engineering*, 53(11), 4967-4991. <https://doi.org/10.1007/s00603-020-02200-5>
- Shakouri, A., Farzay, O., Masihi, M., Ghazanfari, M. H., & Al-Ajmi, A. M. (2019). An experimental investigation of dynamic elastic moduli and acoustic velocities in heterogeneous carbonate oil reservoirs. *SN Applied Sciences*, 1(9), 1023. <https://doi.org/10.1007/s42452-019-1010-6>
- Shen, S., Gao, Y., & Jia, L. (2024). A Comparison of the Relationship between Dynamic and Static Rock Mechanical Parameters. *Applied Sciences*, 14(11), 4487. <https://doi.org/10.3390/app14114487>
- Somerton, W. H. (1958). Some Thermal Characteristics of Porous Rocks. *Transactions of the AIME*, 213(01), 375-378. <https://doi.org/10.2118/965-G>
- Soustelle, V., ter Heege, J., Buijze, L., & Wassing, B. (2022). Thermomechanical parameters of geothermal analogue reservoir sandstones in the West Netherlands Basin. TNO.
- Sumirat, I., Ando, Y., & Shimamura, S. (2006). Theoretical consideration of the effect of porosity on thermal conductivity of porous materials. *Journal of Porous Materials*, 13, 439-443. <https://doi.org/10.1007/s10934-006-8043-0>
- Sun, Q., Chen, S.-e., Gao, Q., Zhang, W., Geng, J., & Zhang, Y. (2017). Analyses of the factors influencing sandstone thermal conductivity. *Acta Geodyn. Geomater*, 14(2), 186. <https://doi.org/DOI: 10.13168/AGG.2017.0001>
- Sun, Q., Lü, C., Cao, L., Li, W., Geng, J., & Zhang, W. (2016). Thermal properties of sandstone after treatment at high temperature. *International Journal of Rock Mechanics and Mining Sciences*, 85, 60-66. <https://doi.org/10.1016/j.ijrmms.2016.03.006>
- Sun, W.-T., Li, Z.-H., Lou, Y.-S., Zhu, L., Wu, H.-M., Kamgue Lenwoue, A. R., & Liu, Q. (2022). Mechanical Properties of Shale-Reservoir Rocks Based on Stress–Strain Curves and Mineral Content. *Geofluids*, 2022(1), 2562872. <https://doi.org/10.1155/2022/2562872>
- Tatar, A., Mohammadi, S., Soleymanzadeh, A., & Kord, S. (2021). Predictive mixing law models of rock thermal conductivity: Applicability analysis. *Journal of Petroleum Science and Engineering*, 197, 107965. <https://doi.org/10.1016/j.petrol.2020.107965>
- Tatham, R. H. (1982). Vp/Vs and lithology. *Geophysics*, 47(3), 336-344. <https://doi.org/10.1190/1.1441339>
- ten Veen, J., Vis, G.-J., Jager, J., & Wong, T. (2025). *Geology of the Netherlands*. Amsterdam University Press.
- Terry, N., Johnson, C., Day-Lewis, F., Parker, B., & Slater, L. (2021). Beware of Spatial Autocorrelation When Applying Machine Learning Algorithms to Borehole Geophysical Logs. *Groundwater*, 59. <https://doi.org/10.1111/gwat.13081>

- TNO (2024). Dutch subsurface portal. <https://www.nlog.nl/datacenter/brh-overview>
- Tureyen, O. I., & Caers, J. (2005). A parallel, multiscale approach to reservoir modeling. *Computational Geosciences*, 9(2), 75-98. <https://doi.org/10.1007/s10596-005-9004-4>
- Van Adrichem Boogaert, H., & Kouwe, W. (1993). Stratigraphic nomenclature of the Netherlands, revision and update by RGD and NOGEPa, 50, Rijks Geologische Dienst. ISBN 9072869346.
- van Adrichem Boogaert, H. A. (1976). Outline of the Rotliegend (lower permian) in The Netherlands. In *The Continental Permian in Central, West, and South Europe: Proceedings of the NATO Advanced Study Institute held at the Johannes Gutenberg University, Mainz, FRG, 23 September–4 October, 1975* (pp. 23-37). Springer.
- Van Hulst, F. (2006). Reservoir quality distribution as tool for better exploration prospect evaluation and estimation of the resource base in the Netherlands. Van Hulst, F. & Lutgert, J. E. (comp.). *Tight gas fields in the Netherlands*, workshop EBN-TNO, 19.
- Van Ojik, K., Silviu, A., Kremer, Y., & Shipton, Z. (2020). Fault seal behaviour in Permian Rotliegend reservoir sequences: case studies from the Dutch Southern North Sea, Geological Society, London, Special Publications, 496, 9–38. <https://doi.org/10.1144/SP496-2018-189>.
- Vardon, P., Abels, H., Barnhoorn, A., Daniilidis, A., Bruhn, D., Drijkoningen, G., Elliott, K., van Esser, B., Laumann, S., & van Paassen, P. (2024b). A Research and energy production geothermal project on the TU Delft campus: project implementation and initial data collection. *PROCEEDINGS, 49th Workshop on Geothermal Reservoir Engineering*, proceedings, 49th Workshop on Geothermal Reservoir Engineering Stanford University, Stanford, California, USA.
- Vardon, P. J., Laumann, S., van Paassen, P., Elliott, K., van den Berg, J., Friebel, M., van Esser, B., Ursem, L., van Schravendijk, B., & Vargas Meleza, L. (2024a). End-of-Well Science Programme Report DEL-GT-01 and DEL-GT-02. Delft University of Technology, Delft, the Netherlands. <https://doi.org/10.4233/uuid:6ce07471-6986-434e-aa24-ad6e1f6714d9>
- Veeningen, R., & Könitzer, S. (2016a). Petrographic study of well Zeerijp-3A (ZRP-3A). <https://www.nlog.nl/brh-web/rest/brh/document/3459601465>
- Veldkamp, J., Van Unen, M., Vrijlandt, M., & van Wees, J. (2022). Aquifer characterization of a marginal part of the Slochteren Formation, TNO. https://www.warmingup.info/documenten/veldkamp-et-al-2022-aquifer-characterisation-of-the-slochteren-formation_warmingup-t4pa1.pdf
- Veltmeijer, A., Naderloo, M., & Barnhoorn, A. (2022). Forecasting of Rock Failure in the Laboratory using Active Acoustic Monitoring Methods. *ESS Open Archive*. April 14, 2022. <https://doi.org/10.1002/essoar.10511107.1>
- Verma, A., Shirole, D., & Sinha, S. (2024). Evaluation of the Sensitivity of Compressional Waves to Assess the Presence of a Macroscopic Flaw in a Pre-Fractured Agaria Marble Specimen 58th U.S. Rock Mechanics/Geomechanics Symposium, Golden, CO, USA, June 2024 <https://doi.org/10.56952/ARMA-2024-0380>

- Vivas, C., & Salehi, S. (2021). Real-time model for thermal conductivity prediction in geothermal wells using surface drilling data: a machine learning approach. 46th Workshop on Geothermal Reservoir Engineering, Stanford University, Stanford, California, USA.
- Vorobiev, S., Zharnikov, T., Vorobyev, V., & AlKawai, W. (2024). Identification of Different Types of Clastic Reservoirs Using Rock-Physics Models. SPWLA Asia-Pacific Regional Conference, Bangkok, Thailand.
- Waldmann, S. (2012). Geological and mineralogical investigation of Rotliegend gas reservoirs in the Netherlands and their potential for CO₂ storage, PhD thesis, Friedrich Schiller University Jena, Germany.
- Wang, L., Rybacki, E., Bonnelye, A., Bohnhoff, M., & Dresen, G. (2021). Experimental investigation on static and dynamic bulk moduli of dry and fluid-saturated porous sandstones. *Rock Mechanics and Rock Engineering*, 54(1), 129-148. <https://doi.org/10.1007/s00603-020-02248-3>
- Waples, D., & Waples, J. (2004). A Review and Evaluation of Specific Heat Capacities of Rocks, Minerals, and Subsurface Fluids. Part 1: Minerals and Nonporous Rocks. *Natural Resources Research*, 13, 97-122. <https://doi.org/10.1023/B:NARR.0000032647.41046.e7>
- Wees, J. D. v., Kronimus, A., van Putten, M., Pluymaekers, M. P. D., Mijnlief, H., van Hooff, P., Obdam, A., & Kramers, L. (2012). Geothermal aquifer performance assessment for direct heat production – Methodology and application to Rotliegend aquifers. *Netherlands Journal of Geosciences - Geologie en Mijnbouw*, 91(4), 651-665. <https://doi.org/10.1017/S0016774600000433>
- Weibel, R., Kristensen, L., Olivarius, M., Hjuler, M. L., Mathiesen, A., & Nielsen, L. H. (2012). Investigating deviations from overall porosity–permeability trends. Proceedings 36th workshop on geothermal reservoir engineering, Stanford University, California, USA.
- Willems, C. J., Nick, H. M., Goense, T., & Bruhn, D. F. (2017). The impact of reduction of doublet well spacing on the Net Present Value and the life time of fluvial Hot Sedimentary Aquifer doublets. *Geothermics*, 68, 54-66. <https://doi.org/10.1016/j.geothermics.2017.02.008>
- Willems, C. J. L., Vondrak, A., Mijnlief, H. F., Donselaar, M. E., & van Kempen, B. M. M. (2020). Geology of the Upper Jurassic to Lower Cretaceous geothermal aquifers in the West Netherlands Basin – an overview. *Netherlands Journal of Geosciences*, 99, e1, Article e1. <https://doi.org/10.1017/njg.2020.1>
- Winkler, K. W., & Murphy III, W. F. (1995). Acoustic velocity and attenuation in porous rocks. In T. J. Ahrens (Ed.), *Rock physics and phase relations: A handbook of physical constants* (Vol. 3, pp. 20–34). American Geophysical Union. <https://doi.org/10.1029/RF003P0020>
- Woodside, W., & Messmer, J. H. (1961). Thermal Conductivity of Porous Media. I. Unconsolidated Sands. *Journal of Applied Physics*, 32(9), 1688-1699. <https://doi.org/10.1063/1.1728419>
- Xayavong, V., Vu, M., Duong, N., & Tuan, V. (2020). Seismic Refraction Exploration for Groundwater Potential Evaluations: A Case Study of Vientiane Province, Laos. *VNU Journal of Science Earth and Environmental Sciences*, 36, 90-101. <https://doi.org/10.25073/2588-1094/vnuces.4651>

-
- Xi, Y., Wang, H., Li, J., Dong, W., Li, H., & Guo, B. (2022). Experimental comparison of mechanical properties and fractal characteristics of geothermal reservoir rocks after different cooling treatments. *Energy Reports*, 8, 5158-5176. <https://doi.org/10.1016/j.egy.2022.03.207>
- Xie, F., Zhu, C., & Tang, B. (2023). An experimental study on anisotropy of thermal conductivity in shale. *Energy Geoscience*, 4(4), 100195. <https://doi.org/10.1016/j.engeos.2023.100195>
- Xie, L., Yu, C., Zhang, Y., He, B., Wang, R., & Liu, J. (2025). Multiscale and quantitative study of thermal conductivity in shale using TDTR measurements and homogenization techniques. *Applied Clay Science*, 267, 107719. <https://doi.org/10.1016/j.clay.2025.107719>
- Xing, Y., Yang, H., & Yu, W. (2023). An approach for the classification of rock types using machine learning of core and log data. *Sustainability*, 15(11), 8868. <https://doi.org/10.3390/su15118868>
- Xu, H., Zhou, W., Xie, R., Da, L., Xiao, C., Shan, Y., & Zhang, H. (2016). Characterization of Rock Mechanical Properties Using Lab Tests and Numerical Interpretation Model of Well Logs. *Mathematical Problems in Engineering*, 2016(1), 5967159. <https://doi.org/10.1155/2016/5967159>
- Yabe, S., Hamada, Y., Kitamura, M., Fukuchi, R., & Hashimoto, Y. (2022). Multiple Types of Porosity – P-Wave Velocity Relationships for the Nankai Trough. *Journal of Geophysical Research: Solid Earth*, 127(7), e2022JB024071. <https://doi.org/10.1029/2022JB024071>
- Yang, L., Peng, X., Hu, Y., & Liu, A. (2025). Shale lithofacies mechanical differences from tectonic-diagenetic coupling and their response to hydraulic fracture network propagation. *Frontiers in Earth Science*, 13, 1594244. <https://doi.org/10.3389/feart.2025.1594244>
- Yin, H., & Nur, A. (1993). Porosity, permeability, and acoustic velocity in granular materials. In *SEG Technical Program Expanded Abstracts 1993* (pp. 775-778). Society of Exploration Geophysicists. <https://doi.org/doi:10.1190/1.1822615>
- Yousaf, H., Amjad, M., Claes, H., Swennen, R., & Weltje, G. J. (2023). Assessment of reservoir quality and heterogeneity in Middle Buntsandstein Sandstones of Southern Netherlands for deep geothermal exploration. *CSPG CSEG CWLS Joint Annual Convention [Geoconvention](Calgary, Canada, 5/6-10/2013) Technical Program*.
- Yuan, G., Yingchang, C., Schulz, H.-M., Hao, F., Gluyas, J., Liu, K., Yang, T., Wang, Y., Xi, K., & Li, F. (2019). A review of feldspar alteration and its geological significance in sedimentary basins: From shallow aquifers to deep hydrocarbon reservoirs. *Earth-Science Reviews*, 191, 114-140. <https://doi.org/10.1016/j.earscirev.2019.02.004>
- Zamora, M., Vo-Thanh, D., Bienfait, G., & Poirier, J. P. (1993). An empirical relationship between thermal conductivity and elastic wave velocities in sandstone. *Geophysical Research Letters*, 20(16), 1679-1682. <https://doi.org/10.1029/92GL02460>
- Zhang, D., Li, Y., Guo, Y., Xia, H., Liu, Y., Yan, J., Wang, F., & Wu, Y. (2025). Research on shale Dynamic and Static elastic modulus and anisotropy Based on Pressurization History. *Frontiers in Earth Science*, 12, 1520486. <https://doi.org/10.3389/feart.2024.1520486>

- Zhang, J., & Bentley, L. R. (2003). Pore geometry and elastic moduli in sandstone. In Expanded abstracts of the 73rd Annual International Meeting of the Society of Exploration Geophysicists (Vol. 15). Society of Exploration Geophysicists, Dallas, TX, United States, October 26–31.
- Zhang, J., Wang, R., Jia, A., & Feng, N. (2024b). Optimization and application of XGBoost logging prediction model for porosity and permeability based on K-means method. *Applied Sciences*, 14(10), 3956. <https://doi.org/10.3390/app14103956>
- Zhang, Y., Gu, Y., Zhou, H., & Yang, L. (2024a). Extracting static elastic moduli of rock through elastic wave velocities. *Acta Geophysica*, 72(2), 915-931. <https://doi.org/10.1007/s11600-023-01139-9>
- Zhang, Y., & Zhao, G.-F. (2023). A multiphysics method for long-term deformation analysis of reservoir rock considering thermal damage in deep geothermal engineering. *Renewable Energy*, 204, 432-448. <https://doi.org/10.1016/j.renene.2023.01.026>
- Zimmer, M. A., Prasad, M., Mavko, G., & Nur, A. (2007). Seismic velocities of unconsolidated sands: Part 1—Pressure trends from 0.1 to 20 MPa. *Geophysics*, 72(1), E1-E13. <https://doi.org/10.1190/1.2399459>
- Zoback, M. D. (2010). *Reservoir geomechanics*. Cambridge University Press. <https://doi.org/10.1017/CBO9780511586477>

Authors Contributions

The chapters were authored by the people listed below. Author contributions are described following the Contributor Role Taxonomy (CRediT) after Brand et al. (2015). Funding for all chapters was acquired by H. (Hemmo) A. Abels, A. (Auke) Barnhoorn, and P. (Philip) J. Vardon.

Chapter 2: Thermal and acoustic characterisation of Permian Rotliegend sandstones: evaluating the effects of porosity and mineralogy on predicting thermal properties

P. Kolah-Kaj: Data curation, Conceptualisation, Investigation, Methodology, Writing – original draft, Formal analysis, Visualisation

H. A. Abels: Conceptualisation, Investigation, Methodology, Supervision, Review and editing

A. Barnhoorn: Conceptualisation, Investigation, Methodology, Supervision, Review and editing

P. Vardon: Conceptualisation, Investigation, Methodology, Supervision, Review and editing

R. Adriaens: Data curation, Investigation, Data interpretation

Chapter 3: Porosity and Mineralogical Controls on Thermal and Acoustic Properties of Sandstones from the Triassic Main Buntsandstein Subgroup and Permian Upper Rotliegend Group in the Netherlands

Parvin Kolah Kaj: Data curation, Conceptualisation, Investigation, Methodology, Writing – original draft, Formal analysis, Visualisation

H. A. Abels: Conceptualisation, Investigation, Methodology, Supervision, Review and editing

A. Barnhoorn: Conceptualisation, Investigation, Methodology, Supervision, Review and editing

P. Vardon: Conceptualisation, Investigation, Methodology, Supervision, Review and editing

R. Adriaens: Data curation, Investigation, Data interpretation

Chapter 4: Coupled mechanical and thermo-physical characterisation of the lower Cretaceous Delft Sandstone Member for geothermal applications

Parvin Kolah Kaj: Data curation, Conceptualisation, Investigation, Methodology, Writing – original draft, Formal analysis, Visualisation

H. A. Abels: Conceptualisation, Investigation, Methodology, Supervision, Review and editing

A. Barnhoorn: Data curation, Conceptualisation, Investigation, Methodology, Writing – original draft, Formal analysis, Visualisation, Supervision, Review and editing

P. Vardon: Conceptualisation, Investigation, Methodology, Supervision, Review and editing

G. Postema: Data curation, Sample preparation, Investigation

Chapter 5: Integrating experimental and log data to predict thermal properties in geothermal plays using machine learning

Parvin Kolah Kaj: Data curation, Conceptualisation, Investigation, Methodology, Writing – original draft, Formal analysis, Visualisation

H. A. Abels: Conceptualisation, Investigation, Methodology, Supervision, Review and editing

A. Barnhoorn: Conceptualisation, Investigation, Methodology, Supervision, Review and editing

P. Vardon: Conceptualisation, Investigation, Methodology, Supervision, Review and editing

G. Rongier: Methodology, Investigation, Review and editing

L. Baez Lozada: Conceptualisation, Investigation, Methodology

Acknowledgments

Of course, I must start with you, **Hemmo**. You were the first person I spoke to about this project, and the person who gave me the wonderful news that I was accepted. Your high standards, honesty, and constant involvement shaped both this project and my development. There were matters that we may did not always agreed on but there is a Persian proverb that translates to: you are hardest on the person you care about the most; This was at least true for me. Throughout the entire journey, you were always supportive, engaged, and available for discussions, whether about work, communication, or direction. For that, I am truly grateful. Dank u wel.

Auke, you were my go-to person whenever I felt insecure, uncertain, or simply stuck. I deeply appreciated the conversations, your openness, and your ability to listen carefully without judgment. You had a way of making complex situations feel manageable again. I also valued how intentionally you kept the group connected, whether by taking us on small adventures, creating space to step outside work, or welcoming us into your home. Those moments of structure, calm, and human connection mattered more than you probably realize, and they made this journey lighter and more sustainable.

And **Phil**, my language Everest. Adjusting to British English, and in particular to your British English, was a challenge in itself. I learned quickly how to nod thoughtfully which did not always mean I understood and strategically use “interesting” and “yes” that could mean many things at once. Beyond the linguistic training, I have always admired your highly strategic approach, and I learned a lot from you. I am also grateful for your support beyond the core project, especially with side activities such as grant writing and introductions that expanded my network. I will always remember how often my introduction became: “Hey, I am Parvin. I do geothermal with Phil.”

I hope that when you look back on these four years, you will remember them with the same with good memories.

Outside my official supervision team, I would like to thank **Anne**, also my committee member. I greatly appreciated our discussions here and there on different topics, and I sincerely hope that these conversations will continue. I found you a caring and strong independent person. I thank **Guillaume** for patiently listening to all my questions and for always trying to find answers on the spot or guiding me toward finding them myself. This support was particularly helpful for Chapter 5.

The help and support from the members of the ProperBase consortium, including **Sjoukje de Vries**, **Jasper Kwee**, **Rieko Adriaens**, **Greg van de Bilt**, and many others, were extremely valuable. Thank you for the feedback, the long trips to Delft for meetings, and for always showing interest in the work.

Acknowledgments

Outside the consortium, I would like to acknowledge the support of Wintershall Noordzee B.V., without which this project would have been almost impossible. Many helpful and supportive people from this company, including **Marten Bron**, made significant contributions to this project.

I thank the laboratory technicians **Christica, Marc, Karel, Jelle, Ellen, and Sian**. The extensive laboratory work would have been very difficult without your support. I am also grateful to **Liliana** for her help in organizing the massive amount of data, despite her heavy responsibilities here.

I would like to thank all the people in my office, including **Emilio, Andrea, Azin, Ellie, Ilshat, David, Jesse, Jasper H., Eddy, Mahmoud, Maria, Zhenja, Hester, Milad, Shiaho, Entela, Tim, Debanjan, Aukje**, and many others. I leave the university with many good memories that will stay in my heart. Thank you for that. I hope to see as many of you as possible in the next stages of my life.

دوستان بسیار عزیز می که در این چند سال اخیر وارد زندگی من شدند؛ اگرچه تعدادشان زیاد نیست، اما حضورشان کاملا کافی و ارزشمند است. نگار، رسول، پرستو، سارا، مرتضی، مژگان، فرهاد، سحر، قباد، امیرحسین، محمدجواد، سنا، حسام، سروش، استر، آرام، هانی، آزاده و ندا عزیزم.

و دوستانی که اگرچه در کنارم نبودند، اما نقش حضورشان در رسیدن من به این مرحله و دلگرمی‌ای که از همراهی آنان دریافت کردم، غیر قابل انکار است. هستی، حاتم، شقایق، و استاد و دوست بسیار خوبم، دکتر ابوذر سلیمانزاده.

از خانواده‌ی عزیزم، پدر و مادر بی‌مانندم، و محبتی و سروش پرمهرم که تمام زندگی من هستند، صمیمانه سپاسگزارم. متولد شدن در این خانواده، زیباترین جبر زندگی من بود. نوشتن این بخش برایم دشوارترین قسمت این کتاب است، زیرا با یادآوری تمام محبت‌های بی‌دریغ و فداکاری‌های بی‌شمار شما در این سی سال، کلمات ناتوان می‌شوند.

تمام صفحات این کتاب نیز برای بیان گوشه‌ای از مهر شما کافی نیست؛ از این رو همه را در قلبم نگاه می‌دارم، تا ارزششان با نوشتن کاسته نشود. در تمام این سال‌ها، هر روز دلتنگتان بوده‌ام، و در این دوازده روز گذشته، که به سبب جبر و جهل دنیا حتی دیدار چهره‌هایتان نیز ممکن نبود، این دلتنگی عمیق‌تر شده است. اشک مجال ادامه‌ی نوشتن نمی‌دهد، و تمام امیدم آن است که روزی دوباره در کنار شما باشم. به قول شاعر:

این خانه قشنگ است ولی خانه‌ی من نیست
این خاک چه زیباست ولی خاک وطن نیست

از خانواده‌ی همسر عزیزم، که حضورشان در دو سال اخیر موجب دلگرمی و آرامش خاطر من بوده است، صمیمانه سپاسگزارم. همراهی و محبت شما باعث شد احساس کنم صاحب دو خانواده هستم، و همین پیوند عاطفی، وداع با ایران را برایم دوچندان دشوار و بازگشت را دوچندان شیرین کرده است.

و در پایان، از احمد عزیزم ممنونم. دیدن تو بهترین اتفاقی بود که در هلند برای من افتاد. تو با قلب مهربانانت روزهای سخت غربت را برای من سهل و شیرین کردی. تو جبران تمام نداشته‌های من در اینجایی. در روزهای خوشی، همراه و در روزهای سخت استوارترین تکیه گاهی. تجربه‌های بسیاری را در کنار هم پشت سر گذاشته‌ایم، و بی‌صبرانه مشتاق ادامه‌ی این مسیر هستم. نوشتن بیش از این از احساساتم برایم دشوار است، اما اطمینان دارم که تو عشق نهفته در این کلمات را درک می‌کنی. شاید هم کمتر نوشتن بهتر باشد. به قول شاملو، عشق را در پستوی خانه نهان باید کرد.

پایان نگارش - دی ماه ۱۴۰۴

در شیون بی پایان این روزگار
به من بگو
بر این مردم خسته چه رفته است
که هزار پیراهن سیاه
کهنه کرده اند و هنوز
اندوه گزار بی فرصت عزا از پی عزا...

سید علی صالحی

Curriculum Vitae

24-09-1995 Born in Ramhormoz, Iran

Education

2021-2025 PhD in Applied Geology
Delft University of Technology, The Netherlands

2019-2021 MSc in Petroleum Engineering – Hydrocarbon Reservoirs
Petroleum University of Technology, Ahwaz, Iran

2017-2018 Junior Geomechanics Simulation Engineer
Iranian Offshore Engineering and Construction Company, Tehran,
Iran

2013-2017 BSc in Petroleum Engineering
Sharif University of Technology, Tehran, Iran

List of Publications

Forthcoming manuscripts (PhD chapters)

1. **Kolah-Kaj, P.**, Barnhoorn, A., Vardon, P. J., Adrieans, R., & Abels, H. A. *Thermal and acoustic characterisation of Permian Rotliegend sandstones: Evaluating the effects of porosity and mineralogy on predicting thermal properties*, *Petrophysics Journal*.
2. **Kolah-Kaj, P.**, Barnhoorn, A., Vardon, P. J., & Abels, H. A. *Porosity and mineralogical controls on thermal and acoustic properties of the Triassic Buntsandstein and Permian Rotliegend for geothermal applications*, *Petrophysics Journal*.
3. **Kolah-Kaj, P.**, Postema, G., Barnhoorn, A., Vardon, P. J., & Abels, H. A. *Coupled mechanical and thermo-physical characterisation of Delft Sandstone for geothermal applications*, *Netherlands Journal of Geosciences*.
4. **Kolah-Kaj, P.**, Baez Lozada, L., Rongier, G., Barnhoorn, A., Vardon, P. J., & Abels, H. A. *Integrating experimental and log data to predict thermal properties in geothermal plays using machine learning*, *Scientific Reports*.

Peer-reviewed journal articles

5. Najafi-Silab, R., Soleymanzadeh, A., **Kolah-Kaj, P.**, & Kord, S. (2023). Electrical rock typing using Gaussian mixture model to determine cementation factor. *Journal of Petroleum Exploration and Production Technology*, 13, 1329–1344. <https://doi.org/10.1007/s13202-023-01612-7>
6. Shad, S., **Kolah-kaj, P.**, & Zivar, D. (2023). Geomechanical analysis of an oil field: Numerical study of wellbore stability and reservoir subsidence. *Petroleum Research*, 8(3), 350–359. <https://doi.org/10.1016/j.ptlrs.2022.08.002>
7. **Kolah-Kaj, P.**, Kord, S., & Soleymanzadeh, A. (2022). Application of electrical rock typing for quantification of pore network geometry and cementation factor assessment. *Journal of Petroleum Science and Engineering*, 208, 109426. <https://doi.org/10.1016/j.petrol.2021.109426>
8. Soleymanzadeh, A., **Kolah-Kaj, P.**, Najafi-Silab, R., & Kord, S. (2021). Correlating rock packing index, tortuosity, and effective cross-sectional area with electrical quality index. *Journal of Natural Gas Science and Engineering*, 96, 104302. <https://doi.org/10.1016/j.jngse.2021.104302>
9. Aboozar, S., **Kolah Kaj, P.**, Kord, S., & Monjezi, M. (2021). A new technique for determining water saturation based on conventional logs using dynamic electrical rock typing. *Journal of Petroleum Science and Engineering*, 196, 107803. <https://doi.org/10.1016/j.petrol.2020.107803>
10. **Kolah-Kaj, P.**, Kord, S., & Soleymanzadeh, A. (2021). The effect of pressure on electrical rock typing, formation resistivity factor, and cementation factor. *Journal of*

Petroleum Science and Engineering, 204, 108757.

<https://doi.org/10.1016/j.petrol.2021.108757>

11. Ashoori, S., Safavi, E., Moghaddasi, J., & **Kolah-Kaj, P.** (2021). Experimental investigation of permeability reduction due to migration of non-swelling clay minerals. *Iranian Journal of Oil and Gas Science and Technology*, 10(3).

Conference contributions

12. Haji Bolouri, E., **Kolah Kaj, P.**, & Bahari Moghaddam, M. (n.d.). Analytical solution of polymer flow equation in porous media. *Chemistry and Chemical Engineering of Iran*.
13. **Kolah Kaj, P.**, Abels, H. A., Barnhoorn, A., & Vardon, P. J. (2024). [Conference abstract]. *Fifth EAGE Global Energy Transition Conference & Exhibition (GET 2024)*. <https://doi.org/10.3997/2214-4609.202421230>

Research dataset

14. **Kolah Kaj, P.**, Abels, H. A., Barnhoorn, A., Vargas Meleza, L., & Vardon, P. J. (2024). *Database of experimental data on three geothermal plays in the Netherlands from the ProperBase project* [Data set]. 4TU ResearchData. <https://doi.org/10.4121/63c28ba2-fbde-486f-9d82-660ab3a5c990>

